SUSPENDED MANUFACTURING OF MULTI-LAYERED BIOPOLYMER HYDROGELS FOR TISSUE ENGINEERING

JESSICA JADE SENIOR

A thesis submitted to the University of Huddersfield in partial fulfilment of the requirements for the degree of Doctor of Philosophy

The University of Huddersfield

Final submission date – December 2020

Copyright statement

Abstract

Tissue engineering is proving a promising tool as an alternative to relying on donor availability in restorative tissue therapeutics. Tissue engineering concepts entail combining cells and materials *in vitro* to generate 3D parts that replicate *in vivo* tissue environments. Much focus has been spent on researching biopolymer hydrogels as scaffolds within tissue engineering constructs as there is vast potential in their tailorability to simulate the extracellular matrices within native human tissues. Although many features within hydrogels may be finely tuned when developing tissue engineering implants, such as water content, mechanical properties, and microarchitecture, current studies in this area are seldom able to recapitulate the physicochemical and mechanical gradients that are exhibited in human tissues, within a single construct. Moreover, the hydrogel precursor solutions used in 3D bioprinting tissue engineering constructs are usually manipulated towards enhancing either print fidelity (by increasing solution viscosity) or to preserve the viability of suspended cells (by decreasing the viscosity of precursor solutions). 3D bioprinted tissue engineering constructs therefore often fail to harbour both optimal print fidelity in conjunction with viable encapsulated cells thus leaving the intended tissue engineering ECM environment poorly reproduced. The work presented in this thesis addresses these problems and demonstrates that the success of a tissue engineering construct need not be compromised by the usual trade-off between print fidelity and cell viability and can in fact possess both of these features that are crucial to the function of the part. This technology uses a supporting gel bed within which multiple cell/hydrogel printing solutions are layered to keep the construct in shape prior to solidifying. The mechanisms behind the function of the supporting gel bed as a suspending agent were first analysed, showing that its shear-thinning behaviour allows material to be deposited within it followed by rapid restructuring to uphold the construct shape. A range of contrasting hydrogels and cell types were then 3D bioprinted into multiple layers and configurations, pushing the boundaries of what can usually be achieved when conventionally 3D printing low viscosity solutions onto a planar surface. As an example of the potential of this technique in becoming commonplace in the clinic, a chronic-depth skin equivalent was 3D printed, complete with hypodermis, dual compartment dermis and epidermis. The construct contained gradients in material chemistry, mechanical properties, microarchitecture, and cell phenotype, and served as an example of the capacity that this system holds in generating highly sophisticated human tissue mimics.

Acknowledgements

I would first like thank my supervisors Professor Alan Smith and Dr Vassilis Kontogiorgos for playing a huge role in shaping me into the researcher I am today. They have guided me, believed in me, and have given me every opportunity, right from the very start. I will be forever grateful to have worked with such brilliant minds. I would also like to thank the lab technicians, including Emma Pinder, Hayley Markham, James Rooney, Ibrahim George, and Felix Owusu-Kwarteng for their valuable assistance in the lab.

My gratitude also goes out to the other research groups within the University who have played a pivotal role in allowing my multidisciplinary research to be realised. I particularly would like to thank the groups of Dr Hans Hennies, Dr Olumayokun Olajide, Dr Nikolaos Georgopoulos, Professor Roger Phillips, Dr Muhammad Usman Ghori, and Dr Jane Harmer for sharing their knowledge, expertise, and equipment. I must also acknowledge Professor Liam Grover at the University of Birmingham for his valued contributions towards our collaborative work.

I would like to say a big thankyou to my wonderful friends, Daisy, Kate, and Georgina, for always cheering me on from the side-lines with a cocktail in hand. Through thick and thin, you have always been there for me. Although they may have been more of a hinderance than help whilst writing my thesis, I would like to give mention to Hamish and Ethel for the love and the comfort they have given.

Last of all, I would like to give my biggest thanks to my family for their unwavering support in everything I have ever done. Thank you to my parents, Sandra and Kevin, without all of your support, encouragement and determination to provide me with everything I ever could have needed, none of this would have been possible. Thank you to my sister who is living her dream in New Zealand, though we are far away in distance, we are as close as ever. Thank you to my Fiancé Steve for being my laughter and my light, and for being strong for me when I have struggled to find the strength.

My final mention goes to my little girl Reeva, whom I carried during the end of my lab work. You are my firecracker, I love you with all my heart, and I will always endeavour to provide you with everything that you may ever need to realise your own aspirations.

Contents

List of Figures

Abbreviations

2D	Two-Dimensional
3D	Three-Dimensional
ADSC	Adipose Derived Mesenchymal Stem Cell
ALM	Additive Layer Manufacturing
$CaCl_2$	Calcium Chloride
CAD	Computed Automated Design
CT	Computed Tomography
DMEM	Dulbecco Modified Eagle Medium
ECM	Extracellular Matrix
EEO	Electroendosmosis
FBS	Fetal Bovine Serum
G′	Elastic Modulus
G″	Viscous Modulus
GAG	Glycosaminoglycan
HDF	Human Dermal Fibroblast
HEK	Human Epidermal Keratinocyte
IBMX	Isobutylmethylxanthine
ID	Internal Diameter
iPSC	Induced Pluripotent Stem Cell
LM	Low Methyl Ester
LVR	Linear Viscoelastic Region
MRI	Magnetic Resonance Imaging
MSC	Mesenchymal Stem Cell
Mw	Molecular weight
PBS	Phosphate Buffered Saline
PVF	Particle Volume Fraction
RGD	Arginine, Glycine, Aspartic Acid
rpm	Revolutions per minute
SEM	Scanning Electron Microscopy
SLAM	Suspended Layer Additive Manufacturing
STL	Stereolithography
TE	Tissue Engineering
UV	Ultraviolet

Publications

Senior, J.S. Cooke, M.E. Grover, L.M. Smith, A.M. (2019) Fabrication of Complex Hydrogel Structures using Suspended Layer Additive Manufacturing (SLAM). Advanced Functional Materials, 29, 49.

Senior, J.S. Grover, L.M. Smith, A.M. A Suspended Layer Additive Manufacturing (SLAM) Approach to the Bioprinting of Tri-Layered Skin Equivalents - Submitted to Biophysics of Biofabrication.

Smith, A.M & **Senior, J.S.** 3D Printing Techniques in Medicine. In: Kalaskar. D. M. 3D printing in Medicine, 2nd Edition, Duxford, UK: Woodhead Publishing – In preparation for submission.

Smith, A.M & **Senior, J.S.** Alginate Hydrogels with Tuneable Properties. Publishing in: Fiechter, A. Tunable Hydrogels: Smart Materials for Biomedical Applications, Advances in Biochemical Engineering/Biotechnology, Berlin; New York: Springer-Verlag

Conference Presentations

11th – 13th June 2019 – TCES & UKSB Joint Conference, Nottingham (UK)

Poster Presentation – Suspended Layer Additive Manufacturing of a Tri-layer Skin Model (J.J Senior & A.M Smith)

9th – 11th January 2019 - RSC Biomaterials Chemistry Annual Conference, Liverpool (UK)

Oral Presentation - Suspended Layer Additive Manufacturing and the Fabrication of Complex 3D Tissue Scaffolds (J.J Senior & A.M Smith) **Award Winner with Free 1 Year RSC Membership**

9th – 13th September 2018 – 29th European Society for Biomaterials, Maastricht (Netherlands)

Session Chair and Oral Presentation - 3D printing chimeric hydrogel scaffolds using suspended additive layer manufacturing (SALM) (J.J Senior, M.E Cooke, E.A.B Hughes, M.U Ghori, V. Kontogiorgos, L.M Grover, A.M Smith)

11th – 13th June 2018 – UKSB 17th Annual Conference, Bath (UK)

Oral Presentation – Chimeric Hydrogels: 3D Printed Tissue Engineering Scaffolds with Chemical and Mechanical Gradients (J.J Senior, S.R Moxon, M.U Ghori, M.E Cooke, L.M Grover, A.M Smith)

10th – 11th January 2018 – RSC Biomaterials Chemistry Annual Conference, Bradford (UK)

Oral Presentation - 3D Printed Multiphasic Biopolymer Scaffolds for Tissue Engineering (J.J Senior, M.E Cooke, E.A.B Hughes, L.M Grover, A.M Smith)

13th September 2017 – 3rd UK Hydrocolloids Symposium, Loughborough (UK)

Oral Presentation - Addressing the Challenges of 3D Bioprinting using Low Viscosity Biopolymers by Employment of Suspended Manufacturing Methods (J.J Senior, S.R Moxon, A.M Smith)

20th June 2017 – UKSB 16th Annual Conference, Loughborough (UK)

Poster Presentation - Suspended Additive Layer Manufacturing: An Alternative Approach to 3D Bioprinting using Low Viscosity Biopolymers (J.J Senior, S.R Moxon, A.M Smith)

Chapter 1

INTRODUCTION TO TISSUE ENGINEERING

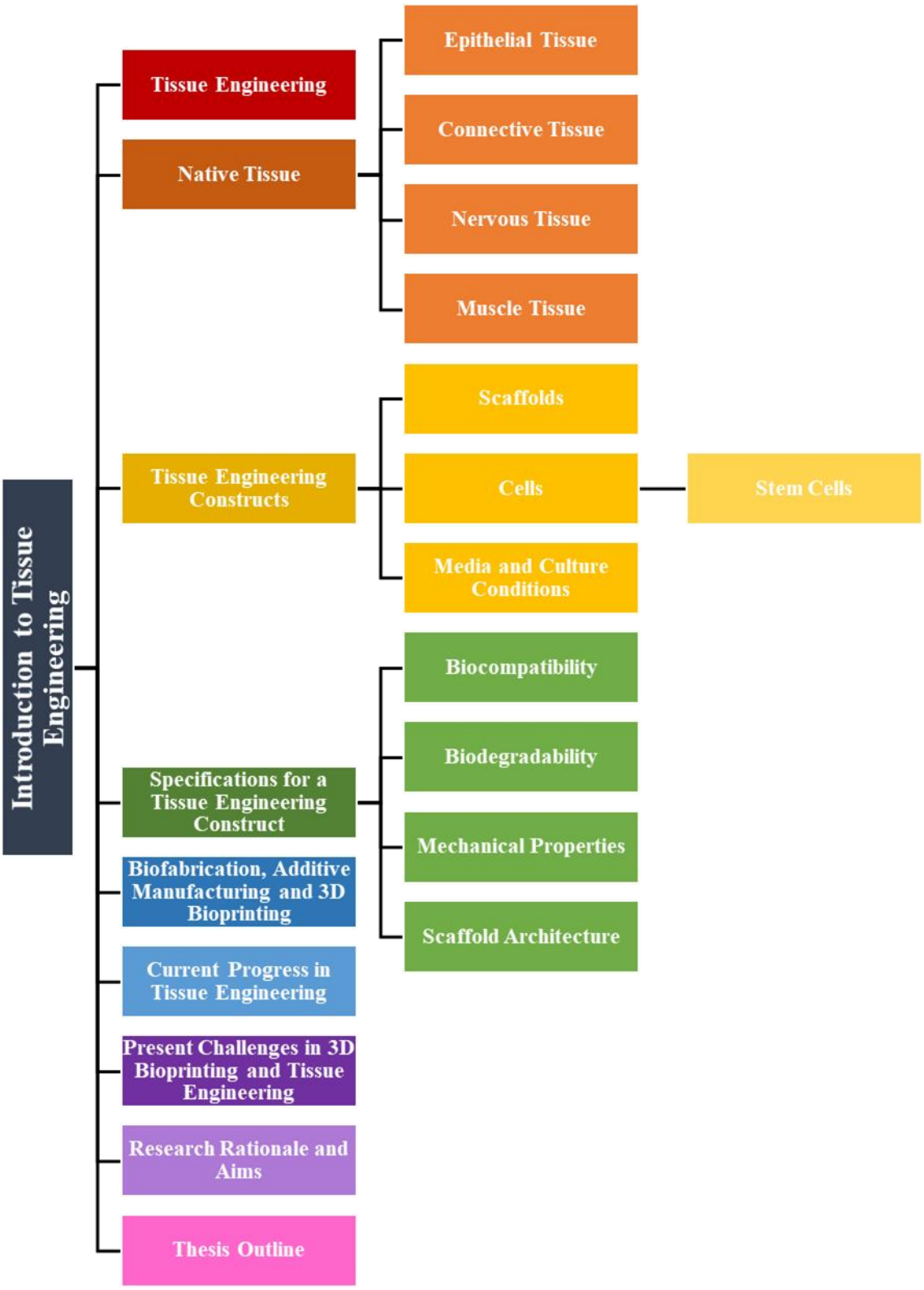
Introduction to Tissue Engineering
Tissue Engineering
Native Tissue
Epithelial Tissue
Connective Tissue
Nervous Tissue
Muscle Tissue
Tissue Engineering Constructs
Scaffolds
Cells
Stem Cells
Media and Culture Conditions
Specifications for a Tissue Engineering Construct
Biocompatibility
Biodegradability
Mechanical Properties
Scaffold Architecture
Biofabrication, Additive Manufacturing and 3D Bioprinting
Current Progress in Tissue Engineering
Present Challenges in 3D Bioprinting and Tissue Engineering
Research Rationale and Aims
Thesis Outline

Chapter 1 – Introduction to Tissue Engineering

1.1 Tissue Engineering

The average lifespan of our ever-growing population has continued to rise ever since records began. In recent years, especially in more developed regions of the world, a decrease in mortality rate is attributed to enhancing medical intervention. However, with increased longevity comes a larger risk of age-associated tissue and organ failure and further therapeutic mediation is needed (Olson et al., 2011). Organ and tissue transplantation or surgical reconstruction is often implemented in order to remedy this, whereby defective tissues are excised and replaced with the healthy tissue of a donor, yet overcoming immune rejection and the clinical demand for organ donors still remain critical challenges (Dzobo et al., 2018). Tissue engineering is a relatively new field of research which has seen tremendous progression towards the successful restoration, maintenance and augmentation of biological function within the human body (Chen & Liu, 2016). Newly emerging tissue engineering strategies have the potential to circumvent the limitations that are present in current conventional therapies when repairing human tissue. These strategies are less invasive in nature and offer an alternative to the growing demand for tissue and organ donors. Tissue engineering also provides a long term and cost-effective solution to the treatment or eradication of disease thus improving quality of life. As a consequence, tissue engineering has received much attention as an attractive approach toward tissue restoration (Peltola et al., 2008).

The phrase ‘tissue engineering’ (TE) as we know it today was first used in 1988 at a National Science Foundation workshop, employing the theoretical bases of engineering and life sciences toward further understanding of the functional mechanisms within healthy mammalian tissue. With this, the production of biological alternatives in order to restore non-healthy tissue could be explored (Lanza et al., 2013). The many disciplines which comprise tissue engineering include medicine, engineering, cellular biology and materials science and each component contributes to the optimisation of the final

engineered part (Howard et al., 2008). Recent advances in this area have allowed the production of more biologically and geometrically relevant constructs *in vitro* that closer mimic their intended *in vivo* environments, meaning that the boundaries and limitations that once stood in the way of tissue engineering are now beginning to diminish. Several approaches are now being used to address the prospect of organ replacement using tissue engineering principles. These include (but are not limited to) i) cell-seeding of a pre-made porous biodegradable scaffold, ii) the decellularization and recellularization of pre-existing extracellular matrix (ECM), iii) cell sheet engineering with self-secreted ECM and iv) cell encapsulation within a supporting hydrogel matrix (**Figure 1.1**) (Do et al., 2015; O'Brien, 2011; Tee et al., 2010). The most commonly practiced methods amongst these are the use of biopolymer materials as cell-loadable scaffolds. This technique involves the design and manufacture of biopolymer constructs for the replication of native ECM (within which cells naturally reside) and will be the main focus within this thesis.

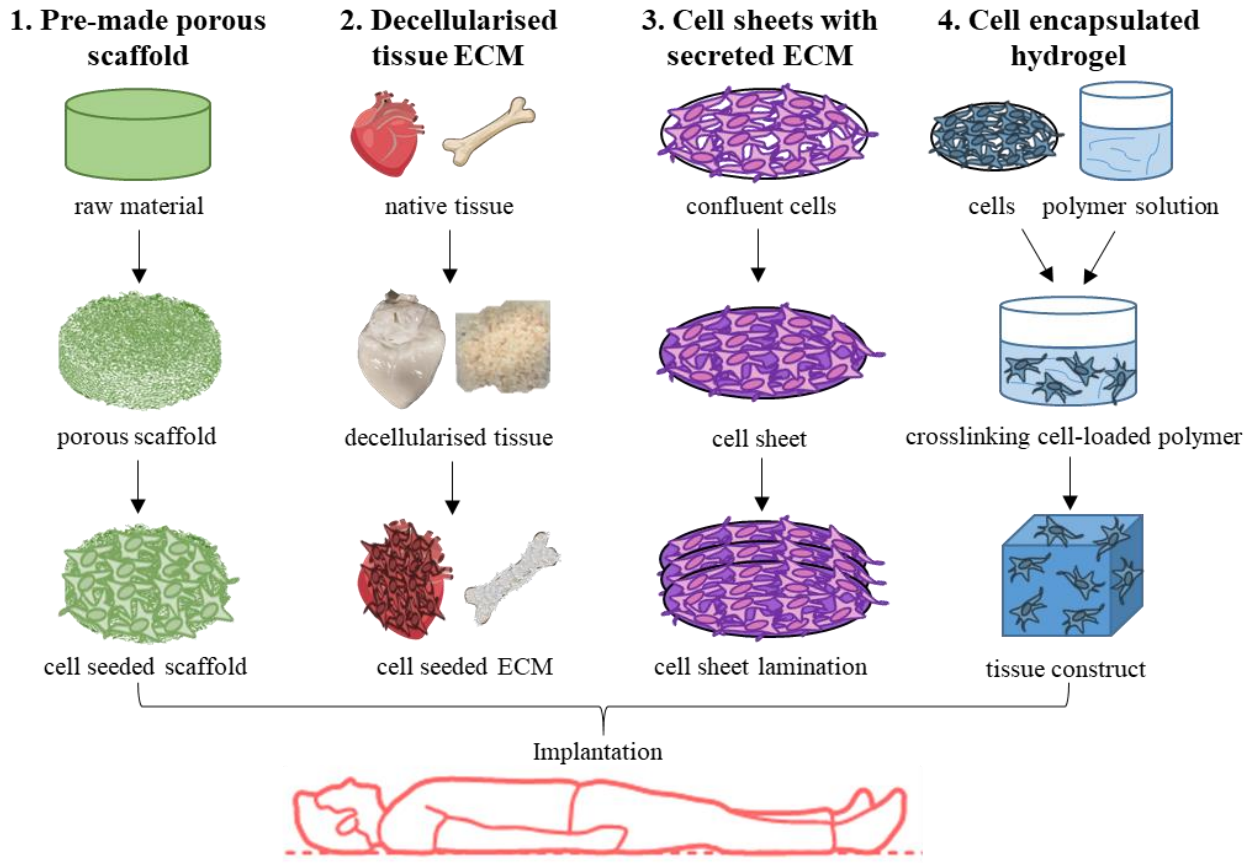

Figure 1.1 – A brief overview of current scaffolding approaches used in tissue engineering for implantation.

1.2 Native Tissue

Within the human body, tissues are an organisation of cells that share a common embryonic origin and work together toward a specific bodily function. In order to achieve this specific function, tissue composition varies greatly down to the molecular level, comprising a multitude of different cellular and extracellular components and also varying in the degree in which these components are present (Andrew & Rawdon, 1987). The extracellular matrix (ECM) portion of tissues supports cells by supplying the biochemical and structural means needed for cellular attachment, proliferation, migration and differentiation. ECM itself is secreted and oriented by residing cells during microenvironment remodelling (Yue, 2014).

There are four main tissue categories, each with their own defining function: epithelial, connective, nervous and muscle tissue. Subsequent ordering of hierarchical tissues forms organs and organ systems for the maintenance of the human body as a whole (Kular et al., 2014). Skin for example contains these four major tissue structures as illustrated below (**Figure 1.2**).

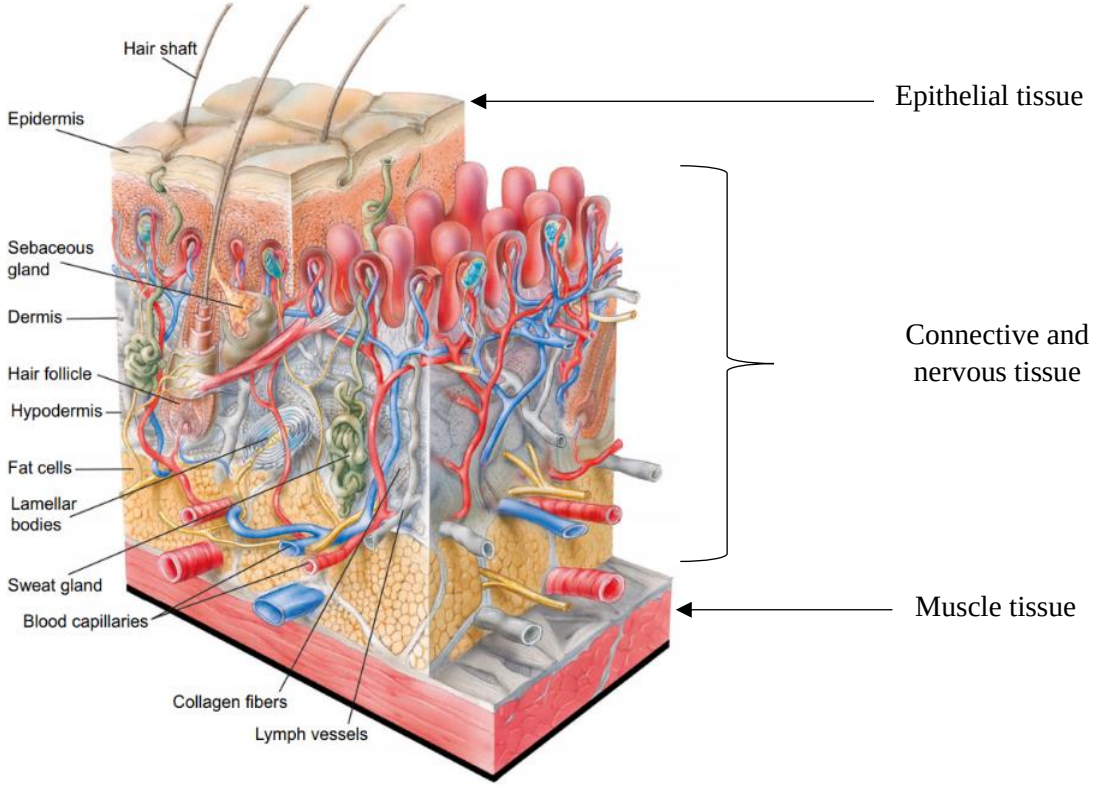

Figure 1.2 - Schematic diagram illustrating the four major types of tissue within the skin organ (adapted from Aldag et al., 2016).

1.2.1 Epithelial Tissue

Epithelial tissues exhibit minimal ECM composition in contrast to other tissue types. They are constituted primarily of cells bound by a strong intracellular cytoskeleton which is attached to the basal lamina via specialised junctions (Alberts et al., 2002). Epithelial tissues line the outer skin (epidermis) as well as the cavities of compartmentalised internal structures and their predominant role in tissue function is to control the passage of water, solutes and cells from adjacent tissues. The basal lamina forms the interface between epithelial cell layers and connective tissues. Although epithelia have a nervous supply, they lack a venous blood supply and therefore rely on the diffusion of molecules from the blood vessels of underlying tissues. Due to the harsh external environments to which epithelia are faced, epithelial tissue homeostasis is a stringently regulated process in which epithelia are constantly renewed by stem cells (Blanpain & Fuchs, 2014).

1.2.2 Connective Tissue

Out of all the tissue types, connective tissue is most abundant in ECM with comparatively fewer cells that are predominantly in the form of fibroblasts. Connective tissue ECM varies vastly and is dependent upon the location at which it is synthesised and secreted (Alberts et al., 2002). Loose connective tissue (such as adipose tissue) is rich in ground substance made of polysaccharides that fill the voids between collagenous, elastic and reticular fibres and cells. Adipose tissue is also regarded as a specialised connective tissue due to the specialised nature of adipocytes that are present within these matrices (Nakajima et al., 1998). Dense connective tissues such as tendons, ligaments and dermis are comparatively more abundant in collagenous fibres than loose connective tissue. Some dense connective tissue structures, including bone, exhibit additional ECM components, such as inorganic calcium phosphate deposits, which contribute to their stiffness and their role in the protection of vital organs. Blood is also considered as connective tissue (Marieb & Hoehn, 2012).

1.2.3 Nervous Tissue

Nervous tissue is defined by its excitability and its capacity to propagate electrical impulses (known as action potentials) which traverse between the central nervous system and the rest of the body. These signals are responsible for allowing internal and external stimuli to be relayed as information to the brain for an appropriate response to be effected by the body (Vecino & Kwok, 2016). The ECM in nervous tissue, which is secreted by neural cells, is rich in collagens and glycosaminoglycans (GAG) such as chondroitin sulphate (CS), heparan sulphate (HS) and hyaluronan (HA). These complexes play a part in neurogenesis, modulation of synaptic connections and pro-inflammatory responses in central nervous system (CNS) autoimmunity (Mueller et al., 2014; Yamaguchi, 2010).

1.2.4 Muscle Tissue

Unlike other tissue types, muscle has contractile capacity thus allowing the actuation of voluntary responses such as body movement, or involuntary responses including mechanical digestion and the systemic transport of blood. As with other tissues, their signature ECM conformations underlie their functional roles. Much of the variations in different muscle ECM can be attributed to the alignment of collagen fibres embedded within a proteoglycan matrix (Schuliga, 2015). Smooth muscle undergoes spontaneous regeneration through the division of pericytes (Berry, 1920). The human body cannot, however, regenerate cardiac muscle and following trauma and subsequent scar tissue formation, loses its contractile capacity. In addition, skeletal muscle has a limited regenerative capacity by the recruitment of satellite cells. If the damage to skeletal muscle exceeds the reparative potential of recruited satellite cells, muscle fibres are replaced with scar tissue during fibrosis and muscle function may be compromised (Purslow, 2008).

1.3 Tissue Engineering Constructs

Some tissues are unable to undergo regeneration by the human body, prevented by limited vascular invasion within large defects, the collapse of surrounding tissue into the defect and excessive mechanical strain in reparative tissue within unstable fractures. As a consequence, there is a clinical need for the introduction of exogenous tissue engineering components in order to facilitate tissue repair (Yannas, 2014). Tissue engineering constructs are designed to mimic the tissues that they are destined to replace, featuring similar cellular and extracellular environments and subsequently degrading at the same rate as new tissue formation is established (Velasco et al., 2015). They are 3D in shape, providing a better representation of native tissues compared with 2D cell culture, which is unable to recapitulate complex *in vivo* environments and the spatial arrangements of cells and tissue ECM. Tissue engineering constructs often employ a triad of components including scaffold material, cells and media / culture conditions for the fabrication of engineered tissue mimics. These constructs may then be destined either for implantation or for research within systems such as drug-disease modelling (**Figure 1.3**).

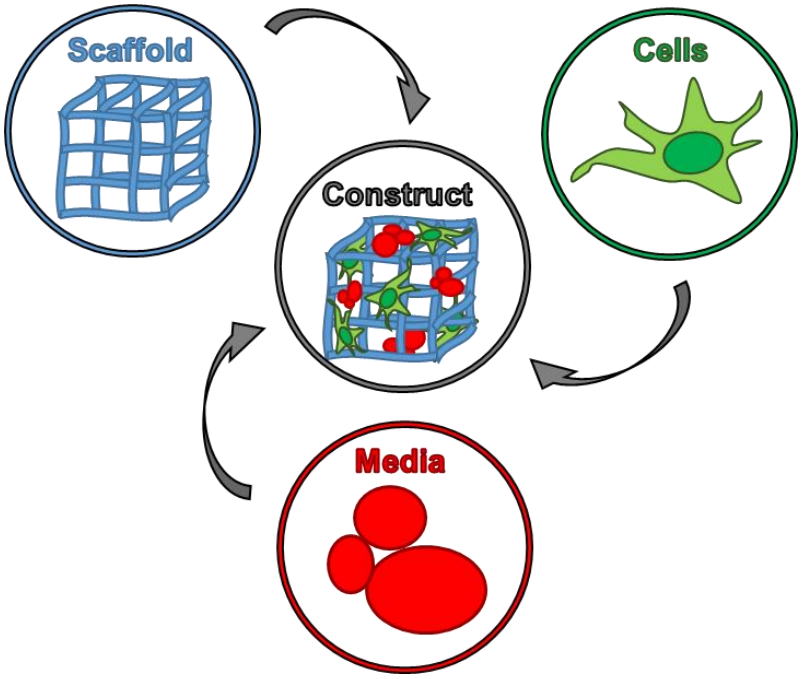

Figure 1.3 - Components of the tissue engineering triad: scaffold, cells and media / culture conditions constitute and define a tissue construct.

1.3.1 Scaffolds

Scaffolding in tissue engineering refers to the material matrix from which the tissue mimic is fabricated. For the successful manufacture of a tissue engineering construct, the scaffold material must resemble the native tissue ECM of which it wishes to replicate (Chan & Leong, 2008). For instance, connective tissues such as adipose, tendons and ligaments contain an abundance of collagens and glycosaminoglycans that provide their structural properties. Therefore, when fabricating tissue engineering scaffolds that aim to mimic these tissues, the incorporation of collagenous and GAG components can generate connective tissue-like environments (Caliari et al., 2011). The scaffolds themselves play multiple roles in tissue augmentation and repair and may either be injected or transplanted within the body. They provide a framework within which exogenous cells and biological molecules can be delivered to the defect site whilst also providing a template within which neighbouring endogenous cells can attach, migrate and proliferate, thus guiding new tissue formation (Koch et al., 2009). Moreover, the placement of an acellular scaffold within an open dermal wound has been seen to prevent premature closure, tissue contraction and scar formation (Wainwright & Bury, 2011). Using this technique, the surrounding cells are provided with anchorage in order to infiltrate the scaffold and healing can occur without the closure of the wound causing deformation.

1.3.2 Cells

When cellular mitotic activity within a tissue is impaired or inadequate, it may be necessary to introduce exogenous cells within the tissue system. Cells may be retrieved for incorporation within a tissue scaffold from several sources. Whilst xenogeneic cell isolation (from a different species) or allogeneic cell sources (from different members of the same species) may provide a larger pool of potential cell sources to be exploited at a lower cost, utilisation of these cells comes with a higher risk of disease transmission and immune rejection following transplantation (Boneva et al., 2001; Michler, 1996). Alternatively, autologous cells isolated from the patient receiving tissue engineering therapy offers a more promising approach to successful cell transplantation as the likelihood of immune

rejection reduces drastically (Langer & Vacanti, 1993). The selection of autologous cells, however, is associated with donor site morbidity and in many cases, few cells can be harvested from the donor site, generating the need for time consuming culture and expansion of cells. Furthermore, the option of autologous cells in the case of diseased tissues and elderly patients might not always be appropriate (Heath, 2000). Despite these drawbacks, grafting and implantation using autologous cells and tissues is currently the most practiced method in tissue restoration.

Another consideration in the selection of cells for integration within a tissue-engineering scaffold is in the election of differentiated or uncommitted cells. Using primary, differentiated cells in tissue constructs involves the isolation of cells that match those to be replaced within a tissue defect, i.e. extracting human dermal fibroblasts from a healthy patient's dermis for culture within a dermal tissue construct. This method is convenient as there is no requirement for a differentiation process to be undertaken (Hench & Jones, 2005). Despite this, using differentiated cells is associated with donor site morbidity and limited availability and cells of this nature encompass a finite proliferative and biosynthetic capacity. Furthermore, primary cells, upon multiple passaging, have a tendency to de-differentiate during *ex vivo* cultivation thus losing their appropriate phenotype (Fitzpatrick & McDevitt, 2015).

1.3.2.1. Stem cells

Perhaps the most promising cell types within tissue engineering are stem cells due to their potential to overcome the issues associated with committed cells. Their prolonged self-renewal capabilities and their ability to differentiate into cells that would otherwise fail to regenerate once committed make them of high interest. Three main types of stem cells are available, each with varying differentiating capacity: embryonic, adult and induced pluripotent stem cells (Chen et al., 2009). The developmental plasticity of human embryos makes them ideal sources for harvesting stem cells. Within the first divisions following fertilisation, embryonic stem cells exhibit totipotency (the ability to give rise to all cell types) and following this period are pluripotent in nature (having the ability to give rise to

many cell types) (Atala et al., 2008). Despite the attraction of having the largest differentiation capacity, they are derived from allogenic sources and are associated with many ethical concerns. In contrast, autologous, multipotent adult stem cells from that of a patient are available for isolation from a variety of tissues including the stroma of bone marrow, dental pulp, hair follicle and subcutaneous adipose (Hodgkinson, Yuan, & Bayat, 2009). The progeny of adult stem cells isolated from these regions display variable degrees of differentiation along mesodermal, endodermal and ectodermal phenotypic lineages (**Figure 1.4**).

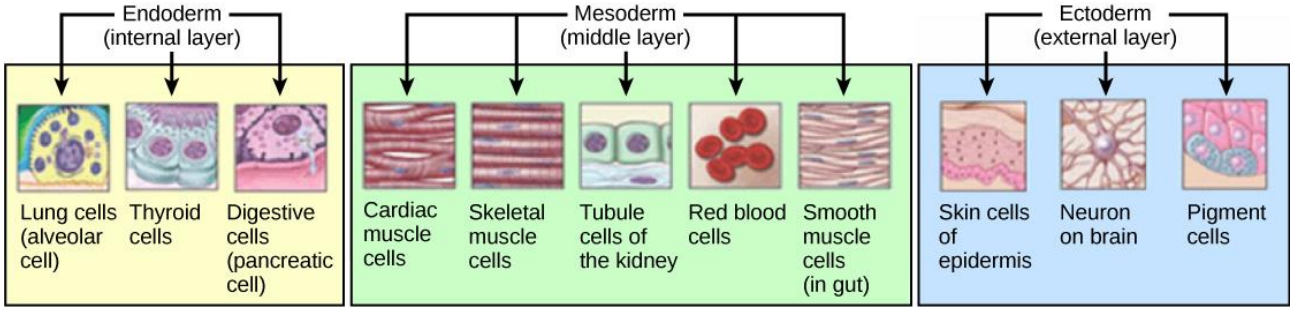

Figure 1.4 - Endodermal, mesodermal and ectodermal germ layers and their differentiated progeny (Kirschstein & Skirboll, 2001).

Other than self-renewal, the role of adult stem cells is to replenish differentiated cell numbers following damage or apoptosis. The fact that they exist at low quantities within tissues, however, requires stringent differentiation procedures following extraction. An alternative source of stem cells termed 'induced pluripotent stem cells' (iPSCs) are thus being investigated, defined as pluripotent stem cells artificially derived from non-pluripotent stem cells (typically from adult progenitor cells). Initially researched in mice in 2006, this technique evolved in 2007 following the introduction of four genes (Oct-3/4, Sox2, c- Myc, and KLF4) into adult human dermal fibroblasts. The morphology, proliferation, gene expression and epigenetic status of pluripotent cell-specific genes within iPSCs are subsequently concurrent with those of embryonic stem cells following gene transfer (Takahashi et al., 2007). Exploration into the use of iPSCs in order to overcome the present issues associated with stem cells is currently at the forefront of interest within tissue engineering.

The purification and homogenisation of cell populations by removal of unwanted cell types is of critical importance when being used in therapeutic intervention as contaminations of undifferentiated iPSCs and human embryonic stem cells are potentially capable of forming teratomas following injection. Moreover, regulatory T (Treg) cells are currently under study as potential candidates in Graft versus Host Disease (GvHD) treatment by promoting tolerance after allogenic cell transplantation, yet ironically share several surface antigens with alloreactive T cells, capable of eliciting GvHD in recipients. Cells can be separated based on their physical properties (such as cell density gradient centrifugation for isolation of leukocytes from whole blood) or biological properties (based on plastic adherence status for separating MSCs from bone marrow aspirates), however, surface antigen-based techniques, including flow cytometric sorting, are capable of generating the highest purity output possible and have been used for the isolation of CD34+ human adipose derived mesenchymal stem cells (ADSC) (Donnenberg et al., 2013; McIntyre et al., 2010).

1.3.3. Media and culture conditions

For the fabrication of a tissue engineering construct, in addition to the careful selection of scaffold material and encapsulation of cells, media and culture conditions are often optimised in order to direct the outcome of the final product. Whilst the scaffolding materials play a major part in determining cellular morphology and behaviour, additional supplements such as amino acids, growth factors, reagents and hormones can provide cells with the biochemical milieus often found in native tissues (Lee et al., 2011). By cultivation of mesenchymal stem cells within defined media, the proliferation and differentiation of multiple cell lineages may be achieved. For instance, when the compound isobutylmethylxanthine (IBMX) is introduced within mesenchymal stem cell (MSC) culture along with indomethacin and dexamethasone, PPARγ (peroxisome proliferator-activated receptors) activation is upregulated and adipogenesis is initiated (Scott et al., 2011). Alternatively, supplementing MSCs with β-glycerophosphate combined with ascorbic acid and dexamethasone at critical levels induces osteogenic gene expression by extracellular related kinase phosphorylation

(Langenbach & Handschel, 2013). The use of basic media containing essential amino acids is typically standard across most tissue engineering practices, providing cells with the metabolites that are essential in cell survival and proliferation (Todd, 2014).

Tissue constructs may be further subjected to a modulated external environment in order to recapitulate the environments experienced by native tissues. By tailoring oxygen concentrations, hypoxic, normoxic and hyperoxic conditions may be simulated that reflect target tissue environments. Culturing keratinocytes at the air-liquid interface in a similar mechanism to how skin epidermis is propagated *in vivo* is one example of how oxygen modulation can be achieved. In other circumstances, application of mechanical loading portrays the forces endured by tendons and ligaments *in vivo*, thereby guiding cell phenotype into tenocyte and fibrocyte lineages (Benhardt & Cosgriff-Hernandez, 2009; Yazdani, 2016). Using the tissue engineering triad, the specifications for a tissue-engineering construct can be met.

1.4 Specifications for a Tissue Engineering Construct

Several key parameters need to be met in all tissue-engineering constructs so that the prospective implant is successfully integrated within human tissue. In general, constructs must be conducive to the *in vitro* propagation of cells in a way that the native tissue being replicated develops *in vivo.* The suitability of a construct for tissue engineering purposes is usually defined by the following: biocompatibility, biodegradability, mechanical properties and scaffold architecture (O'Brien, 2011) (**Figure 1.5**).

1.4.1 Biocompatibility

Perhaps the most important principle in the assembly of an effective cell-scaffold complex is biocompatibility. It is essential that cells infiltrate the tissue scaffold, assume normal function and eventually replace the supporting scaffold by secreting their own ECM without evoking the generation of an immune response (Remes, 2006). Many factors can affect the biocompatibility of a

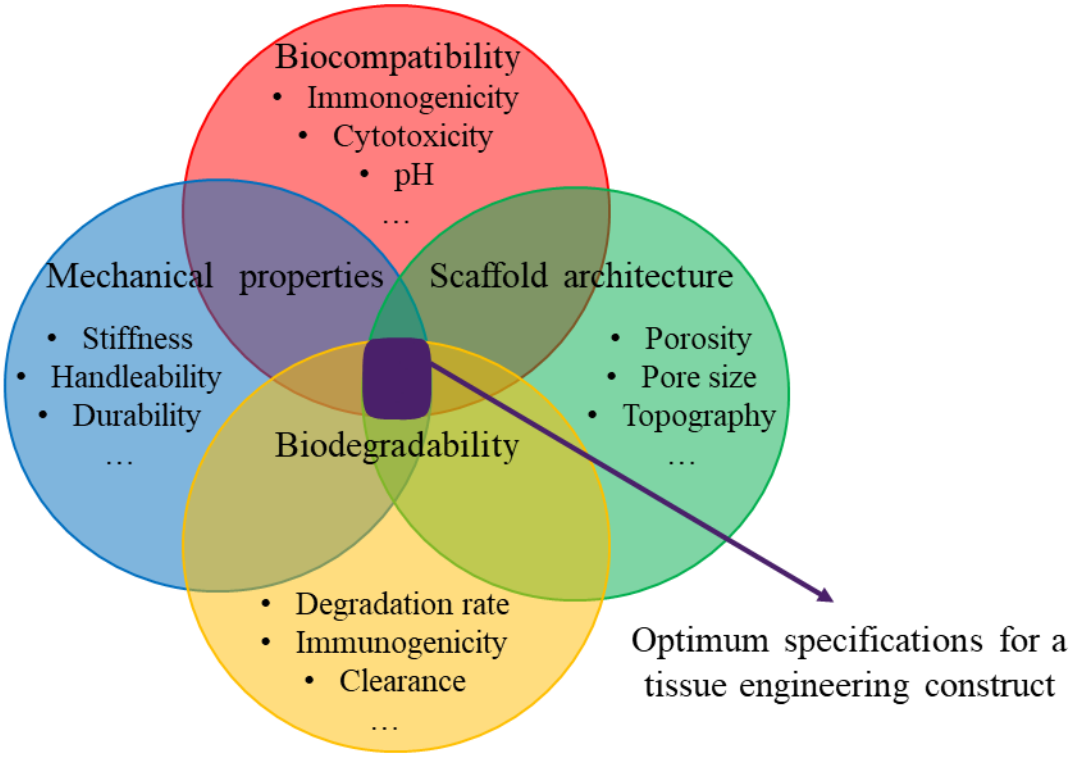

Figure 1.5 - Tailoring biocompatibility, scaffold architecture, biodegradability and mechanical properties in TE.

tissue construct including cell source and scaffold material. Unless immunosuppressive therapy is administered upon transplantation of allogenic and xenogenic cells, the transfer of foreign antigens often elicits an inflammatory response within the host, causing rejection of the implanted part. Regarding scaffold material, natural material sources are usually favoured over the use of synthetic materials as they better resemble the chemical structures of native tissues (Ikada, 2006).

1.4.2 Biodegradability

Another consideration when designing a tissue engineering construct is the biodegradability of the material within a tissue scaffold. The sole purpose of the scaffold is to encourage cells to establish their own ECM network and thus eventually replace the engineered part (Tan & Marra, 2010). Material biodegradability should occur in tandem with the rate at which neo-tissue formation occurs at the site of implantation. Scaffold by-products should also be excreted from the body without impedance on normal bodily function (Brown et al., 2009).

1.4.3 Mechanical Properties

Additional parameters that are key to the successful culture of a tissue engineering construct are the mechanical properties of the tissue equivalent. Cells are capable of surveying external mechanical influences via mechanotransduction and respond appropriately to such stimulation through mechanoreciprocity. Within mechanically static or compliant tissues such as the neural network, tissues exhibit low stiffness. In contrast, tissues that are exposed to a high degree of mechanical loading, including bone or skeletal muscle, exhibit ECM stiffness that is several orders of magnitude greater (Engler et al., 2006). Therefore, the behaviour of cells is inherently tissue-specific and is highly dependent upon the stiffness of the substrate in which they reside. Furthermore, in studies of mechanical influence on cell behaviour, adult lung cells of fibroblastic origin that have been grown on rigid substrates undergo myofibroblast differentiation and assume a contractile phenotype. Cells retain these behaviours even when transferred to soft substrata, implying that cells retain memory of past mechanical environments (Humphrey et al., 2014).

1.4.4 Scaffold Architecture

Though mechanical properties are important, it is also imperative that a certain degree of porosity exists within the construct in order for cell infiltration, the establishment of vascular tissue and subsequent diffusion of waste products away from the tissue construct (Hollister, 2005). Within scaffolds containing little porosity, pore size and interconnectivity, cell growth and invasion is limited due to restricted space and minimal access of cell metabolites. For scaffolds exhibiting high porosity, pore size and interconnectivity, insufficient tethering reduces cell traction and limits cell migration (Loh & Choong, 2013). The critical balance of ambient porosity conditions is therefore essential for the fabrication of a tissue scaffold. Furthermore, surface topography also procures alternative mechanisms for cell-biomaterial interplay and regulates cell response. As previously seen, cells cultured on rougher surfaces are bound and constrained by high ridges and low valleys as opposed to widespread cells on smoother substrata that establish strong actin networks (Wu & Zhang, 2015).

1.5 Biofabrication, Additive Manufacturing and 3D Bioprinting

In its first instance in 1994, the term 'biofabrication' was used towards the naturally occurring process of the biomineralisation of pearls, but in the world of tissue engineering is commonly related to the use of biological materials and cells using specific mechanisms for construction (Groll et al., 2016). Additive manufacturing (or additive layer manufacturing) is a set of technologies used to describe the build-up of 3D objects in a layer-by-layer fashion, and has been applied as a technique to achieve the manufacture of biofabricated constructs in tissue engineering. 3D bioprinting is an example of additive manufacturing, in that combinations of cells and materials are deposited in a subsequential manner to form 3D tissue or organ-like structures. These three terms, biofabrication, additive manufacturing and 3D bioprinting, are often used like-for-like within the literature, but for the sake of clarity, they indeed have slightly different definitions when referred to in different contexts (Van Kampen et al., 2019).

1.6 Current Progress in Tissue Engineering

Once a topic implicated with numerous hurdles, tissue engineering has seen monumental advancements towards tissue restoration within the past decade. Several major challenges associated with identifying renewable cell sources, tuning biomaterial properties and improving vascularisation and host responses have been addressed, allowing for more intricate and intelligently designed tissue constructs to be researched and utilised (Khademhosseini & Langer, 2016). Arguably, one of the most impressive technological advancements in recent years is the realisation of 3D printed implants. Multiple 3D printed scaffolds have been approved by the Food and Drug Administration (FDA) and European Medicines Agency (EMA) - all within the last 10 years (Dzobo et al., 2018). 3D printing and additive manufacturing have already seen the fabrication of custom-made medical implants including a bronchial splint (Zopf et al., 2013), a cranial plate (Di Prima et al., 2016) and an artificial knee (Koeck et al., 2011). Currently, efforts are focused on making the transition of tailor-made 3D bioprinted constructs, containing cells, from the laboratory to market.

1.7 Present Challenges in 3D Bioprinting and Tissue Engineering

Due to the interdisciplinary nature of the tissue engineering field and the high degree of variation within tissues between patients, there are still many challenges that need to be addressed before tissue engineering patient-specific constructs becomes commonplace in the clinic. One of the biggest hurdles on the clinical translation of tissue engineered constructs is in the standardisation of bioprinting materials, techniques and software to reduce tissue engineering construct variances and to better predict patient outcome (Chandra, Soker, & Atala, 2020; Grounds, 2018).

Although 3D bioprinters can be used to print patient-specific implants that conform specifically to the patient's defect, one of the major difficulties in 3D bioprinting soft materials is in retaining construct resolution once deposited onto a planar surface. Some research has been undertaken in a bid to improve shape fidelity by using co-extrusion, crosslinking during printing and also broadening of the scaffold base. Other efforts have been made in a bid to rectify this issue by using high viscosity materials such as hydroxyapatite thus improving structure integrity (Kang et al., 2016). The mechanical properties of the matrix in which cells reside, however, have been seen to dictate cell phenotype and proliferation in mesenchymal stem cells (MSCs) (Huang et al., 2015), rendering this approach as unsuitable in culturing cells which require much softer substrates like adipocytes. Another problem with 3D bioprinting lies with the difficulty in integrating multiple layers of mechanically varying materials, preventing the production of multi-layer constructs with regional variations in mechanical features. This impacts on the *in vitro* fabrication of structures that mimic the complex environments within native tissue *in vivo*. The work presented in this thesis is aimed at addressing these problems to produce tissue engineering constructs that more appropriately replicate native tissue heterogeneity, biochemistry and architecture.

1.8 Research Rationale and Aims

Biopolymer hydrogels are frequently used in tissue engineering scaffolds as they have physicochemical similarities to extracellular matrix (ECM). The anisotropic nature of ECM in both material and cellular composition, however, is particularly challenging to replicate. Therefore, to facilitate the creation of more native environments, techniques to integrate multiple materials with different chemical and mechanical behaviour into a single construct are of great interest. 3D bioprinting using Additive Layer Manufacturing (ALM) is one approach that has showed promise to create detailed constructs of defined shapes. Recently in our laboratories, we have developed a technique to create cell-laden constructs from low viscosity biopolymers with the potential to design distinctly anisotropic structures from multiple materials using suspended manufacture. This technique involves the employment of a sacrificial supporting medium that suspends the tissue construct as it is being fabricated, prior to solidification, extraction and subsequent culture of the tissue construct.

Initially, the supporting medium used in suspended manufacture for tissue construct engineering was characterised. The potential of suspended manufacture was then investigated, combined with the use of a 3D bioprinter for upscale automation of tissue construct fabrication and thus seeing the evolution of Suspended Layer Additive Manufacturing (SLAM). Following this, the generation of multi-layer gradient constructs was explored in order to assess the feasibility of producing heterogeneous tissue constructs that are akin to native tissues. Finally, a tri-layer skin model was designed and manufactured in order to demonstrate the capacity of the system to print organ-like structures.

1.9 Thesis Outline

This thesis comprises an introductory section on tissue engineering, native tissue and the manufacture of tissue engineering constructs including current progress and present challenges to date (Chapter 1). The research rationale and aims are also outlined within this section.

A further two introductory chapters are presented to cover the common themes throughout the thesis. Chapter 2 focuses on the importance of biopolymer hydrogels as ECM mimics in tissue engineering. Their use in therapeutic applications is touched upon with a greater emphasis on their role in tissue engineering constructs. Six biopolymers in particular are discussed in detail, namely agarose, gellan gum, ι-carrageenan, pectin, alginate, and collagen. These materials are featured within the results chapters later in the thesis. The current roles and implications of these materials within tissue engineering are also highlighted and the significance of mechanical behaviours is discussed.

In Chapter 3, 3D bioprinting is introduced with an emphasis on its role in the creation of tissue engineering constructs. The process of 3D bioprinting tissue constructs, from the design of the print file to structure fabrication, is discussed in detail. Furthermore, the utilisation of embedded printing techniques is explored with a specific interest in suspended manufacture and fluid gel formation – a common feature throughout the thesis results sections.

Chapter 4 is the first of the results sections comprised of the analysis and characterisation of the supporting bed. In order to define the mechanisms of suspended manufacture and define print resolution, brightfield and scanning electron microscopy, particle size, particle volume fraction, rheological, resolution and diffusion studies were undertaken. An alternative approach using an agarose microparticle slurry was investigated versus the use of an agarose fluid gel as a supporting medium.

The development of the Suspended Layer Additive Manufacturing method is presented in Chapter 5. Firstly, cell-laden tissue constructs are printed by hand, demonstrating the method viability. The construct fabrication process is then refined using a commercially available 3D bioprinter for the manufacture of a variety of structures using a range of cells and polymers.

Following on from this work, Chapter 6 features the fabrication of multi-layered gradient constructs that are synonymous to those of native tissue environments. The organisation of cellular, micro-architectural, mechanical and biochemical gradients within a single construct is demonstrated using a selection of cells and polymers in multiple configurations. These tissue constructs have the potential to replicate tissues by intelligently tailoring and designing construct microenvironments that mimic target tissues *in vivo*.

In Chapter 7, the creation of tissue / organ-like structures by example of a multi-layered skin model is investigated. Models feature a subcutaneous layer complete with adipocytes, upon which a dual compartment dermis is integrated followed by a surface seeded keratinocyte layer. This section of work sees the design and development of a three-tier skin construct designed for therapeutic implantation within chronic non-healing wounds. Firstly, the extraction, isolation and culture of adipose derived mesenchymal stem cells (ADSC), human dermal fibroblasts (HDF) and human epidermal keratinocytes (HEK) from a human abdominoplasty is described. Tissue engineering skin constructs are meticulously designed and manufactured, featuring gradients in cell densities and phenotypes and material composition to direct the anisotropic ordering throughout the construct as displayed in native human skin tissues. Analysis of skin models was undertaken using histological and immunohistochemical staining, brightfield and scanning electron microscopy, shear rheology and by incorporation into an *ex vivo* porcine wound model.

Finally, Chapter 8 provides a summary of the works featured within this thesis along with conclusions that may be drawn from each section and recommended future directions for the works exhibited.

Chapter 2

BIOPOLYMER HYROGELS FOR TISSUE ENGINEERING CONSTRUCTS

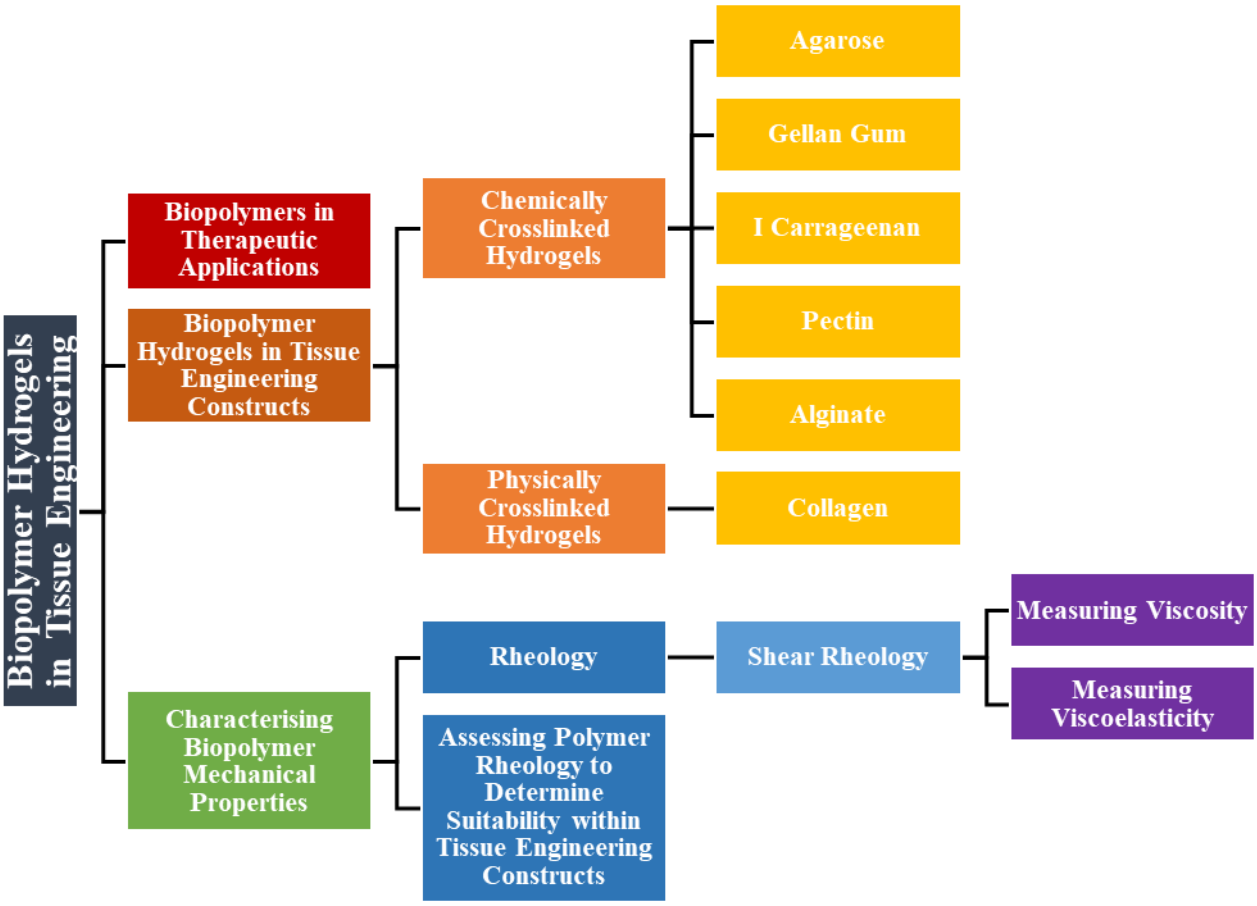
Biopolymer Hydrogels in Tissue Engineering
Biopolymers in Therapeutic Applications
Biopolymer Hydrogels in Tissue Engineering Constructs
Characterising Biopolymer Mechanical Properties
Chemically Crosslinked Hydrogels
Physically Crosslinked Hydrogels
Agarose
Gellan Gum
I Carrageenan
Pectin
Alginate
Collagen
Rheology
Assessing Polymer Rheology to Determine Suitability within Tissue Engineering Constructs
Shear Rheology
Measuring Viscosity
Measuring Viscoelasticity

Chapter 2 – Biopolymer Hydrogels in Tissue Engineering

2.1 Biopolymers in Therapeutic Applications

Biopolymers are polymeric substances derived or extracted from living organisms. They have become highly popular within the biomedical, agricultural and industrial disciplines within the last half century and are used in drug delivery, controlled pesticide release and food preparation applications. Due to their natural origins, many biopolymers elicit minimal host immune responses and exhibit biodegradable properties once incorporated into the human body, making them of high interest in therapeutic applications (Vert, 2001). Biopolymers can be processed in the form of sponges, films, electrospun fibres, nanoparticles and hydrogels and the selection of both biopolymer and processing strategy is crucial when incorporating into a therapeutic system. For instance, processing soft materials into films, sponges and nanoparticles can further reduce mechanical stability causing premature degradation (Reddy et al., 2015). Also, using dense materials to form electrospun fibres can cause insufficient porosity for the facilitation of cell migration and media infiltration (Tiwari et al., 2016). Biopolymer hydrogels are often employed in tissue engineering constructs as their tuneable chemical and mechanical characteristics allow greater freedom and versatility over tissue model fabrication. As well as natural hydrogels, tissue constructs can also be synthesized from synthetic hydrogels such as polyamides and polyethene glycol, however they are typically less biocompatible.

2.2 Biopolymer Hydrogels in Tissue Engineering Constructs

Biopolymer hydrogels are water swollen polymeric materials that feature highly organised intrinsic networks. These materials are of particular interest when designing 3D tissue scaffolds and constructs as their microarchitecture and mechanical properties largely resemble native ECM (Park et al., 2010). A multitude of parameters including porosity and mechanical strength may be manipulated within biopolymer hydrogels by tuning polymer concentration, crosslinking density and by careful manipulation of key conditions during sol-gel transition.

Many biopolymer hydrogels undergo sol-gel transition, whereby a disordered solution containing randomly dispersed polymers assembles to form a well ordered network of polymer molecules thus creating a more stable structure (Rudé Payró & Llorens Llacuna, 2006). Some hydrogels achieve crosslinking via thermal means by appropriately raising or reducing solution temperature in order to trigger optimum sol-gel transition kinetics. Others require further initiation via ionotropic mediation, such as the addition of ions to charged biopolymers, or alternatively by assembly with an oppositely charged polymer through complex coacervation (Gasperini et al., 2014). Furthermore, by chemically crosslinking polymers, gelation is mediated through the formation of covalent bonds between the polymer and crosslinker and ultraviolet (UV) radiation can be used in order to initiate crosslinking in modified biopolymers containing methacrylates (Hoare & Kohane, 2008). The latter two routes of achieving gelation, however, exert much harsher external environments on tissue culture systems and are therefore not investigated any further within this thesis.

2.2.1 Chemically Crosslinked Hydrogels

2.2.1.1 Agarose

Agarose is a natural polysaccharide that is purified from components of the cell walls of red algae (Rhodophyta). It is commonly used in biological applications as a diagnostic tool in the separation of DNA fragments in gel electrophoresis and has also more recently found a place in tissue engineering approaches – especially in cartilage repair (Kim et al., 2011). Agarose exists as a repeating disaccharide unit of β-D-galactose and anhydro-α-L-3,6 galactose (**Figure 2.1A**). The gelation mechanism that occurs when cooling agarose from a solution to a gel is a physical and thermo-reversible crosslinking process. When the critical sol-gel temperature is exceeded (above 80 °C), agarose exists as random coils in deionised water. Upon cooling, these random coils rearrange forming single helices and transition into a highly ordered double helix structure once quiescently cooled to around 37 °C (depending on hydrogel concentration) (**Figure 2.1B**).

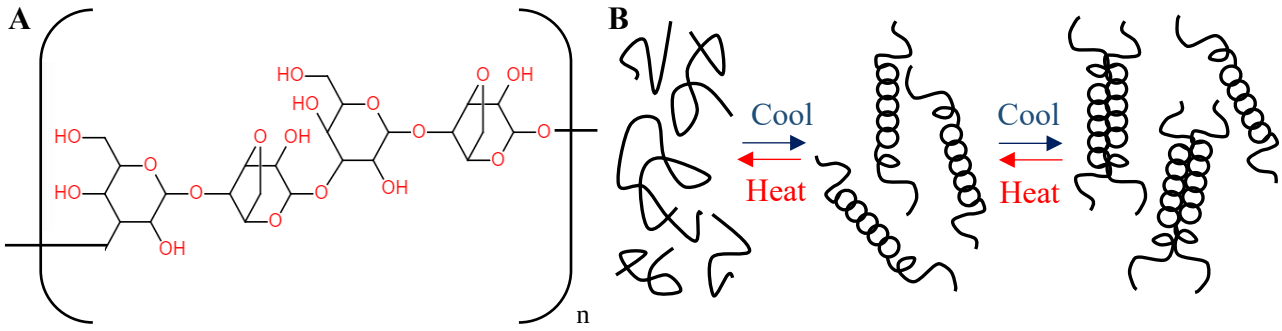

Figure 2.1 - A) The chemical structure of agarose containing 1,3 linked β-D-galactose and 1,4 linked anhydro-α-L-3,6 galactose subunits. B) The thermal gelation mechanism of agarose: first stage exhibits random coils in an 80 °C+ solution, random coils transition to single helices in the intermediate stage and form double helices in the final gel state upon cooling below 37 °C.

2.2.1.2 Gellan gum

Gellan gum (gellan) is an anionic polysaccharide produced from an aerobic fermentation by-product within the bacteria *Sphingomonas elodea*. The manufactured product is commonly available as either a high acyl or low acyl isoform, characterised by their potential to create a soft gel or a hard gel respectively (Miyoshi et al., 1996). Both isoforms are capable of undergoing the transition from random coils in a hot solution to a well-ordered gel containing double helices upon cooling and the addition of cations further establishes the creation of a stable hydrogel through the formation of junction zones (Matricardi et al., 2009).

Gellan is an ideal candidate for the encapsulation of cells as the gelation mechanisms of gellan are gentle and have no adverse effects on cell viability. Gellan itself does not contain cell attachment moieties and can therefore be used as a cell carrier within tissue constructs or alternatively can undergo further modification by incorporation of arginyl-glycyl-aspartic acid (RGD) sequences that are conducive to the attachment of cells (Stevens et al., 2016). The chemical structures of the tetrasaccharide repeating units 2 D-glucose:1 D-glucuronic acid:1 L-rhamnose and the chemical crosslinking mechanisms within gellan hydrogels are presented below (**Figure 2.2**).

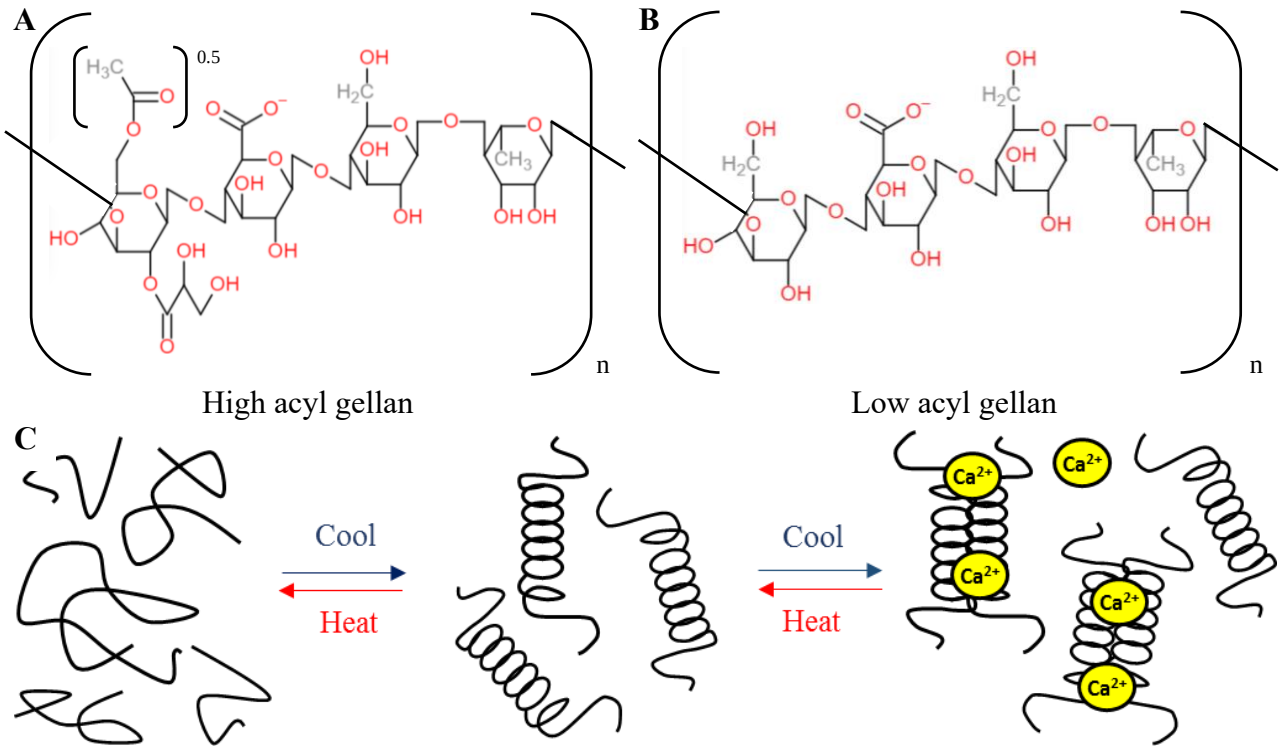

Figure 2.2 - Chemical structures of A) high acyl gellan and B) low acyl gellan. C) The ionotropic crosslinking mechanism for the gelation of gellan: first stage exhibits random coils in an 85 °C solution, helices form upon cooling in the intermediate stage and form double helices with the addition of cations in the final gel state.

2.2.1.3 ι Carrageenan

There are three principal members within the carrageenan family named iota (ι), kappa (κ) and lambda (λ) (**Figure 2.3**), all of which are extracted from red algae (Rhodophyta). Each isoform differs chemically based on the degree of sulphation and subsequently the characteristics of the gels also differ, with only ι and κ isoforms being capable of producing self-supporting gels (Chandrasekaran, 1998). Iota carrageenan (which forms soft elastic gels) is made of an alternating sequence of β1-3 linked and α1-4 linked D-galactose residues with one sulphate on every residue as opposed to per disaccharide repeat unit in κ carrageenan (which forms stiff, brittle gels). Gelation of ι carrageenan, as featured later in this thesis, is mediated through cooling of polymer solutions triggering the formation of intermolecular double helices and the addition of cations further increases polymer ionic strength (Piculell et al., 2011). Alternatively, salts within cell culture media are sufficient enough to initiate crosslinking within an ι carrageenan tissue construct (Mehrban et al., 2009).

Relatively little research has been done on the use of ι carrageenan in tissue engineering scaffolds compared with other polysaccharide hydrogels such as alginate, with contradictions in the available literature on the cytotoxicity of ι carrageenan on cells (Calvo et al., 2019; McKim et al., 2016). In other research, the potential of ι carrageenan as a material for cell encapsulation has been highlighted, exhibiting proliferation and even attachment of entrapped cells and suitable mechanical properties (Mehrban et al., 2010).

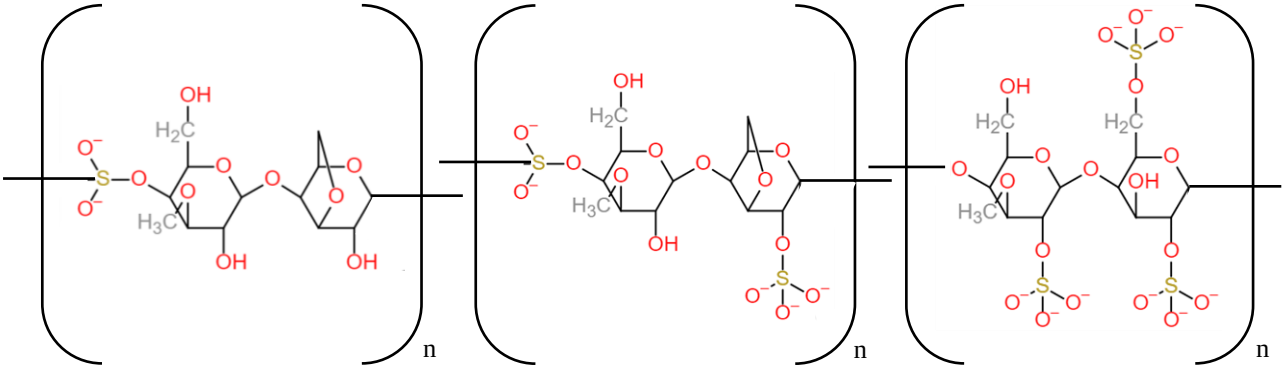

Figure 2.3 - Chemical structures of kappa (κ), iota (ι) and lambda (λ) carrageenan.

2.2.1.4 Pectin

Pectins are a family of complex carbohydrates extracted from plant cell walls including citrus peels and like agarose, gellan gum, ι carrageenan and alginate, they have a place in the food industry as food stabilisers, viscosity builders, emulsifiers and satiety increasers. The chemical composition of this negatively charged hydrocolloid consists of a 1,4-linked α-d-galacturonic acid backbone and occurs with varying degrees of methyl esterification (DE) with high (>50% esterified acid units) and low (<50% methyl ester groups) variants (Sudheesh Kumar et al., 2013) (**Figure 2.4**). Rhamnose residues appear at random intervals on the main chain causing a kink in the otherwise linear chain and side chains of arabinans and galactans also feature within pectin molecules (Morris et al., 2008). High methyl ester (HM) pectin gelation requires low pH and water activity by the addition of sugar and acid whereas low methyl ester (LM) pectin forms gels in the presence of divalent cations in the formation of the ‘egg box’ model.

In tissue engineering, there have been some reports of the use of pectin in scaffolds and constructs, but most often are incorporated with other materials. Examples include pectin blended with silk fibroin for skin tissue engineering (Türkkan et al., 2018), calcium phosphate for bone tissue engineering (Munarin et al., 2011) or modified to contain RDG complexes also for bone tissue engineering (Zhao et al., 2016). Pectin in conjunction with carboxymethylcellulose has also been demonstrated as a suitable candidate in the healing of partial thickness wounds in a rat model, with indications of ECM deposition, re-epithelialisation and promoting skin regeneration (Ninan et al., 2014).

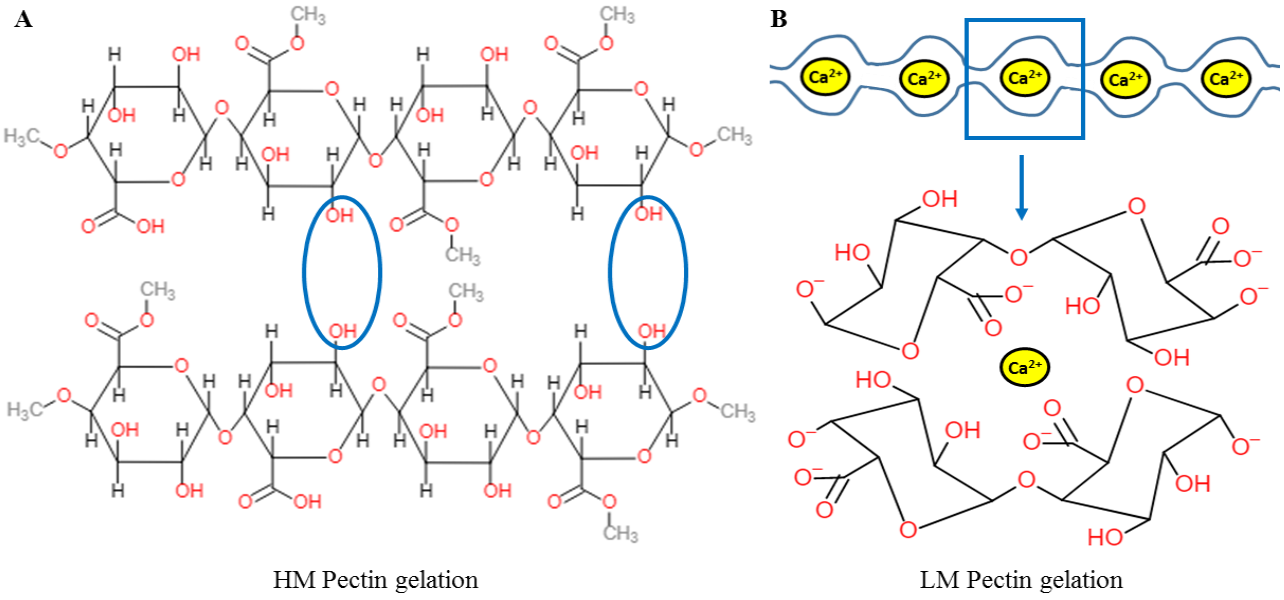

Figure 2.4 - Gelation mechanism of A) high methoxyl (HM) and B) low methoxyl (LM) pectin.

2.2.1.5 Alginate

Alginate is a negatively charged polysaccharide and is mainly extracted either from the cell walls of brown algae such as *Laminaria* and *Ascophyllum* species or from bacterial exopolysaccharide including Pseudomonas and Azotobacter. Alginates can vary based on the ratios of which the uronic acid residues (1-4′)-linked β-d-mannuronic acid (M blocks) and α-l-guluronic acid (G blocks) are present. Copolymerisation of M and G blocks form linear blocks (GM blocks) (Aramwit, 2016) (**Figure 2.5**). Alginates with a high content of G blocks are associated with the formation of stiffer gels than those with higher M content as the induction of crosslink formation is mediated by

interactions between divalent cations and carboxylic acid groups within the G blocks (Park et al., 2009). Alginates also assume the 'egg box' structure when crosslinked through a similar mechanism to the gelation of pectin (Gotoh et al., 2004).

Alginate is capable of absorbing water and body fluids up to 20 times its mass and is often employed in many commercially available wound dressings, such as AlgiDERM, for the maintenance of moist wound environments and for its active wound healing properties (Paul & Sharma, 2004).

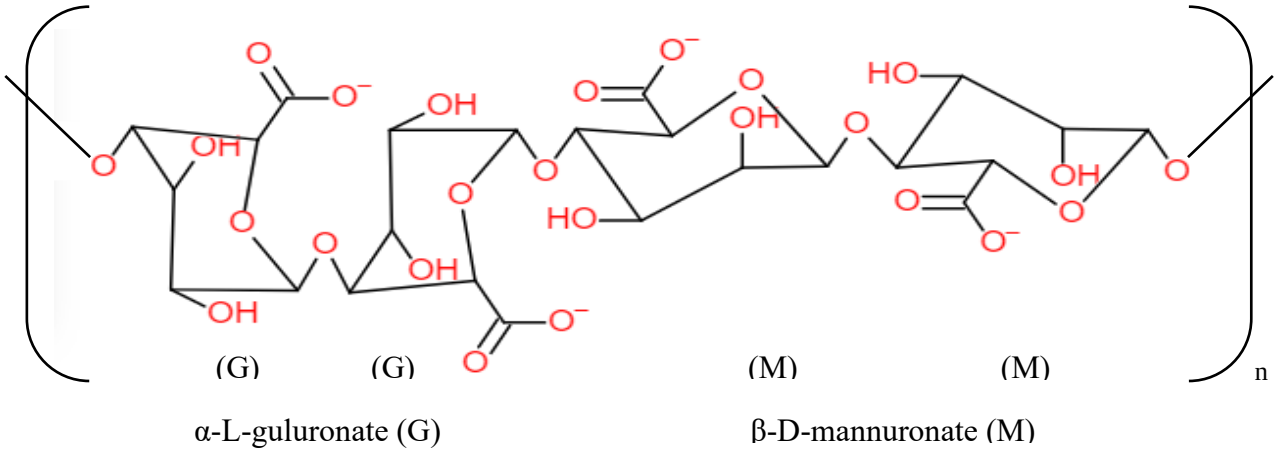

Figure 2.5 - Chemical structure of alginate containing linear blocks α-L-guluronate (G) and β-D-mannuronate (M) with a variation in composition and sequence.

2.2.2 Physically Crosslinked Hydrogels

2.2.2.1 Collagen

Collagen is present in all connective tissues and is therefore one of the most extensively studied protein hydrogels within the tissue engineering field. Made predominantly by fibroblasts, there are 29 distinct collagen variants which have been identified and all display a left handed triple helix structure (Parenteau-Bareil, Gauvin, & Berthod, 2010). Each collagen molecule consists of an assembly of three α chains that are packed into a tight formation. Each α chain is composed of more than a thousand amino acids following the sequence Gly-X-Y-, where the X and Y locations are most often occupied by proline and 4-hydroxyproline (Prockop, 1995) (**Figure 2.6**). Type I collagen exists in fibrils in its polymerised form at neutral pH, is distributed throughout bone, skin, tendons ligaments and cornea and represents 90% of total collagen in the human body (Alberts et al., 2002).

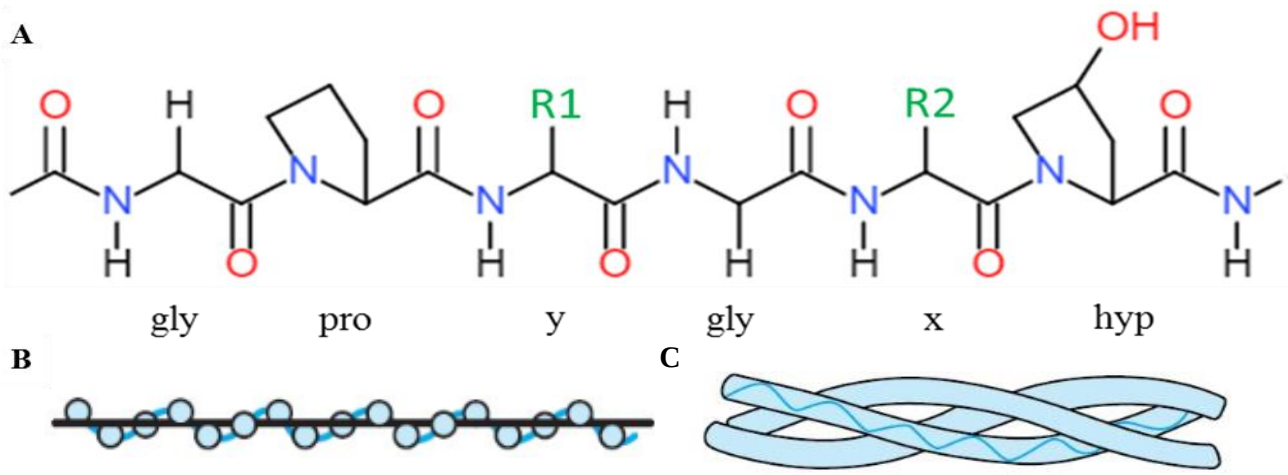

Figure 2.6 - Chemical structure of collagen type I. A) Primary amino acid sequence, B) secondary left-handed helix and C) tertiary right-handed triple-helix structure.

Factors that control the polymerisation process for the formation of a collagen gel matrix include temperature, pH, ionic strength and concentration. Furthermore, the addition of more crosslinking agents can also affect fibrillogenesis (Antoine et al., 2014). The final outcome of the collagen gel when processed under a variation of these conditions can display differences in gel mechanics and fibre structure, with reports of higher pH and lower gelation temperatures producing more mechanically robust gels with increased collagen fibril packing and decreased fibre diameter (Achilli & Mantovani, 2010).

2.3 Characterising Biopolymer Mechanical Properties

The mechanical characterisation of biopolymer hydrogels is imperative in their utilisation within tissue engineering scaffolds and constructs. It provides critical information on the hydrogel's mechanical behaviour during printing and handling, integrity following gelation and can aid in describing potential relationships between hydrogel stiffness and cell behaviour. These data are invaluable when comparing the mechanical milieus within candidate biopolymer scaffolds to those found in native tissues. Rheology is one method that is used to assist in characterising the mechanical properties of biopolymers (Zuidema et al., 2014). It is therefore pertinent that an introduction on

rheological terminology is presented in order to outline how these materials may be studied as featured within the results section of this thesis.

2.3.1 Rheology

The term rheology comes from the Greek words “rheo” (meaning to flow) and “logos” (meaning study) and is the science of deformation of matter in response to an applied mechanical force (Struble & Ji, 2001). The effect of the force applied is represented by the materials’ liquid or solid like behaviour – as denoted numerically by viscosity and viscoelasticity. Most materials are not exclusively liquid or solid and exhibit an intermediate characteristic of both under a given applied stress. However, the Newtonian liquid and Hookean solid models serve to represent the extreme ends of the scale. Elastic “solid-like” matter is seen to fracture upon an applied influential force whereas viscous “liquid-like” matter is seen to flow and it is the degree to which matter fractures or flows from which rheological behaviour may be determined (Kavanagh & Ross-Murphy, 1998).

Stress can be applied in three ways in order to determine the moduli of a material, i) compression/tension, ii) bulk compression and iii) shear (**Figure 2.7**). Compression and tension testing are used to determine the Young’s modulus (E, (Pa)) of a material and is quantified by dividing perpendicular stress by strain (Mohammed H. Mahdi, 2016). Bulk testing is seldom practised on soft materials such as biopolymer hydrogels, however this method incorporates the application of isostatic compression divided by the volumetric strain for calculation of the bulk modulus (K, (Pa)) (Biron, 2015). Finally, shear modulus (G, (Pa)) is measured by applying a lateral shear upon a sample’s surface and is a more suitable approach to measuring the mechanical characteristics of samples that are not fully self-supporting (Sunthar, 2010).

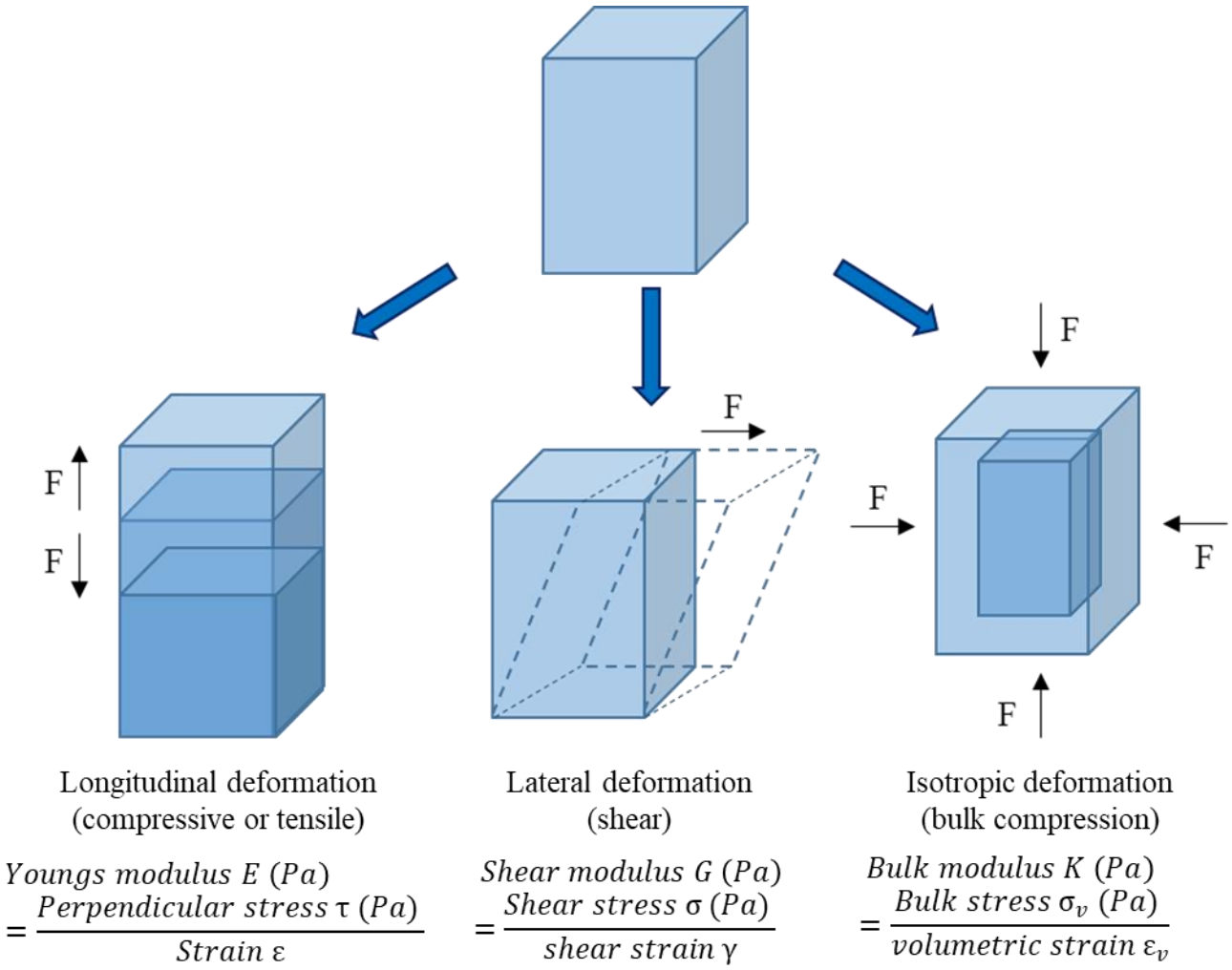

Figure 2.7 - Schematic illustration of longitudinal, lateral and isotropic deformation for moduli measurement.

2.3.1.1 Shear rheology

In the case of shear rheology, the force applied to the material is described either in terms of shear stress, measured by force applied per unit area (**Equation 2.1**), shear strain, defined as a ratio of extension per unit length (**Equation 2.2**) or shear rate, calculated by the change in strain over the change in time (**Equation 2.3**).

$$Shear\ stress\ \sigma\ (Pa) = \frac{force\ F\ (N)}{surface\ area\ A\ (m^2)} \qquad \textbf{Equation 2.1}$$

$$Shear\ strain\ \gamma = \frac{deformation\ u}{hight\ d} \qquad \textbf{Equation 2.2}$$

$$Shear\ rate\ \dot{\gamma}(s^{-1}) = \frac{change\ in\ strain\ \delta\gamma}{change\ in\ time\ \delta t\ (s)} \qquad \textbf{Equation 2.3}$$

The shear mechanical behaviour of a material may be quantified as a function of material flow or deformation. The degree to which a material resists flow upon an applied force is defined by viscosity and is important in tissue engineering biopolymer scaffolds during biopolymer solution preparation and handling. Deformation of matter, on the other hand, deals with how a sample behaves before it flows and determines sample properties in terms of viscoelasticity (Lyklema, 2005).

2.3.1.1.1 Measuring viscosity

Viscometric tests produce analytical data on material viscosity following the application of shear. Here, a sample is loaded onto a flat lower plate and an upper cone plate rotates uni-directionally, over a set range of shear rates, across the sample's surface. The cone creates a uniform shear across the whole of the sample unlike a parallel plate and the range of shears used within the test are used to replicate the range of shear forces experienced by the material during handling. For example, very low shear rates of ~0.001s^{-1} simulate the shear forces experienced by a material during storage and can indicate sample quality and stability. Alternatively, high shear rates of ~100s^{-1} can simulate higher shear forces such as dispensing and applying a colloidal hand cream (Malvern Panalytical, 2016). Apparent viscosity is thus calculated by the shear stress divided by the shear rate (**Equation 2.4**).

$$Apparent\ viscosity\ \eta\ (Pa\ s) = \frac{Shear\ stress\ \sigma\ (Pa)}{Shear\ rate\ \dot{\gamma}\ (s^{-1})} \qquad \textbf{Equation 2.4}$$

There are three general flow behaviours of a sample when measuring viscosity: Newtonian, shear thinning (pseudoplastic) and shear thickening (dilatant) (**Figure 2.8**). For Newtonian fluids such as silicone oil, the viscosity is constant and equal to the Newtonian viscosity of the fluid, however for non-Newtonian fluids, the viscosity of the material is shear rate dependent. As viscosity is also time dependant, shear-thinning materials such as polymers and shear-thickening materials including cornflour often exhibit a hysteresis loop. Here, upon the removal of shear, polymer chain re-entanglement is not proportional to polymer dis-entanglement – a phenomenon known as thixotropy and rheopecty in shear thinning and shear thickening materials respectively (Darvell, 2018).

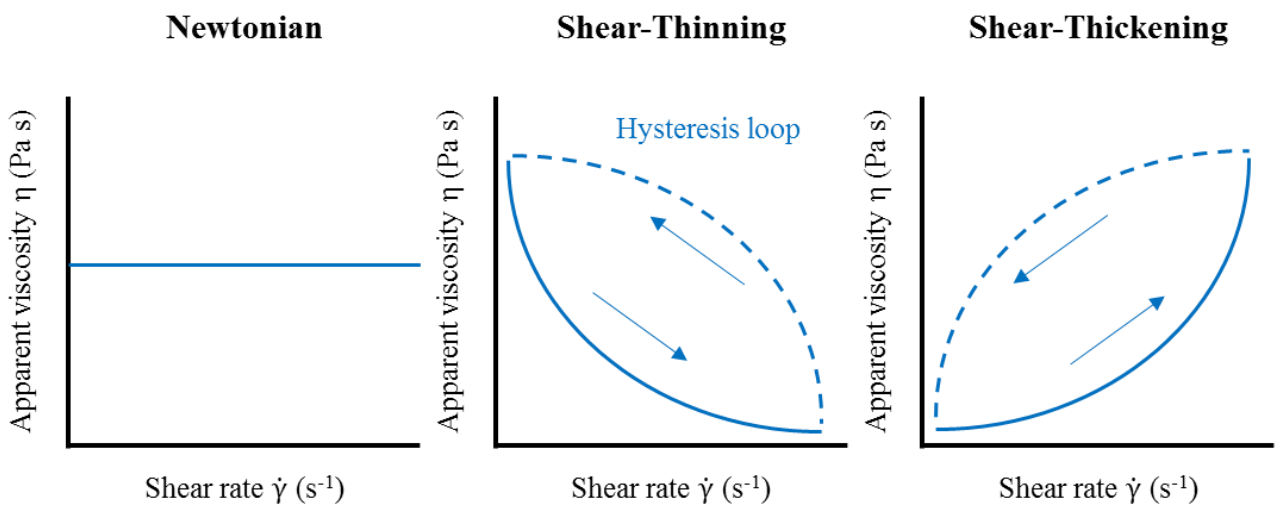

Figure 2.8 - Flow behaviour of materials when measuring sample viscosity: Newtonian, shear thinning (pseudoplastic) and shear thickening (dilatant).

Factors that influence the viscosity of a polymer include molecular weight, polymer concentration and particle size. Polymers with a higher molecular weight have a larger intrinsic viscosity (contribution of viscosity to a solution) and stronger forces between intermolecular entanglements, which are causative of more viscous properties (Kasaai et al., 2000).

From these data, information on the material at rest may also be ascertained by observing yield stress and zero shear viscosity. Samples with a yield stress exhibit an ever-increasing viscosity as shear rate approaches zero meaning the material is solid like and non-flowing when stationary. This is important in materials such as paint, in that emulsions have good stability during storage and will shear thin upon a given applied shear to allow spreading before restructuring to prevent drippage from surfaces. Materials with zero shear viscosity exhibit a plateau as the shear rate approaches zero and indicates that the material is liquid like when stationary. Viscosity tests using shear rheology can measure material characteristics by applying a single shear rate or subjecting to a range of shear rates (Cheng, 1986). These data are invaluable, especially within industrial processes, in designing materials for different printing platforms which require specific ranges of viscosities to allow dispensing.

2.3.1.1.2 Measuring viscoelasticity

A large proportion of materials exhibit an intermediate of solid-like and liquid-like behaviour, which can be quantified simultaneously by measuring viscoelasticity. Using oscillating shear rheology, a sinusoidal stress (or strain) is introduced upon a sample located between an oscillatory upper plate and a static bottom plate. The applied sinusoidal stress is conducted through the sample and either dissipated by friction in viscous materials or transmitted in elastic materials (Deshpande, 2018). By using the values of input shear stress and measured strain, the complex modulus (G*) (and thus the material stiffness) can be calculated (**Equation 2.5**).

$$Complex\ modulus\ G^*(Pa) = \frac{Shear\ stress\ \sigma\ (Pa)}{Shear\ strain\ \gamma} \qquad \textbf{Equation 2.5}$$

Different types of material display different phase angles between the applied and measured sinusoidal signal and can be used to determine viscoelasticity. Materials that demonstrate purely elastic behaviour are said to have a stress and strain that are 'in phase' with a phase angle of zero, whereas purely viscous materials have a stress and strain that are one quarter of a cycle 'out of phase' and therefore have a phase angle of 90 ° (Malvern Panalytical, 2016) (**Figure 2.9**).

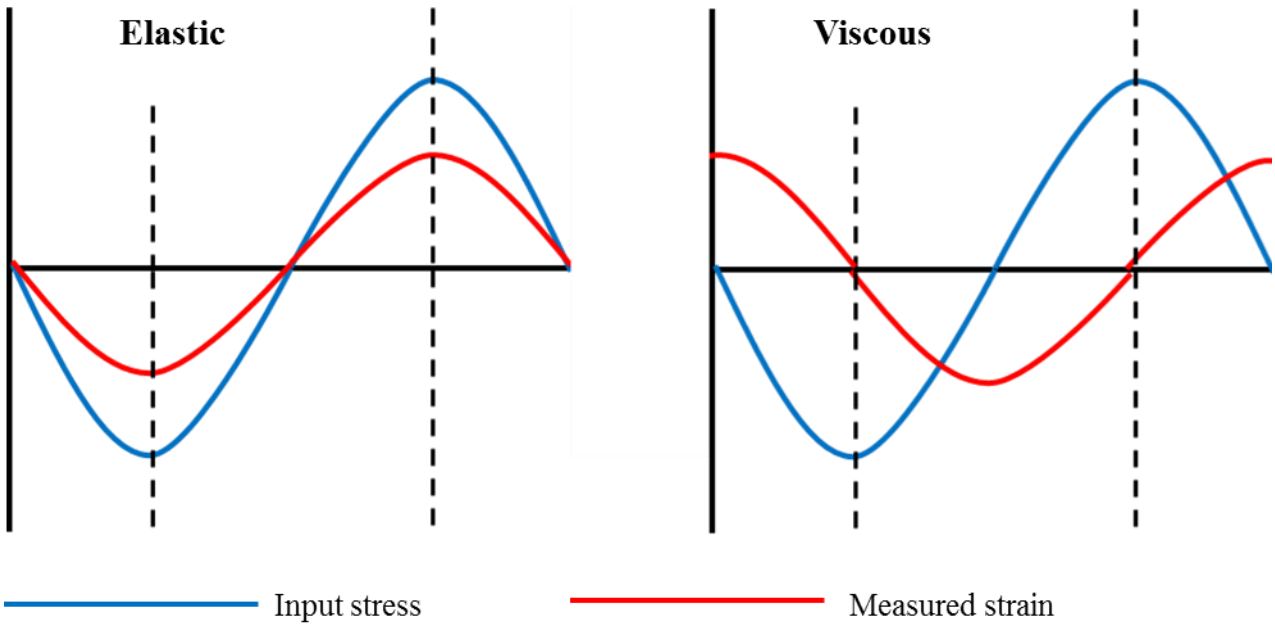

Figure 2.9 - Characterisation of elastic 'in phase' and viscous 'out of phase' materials.

When defining elastic (storage - G′) and viscous (loss - G″) moduli separately, storage modulus is calculated using the Sin function whereas loss modulus is calculated using the Cos function (**Equations 2.6 and 2.7**). If the phase angle is less than 45 °, G′ > G″ and the sample is more solid like, whereas if the phase angle is greater than 45 °, G′ < G″ and the sample is more liquid like.

$$Storage\ modulus\ G'\ (Pa) = \frac{Stress\ \sigma\ (Pa)}{Strain\ \gamma}\ Cos\delta \qquad \textbf{Equation 2.6}$$

$$Loss\ modulus\ G''\ (Pa) = \frac{Stress\ \sigma\ (Pa)}{Strain\ \gamma}\ Sin\delta \qquad \textbf{Equation 2.7}$$

There are two parts of the oscillation that can be controlled in order to measure different parameters of viscoelasticity: oscillation amplitude and oscillation frequency. In general, amplitude stress (or strain) sweeps are first conducted in order to determine the linear viscoelastic region (LVR) of a sample (**Figure 2.10**). Here, the amount of stress required to break a material can be ascertained, indicating the stability of a colloid. Data is acquired at constant frequency and G′ is typically more sensitive to the LVR. Shear stresses within the LVR measure small deformations in a sample whereas shear stresses that exceed the LVR measure large deformations and cause the sample to fracture. Once the LVR of a sample has been studied, the effect of oscillatory frequency can be analysed.

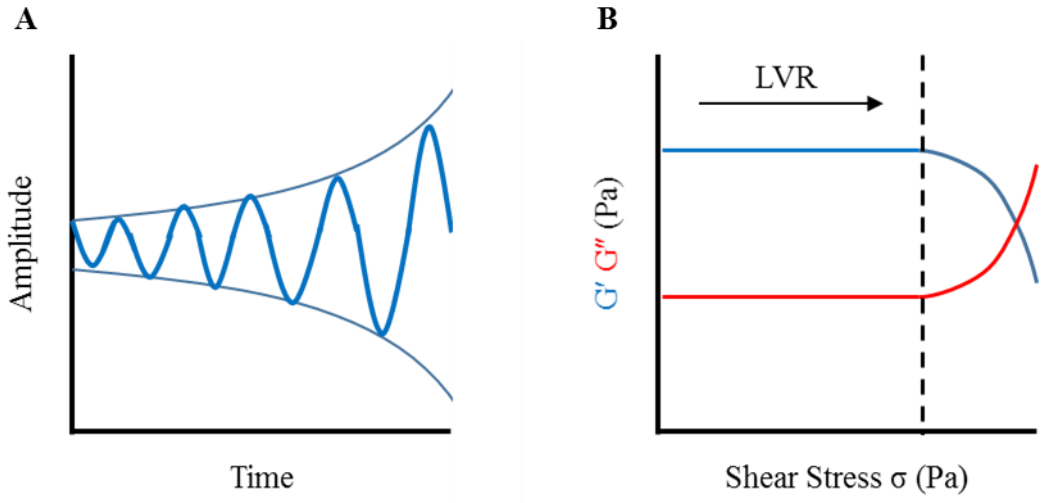

Figure 2.10 - Amplitude stress sweeps A) Time vs amplitude and B) shear stress vs elastic (G′) and viscous (G″) moduli.

By recording G′ and G″ moduli over a range of frequencies under a set shear stress that falls within the LVR, a fingerprint spectrum of the material can be obtained. The material phase angle at rest (0 Rad $^{s-1}$) is then used to classify samples into one of three general behaviours: viscoelastic solid (δ = 0 °), gel (δ is independent of frequency) or viscoelastic liquid (δ = 90 °) (**Figure 2.11**).

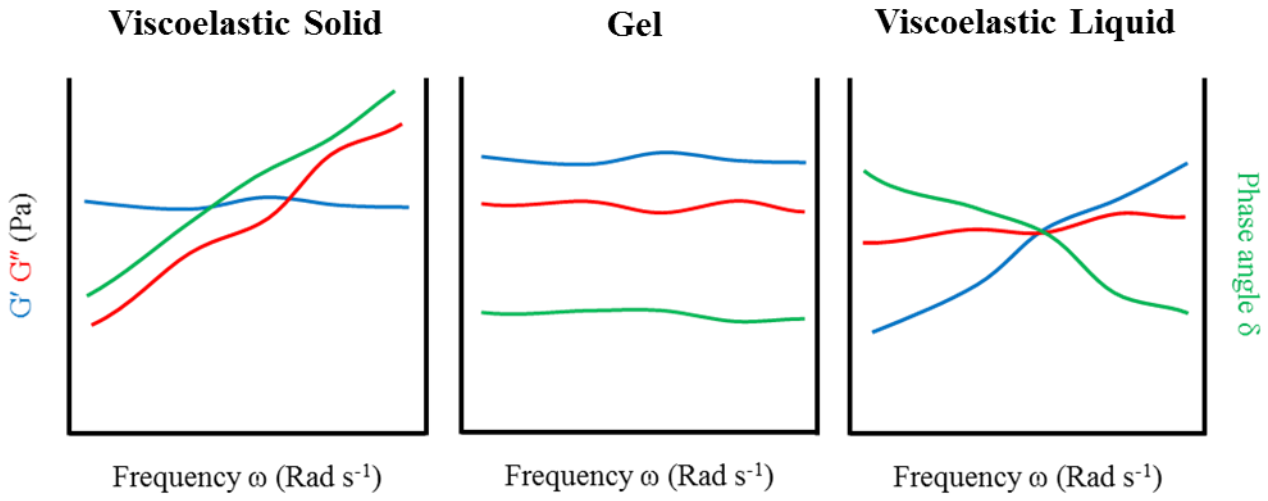

Figure 2.11 - Frequency sweeps for the determination of viscoelastic solid, gel and viscoelastic liquid behaviour of a material.

During a frequency sweep, low frequencies are used to measure longer timescales whereas high frequencies are used to measure more rapid successions of oscillatory shear. Viscoelastic solids are defined by a dominance of G′ over G″ at low frequencies and become more liquid-like as frequency increases. Alternatively, viscoelastic liquids exhibit a dominance of G″ over G′ at low frequencies and become more solid like as frequency increases. Gels on the other hand exhibit no dependency on angular frequency. Using these principles, play putty is classified as a viscoelastic liquid in contrast to hand cream, which is characterised as being a viscoelastic solid.

2.3.2 Assessing Polymer Rheology to Determine Suitability within Tissue Engineering Constructs

When carrying out rheological measurements on polymers as potential tissue engineering resources, temperature is another parameter that should be assessed. The viscoelasticity of a sample can be analysed under a set shear rate over a range of temperatures in order to determine gelation kinetics

within polymers that thermally undergo sol-gel transition. Temperature can also be controlled and set to a physiologically relevant value during an amplitude stress sweep in order to determine polymer suitability within a tissue scaffold or construct destined for implantation. Ultimately, shear rheology is an effective way of determining not only the suitability of materials within tissue engineering implants, but also on the materials during handling and printing. Without the feasibility of 3D bioprinting a material, the envisaged tissue engineering construct may not be realised.

Chapter 3

3D AND EMBEDDED BIOPRINTING

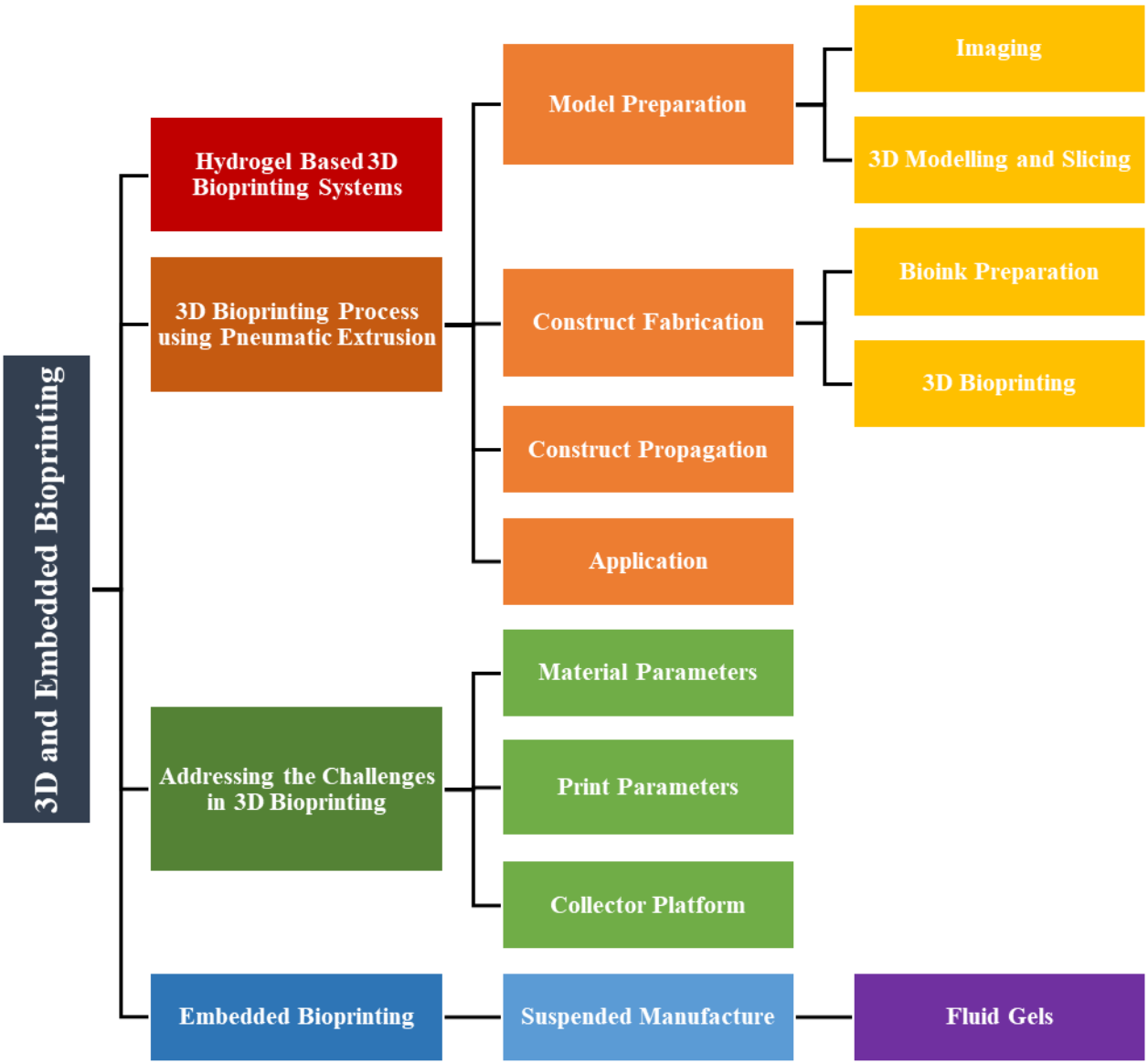
3D and Embedded Bioprinting
Hydrogel Based 3D Bioprinting Systems
3D Bioprinting Process using Pneumatic Extrusion
Model Preparation
Imaging
3D Modelling and Slicing
Construct Fabrication
Bioink Preparation
3D Bioprinting
Construct Propagation
Application
Addressing the Challenges in 3D Bioprinting
Material Parameters
Print Parameters
Collector Platform
Embedded Bioprinting
Suspended Manufacture
Fluid Gels

Chapter 3 – 3D and Embedded Bioprinting

3.1 Hydrogel Based 3D Bioprinting Systems

Three-dimensional (3D) printing is an additive layer manufacturing (ALM) process in which natural (including biopolymer hydrogels) or synthetic material is layered for the construction of a 3D model. The potential of 3D printing has been realised within the engineering, manufacturing and medical sectors and is currently seeing an evolving extension of applications further afield. More specifically, 3D bioprinting is used to design cell-laden constructs of defined shape which are either destined for implantation or for *in vitro* testing (Grogan et al., 2012). Biopolymer hydrogels will be the focus in this thesis due to their printability and their potential in mimicking native human tissue matrices.

There are three main methods in which biopolymers may be 3D bioprinted based upon the type of bioprinter used for construct fabrication: i) laser assisted, ii) inkjet and iii) micro-extrusion (**Figure 3.1**). Choosing the appropriate printer depends predominantly on the nature of the scaffolding material which is to be printed (Murphy & Atala, 2014). Laser assisted bioprinters (used in a method commonly known as laser-induced forward transfer) are the most attractive in respect to cell viability and they also exhibit the most desirable print resolution at the microscale level, yet are also the most costly and time consuming during print preparation (Guillemot et al., 2010). These types of printer operate by focusing laser pulses onto an adsorbing layer of glass ribbon that generates a high-pressure bubble, thus propelling the bioink towards a collector substrate. Inkjet printers are a suitable method of 3D bioprinting when dealing with very low viscosity materials (3.5–12 mPa/s) and they perform with admirable preparation and print timescales. They operate on either a thermal or acoustic basis, creating bioink droplets through electrical heating of the printhead producing air pressure pulses, or using vibrations for alternating current (AC) propagation in piezoelectric crystals. These are the cheapest and most predominantly used bioprinters and were originally adapted from 2D ink-based commercial printers (Kim et al., 2010).

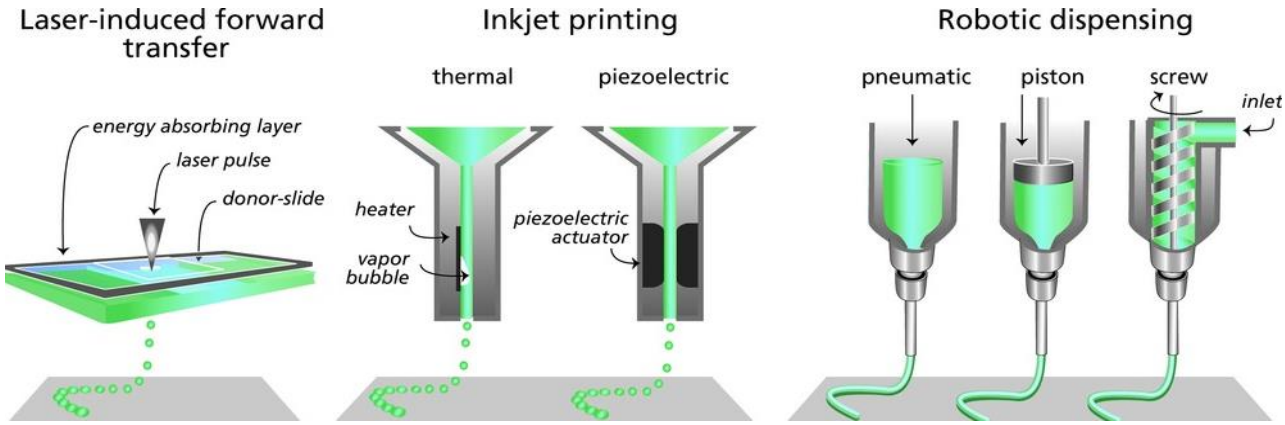

Figure 3.1 – Current 3D bioprinting methods used for dispensing hydrogel bioinks (Malda et al., 2013).

Pneumatic based bioprinters use an automated robotic arm which controls extrusion of material over X, Y and Z axis coordinates. Compressed air is supplied to a cartridge whose piston extrudes material through a nozzle and material is deposited onto a Z-stage collector. These techniques offer greater cell density capabilities over a larger range of material viscosities and gelation methods. Within many micro-extrusion based units, deposited material can be crosslinked by adjusting temperature, introducing crosslinking agents or subjecting the 3D model to UV radiation (Murphy & Atala, 2014). The technology employed in this thesis is focused on robotic, pneumatic, micro-extrusion printing.

3.2 3D Bioprinting Process using Pneumatic Extrusion

Like other 3D biofabrication methods, pneumatic extrusion-based printing starts with a model preparation stage and the generation of a 3D print file for the printer to replicate. A 3D model may be obtained using medical imaging techniques or by fabrication within computer automated design (CAD) software. The 3D model is then translated into a series of printable layers using coding language as instructions for the printer to follow. Depending on the type of file that the printer processor reads, the file may undergo conversion into another file format. The bioink is formulated by mixing cells and material and a range of printing parameters may then be adjusted in order to optimise the generation of the final printed part during the construct fabrication stage. The construct may then undergo further propagation before being used for its intended application (**Figure 3.2**) (Yan et al., 2018).

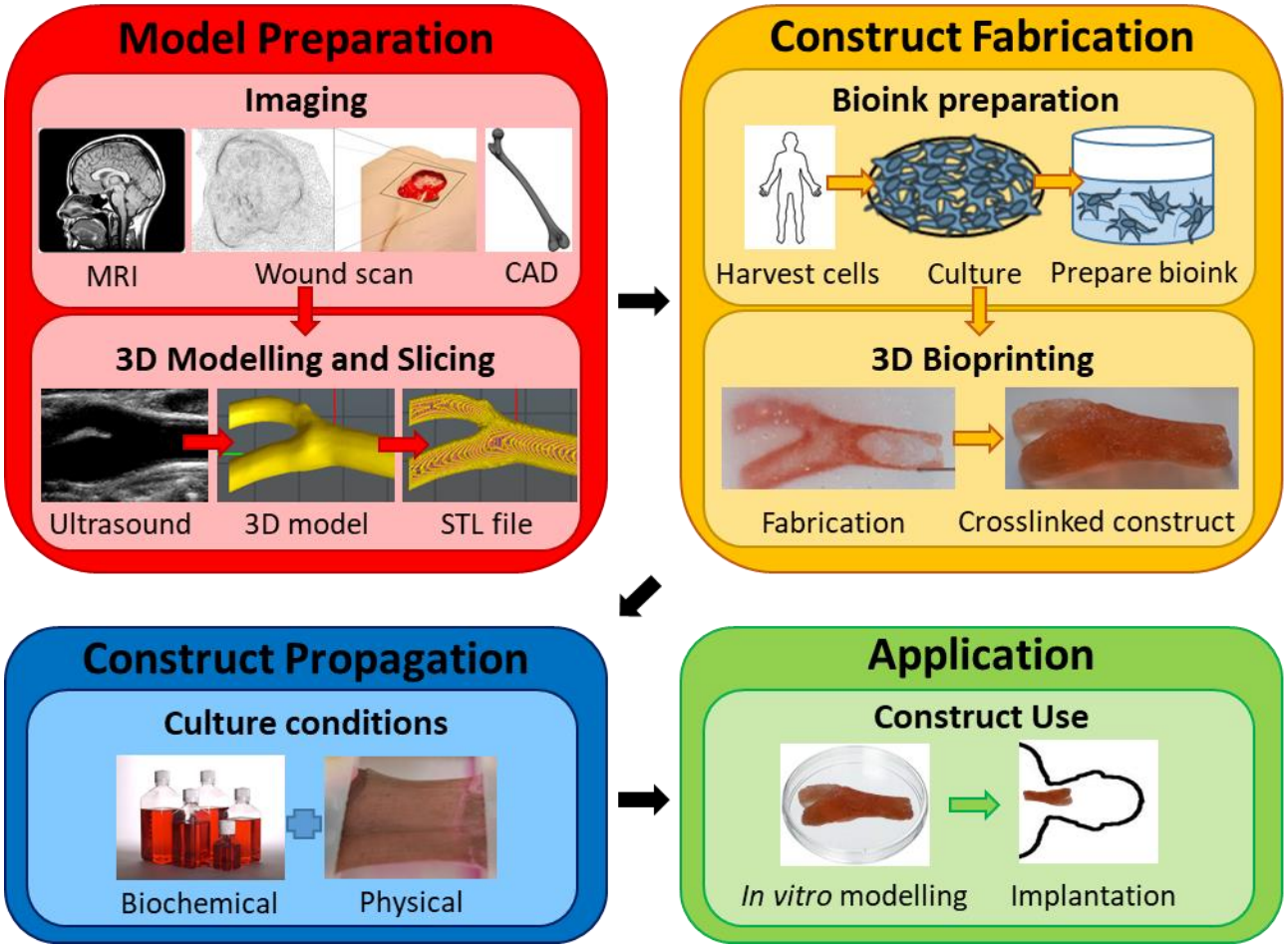

Figure 3.2 – Chronological stages for the design and production of a 3D bioprinted construct for tissue engineering.

3.2.1 Model Preparation

Preparing to 3D bioprint a tissue construct is constituted mainly of two parts, namely i) imaging data acquisition and ii) 3D model reconstruction. The use of either medical imaging or computer aided design (CAD) software produces anatomic data which can then be transformed into a readable language which complies with 3D bioprinter operation (Vijayavenkataraman et al., 2018).

3.2.1.1. Imaging

Before 3D bioprinting can commence, it is important to interpret the target tissue architecture in order to fully capture the structure's dimensions and to enhance the scaffold's performance as an implant or tissue model. The selection of imaging software can be tailored to specific situations appropriately, in that computed tomography (CT) is more suitable in imaging hard tissues such as bone and tumour,

whereas MRI imaging is more appropriate for the assessment of soft tissue (Chua & Yeong, 2014). Further considerations into imaging choice include target tissue accessibility, resolution and exposure to potentially harmful radiation (Ballyns & Bonassar, 2009; Nam et al., 2014).

3.2.1.2 3D modelling and slicing

Following imaging data acquisition, 3D models may be subjected to further modification via the introduction of internal contours, pores and channels in order to facilitate cell attachment, proliferation, nutrient flow and subsequently, tissue maturation (Ozbolat et al., 2012). Scaffold design may also be initiated during the 3D modelling step using CAD software, such as SOLIDWORKS®, as opposed to using medical imaging software. These 3D models are usually presented in stereolithography (STL) file format which describes surface geometry using a series arrangement of surface tessellations for complete build-up of the whole structure (Kai et al., 1997). It is also at this point that certain printing parameters may be selected, such as the infill pattern, infill density, printing speed, printing temperature and the inclusion of overhang-supporting material.

Once the geometry surface has been defined, models undergo manufacturing through slicing software such as Slic3r. This type of processing renders the model in a stack of horizontal layers which the 3D bioprinter uses to extrude material following the principles of additive layer manufacture (ALM). In some cases, it is necessary to convert the file into G-code file format for language compatibility between the file and the printer. The G-code comprises a series of instructions manifested as letters and numbers that assign a printer function (Rajapakse et al., 2018). These functions range from directing valve opening and closing times in order to orchestrate material extrusion, to determining nozzle location at pre-defined coordinates. For example, the code ‘M760’ opens the valve for printhead 1 and the code ‘G1 X1.236 Y4.611 E0.01212 ; perimeter’ linearly moves the extruder to these X, Y and Z coordinates when using the INKREDIBLE 3D bioprinter (Cellink, Sweden). Once the 3D model has been created and the print path fully defined, bioinks may be formulated, print parameters may be selected and construct fabrication can commence.

3.2.2 Construct Fabrication

During the processing stage of 3D bioprinting using biopolymer hydrogels, construct fabrication is undertaken. Initially, the bioinks are formulated by mixing the relevant materials and cell types that are appropriate as intended tissue mimics. The bioinks are then loaded into the printer cartridges and the printer is calibrated in order to achieve maximum attainable resolution whilst also preserving cell viability.

3.2.2.1 Bioink preparation

Once the appropriate materials and cells that replicate target tissue ECM have been identified, as directed by the specifications of a tissue engineering construct, the components are mixed for bioink formulation. While practicing sterile techniques, biopolymer materials are processed using specific concentrations and precise formulation methods in order to limit batch-to-batch variability between solutions. Culture of cells is also undertaken until an ample population is obtained for suspension within biopolymer solutions at pre-defined densities. A number of polymers and cell types can be mixed within a single bioink or, alternatively, a number of cartridges containing different bioink formulations may be installed within the bioprinting setup so that the complex heterogeneous nature of native tissue may be captured within a single construct (Gungor-Ozkerim et al., 2018).

3.2.2.2 3D Bioprinting

During the 3D bioprinting step, the fabrication of the tissue construct is realised. Initially, the printer Z-stage collector platform and X,Y robotic arm (with inserted cartridge and nozzle) are calibrated so that the dispensing coordinates are in reference with the collector platform on which the bioink will be dispensed. This step accounts for different needle lengths that are inserted within the cartridge holder and thus the positioning of the robotic arm respectively. The extrusion pressure is then selected for each bioink so that an appropriate flow rate is achieved. Printing is then initiated upon selection of the 3D model and the part is printed, layer by layer, according to the G Code (Cellink, 2020).

3.2.3 Construct Propagation

Culturing of tissue engineering constructs is as important as the 3D bioprinting process in that the conditions to which a 3D construct is exposed can define the success of the part. The propagation of a construct is also dependent on the intended application of the construct. In some instances, bioreactors allow semi-automated cell and tissue culture by the maintenance of specific physicochemical culture parameters as well as physical conditioning of developing tissues (Wendt et al., 2009). The tissue mimic is subjected to specific biochemical and physical cues to replicate the environments experienced within either healthy or diseased tissue for a time period that is suitable until the 3D model is fit for purpose.

3.2.4 Application

The four main 3D bioprinting applications include drug discovery, cosmetics testing, tissue regeneration and medical devices (Vijayavenkataraman et al., 2018). Drug screening on biomimetic constructs versus 2D models provide better results based on their ability to mimic the spatial and chemical attributes of native tissues (Peng et al., 2017). Bioprinting models for cosmetic testing, on the other hand, is mainly practiced in order to bypass animal testing in the first instance (Vijayavenkataraman et al., 2016). For tissue regeneration purposes, 3D bioprinting is used to produce artificial tissues such as skin, bone, cardiovascular tissue and cartilage in an attempt to overcome organ donor shortages. Finally, 3D models destined as medical devices have been used in applications such as in the prevention of biofilm formation (Sandler et al., 2014), as stents (Cabrera et al., 2017) and in dental restoration practises (Dawood et al., 2015).

3.3 Addressing the Challenges in 3D Bioprinting

Out of all the bioprinting modalities, micro-extrusion based printers are the only platforms that can achieve human-scale tissues due to the continuous flow of bioink and large deposition rate (Vijayavenkataraman et al., 2018). There are two main issues that are associated with the use of

bioprinters, however, firstly being able to achieve optimum print fidelity of a scaffold whilst secondly preserving cell viability. High viscosity bioinks are often employed in order to tackle the issues associated with print fidelity for micro-extrusion printing, although cell viability can be somewhat compromised using this method (Peltola et al., 2008). Likewise, low viscosity bioinks better perpetuate cell viability at the cost of compromising print fidelity. Several printing variables may be adjusted in order to overcome these issues by optimising the material parameters (including gelation and hydrogel properties), print parameters (including nozzle gauge, print pressure and print speed) and collector platform (**Figure 3.3**).

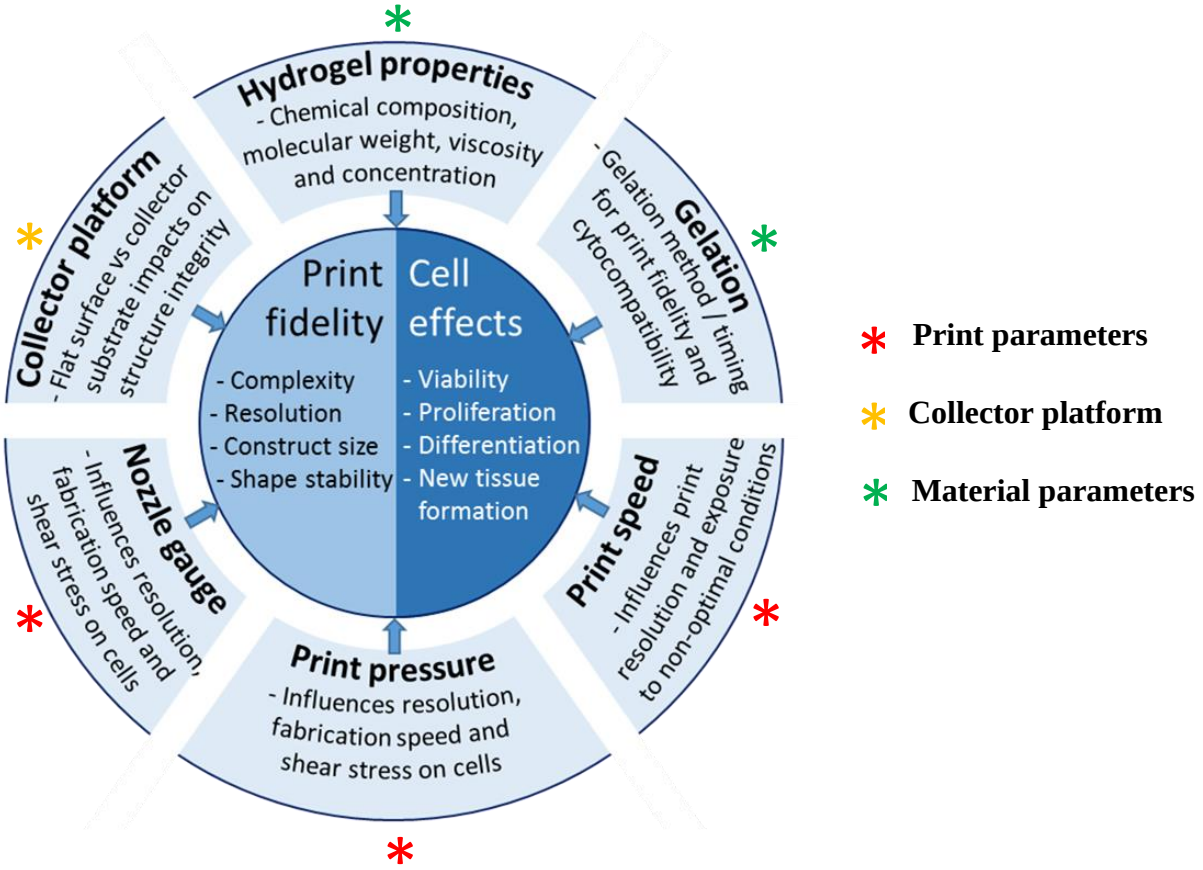

Figure 3.3 – Optimisation of print parameters that are critical for successful biofabrication in tissue engineering.

3.3.1 Material Parameters

During tissue construct fabrication, materials for incorporation into a bioink are often elected based upon their suitability as a target tissue ECM mimic. Print parameters are then tailored in order to accommodate material printability and subsequent gelation of the construct. That being said, it is also possible to modify hydrogel properties and gelling mechanisms to a certain degree for printing

optimisation accordingly. The main hydrogel properties that affect printing specifications are threefold – chemical constituents, molecular weight and concentration (the latter two properties contributing to material viscosity) (Kyle et al., 2017).

With regards to the chemical properties of a printing material, different material chemistries require specific crosslinking mechanisms which can impact on biofabrication window time. It is paramount that the printed construct geometry is consistent with the geometry of the 3D model whilst also maintaining cell viability. In order to achieve this, *in situ* gelation is often initiated, whereby material is crosslinked as it is printed, layer by layer, in order to achieve maximum print fidelity. This technique is useful when the time to generate the overall print is lengthy, when the viscosity of the bioink solution is low, and when gelation mechanisms are slow, yet is limited to the manufacture of single materials as biopolymers are difficult to integrate once gelled (Galarraga et al., 2019).

3.3.2 Print Parameters

Once suitable material parameters have been selected, printer operating modalities can be optimised for tissue construct fabrication using micro-extrusion-based printing. Amongst these modalities are print speed, print pressure, nozzle gauge and extrusion flow rate and each criterion directly impacts upon each other as well as print fidelity and cell viability within a printed construct. It is generally the consensus that print speed is the first parameter to be tailored as it is most dependent upon the material being printed. However, when the bioink being extruded is stable following deposition, slicing software can automatically calculate print speed based on input nozzle gauge so that a line width between 20% – 50% larger than the needle aperture is achieved. This is so that, for extrusion of high viscosity polymers without any supporting apparatus, over-extrusion and increase in layer height or under-extrusion and discontinuous layer deposition can be prevented (Carrier, 2018). Hydrogels exhibiting low viscosity require more rapid print speeds in favour of completing structure fabrication before the printed part loses its structural integrity.

Selecting nozzle gauge can often be a trade-off between print resolution and exposure of bioinks to shear stresses. Larger nozzle apertures can reduce nozzle induced stresses on bioinks due to a reduction in polymer flow resistance yet jeopardises print resolution. Conversely, smaller nozzle diameters achieve better resolution but can compromise the viability of a bioink's cell cargo. The delicate balance between resolution and shear stress is further apparent when tuning print pressures in pneumatic extrusion. High print pressures can result in poor resolution and exertion of shear stresses on cells, whereas low print pressures cause disruptions in polymer flow yet with less negligible effects on cell viability (Webb & Doyle, 2017). Nozzle gauge and print pressure, in addition to viscosity, determine polymer flow rate and must also work in conjunction with print speed.

3.3.3 Collector Platform

Within conventional bioprinting systems, bioinks are deposited onto a z-stage collector platform during additive layer manufacture of a scaffold or construct. Some scaffolds incorporate additional supporting features which are built-in within the 3D model and are later severed from the part following reinforcement by gelation. The extra scaffolding material is used to support overhanging features that would not otherwise be printable in 3D. It is only relatively recently that research directed into the use of a supporting sacrificial matrix has been investigated.

3.4 Embedded Bioprinting

Embedded bioprinting is defined by a range of techniques that use a secondary substrate for the build-up of complex hydrogel structures. Using embedded bioprinting, one is not subjected to the usual constraints found in conventional methods when printing onto a planar surface and instead, the fabrication of intricate shapes can be realised with greater success. This technique is conducive to the production of constructs featuring overhanging or hollow structures which would otherwise collapse without the supporting matrix resulting from gravitational forces. Within the literature, one of the first reports of using a secondary substrate in additive layer manufacture dates back to 2011. Wu et

al., (2011) documented using a modified Pluronic F127 reservoir into which an unmodified Pluronic F127 fugitive ink was deposited for the manufacture of microvascular networks. This approach generated a perfusable network within the supporting reservoir which would later be photocrosslinked. The fugitive phase was subsequently liquefied under vacuum at 4 °C leaving an embedded vascular structure.

Since this method of forming the final part within the reservoir phase, it has become more commonplace to print a retrievable tissue construct within a sacrificial supporting matrix. Support materials such as a carbopol granular medium (Bhattacharjee et al., 2015) and a gelatin slurry (Hinton et al., 2015) have both been used to this effect for the generation of complex, self-supporting freeform structures using the printing materials PDMS, alginate, collagen and fibrinogen. Despite significant efforts, these manufacturing processes have fallen short of generating constructs with regional variations in mechanics, material chemistry and cell phenotypes, require stringent temperature constraints to prevent the support bed from prematurely liquefying under cell culture conditions and prove difficult in liberating the final product from the supporting matrices. An alternative method known as Suspended Manufacture has since been coined which meets the criteria of achieving multi-layer hydrogel structures that are akin to native human tissues, under ambient conditions, with relative ease and accurate shape-specificity.

3.4.1 Suspended Manufacture

Suspended manufacture is a process in which cell laden biopolymer solutions are extruded into a bed of micrometre-sized agarose gel particles that provide sufficient support to prevent the structure collapsing under its own weight. Once construct printing is complete, it may be solidified, extracted from the supporting gel bed and cultured for its intended use (**Figure 3.4**). This technique has proven successful in a previous study with Moxon et al., (2017) whereby cell laden gellan was extruded by hand into a supporting fluid gel bed to create an osteochondral plug which was later transplanted into a defect containing interfaced cartilage and bone.

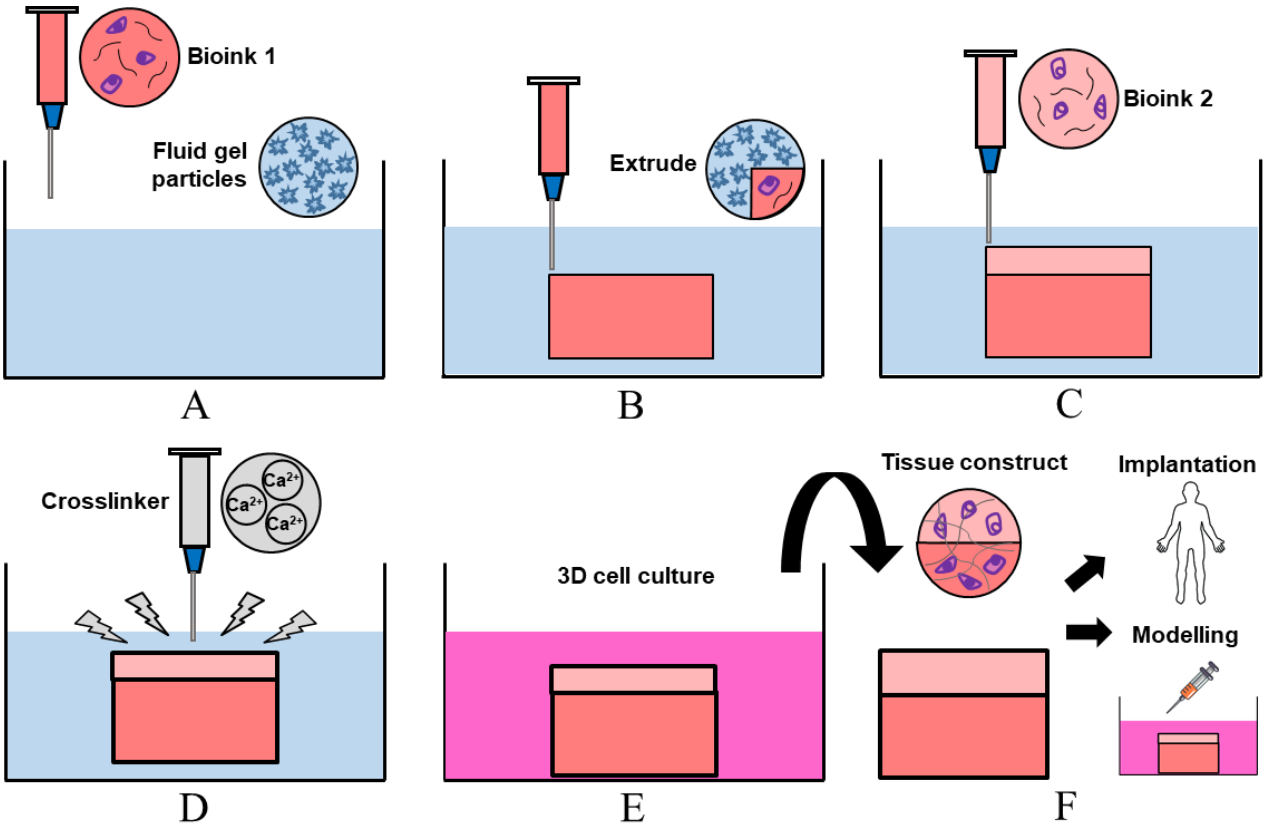

Figure 3.4 – Suspended manufacture process. A) Bioink containing polymer and cells is loaded into a dispensing cartridge and agarose fluid gel is poured into a container to form the supporting bed. B) The bioink solution is extruded within the supporting gel. C) Multiple other bioinks with differing polymer chemistries and encapsulated cell phenotypes may be extruded atop the previous extrude. D) Crosslinking solution is used to solidify charged polymers. E) The construct is extracted and 3D cultured until maturity is reached. F) The tissue construct is ready for its intended use, either for implantation or drug-disease / cosmetics modelling.

This technology enables the printing of constructs from low viscosity precursor solutions with greater complexity and shape specificity without limitation over build direction, supports or overhangs. It is the inherent behaviour of the fluid gel particles themselves that allows the success of suspended manufacture.

3.4.1.1 Fluid gels

Fluid gels are characterised by their self-supporting ability at rest and will subsequently flow upon the application of shear. They are generated when a shear force is applied during the gelation process of a polysaccharide hydrogel. The end-product of this technique consists of micrometre sized gel particles within a liquid continuous phase as opposed to a bulk, firm gel following quiescent gelation

(**Figure 3.5**). The weakly interacting structure of fluid gels that allows this temporary flow and spontaneous reformation phenomenon has been exploited within the food industry as they are renowned for their flavour release and pleasant mouthfeel properties. Several examples of fluid gels have been documented in the literature, including gellan (Sworn et al., 1995), alginate (Fernández Farrés & Norton, 2014), κ-carrageenan (Mahdi, 2016), agar (Fernández Farrés et al., 2014) and agarose (Moxon et al., 2017). In this thesis, agarose has been used in fluid gel formulation as it requires thermal gelation kinetics at high temperatures and is relatively neutral, meaning that culture of constructs within it will not cause matrix interaction and is also conducive to cell culture temperatures.

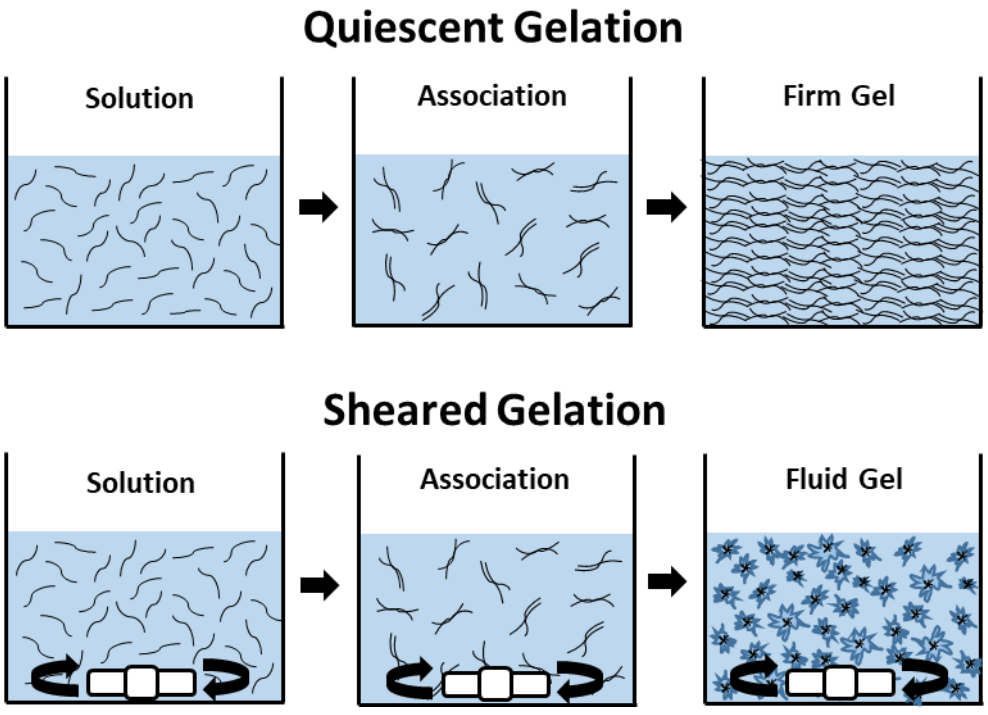

Figure 3.5 – Schematic diagram of the quiescent gelation of a firm gel and sheared gelation of a fluid gel.

The proposed underlying mechanism for agarose fluid gel formation in particular is described by a nucleation and growth process, in that particle growth is dependent upon the shear environment experienced by the solution (Norton et al., 1999). During cooling of an agarose solution, an increase in viscosity is attributed to aggregation of ordered domains during what is known as a spinodal decomposition event, causing phase separation during molecular ordering. Under shear, the potential

nucleation sites are disassociated from one another, limiting the molecular ordering to within distinct fluid gel particles. The extent of particle growth is in turn dictated by the magnitude of the shear force applied to the agarose solution, where polymer chains are recruited from the surrounding un-gelled matrix and the particles are also physically forced to aggregate by shear flow forces. This enables the modulation of the hydrogel's physical attributes without changing the chemical properties at the molecular level.

The particles formed by sheared gelation display a higher polymer density at the core of the particle with a descending gradient to the outer edge, ascribed by the weak intermolecular tension at the gelled and non-gelled polymer interface and the increased flow field at the particles' surface (Fernández Farrés et al., 2014b). Within these lower density regions at the particles' surface exist fewer helical domains and aggregates, leading to the evolution of particle hairs. Varying polymer concentration and applied shear during fluid gel formation have also been seen to generate rheological variances (Dong et al., 2009). Within a high concentration agarose solution, as the particles are being formed under a sufficient shear rate, the higher population of disordered coils within the solution is causative of higher viscosity solutions. This results in an increase in local shear stresses on the particles within the system, thus reducing the potential of aggregation and nucleation of neighbouring particles and generating a larger variance in particle size populations.

To successfully support the printed structures during suspended manufacture, the agarose fluid gel bed should sufficiently flow to allow deposition of the printed material, yet also demonstrate ample structural integrity following deformation and a capacity to self-heal. It is therefore crucial that an understanding of the mechanisms underlying fluid gel formation and the behaviour of the fluid gel post-formulation is clearly outlined. The first of the results chapters deals with the preparation and characterisation of the agarose fluid gel bed.

Chapter 4

CHARACTERISATION OF THE SUPPORTING FLUID GEL BED

Aspects of this chapter are published in *Advanced Functional Materials*

Senior, J.S. Cooke, M.E. Grover, L.M. Smith, A.M. (2019) Fabrication of Complex Hydrogel Structures using Suspended Layer Additive Manufacturing (SLAM). *Advanced Functional Materials*, 29, 49.

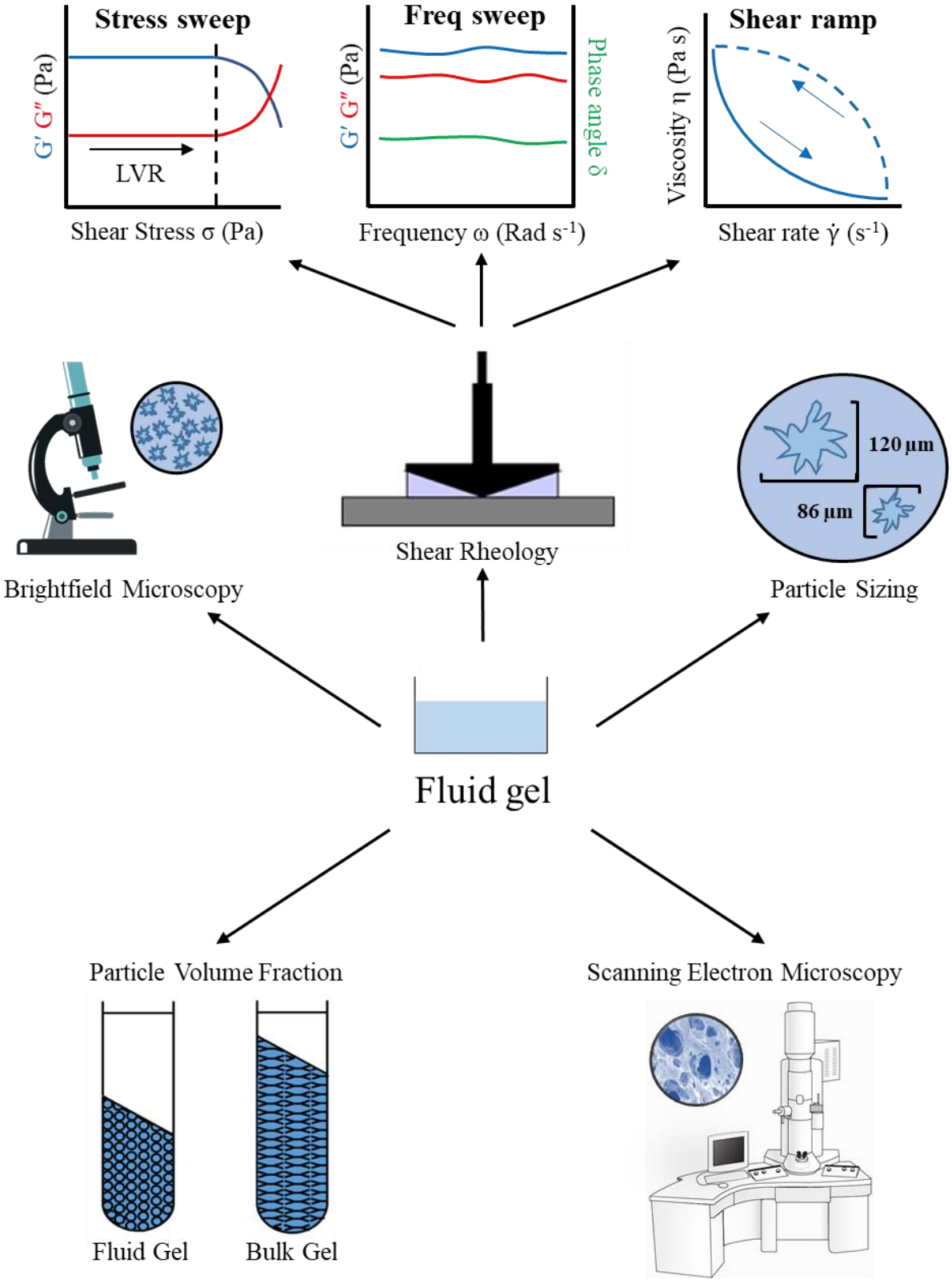
Stress sweep
G′ G″ (Pa)
LVR
Shear Stress σ (Pa)
Freq sweep
G′ G″ (Pa)
Phase angle δ
Frequency ω (Rad s-1)
Shear ramp
Viscosity η (Pa s)
Shear rate γ̇ (s-1)
Brightfield Microscopy
Shear Rheology
120 µm
86 µm
Particle Sizing
Fluid gel
Particle Volume Fraction
Fluid Gel
Bulk Gel
Scanning Electron Microscopy

Chapter 4 – Characterisation of the Supporting Fluid Gel Bed

4.1 Introduction

An extensive number of reports have recently been made on fabricating complex, 3D bioprinted, cell-laden hydrogels. Numerous approaches towards this end have been described, however, given the nature and fragility of the liquid precursors, the most successful approaches employ a supporting particulate gel phase (Senior et al., 2019). Using this supporting feature, the fragile part is protected during printing and the 3D model features are maintained in the liquid form prior to gel initiation. Without such, one must incorporate high viscosity materials and rapid gelation mechanisms as well as a broad geometrical base and built-in supports for overhanging structures for the successful realisation of a 3D biofabricated construct (Cooke et al., 2018).

The characteristics of the supporting gel bath are key in creating model tissue replicas by ensuring shape-specificity whilst also maintaining the viability of its cell cargo. The supporting matrix must have the ability to uphold the deposited material without the need to modify the 3D model in order to ensure that an accurate representation in shape geometry is achieved (Highley et al., 2015). Moreover, the support must allow the layered deposition of multiple bioinks if one wishes to fabricate anisotropic tissue-like structures (Moxon et al., 2017). Following material extrusion within the support bath which causes subsequent deformation, the gel must exhibit rapid recovery in order to preserve 3D print fidelity and to prevent the formation of voids within the support matrix as a result of needle and bioink-induced shear (Rocca et al., 2018). It is also essential that fabricated constructs can be cross-linked and liberated from the support bed without impedance on cell culture-conducive conditions. Lastly, the supporting medium within which bioinks are deposited must demonstrate biocompatibility, eliciting no adverse effects on encapsulated cells and having no chemical interaction with the tissue construct.

Fluid gels made from agarose and generated under specific conditions can fulfil these criteria. They have shear-thinning capabilities that allow extrusion of material between particle interstices and allow rapid restructuring upon the removal of shear (Senior et al., 2019) (**Figure 4.1**). They allow the suspension of a large range of polymers and crosslinking strategies, having no interaction upon the addition of ions that solidify suspended charged polymers and are also conducive to cell culture media and temperatures. This natural polymer is also biocompatible, attributed to its natural origins, net neutral charge and non-cytotoxicity and also lacks non-specific adsorption of biomolecules and cellular attachments to the gel matrix in unmodified gels (Fernández-Cossío et al., 2007; Keren, 2003; Zarrintaj et al., 2018).

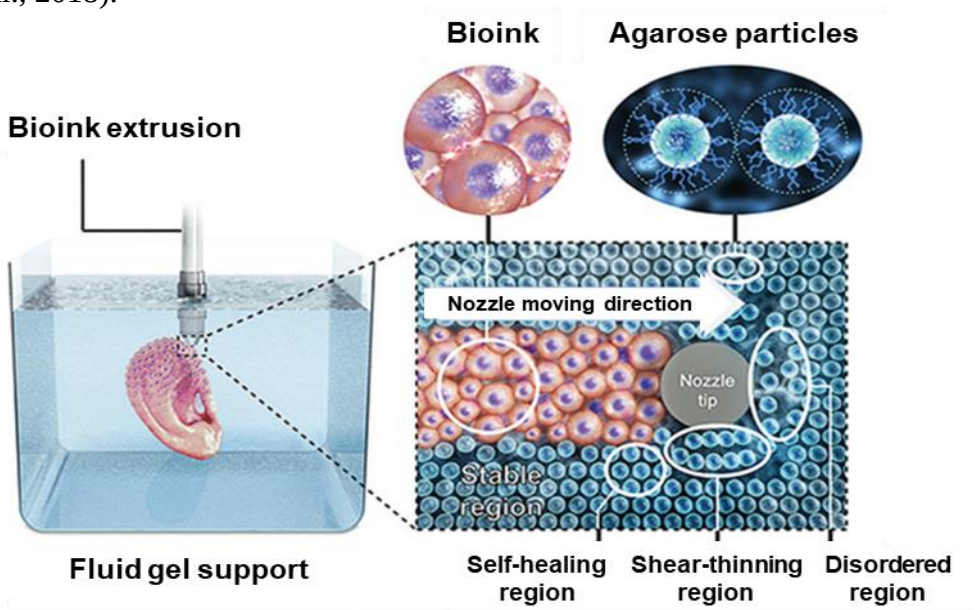

Figure 4.1 – Shear-thinning and self-healing agarose fluid gel bed in suspended manufacturing (adapted from Jeon et al., 2019).

Despite the apparent similarities between supporting particulate beds that have been reported in the literature, the way in which particles are generated strongly influences particle interaction and has a definitive effect on suspended product quality. Using an agarose fluid gel bed as a supporting matrix has previously been validated by Moxon et al., (2017) who printed an osteochondral unit by hand. Some analysis on the characterisation of the agarose fluid gel as a suspending matrix was undertaken by studying rheological behaviour and particle microscopy.

In this chapter, to gain a better understanding of the mechanisms underlying suspended manufacturing, the physical characteristics of the supporting fluid-gel matrix were explored. Initially, the mechanical characterisation of agarose fluid gels was explored by shear rheology. A secondary fluid gel formulation regime was also studied by dilution of freshly prepared agarose fluid gels to given concentrations, demonstrating the critical importance of formulation technique on the behaviour of the supporting matrix. Assessment of particle size distribution, morphology and volume fraction by using particle sizing, brightfield and scanning electron microscopy and centrifugation techniques further consolidates agarose fluid gel behaviour, providing additional insight into suspended manufacturing function.

4.2 Methods

4.2.1 Agarose gel formulation

Fresh agarose fluid gels (type I low EEO, purchased from Sigma-Aldrich, Dorset, UK) were prepared by autoclaving solutions of agarose mixed with deionised water (121°C temperature and 1.4 bar pressure) (Prestige Medical™ bench top autoclave) at concentrations of 0.25%, 0.50%, 0.75% and 1.00% w/v and cooling to 25 °C under a constant shear of 700 rpm using a magnetic stirrer.

Diluted agarose fluid gels were formulated by the addition of deionised water to freshly prepared agarose fluid gels at 1.00% w/v to make subsequent concentrations of 0.25%, 0.50% and 0.75% w/v agarose.

Quiescent agarose firm gels were made by quiescently cooling autoclaved agarose solutions to 25 °C absent of shear to give final concentrations of 0.25%, 0.50%, 0.75% and 1.00% w/v.

4.2.2 Shear rheology

All rheological testing was undertaken in triplicate using a Bohlin Gemini rheometer (Malvern Panalytical, UK) fitted with a 2°/55 mm cone and plate geometry at 25 °C.

4.2.2.1 Amplitude sweeps

Amplitude sweeps were carried out to compare and characterise the liner viscoelastic region (LVR) of fresh and diluted fluid gels. G′ and G″ moduli (Pa) were measured with an increasing shear stress from 0.1 to 100 Pa and a constant angular frequency of 10 rad s^{-1}.

4.2.2.2 Frequency sweeps

Frequency sweeps were performed to characterise the viscoelastic behaviour of fresh and diluted fluid gels. G′ and G″ moduli (Pa) were measured with increasing oscillatory frequencies from 0.1 to 100 rad s^{-1} at a constant strain of 0.05%.

4.2.2.3 Shear ramps

Shear ramps were conducted to characterise the viscosity of fresh and diluted fluid gels. Viscosity (Pa s) was measured with an increasing shear rate of 0.01 to 100 s^{-1}.

4.2.3 Particle size distribution

Particle size distribution within fresh agarose fluid gels was examined using a Malvern Mastersizer 2000. Fluid gel samples of 0.25%, 0.50%, 0.75% and 1.00% w/v were diluted in deionised water followed by agitation at 2450 rpm using a small volume sample dispersion unit (Hydro 2000 SM) in order to give a homogenous dispersion of particles prior to particle sizing analysis. A refractive index of 1.42 and 1.33 was used for agarose and deionised water, respectively.

4.2.4 Brightfield microscopy

For visualization of the particulate structure within fluid gels, small samples of 0.25%, 0.50%, 0.75% and 1.00% concentration were loaded onto microscope slides and mounted with a cover slip before leaving to air-dry and imaging using a VWR IT 400 Inverted Microscope (VWR, UK).

4.2.5 Particle volume fraction

For the determination of fluid gel particle volume fractions, agarose fluid gel samples at concentrations of 0.25%, 0.50%, 0.75% and 1.00% were centrifuged at a given range of centrifugal forces (RC5C Sorvall Instruments-Dupont, Wilmington, DE) in order to separate fluid gel particles from the continuous aqueous phase. The solid phase volume of the fluid gel following centrifugation (*φFG)* was then calculated as a fraction of the mass of sedimented solid (*MFG.s*) compared with the total pre-centrifuged fluid gel (*MFG.0*) as displayed below (**Equation 4.1**).

$$\varphi\mathrm{FG} = \frac{MFG.s}{MFG.0} \qquad \textbf{Equation 4.1}$$

In order to account for the fluid released from the particles themselves during the centrifugation process, quiescent agarose bulk gels of identical concentrations were also centrifuged. The solid phase volume of the quiescent bulk gel following centrifugation (*φQG)* was then calculated as a ratio of the mass of sedimented solid (*MQG.s*) compared with the total pre-centrifuged quiescent bulk gel (*MQG.0*) as reported in **Equation 4.2**.

$$\varphi\mathrm{QG} = \frac{MQG.s}{MQG.0} \qquad \textbf{Equation 4.2}$$

The fluid expelled from fluid gel particles due to particle compressibility can therefore be expressed as 1 – *φQG.*

Finally, a third contributor to liquid expulsion can be attributed to gel relaxation - also known as syneresis (*φsyn).* This was quantified as the mass of the fluid released from quiescent gels following a 72-hour period divided by the total original mass of quiescent bulk gels for given concentrations.

The fluid gel particle volume fraction for a given polymer concentration and centrifugal force may then be ascertained according to **Equation 4.3**.

$$\Phi FG = \varphi FG + [(1 - \varphi QG) - \varphi syn] \qquad \textbf{Equation 4.3}$$

The process of determining particle volume fraction from centrifuged fluid gels is further outlined in **Figure 4.2**.

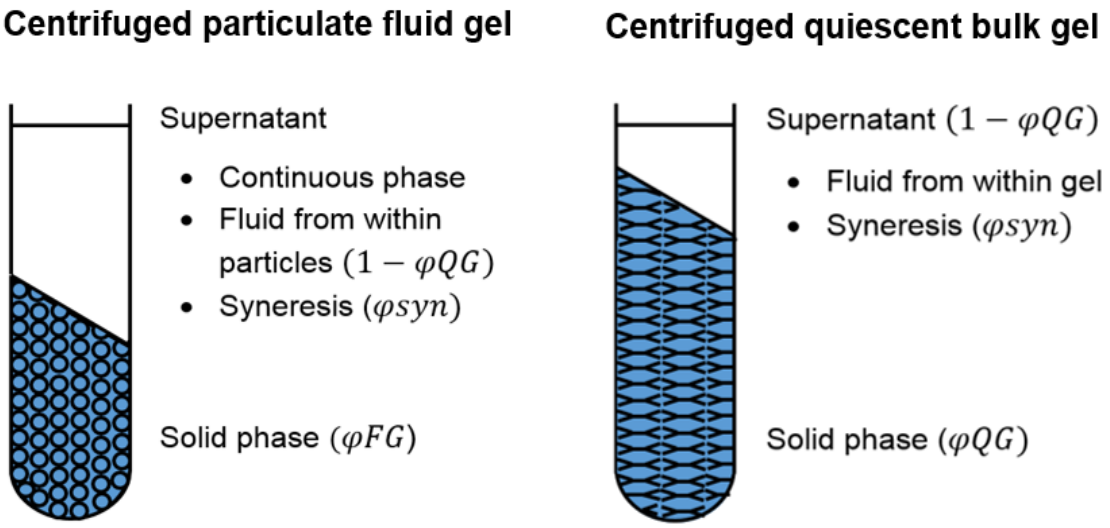

Figure 4.2 - Schematic illustration of the phases within agarose particulate fluid gels and quiescent bulk gels post-centrifugation.

4.2.6 Lyophilisation

Samples of 0.50% agarose fluid gel and quiescent bulk gel, as well as solid and supernatant phases of both centrifuged fluid gel and bulk gel, were subjected to lyophilisation. Freshly prepared 1.00% agarose and 0.50% diluted agarose fluid gels were also freeze-dried. Samples were frozen at -80 ºC for 24 hours and then a 72 hour freeze drying cycle was implemented at -76 ºC and 0.0010 mbar (Christ ALPHA 2–4 LD plus). Dry samples were stored in a desiccator for the preservation of aridity.

4.2.7 Scanning Electron Microscopy (SEM)

Lyophilised agarose fluid gels (fresh 0.50%, 1.00% and diluted 0.50%), quiescent bulk gel (0.50%), and solid and supernatant phases of centrifuged fluid gel were sputter coated with gold using a Quorum SC7620 sputter coater under a low bleed of argon. The internal networks of the materials were then studied using a field emission scanning electron microscope (FEI Quanta 250 SEM) operated in high vacuum mode at an accelerated electron energy of 10 kV. Several images were collected at various magnifications using a back scattered electron detector.

4.3 Results

4.3.1 Amplitude sweeps

Amplitude sweeps were conducted to ascertain the linear viscoelastic region (LVR) and therefore the critical stress at which intermolecular associations are forced to collapse in samples of agarose that were freshly prepared (F) and diluted from a pre-formulated stock of 1.00% agarose (D). As concentration descended, elastic (G′**)** and viscous **(**G″) moduli decreased across both formulation regimes (**Figure 4.3**). Diluted samples exhibited reduced G′ and G″ moduli in comparison to the corresponding concentrations of agarose that were freshly prepared. This caused a reduction in the length of the LVR resulting in polymer network deformation at lower shear stresses. **Table 4.1** highlights and compares the key initial elastic and viscous moduli along with the contrast in LVR between freshly prepared and diluted agarose samples.

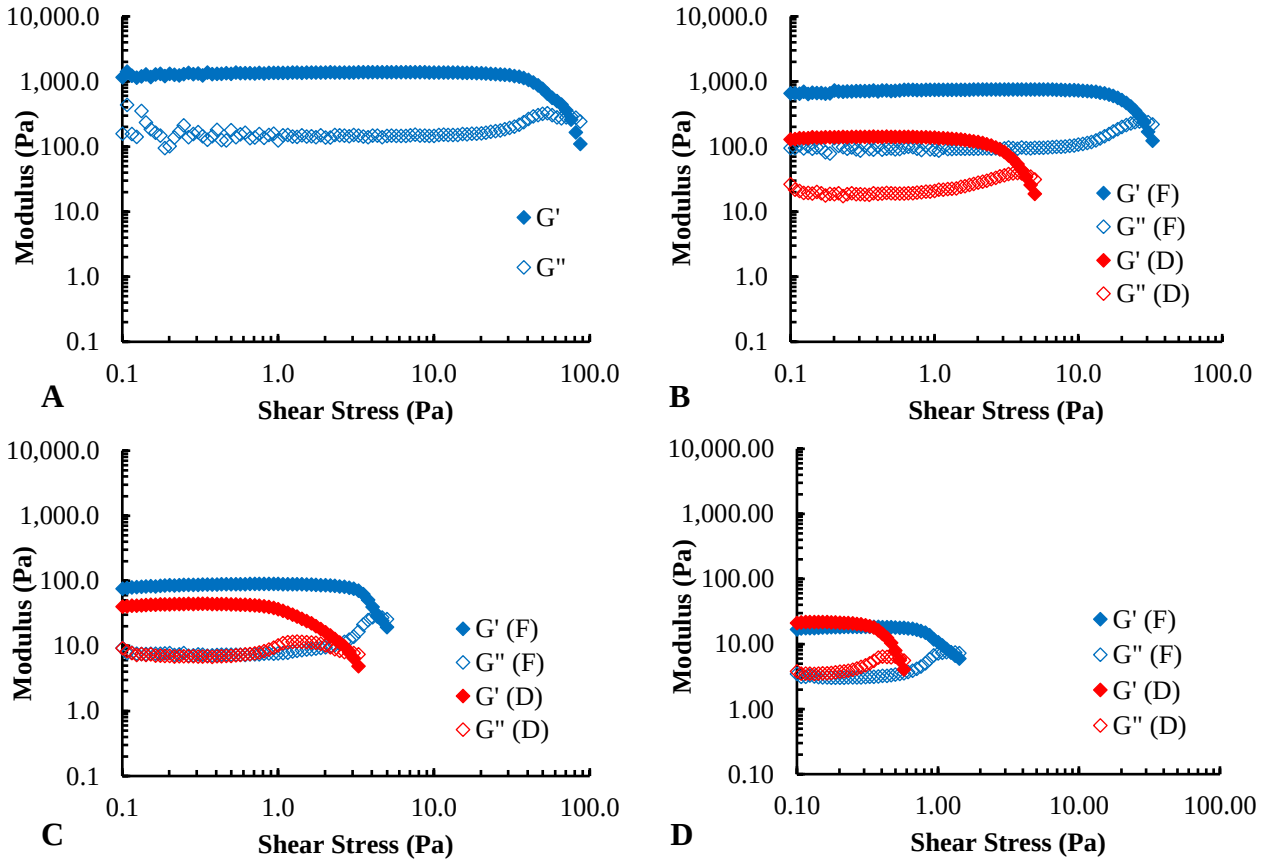

Figure 4.3 - Amplitude sweeps displaying elastic (G′) and viscous (G″) moduli of A) 1.00% w/v agarose stock and the comparison of moduli between freshly prepared (F) and diluted from stock (D) in B) 0.75% C) 0.50% and D) 0.25% w/v agarose over a shear stress of 0.1 to 100.0 Pa.

Table 4.1 – Comparison of freshly prepared agarose with agarose diluted from 1.00% stock on initial G′ and stress where G′ = G′.

Description of Agarose	Initial G′ (Pa)	Stress where G′ = G″ (Pa)
1.00% Stock	1164.33	74.55
0.75% (F)	658.50	27.34
0.75% (D)	128.63	4.19
0.50% (F)	75.68	4.42
0.50% (D)	40.03	3.16
0.25% (F)	16.70	1.23
0.25% (D)	21.07	0.52

4.3.2 Frequency sweeps

Small deformation oscillatory rheology within the linear viscoelastic region (LVR) was performed on agarose fluid gels to determine a mechanical spectrum. This revealed that gels of all concentrations and formulation regimes were moderately frequency dependent (**Figure 4.4**), suggesting characteristics of a structured fluid with a dominance of solid (G′) over liquid behaviour (G″) across the frequency range tested. It was apparent that as concentration decreased, there was a subsequent decrease in elastic and viscous moduli in both freshly prepared and diluted agarose fluid gel regimes. Frequency sweeps also gave evidence that preparing diluted (D) compared with fresh (F) agarose fluid gels at corresponding concentrations reduces the elastic and viscous moduli. Furthermore, diluting agarose seems to have a much more profound effect on moduli in higher concentrations in comparison to low, with a variation in G′ between F and D of 1142, 320 and 45 Pa in 0.75%, 0.50% and 0.25% w/v agarose respectfully.

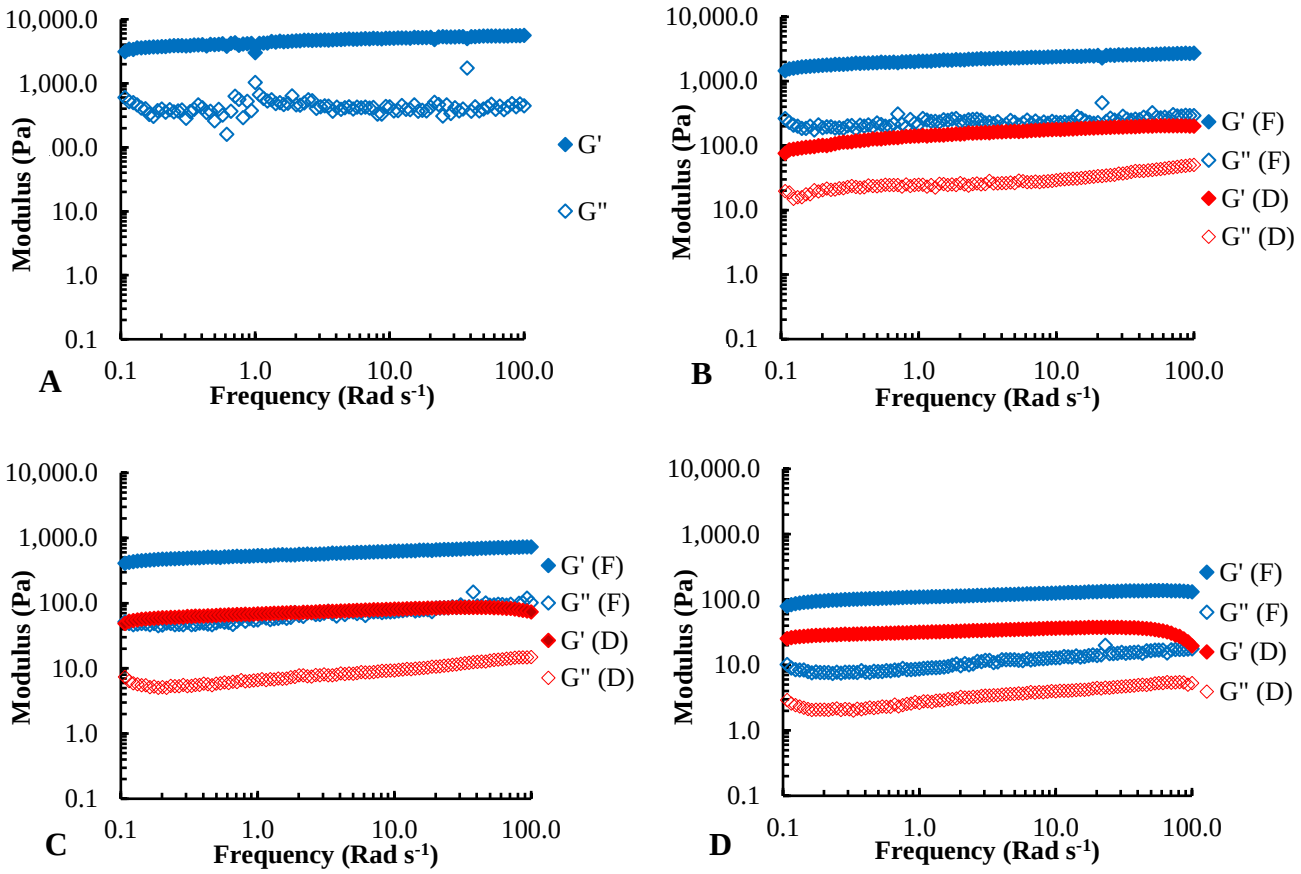

Figure 4.4 - Frequency sweeps displaying elastic (G′) and viscous (G″) modulus of A) 1.00% w/v agarose stock and the comparison of moduli between freshly prepared (F) and diluted from stock (D) in B) 0.75%, C) 0.50% and D) 0.25% w/v agarose over a frequency of 0.1 to 100.0 Rad $^{s-1}$.

4.3.3 Shear ramps

Upon analysis of freshly prepared and diluted agarose using shear ramp parameters, it is visible that increasing shear rate causes a decrease in viscosity in all cases (**Figure 4.5**). The viscosity of each fluid gel (both freshly prepared and diluted) also decreases as concentration descends. Additionally, diluted agarose samples exhibit lower viscosities compared with freshly prepared agarose at equivalent concentrations over identical shear rates. These results are in concordance with **Figures 4.3 and 4.4** in that diluted agarose presents weaker fluid gels compared with agarose which was freshly prepared to an equivalent concentration.

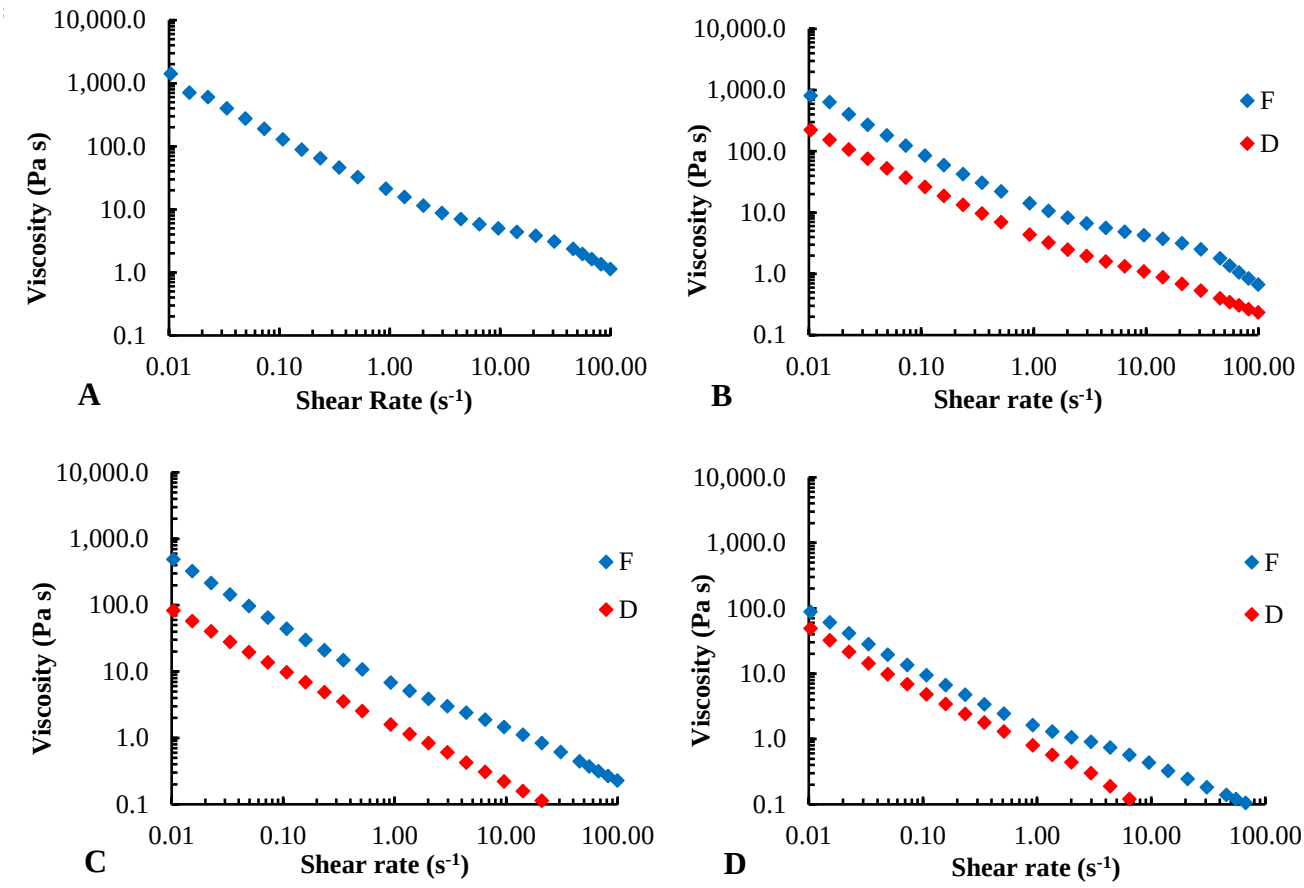

Figure 4.5 - Viscosity (Pa s) of A) 1.00% w/v agarose stock and the comparison of viscosity between freshly prepared (F) and diluted from stock (D) in B) 0.75%, C) 0.50% and D) 0.25% agarose over a shear rate of 0.01 to 100.00 s^{-1}.

4.3.4 Particle size distribution

To decipher the optimum fluid gel formulation for printing, fluid gels were prepared at different concentrations of 0.25% – 1.00% w/v agarose and the particle sizes were quantified.

The span was calculated in order to represent the width of particle size distribution, where the smaller the span, the narrower the distribution becomes. Span is calculated as per **Equation 4.4**, where $d(0.9)$, $d(0.1)$ and $d(0.5)$ is the size of particle (µm) below which 90%, 10% and 50% of the sample lies, respectively. Here, a rise in the span of particle size distributions is featured as fluid gel concentration increases (**Figure 4.6**, **Table 4.2**).

$$\frac{d(0.9)-d(0.1)}{d(0.5)}$$ **Equation 4.4**

The volume weighted mean D [4, 3] (also known as the De Brouckere mean diameter or mass moment mean) is analogous to the moment of inertia with a volume or mass dependence, therefore indicating particle size distribution in terms of volume (**Equation 4.5**, where d is particle size (µm)). For agarose fluid gels of increasing concentration, the volume weighted mean was also seen to increase.

$$\frac{\sum d^4}{\sum d^3}$$ **Equation 4.5**

Likewise, the median of the volume distribution (also termed $d\ (0.5)$) and sizes of particles within which 90% of the population distribution lie below (also termed $d\ (0.9)$) showed a general increase with increasing polymer concentration. Distribution of particle sizes within lower polymer concentrations display a more Gaussian trend as reported by the bell-shaped curves, where mean and median coincide. Higher concentrations of fluid gels, on the other hand, exhibit dual populations in particle diameter prevalence, as attributed by the double bell-shaped curves and larger span sizes.

Uniformity, as measured by the absolute deviation from the median, is calculated as indicated in **Equation 4.6**, whereby $d(0.5)$ is the median size of the distribution and d_i and x_i are respectively the mean diameter of, and result in, size class i.

$$\frac{\sum x_i\, d(0.5)- d_i}{d(0.5)\sum x_i}$$ **Equation 4.6**

In agreement with the previous data, as polymer concentration increases, uniformity decreases. Finally, the size of the smallest and largest particles within agarose fluid gels generally increases with increasing concentration, with exception of the highest concentration of 1.00% which is preceded by that of 0.75%.

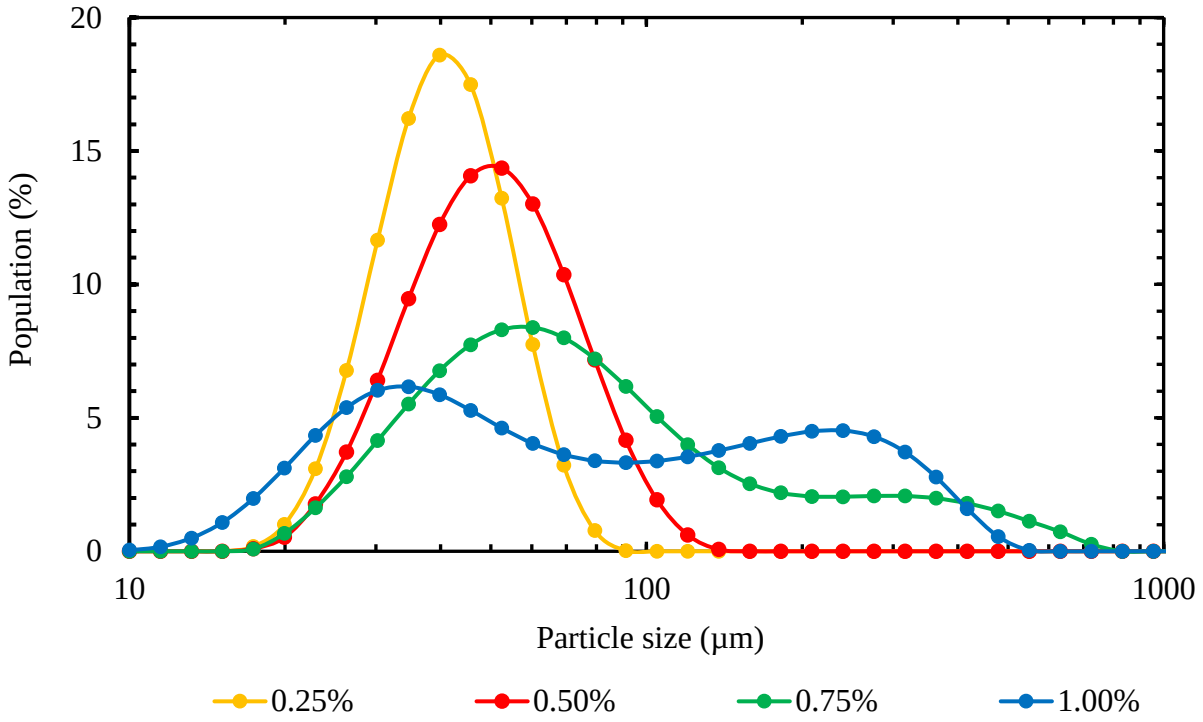

Figure 4.6 - Particle size distribution within agarose fluid gels produced at concentrations of 0.25%, 0.50%, 0.75% and 1.00% w/v under 700 rpm agitation.

Table 4.2 – Particle size span, volume weighted mean (D [4, 3]), median of the volume distribution ($d(0.5)$), size of particle below which 90% of the population lie ($d(0.9)$), uniformity and particle size range in agarose fluid gels varying from 0.25 – 1.00% w/v concentration (green and red are lowest and highest values respectively).

	Agarose fluid gel concentration (%)			
Measurement	**0.25**	**0.50**	**0.75**	**1.00**
Span (AU)	0.74	0.97	3.65	3.81
D [4, 3] (µm)	33.93	49.40	123.77	124.45
$d(0.5)$ (µm)	32.81	43.38	73.97	72.82
$d(0.9)$ (µm)	46.84	74.07	305.67	302.77
Uniformity (AU)	0.23	0.31	1.01	1.18
Particle size range (µm)	13.18 – 79.43	17.38 – 138.04	19.95 – 831.76	11.48– 630.96

4.3.5 Brightfield microscopy

For the inspection of individual agarose fluid gel particles, particle morphology was determined using brightfield microscopy. Fluid gels of all concentrations (0.25% - 1.00% w/v) exhibited 'hairy' inter-particle associations presenting a 'beads on a string' model (**Figure 4.7**). As concentration increased, the heterogeneity in particle morphology and size distribution also increased in agreement with particle sizing analysis.

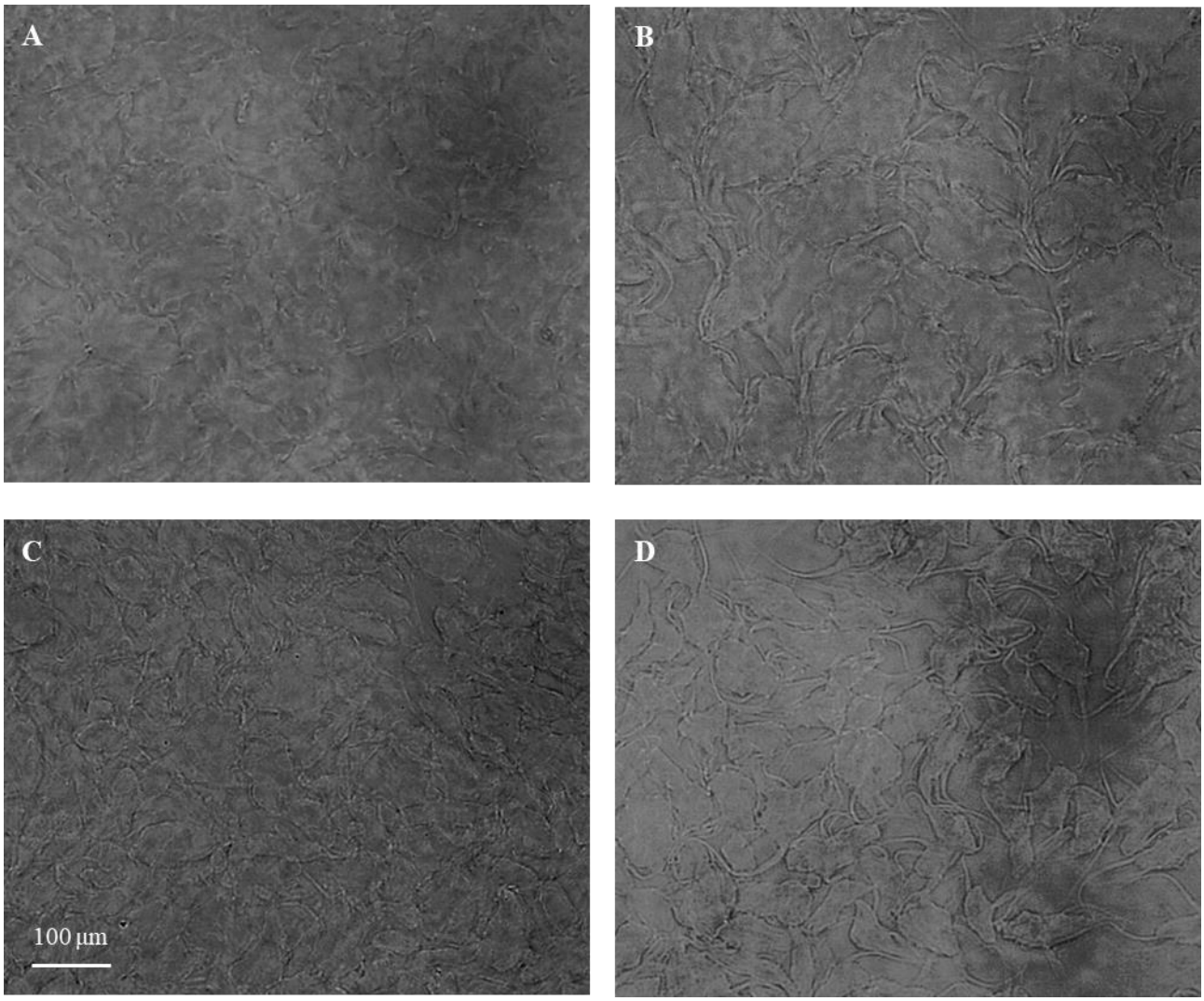

Figure 4.7 – Brightfield micrographs of agarose fluid gel particles at concentrations of A) 0.25%, B) 0.50%, C) 0.75% and D) 1.00% w/v.

4.3.6 Particle volume fraction

Fluid gels consist of a suspension of gelled particles within a continuous medium. To understand the influence of concentration on particle volume fraction, fluid gels were subjected to a range of centrifugal forces. Solid phase volume fractions within fluid gels (φFG) and quiescent gels (φQG) were determined under four increasing modes of centrifugation (5000, 17,500, 30,000 and 47,800 g). It was deduced that 0.50% quiescent gel solid phase fractions were 1.14, 1.21, 1.26 and 1.33 times larger than those of their fluid gel counterparts for each increasing centrifugal force (**Figure 4.8A**). Increasing centrifugal force, therefore, only had a slight effect on solid phase volume fractions between both quiescent and fluid gel preparations. Particle volume fractions account for the fluid lost to within the supernatant that is attributed to particle compressibility and gel relaxation. The particle volume fractions for the lowest given centrifugal force of 5000 g were 0.76, 0.88, 0.92 and 0.92 for agarose concentrations of 0.25%, 0.50%, 0.75% and 1.00% respectively (**Figure 4.8B**). For the highest applied centrifugal force of 47,800 g, particle volume fractions were 0.78, 0.83, 0.86 and 0.88. It can thus be determined that fluid gel particle volume fraction is dependent on concentration.

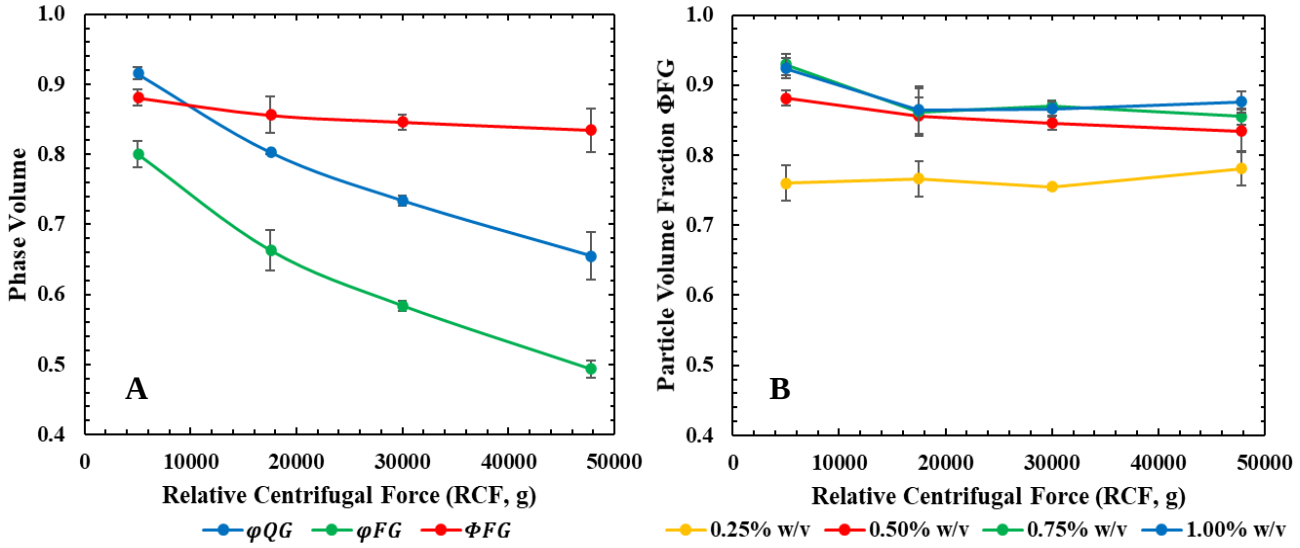

Figure 4.8 – Relationship of relative centrifugal force (RCF) on A) phase volumes within 0.50% agarose gels and B) fluid gel particle volume fractions for agarose particulate fluid gels of 0.25%, 0.50% and 0.75% and 1.00% w/v concentration.

4.3.7 Scanning Electron Microscopy (SEM)

Scanning electron microscopy (SEM) was performed in order to compare the microstructures of agarose gels when prepared under defined conditions. Lyophilised 0.50% agarose quiescent and fluid gels differ in that quiescent gels are comprised of thin, film-like sheets whereas fluid gels display an interconnected porous network (**Figures 4.9A and B**). The solid fraction (SF) of the gels were quantified as a percentage of dry weight versus total weight and were calculated at 0.49% and 0.42% respectively.

Following centrifugation, the particle fraction (PVF) and supernatant of 0.50% agarose fluid gels were also lyophilised and imaged using SEM (**Figures 4.9C and D**). The consistency of freeze dried PVF was like that of polyethylene foam and particle hairs could be seen at the microscale, consistent with particles imaged using brightfield microscopy. Given that the supernatant was removed prior to lyophilisation, the solid fraction was larger than that of fluid gels, measuring at 1.27%. In contrast, the supernatant exhibited a cotton wool-like appearance that was light and sparse, represented by the solid fraction of 0.02%.

To characterise the microstructural differences of freshly prepared and diluted agarose fluid gels, both freshly prepared 1.00% w/v and 0.50% diluted fluid gels prepared from a 1.00% stock were lyophilised and imaged using SEM (**Figures 4.9E and F**). Fluid gels prepared at 1.00% w/v presented a thick mesh-like network in comparison to the less inter-connected network seen in agarose fluid gels prepared at 0.50% w/v. When fluid gels are prepared following dilution to 0.50% w/v from a 1.00% stock however, a much sparser network is exhibited.

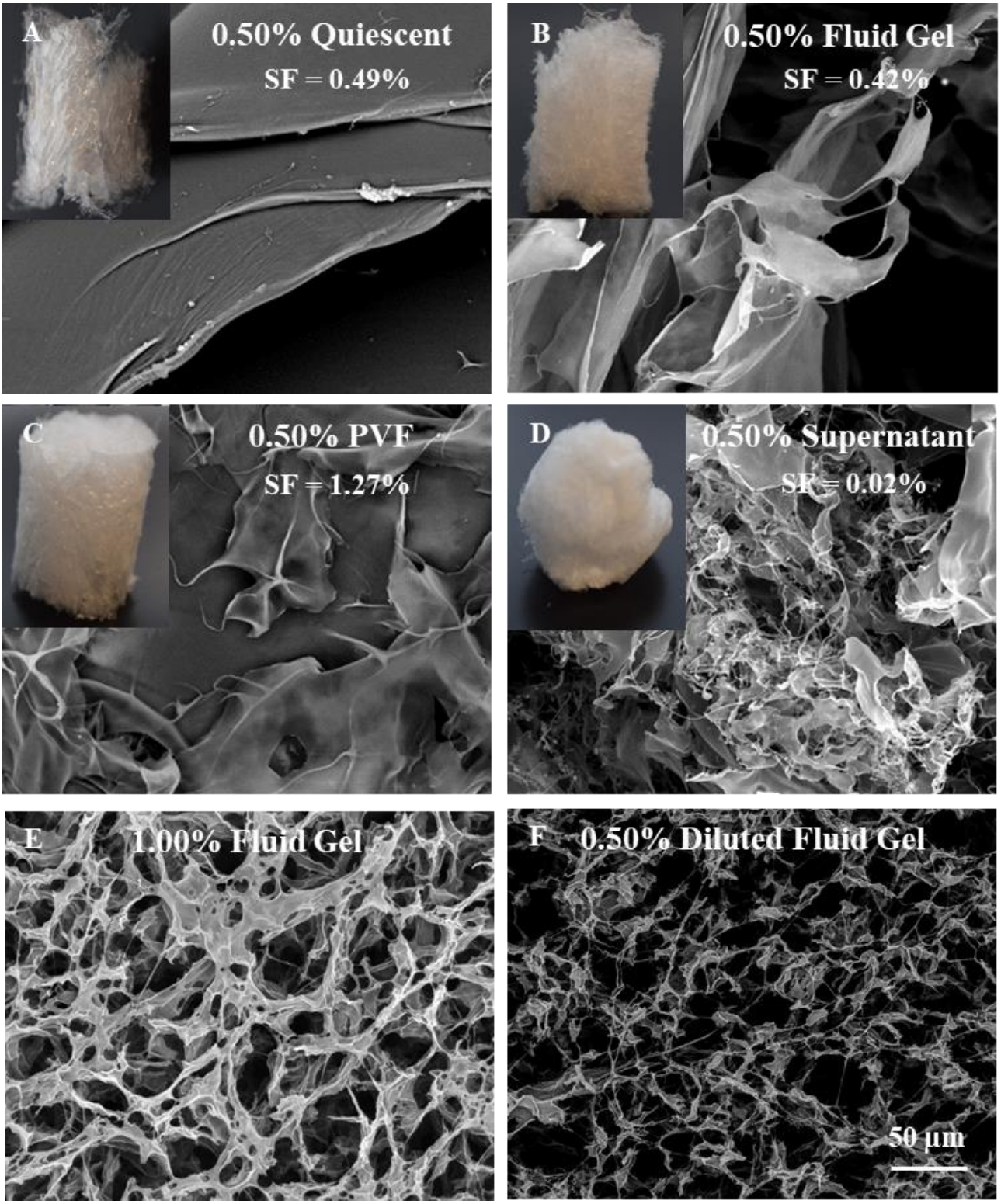

Figure 4.9 – Scanning electron micrographs showing the microarchitecture of freeze-dried agarose gels. A) 0.50% quiescent gel, B) 0.50% fluid gel, C) 0.50% centrifuged fluid gel particle fraction, D) 0.50% centrifuged fluid gel supernatant, E) 1.00% fluid gel and D) 0.50% fluid gel diluted from a 1.00% stock (scale bar = 50 µm).

4.4Discussion

Biopolymer hydrogels such as agarose are valuable resources in tissue engineering applications due to their tuneable microarchitectures and mechanical properties. When 3D bioprinting a desired shape, the complexity, resolution and dimensional accuracy of the product is influenced by the material that is being printed and also the platform or supporting network into which the bioink is extruded. However, many implications arise when 3D bioprinting scaffolds onto a solid, planar surface. This technique is limited to printing relatively basic designs with the use of only high viscosity materials that require curing *in-situ*. Another method by the name of suspended manufacturing uses a supporting particulate bed for the creation of distinguished bioprinted scaffolds. The suspended manufacturing method in supporting a construct has proven a reputable solution to the flowing and deformation of scaffold architecture and has been likened to the way in which the amniotic fluid cradles a developing foetus (Moxon et al., 2017).

Both natural (polysaccharide and protein) and synthetic gelling polymers can form fluid gels. The resultant gel properties when produced under a given shear field create a fluid or paste-like consistency as opposed to quiescent, bulk gels formed through traditional static cooling. Rheological analysis was used to assess the viscoelastic qualities which manifest within agarose fluid gels over set ranges of shear stresses, shear rates and oscillatory frequencies. These parameters are representable of the forces experienced by the gel during extrusion and handling. Particular attention was given to assessing the differences between agarose gels that were freshly prepared (F) to a given concentration or diluted (D) to a corresponding concentration from 1.00% w/v stock in order to demonstrate the critical importance of the fluid gel formulation method.

On first analysis, with a decreasing concentration of agarose comes a reduction in yield stress and viscoelastic strength in both freshly prepared and diluted samples over a range of set shear stresses (**Figure 4.3**). Additionally, a decrease in G′ and G″ over identical oscillatory frequencies occurs as

agarose concentration decreases and viscosity decreases over set shear rates as concentration is reduced (**Figure 4.4 and 4.5**). The decrease in polymer concentration results in weaker gels due to a reduction in particle density and a simultaneous decrease in particle-particle interactions. In addition to this, hydrogels of lower concentrations exhibit lower viscosities as they contain fewer crosslinks and a higher mesh size (Annabi et al., 2010; Zhang et al., 2017). Upon comparison of freshly prepared fluid gels with those diluted from a 1.00% w/v stock, preparation methods have a large impact on fluid gel mechanical behaviour. When samples were diluted to 0.75%, 0.50% and 0.25%, it was apparent that this preparation method resulted in gels with lower mechanical strengths compared with fluid gel samples that were freshly prepared to corresponding concentrations. This effect was more noticeable in the higher concentrations in contrast to lower concentrations, in that there was a larger difference in initial viscosity between fresh and diluted samples in 0.75% agarose than in 0.50% and 0.25% concentrations, respectively.

It has previously been reported that fluid gels of different concentrations contain a diverse range of particles. One main difference between freshly prepared and diluted agarose fluid gels when formulating to equivalent concentrations must therefore be particle size and morphology. To understand the connection between concentration and particle distribution, one must therefore analyse the particles within a range of fluid gel concentrations. At concentrations above 0.50%, there was the emergence of a dual particle size population (**Figure 4.6**). In these higher concentration fluid gels, the greater heterogeneity in particle size causes localized areas of increased viscoelasticity, thus generating a secondary population of particles of smaller size as well as allowing other particles to agglomerate and grow to equilibrium, unaffected by local shear. As 1.00% w/v agarose fluid gels generate a secondary, larger particle population under shear, the formulation of a diluted fluid gel to 0.50% w/v concentration involves the transfer of larger agarose particles. Given that larger particles have a much smaller surface area to volume ratio (Norton et al., 1999), particle-particle interactions are not as profound compared with gels freshly formulated to equivalent concentration with a larger

abundance of smaller particles. This would subsequently cause diluted agarose fractions to be less viscous compared to the freshly prepared fractions at equivalent concentrations. In addition, once water has bound to the gel via either the hydrophilic groups contained within the polymer network (known as primary bound water) or to the exposed hydrophobic groups upon polymer swelling (known as secondary bound water), any excess water will be imbibed towards infinite dilution (Piculell et al., 2011). From these analyses, it could be deduced that total bound water (primary and secondary bound water combined) has been transferred with the fraction of preformed 1.00% stock and the additional deionised water ultimately exists as free or bulk water within the agarose solution creating less viscous gels following dilution in comparison with freshly prepared agarose.

The proposed mechanism for the generation of individual gel nuclei suggests a nucleation and growth event, whereby particles will grow to equilibrium permitted by the given shear environment. When molecular ordering is initiated during cooling, the sol-gel transition causes a rise in solution viscosity and ordered domains begin to aggregate. As shear forces cause disruption during molecular ordering, a phase separation event occurs via spinodal decomposition (Norton et al., 1999). The particles formed during this practice display a higher polymer density at the core of the particle with a descending gradient to the outer edge, ascribed by the weak intermolecular tension at the gelled and non-gelled polymer interface and the increased flow field at the particles' surface (Fernández Farrés et al., 2014a). Within these lower density regions at the particles' surface exist fewer helical domains and aggregates, leading to the evolution of particle hairs as described by the 'beads on a string' model (**Figure 4.7**).

Another factor that plays a large role in dictating flow behaviour is the particle volume fraction within the fluid gel system. NMR relaxation studies have attempted to define these fractions; however, these methods are not applicable to systems containing hairy particles compared with those containing defined or absolute particles (Norton et al., 1999). Measuring particle volume fraction by means of centrifugation was therefore proposed (Garrec et al., 2013). Here, it may be observed that increasing

centrifugal force on quiescent and fluid gel agarose systems causes a reduction in solid phase volumes (**Figure 4.8A**). This is likely a consequence of larger centrifugal forces being required to attain maximum capacity of the supernatant rather than a reduction in the solid phase fraction itself. This would explain that when fluid gel particle volume fractions are normalised to that of quiescent gels, taking into account the fluid released from particle compressibility and syneresis, fluid gel particle volume fraction is relatively constant across all centrifugations. This would be expected as particle volume fractions would not deviate between samples of the same concentration and preparation method. Furthermore, particle volume fraction can be seen to increase with ascending polymer concentration (**Figure 4.8B**). This is in agreement with the particle size distribution analysis as larger particle populations exist within higher concentrations of agarose fluid gel and therefore contain higher particle volume fractions (Fernández Farrés et al., 2014a).

Analysis of SEM micrographs of lyophilised quiescent and fluid gels displayed major dissimilarities due to preparation technique. Though the helical residues formed within quiescent gels is equal to that formed in fluid gels, quiescent gels were exposed as having more continuous networks than those within fluid gels at equivalent concentrations (**Figure 4.9**). Also, the particle volume fraction (PVF) and supernatant fraction from centrifuged 0.50% w/v agarose fluid gels displayed agarose gel particles and unbound polymer, respectively. Freshly prepared and diluted agarose fluid gels produced at equivalent concentrations presented contrasting network profiles. Fluid gels prepared at 1.00% w/v exhibit much more interconnected networks compared with fresh 0.50% w/v fluid gels. When fluid gels are prepared following dilution to 0.50% w/v from a 1.00% w/v sample however, a much sparser network is exhibited. Further to these assessments, the solid fraction of each sample was quantified as a percentage of dry weight versus wet weight prior to lyophilisation. Quiescent gels comprised 0.49% dry weight, fluid gels 0.42%, PVF 1.27% and supernatant 0.02%. Further research would need to be undertaken to study the critical concentration at which polymer overlap occurs to assess correlations with free polymer within the supernatant.

4.5Conclusions

Assessment into the characteristics of agarose fluid gels has highlighted the critical importance of fluid gel formulation and formation. Different concentrations of agarose fluid gels have a marked impact on mechanical properties, particle distribution, particle volume fraction and microarchitecture and are highly tuneable in directing desired gel properties. Also, the technique used for fluid gel formation is paramount, in that agarose must be freshly prepared to preserve the key parameters that are necessary for use as a supporting medium during suspended manufacturing.

This chapter has outlined the fundamental assets within agarose fluid gels, building on previous research by Moxon et al., (2017) to elucidate exactly the mechanisms that have made suspended manufacturing so successful. Despite this success, further refinement is required, replacing hand-printed tissue engineering constructs with a fully automated 3D bioprinter to make the potential of patient-specific tissue constructs more tangible. Chapter 5 is focused on integrating a commercially available 3D bioprinter within the suspended manufacturing technology. The potential of Suspended Layer Additive Manufacturing (SLAM) is reviewed by assessing the resolution of the system as well as demonstrating a range of construct geometries using various polymers and cell types.

Chapter 5

SUSPENDED LAYER ADDITIVE MANUFACTURE

Some aspects in this chapter are published in *Advanced Functional Materials* and other aspects are in preparation for submission to *Biophysics of Biofabrication*

Senior, J.S. Cooke, M.E. Grover, L.M. Smith, A.M. (2019) Fabrication of Complex Hydrogel Structures using Suspended Layer Additive Manufacturing (SLAM). *Advanced Functional Materials*, 29, 49.

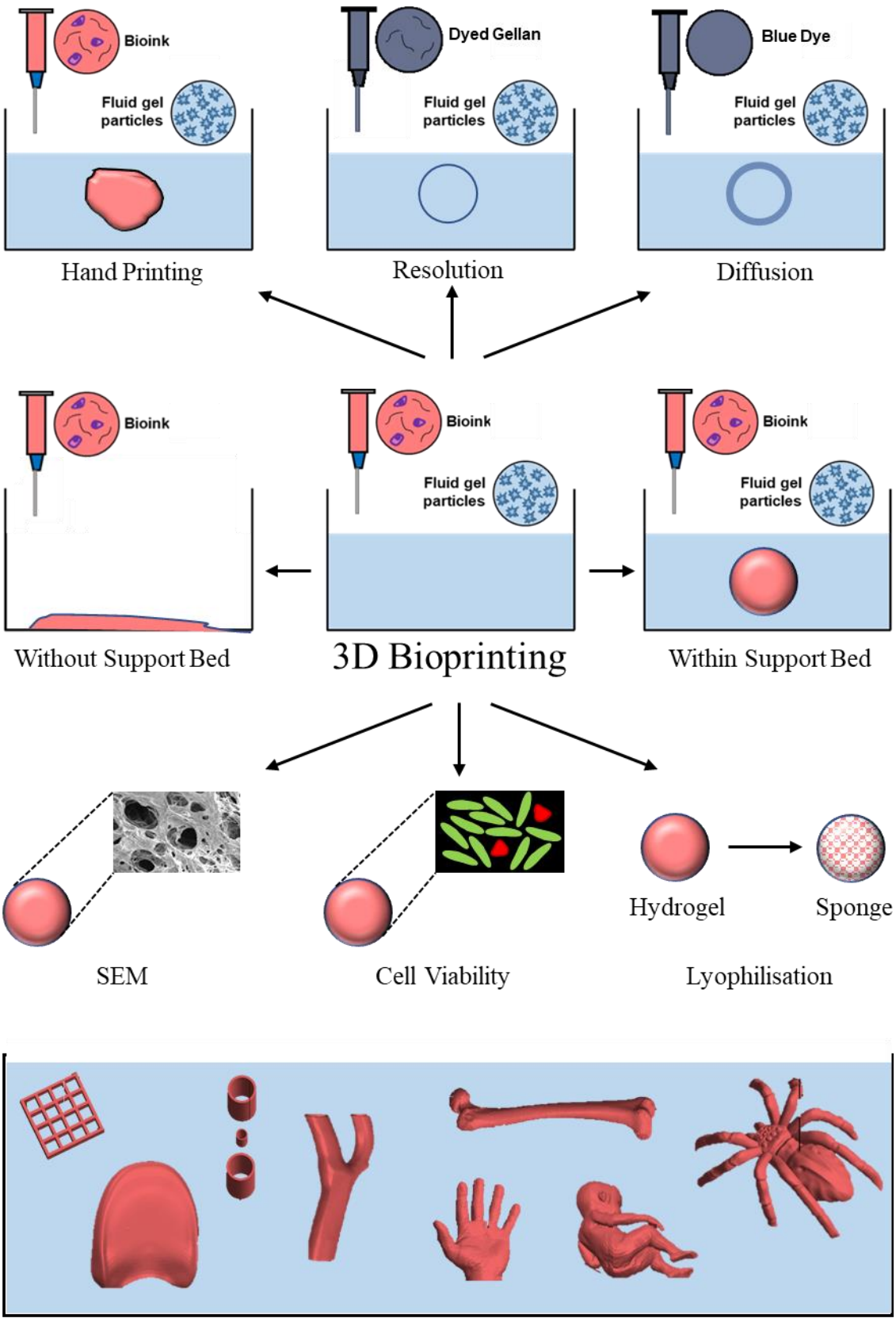

Complex Structures

Chapter 5 – Suspended Layer Additive Manufacturing (SLAM)

5.1 Introduction

Additive layer manufacturing (ALM) has been used for some time for the construction of human tissue equivalents and is constantly seeking new solutions in response to 3D printing challenges (Melchels et al., 2012). Currently, 3D printed constructs that are dynamic and complex in shape are often limited by poor print fidelity when extruding low viscosity biopolymers. Because of these limitations, there is often an oversight in selecting optimal print parameters, as the choice in print specifications such as print speed, bioink material and curing method is not at the discretion of the user, but instead is restricted and dictated by the 3D printing technique (Tamay et al., 2019). For instance, researchers have often employed high viscosity polymers in order to overcome the issues associated with the collapse of low viscosity materials once deposited (Duan et al., 2013). This would necessitate a fast print speed to be implemented and in turn, the curing of material to occur *in situ* during printing in order to limit distortion of the intended model dimensions. These criteria directly impact upon the successful fabrication of complex constructs that contain the biochemical and geometrical facets of functioning tissues.

Suspended manufacturing, developed by Moxon et al., (2017), uses an agarose fluid gel bed and offers an opportunity to allow greater freedom in the selection of print parameters that are conducive to the production of constructs with admirable print fidelity and cell viability. The principle mechanisms behind this technique enable extrusion of bioinks over a range of viscosities within a self-healing fluid gel that acts as a temporary support prior to solidification and extraction. This is due to the shearing action of the dispensing nozzle upon the gel support, allowing deposition of printing material between the fluid gel particles by polymer disentanglement before rapidly restructuring to support the construct upon the removal of shear (Cooke et al., 2018). Alternatively, within standard additive manufacturing practices, bioinks are deposited onto a planar collector

platform leading to loss of structural integrity of extruded bioinks unless further intervention is undertaken. By utilising a supporting gel bed during layer extrusion, the geometrical dimensions of the print model are only limited by the dimensions of the reservoir enclosing the supporting matrix. Another major benefit of suspended manufacturing is that print designs require no further modification, such as the use of bridges or forks, that otherwise compromise scaffold architecture. Perhaps of upmost importance, the candidate scaffold material can be selected on a basis of compatibility with the native extracellular matrices being replicated as opposed to enabling print conduciveness. This means that the materials employed within the bioink are not limited to exhibiting high viscosities in order to prevent structure collapse following extrusion, but in fact can reflect the true mechanics of the tissue being replicated.

Other efforts towards tissue printing have also used an embedding phase to cradle the print model during fabrication. Some examples include printing PDMS within a Carbopol support bath (Abdollahi et al., 2018), printing a supramolecular modified hyaluronic acid hydrogel within a secondary modified HA hydrogel of different concentration (Highley et al., 2015) and printing alginate within a gelatin microparticle bath (Hinton et al., 2015). These techniques enable the printing of more complex constructs from low viscosity precursors, yet the implications within these systems still require addressing. One issue lies with preserving the structural integrity of the construct during retrieval from the supporting bed, whilst other printed models require additional mechanical reinforcements using a webbed fork. These issues pose a problem regarding the suitability of printed constructs in tissue engineering and research contexts, with scaffold handleability and the manufacture of scaffolds with distinct dimensions, without the need for additional supports, being compromised. Another limitation is that the curing temperatures required for some of these materials are not conducive to cell culture conditions, and in cases where defective tissues exhibit compromised cellular mitotic activity, intervention through the incorporation of exogenous cells within biofabricated constructs is pertinent.

In previous studies, suspended manufacturing has been used to produce complex structures, demonstrated by the fabrication of a freeform helix (Moxon et al., 2017). A more comprehensive characterisation of the mechanisms behind extrusion within an agarose fluid gel bed was documented in the previous chapter of this thesis. In this chapter, hand-printing tissue constructs using suspended manufacturing was further refined and revolutionised by the introduction of a 3D bioprinter in a technique coined as suspended layer additive manufacturing (SLAM). By using SLAM, the printing conditions were tuned in order to assess ultimate print fidelity without compromising cell behaviour. Cell-laden constructs were first printed by hand to document the evolution of the process in which hand-extrusion was replaced by a commercially available 3D bioprinter. An alternative support medium was then formulated, manufactured as an agarose microparticle slurry as opposed to an agarose particulate fluid gel to highlight and assess the importance of support bed formulation using brightfield microscopy and rheology. The resolution of the system was then inspected by tailoring flow rate, print pressure and nozzle gauge using a diverse spectrum of different polymers, and dyes of differing molecular weight were extruded in order to study diffusion within the support bed. Finally, a range of constructs were 3D printed using SLAM technology, demonstrating that various dynamic model configurations and dimensions can be replicated at the human-scale in hydrogel form.

5.2 Methods

5.2.1 Fluid gel formulation

Agarose fluid gels (type I low EEO, purchased from Sigma-Aldrich, Dorset, UK) were prepared by autoclaving solutions of agarose mixed with deionised water (121°C temperature and 1.4 bar pressure) (Prestige Medical™ bench top autoclave) at 0.50% w/v concentration and cooling to 25 °C under a constant shear of 700 rpm using a magnetic stirrer.

5.2.2 Slurry gel formulation

Agarose slurry gels were formed by quiescently cooling autoclaved agarose solutions to 25 °C (absent of shear) to give a final concentration of 0.50% w/v. Quiescent gels were then blended in a commercially available food-grade blender followed by homogenising using a T18 basic ULTRA TURRAX® homogenizer (IKA, UK).

5.2.3 Preparation of polymer solutions for printing

The materials used for printing were low acyl gellan gum (molecular weight 300,000 – 500,000 g/mol) and ι-carrageenan (molecular weight ~500,000 g/mol) (purchased from Special Ingredients, UK), alginate (alginic acid sodium salt, M:G ratio of 1.56, molecular weight 120,000 – 190,000 g/mol, purchased from Sigma–Aldrich, UK), low methoxy (LM) pectin (molecular weight ~200,000 g/mol, purchased from CP Kelco, UK) and collagen (PureCol EZ Gel, Advanced BioMatrix, molecular weight ~300,000, purchased from Sigma–Aldrich, UK). Gellan, ι-carrageenan, alginate and pectin powders were dispersed in deionized water at concentrations of 1%, 2%, 3% and 5% w/v respectively and allowed to cool to 25 °C following autoclaving to form working solutions. Collagen solutions were stored at 4 °C prior to use.

5.2.4 Cell culture expansion

Mouse calvaria-derived pre-osteoblasts (MC3T3) were cultured from stock vials (passage 15) (Sigma Aldrich, UK). A single vial containing 1 x 10^6 cells was removed from storage in liquid nitrogen and defrosted in a water bath at 37 °C (Grant Instruments™ - Fisher Scientific, UK). Once thawed, cells were transferred to a centrifuge tube along with supplemented Dulbecco Modified Eagle Medium (DMEM) (10% FBS, 2.5% L-glutamine, 2.5% HEPES buffer and 1% penicillin/streptomycin) and centrifuged at 1000 rpm for 3 minutes using a benchtop centrifuge (ThermoFisher Scientific, UK). The supernatant was removed and fresh supplemented DMEM was added prior to transferring to a cell culture flask. Cells were kept at 5% CO_2 and 95% air and incubated at 37 ºC (Triple Red, UK).

Media was aspirated and replaced every 3 days and cells were passaged at 80% confluence.

5.2.5 Cell culture passage

For the trypsinisation process, media was aspirated from cultures and cells were washed using Phosphate-Buffered Saline (PBS). TrypLE™ dissociation reagent was added and flasks were incubated at 37 ºC for 2 minutes. Cultures were then observed for cell lifting using a VWR IT 400 Inverted Microscope (VWR, UK). If cells had not detached, a further 2-minute incubation period was provided. In order to halt the enzymatic activity of TrypLE™, supplemented DMEM was added. Cell suspensions were centrifuged at 1000 rpm for 3 minutes after transferring into sterile centrifuge tubes and the supernatant was removed. Cell counting using a haemocytometer determined the volume needed from the cell suspension to seed new flasks and media was added.

5.2.6 Hand-printing tissue constructs

Following the trypsinisation and cell counting processes, cells were suspended in sterile 1% w/v gellan at a density of 3 x 10^5 cells / mL. Agarose was then added to each well of a 6 well plate and the gellan / cell suspension was extruded by hand within the agarose beds into 3 defined shapes – the letter 'J', a ring and a solid disc using a 10 mL syringe and a 21 gauge needle (337 µm inner diameter). A VWR IT 400 Inverted Microscope (VWR, UK) was used to check for successful cell encapsulation without diffusion into the surrounding bed support. 200 mM $CaCl_2 \cdot 2H_2O$ was then extruded around the perimeters of the constructs for crosslinking and DMEM was added prior to incubation at 37 ºC. Media was aspirated and replaced every 3 days and cells were cultured for a given number of days prior to cell viability assays using live/dead staining.

5.2.7 Cell viability

To assess cell viability, media was aspirated and constructs were washed in PBS. 7 µL of calcein AM was added to the constructs for the staining of live cells (green) and 25 µL of propidium iodide was added for the staining of dead cells (red). Photographic images of the constructs were taken prior to

mixing with live/dead stains. Cells were incubated for 20 minutes at 37 ºC, small sections were transferred onto slides and an Evos cell imaging microscope (ThermoFisher Scientific, UK) was then used to image live and dead cells for the analysis of cell viability within the manufactured constructs.

5.2.8 Rheology of printing solutions

Rheological analyses of the printing polymer solutions for assessing resolution were performed in triplicate at 25 °C (apart from collagen which was measured at 4 °C) using a Bohlin Gemini rheometer (Malvern Panalytical, UK) with a double gap cup and bob geometry (DG 24/27). Shear rate was ramped from 0.1 to 100 s^{-1} and shear viscosity (Pa.s) was recorded.

5.2.9 Tuning print resolution

Upon introduction of a commercially available 3D bioprinter into the suspended manufacturing system, giving rise to the evolution of suspended layer additive manufacturing (SLAM), the resolution of the technique was assessed. Dyed blue gellan rings with a diameter of 15 mm were printed using an INKREDIBLE 3D bioprinter (Cellink, Sweden) within an extra-depth petri dish filled with agarose fluid gel. Parameters that were controlled included extrusion pressure (5 – 25 kPa in 5 kPa increments), flow rate and nozzle internal diameter (150, 200, 250, 410 and 610 μm). The range of pressures and nozzle internal diameters were selected on the basis that they covered values considered from the lower ends to higher ends of the scale and with sufficient intermediate values to determine linearity. The width of the extrude was then measured using digital callipers. A flow rate of 3.8 μL s^{-1} was used as the minimum flow necessary in order to print a continuous extrude when operating at a print speed of 10 mm s^{-1}. The print pressure required to achieve this flow rate using each nozzle gauge was then noted. To assess the effects of printing pressure on resolution, the needle aperture was kept at 410 μm whilst increasing pressure for each subsequent print. To assess the impact of internal needle diameter on printing resolution, the minimum required pressure to extrude material

from the smallest aperture (150 μm) was used across all nozzle gauges and the width of the extrude was reported.

5.2.10 Diffusion studies

Methylene blue (Mw = 319 g/mol) and dimethylmethylene blue (Mw = 416 g/mol) rings with a diameter of 15 mm were printed using an INKREDIBLE 3D bioprinter (Cellink, Sweden) within an extra-depth petri dish filled with agarose fluid gel. Images were taken at given time points and diffusion was measured by assessing the width of the extrude using digital callipers.

5.2.11 Rheology of print beds

Rheological analyses of the agarose fluid gel and agarose slurry were performed in triplicate at 25 °C using a Kinexus Ultra+ rheometer (Malvern Panalytical, UK). To investigate the shear thinning behaviour, the shear rate was ramped from 0.1 to 100 s^{-1}. Three-step thixotropic measurements were then performed at 0.1–100–0.1 s^{-1} to analyse the flowing and healing of the gels during and upon removal of shear.

5.2.12 Brightfield microscopy

For visualization of the particulate structures within fluid gels and slurry gels, small samples were loaded onto microscope slides and mounted with a cover slip before imaging using a VWR IT 400 Inverted Microscope (VWR, UK).

5.2.13 3D modelling

3D lattice scaffolds were designed using computer-aided design (CAD) software SolidWorks and saved in stl (stereolithography) file format, which describes the 3D model in a surface tessellated arrangement. A simple cylinder shape (10 mm diameter and 5 mm depth) was also constructed for printing cell / polymer solution suspensions and to confirm the viability of cells following printing (0 hours) and culture (7 days). Models in the form of an S shape, T7 intervertebral disc, carotid artery,

hand, femur, foetus and spider were downloaded from thingiverse (**https://www.thingiverse.com/**) and scaled to an appropriate size (if applicable). Blood vessel and ear models were preloaded onto the SD card within the bioprinter, courtesy of Cellink. The stl to G-code conversion programme Slic3r was then used to slice the models into layers and translate the coordinates into commands for the 3D bioprinter.

5.2.14 3D printing complex shapes using SLAM

For printing of 3D structures by SLAM, bioink cartridges were loaded with hydrogel precursor solutions (gellan, collagen, ι-carrageenan, pectin or alginate), attached to a conical nozzle with an internal diameter (ID) of 410 µm and inserted into an INKREDIBLE 3D bioprinter (Cellink, Sweden). In some cases, phenol red or red/blue food dye was added to the hydrogel solutions for improved visualization of the printed parts. The 3D bioprinter was calibrated to a specified pressure (6 kPa) followed by placement of the petri dish containing the agarose fluid bed upon the z-stage. Gellan gum, ι-carrageenan, pectin and alginate were ionically crosslinked by extruding 200 mM of $CaCl_2 \cdot 2H_2O$ solution around the structure via a hypodermic needle, whereas collagen gelation was induced thermally by raising the temperature to 37 °C. Finally, the constructs were retrieved from the agarose bed using a spatula and gently washing with deionized water. An S shape was printed with and without an agarose fluid gel bed for comparison.

5.2.15 Generation of monolayer sponges

Following the 3D printing process, 3D scaffolds destined for transformation into monolayer sponges were subjected to lyophilisation. Scaffolds were placed in -80 ºC conditions for 24 hours and then a 72-hour freeze drying cycle was implemented at -76 ºC and 0.0010 mbar (Christ ALPHA 2–4 LD plus). Dry samples were stored in a desiccator for the preservation of aridity.

5.2.16 Scanning electron microscopy

Monolayer sponges were prepared by sputter coating with gold using a Quorum SC7620 sputter coater under a low bleed of argon. The internal networks within the scaffolds were then studied using a field emission scanning electron microscope (FEI Quanta 250 SEM) operated in high vacuum mode at an accelerated electron energy of 10 kV. Several images were collected at various magnifications using a back scattered electron detector.

5.3 Results

5.3.1 Hand printing tissue constructs

Hand-printed tissue constructs of cell-loaded gellan were successfully fabricated within an agarose supporting bed using the suspended manufacturing method. Structures shaped as a solid disc, letter 'J' and a ring shape retained structural integrity during extrusion within the agarose platform support prior to crosslinking of the constructs (**Figure 5.1A**). As neither a template nor specific dimensions were followed, the shapes generated were imperfect, resulting from lack of control during hand-printing. More positively, cells remained confined to the location of extrusion without the bioink leaching into the supporting particulate bed (**Figure 5.1B**) and constructs were also successfully removed (**Figure 5.1C**). Moreover, following 8 days of culture, cell viability within hand-printed constructs was assessed and a high percentage of cells were viable (**Figure 5.1D**).

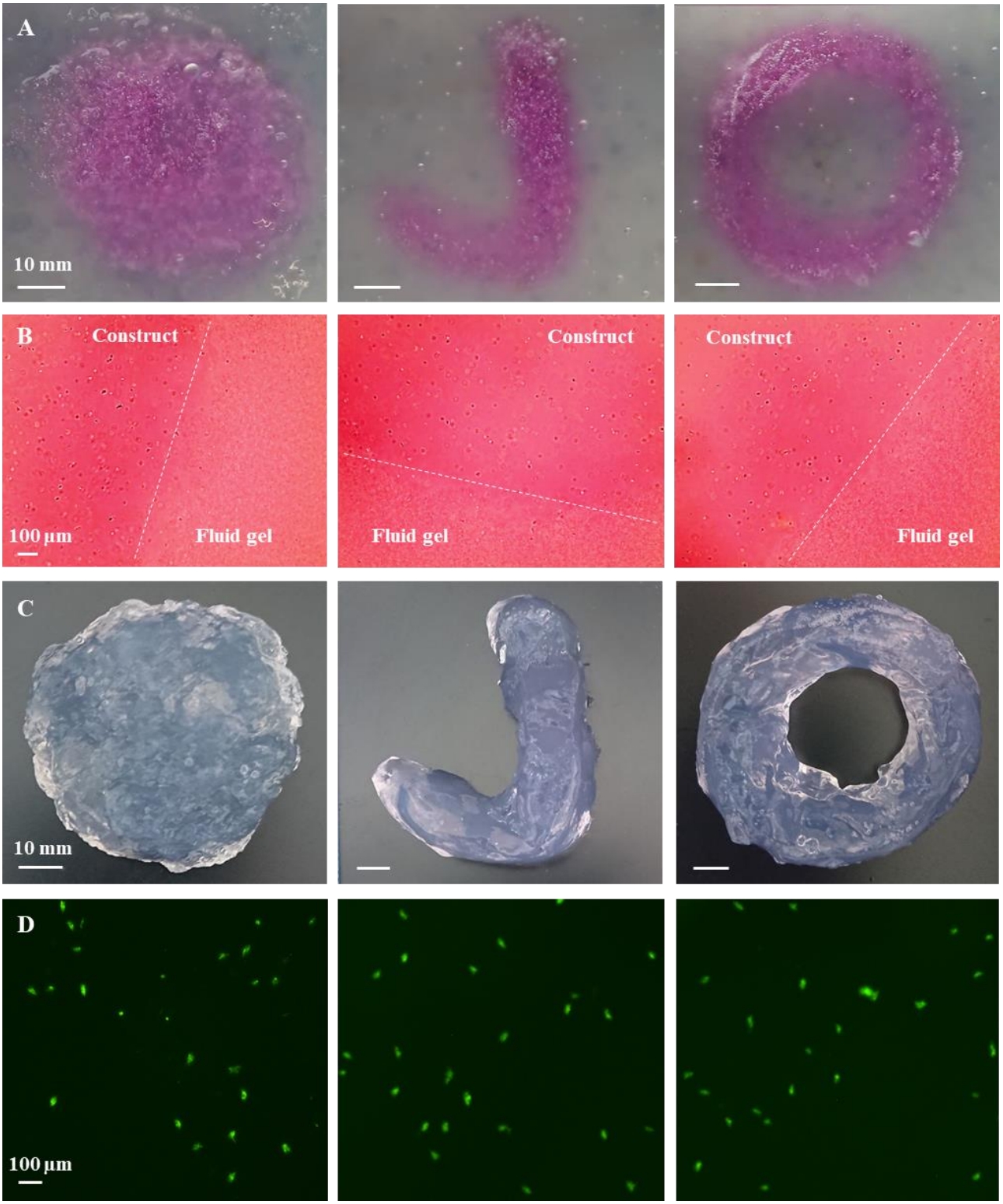

Figure 5.1 – Suspended manufacturing of hand printed constructs. A) Solid disc, letter J and ring-shaped constructs within an agarose fluid gel. B) Localisation of constructs within fluid gel at the micro-scale. C) Solid disc, letter J and ring-shaped constructs following removal from the fluid gel bed. D) Live / dead cell viability showing live (green) and dead (red) cells.

5.3.2 Tuning print resolution

When engineering a tissue construct using 3D micro-extrusion printing, careful consideration must be taken when selecting printer operating modalities. Amongst these modalities are print speed, print pressure, extrusion flow rate and nozzle gauge and each criterion directly impacts upon each other as well as print fidelity and cell viability within a printed scaffold. Initially, the viscosities of a range of different biopolymers (pectin, alginate, ι-carrageenan, gellan and collagen) were measured over a range of shears that simulate the shear forces experienced by the materials during extrusion (**Figure 5.2A**). In all cases, materials exhibited shear thinning behaviour allowing the extrusion of polymer with great ease. The polymer viscosity during extrusion was then compared with the pressure required to achieve a constant printing flow rate (3.8 µL s^{-1} (equating to one drop every four seconds)). As expected, a higher print pressure was required to extrude materials of higher viscosities and a proportional linearity can be reported (R^2 = 0.98) (**Figure 5.2B**).

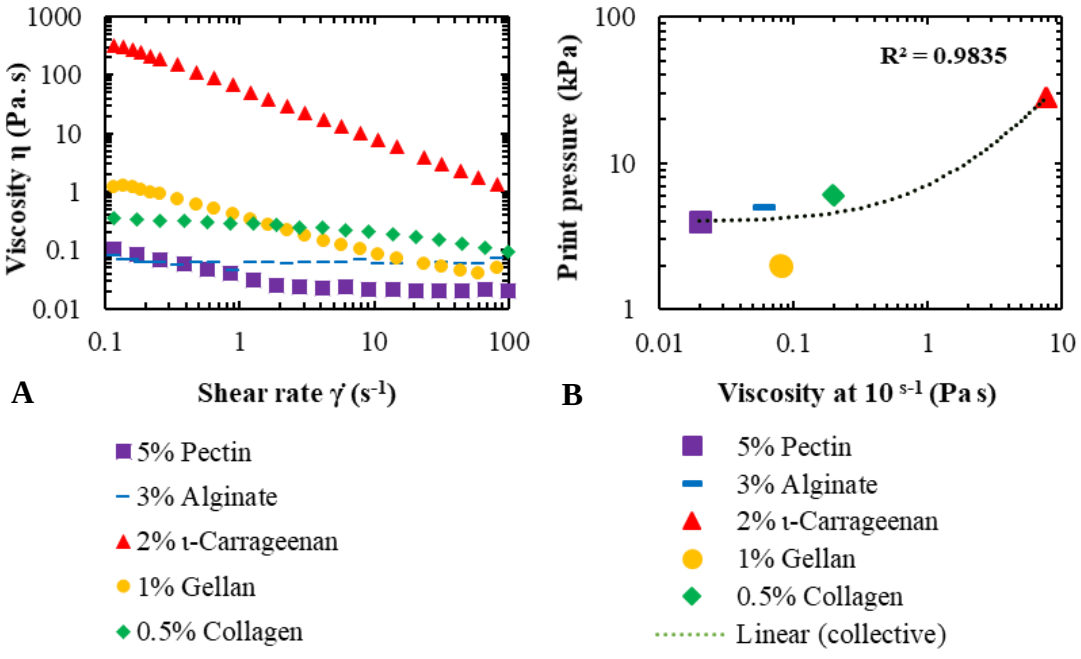

Figure 5.2 - Relationships between a range of materials' viscosities and printing pressure. A) Shear viscosity of pectin, alginate, ι-carrageenan, gellan and collagen solutions. B) Print pressure required in order to achieve a constant flow rate of 3.8 µL $^{s-1}$ versus printing solution viscosity at 10 $^{s-1}$.

In order to assess print resolution, the effects of a range of hydrogel chemistries and viscosities, extrusion flow rates, nozzle gauges (internal diameters – ID) and print pressures on print resolution were studied while the fluid gel supporting bed was kept constant. In order to achieve this, dyed gellan was extruded within the fluid gel under various combinations of parameter conditions and then the width of the extrudes were measured with digital callipers as an indication of resolution. The same experiment was then repeated within an agarose slurry gel to examine the impact of supporting gel formulation method on resolution.

To determine the minimum achievable extrude thickness and thus the optimum resolution within fluid gels and slurries for each nozzle gauge, the print pressure was adjusted for each nozzle ID accordingly (150, 200, 250, 410 and 610 μm) so that gellan was extruded at 3.8 μL s^{-1}. Within both fluid and slurry gel systems, as the nozzle ID increased, the pressure required to extrude dyed gellan at a constant rate decreased due to a decrease in resistance to polymer flow. The potential resolution, however, decreased linearly as the nozzle ID increased when flow rate was kept constant (**Figures 5.3Ai-ii and D left**). The resolution of the extrude was slightly higher in fluid gels compared with agarose slurries with thicker, less continuous extrudes. When print pressure increased and nozzle ID was kept constant (and therefore polymer flow rate also increased), resolution decreased in a linear fashion (**Figures 5.3B and D middle**). For the evaluation of nozzle ID on resolution, the lowest pressure required to extrude gellan material from a nozzle with the smallest ID was selected and kept constant across the whole range of nozzle gauges. Likewise, when print pressure was kept constant and nozzle ID ascended (and therefore polymer flow rate also increased), resolution decreased in a linear trend (**Figures 5.3C and D right**). In the case of gellan extruded through a needle with an ID of 610 μm and a pressure of 24 kPa, the gross extrusion pressure combined with minimal resistance to flow (due to a large needle aperture) caused excessive shear forces on the fluid gel material thus propelling the gellan through the supporting matrix as opposed to carefully placing bioink within a defined region.

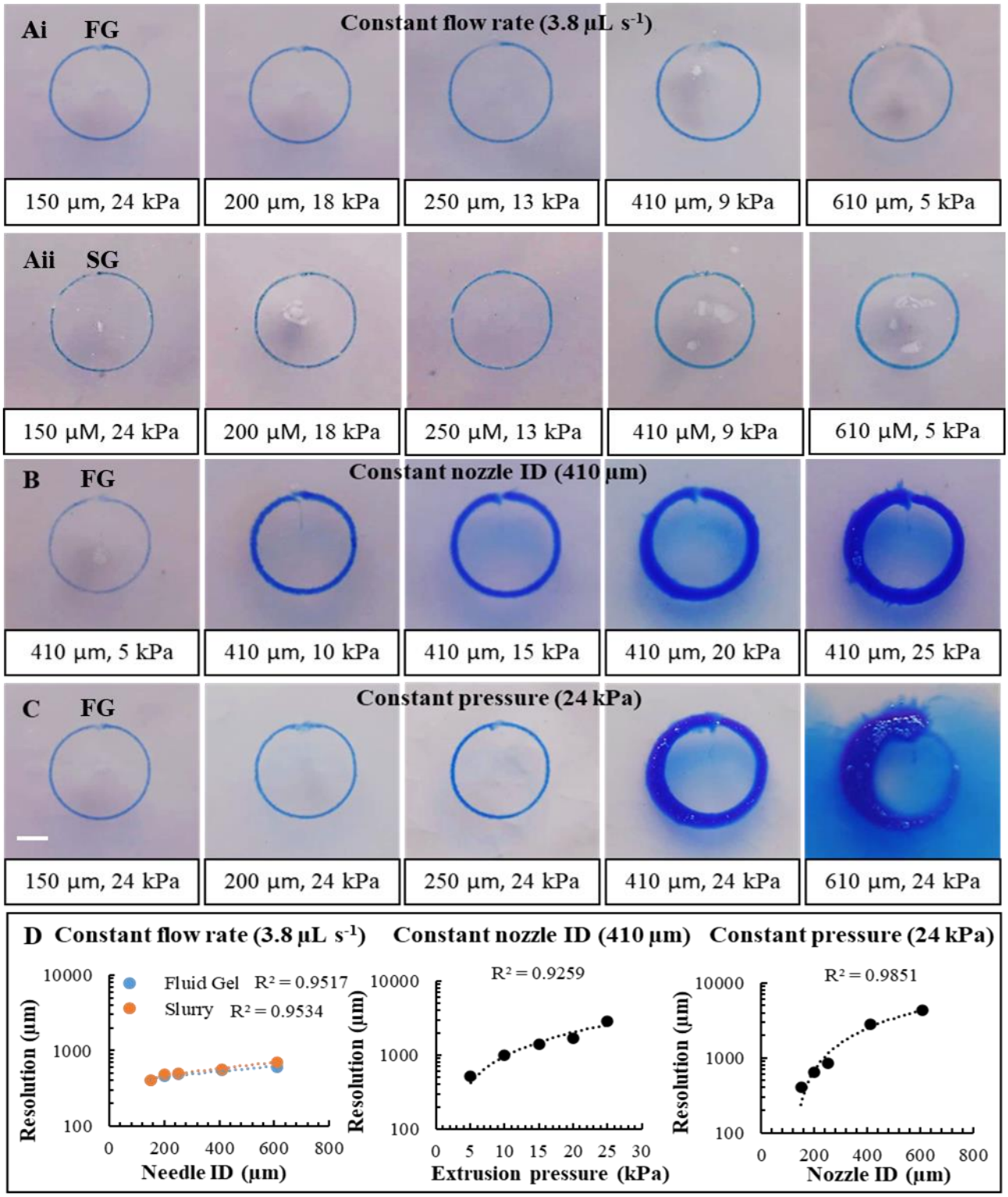

Figure 5.3 - Controlling print parameters for tuning 3D bioprinting resolution in SLAM. 3D printed dyed gellan rings with constant flow rate and varying nozzle ID and print pressure in Ai) fluid gel (FG) *versus* Aii) slurry gel (SG). B) constant nozzle ID and varying flow rate and print pressure and C) constant print pressure and varying flow rate and nozzle ID (scale bar = 5 mm). D) Linear plots of corresponding parameters within A, B and C.

5.3.3 Diffusion studies

Two dyes of differing molecular weight (methylene blue, Mw = 319 g/mol and dimethyl methylene blue Mw = 416 g/mol) were 3D printed within the fluid gel print bed to characterise diffusion rates. This was to ascertain how different printing solutions containing different sized molecules behave following deposition within the fluid gel bed and also as an insight into how crosslinker solutions may diffuse within the suspended construct. The minimum pressure required to extrude each dye to form a 15 mm diameter ring was used (16 kPa and 2 kPa respectively) and the diffusion was quantified by measuring the thickness of the extrude over time (**Figures 5.4 and 5.5**). As methylene blue has a lower molecular weight, this dye was able to diffuse further across the fluid gel than dimethyl methylene blue which plateaued at around 2.2 mm after 90 minutes (**Figures 5.6A and B**).

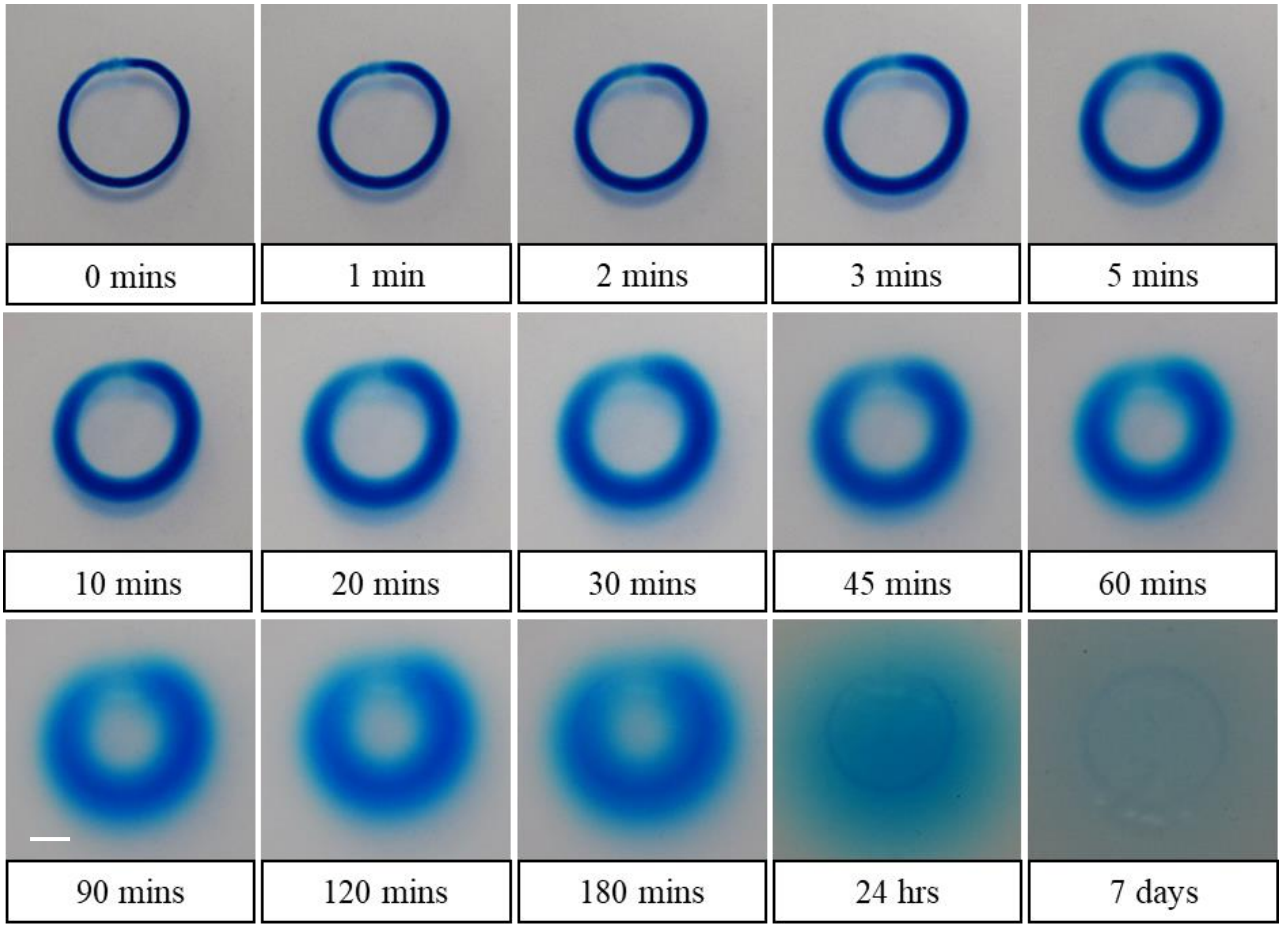

Figure 5.4 – Diffusion of a 15 mm diameter methylene blue ring (Mw = 319 g/mol) within an agarose fluid gel over 7 days (scale bar = 5 mm).

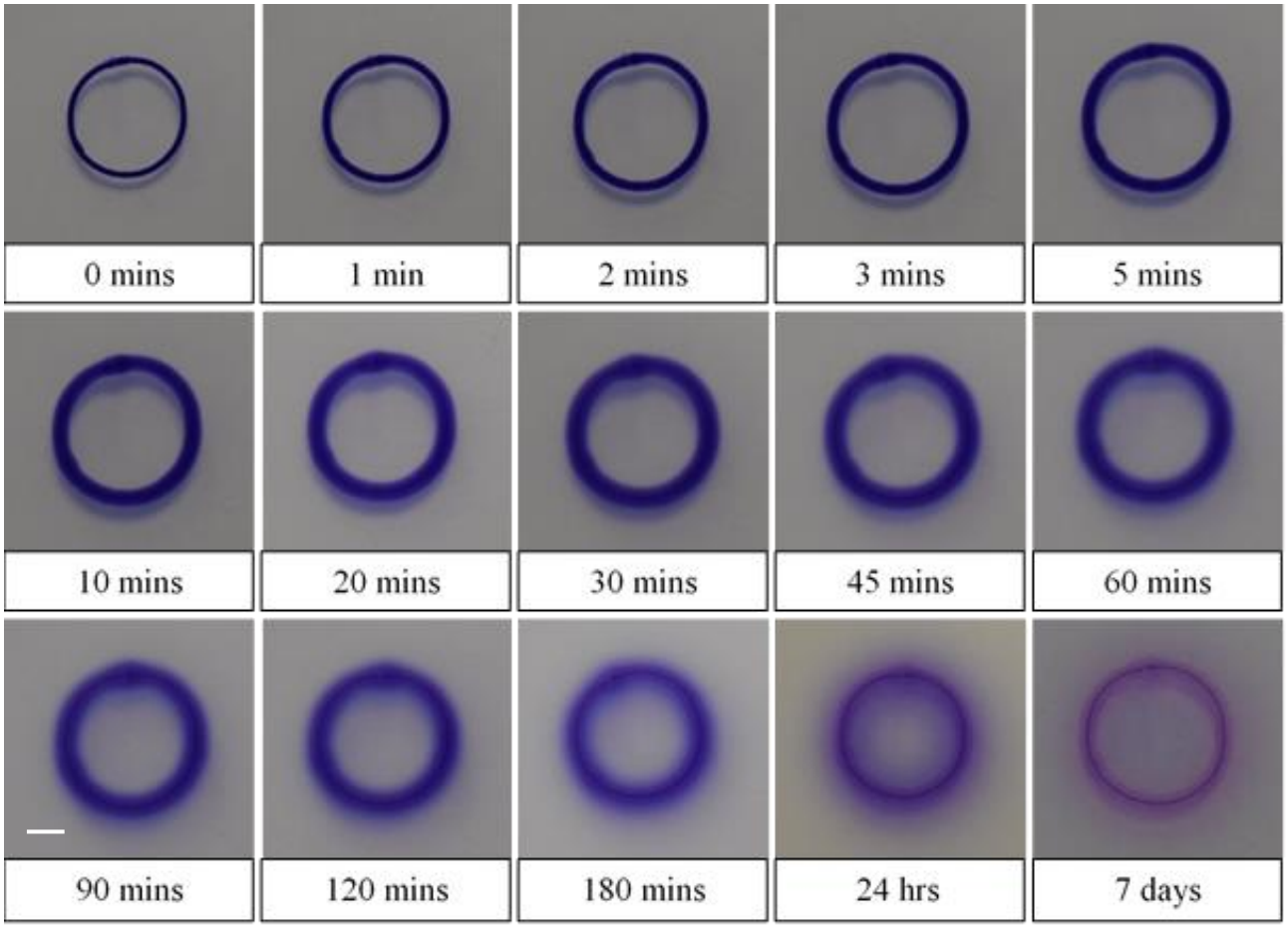

Figure 5.5 – Diffusion of a 15 mm diameter dimethyl methylene blue ring (Mw = 416 g/mol) within an agarose fluid gel over 7 days (scale bar = 5 mm).

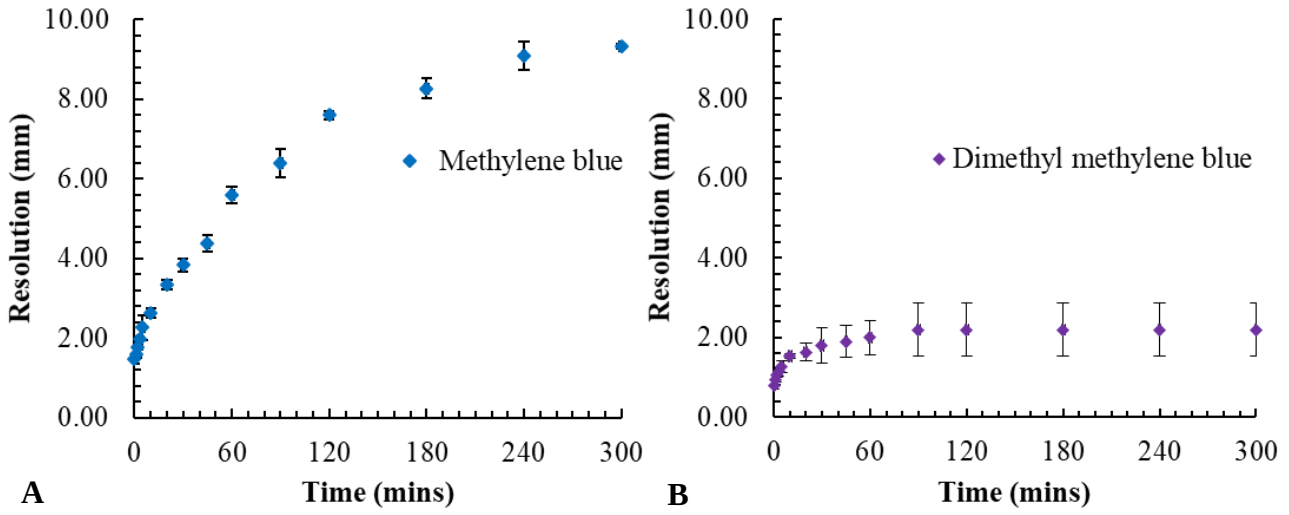

Figure 5.6 – Diffusion of a A) methylene blue (Mw = 319 g/mol) and B) dimethyl methylene blue (Mw = 416 g/mol) 15 mm diameter ring within an agarose fluid gel over 5 hours.

5.3.4 Rheology of print beds

The mechanical properties of the print bed are a crucial parameter in SLAM as they can impact on the resolution and complexity of the suspended construct. Freeform reversible embedding of suspended hydrogels (FRESH) is another embedded printing technique that uses a gelatin slurry support bath (Hinton et al., 2015), however the rheological behaviour of a particle slurry as a suspending agent has not yet been investigated. Here, the rheological behaviour of agarose fluid gels and slurry gels were compared. A gelatin slurry gel was not considered for inclusion within this thesis as its features of liquifying at cell culture temperatures renders it unsuitable for suspending cell-loaded constructs and for these reasons is considered futile. The viscosity was measured with increasing shear to replicate the shear action of the cartridge needle and extruded polymer within the print bed (**Figure 5.7A**). Both formulations showed shear-thinning behaviour which is critical in allowing movement of the needle through the gel during printing without causing dragging of previously deposited layers. Agarose fluid gels versus slurry gels exhibited lower viscosities though both were prepared at the same concentration of 0.5% w/v, yet a more stable recovery was featured in fluid gels (**Figure 5.7B**).

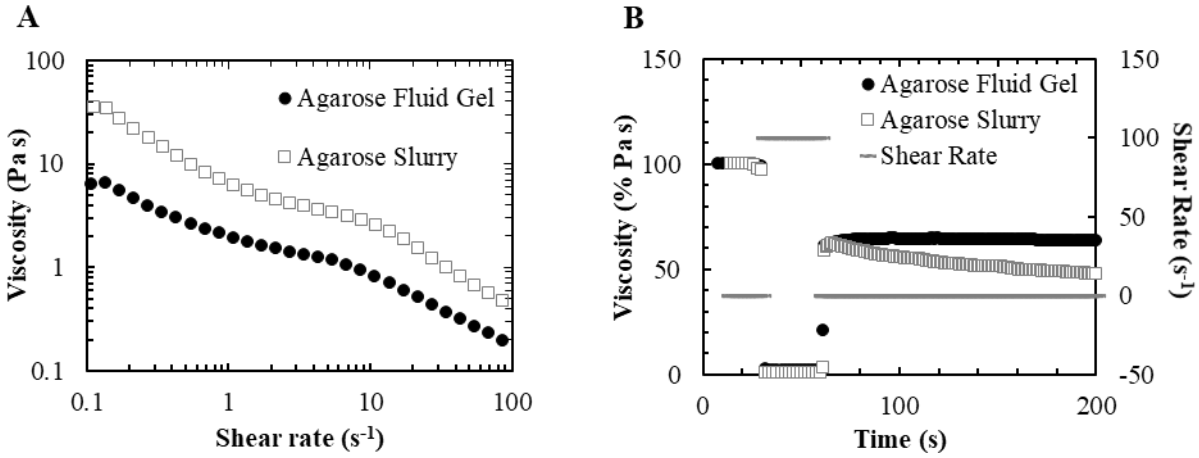

Figure 5.7 – Mechanical spectra of the fluid-gel bed and comparison with agarose slurry by shear rheology. A) Shear viscosity of agarose fluid gel (filled circles) and agarose slurry (blank squares) in which fluid gels exhibit lower viscosity. B) Shear recovery of agarose fluid gels versus agarose slurry featuring a more rapid and stable recovery following shear removal within agarose fluid gels.

5.3.5 Brightfield microscopy

Following rheological characterisation of agarose fluid gels versus slurry gels, the particle morphologies within each gel were studied using brightfield microscopy. Fluid gel particles were formed of small subunits that interacted to form larger, hairy particles of around 100–150 µm and were heterogeneous and irregular in shape as a result of generation through sheared gelation (**Figure 5.8A**). In contrast, agarose slurry particles generated through fracturing a solid, bulk gel exhibited a smooth and angular morphology with an even greater variation in size (**Figure 5.8B**).

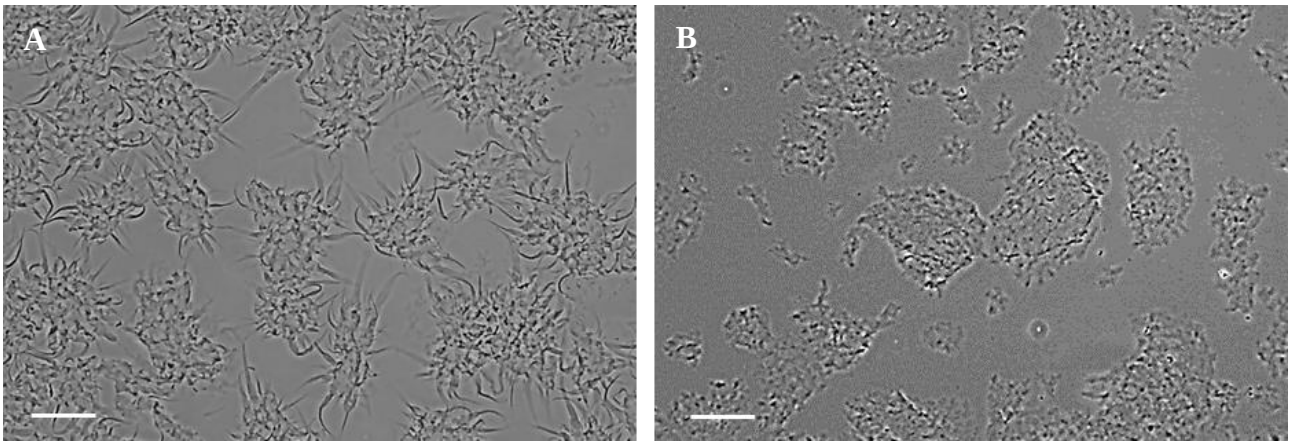

Figure 5.8 – Brightfield micrograph of a 0.5% w/v agarose A) fluid gel containing particles comprised of smaller subunits made by shear cooling and B) slurry gel showing angular particles made by fracturing a solid bulk gel (scale bars = 150 µm).

5.3.6 3D printing complex shapes using SLAM

The design and manufacture of constructs by combining 3D bioprinting and suspended manufacturing was successfully achieved. The generation of a G code file from an stl file was accomplished using Slic3r file conversion software (**Figure 5.9A**). An 'S' shape was printed using 1.0% gellan with and without a 0.5% w/v agarose particulate bed and crosslinked. Constructs that were printed onto a planar surface lost all structural integrity, collapsing under their own weight and spreading across the petri dish (**Figure 5.9B**). Constructs that were printed within the particulate bed, however, were seen to retain accurate dimensional conformation before and after crosslinking (**Figures 5.9C and D**).

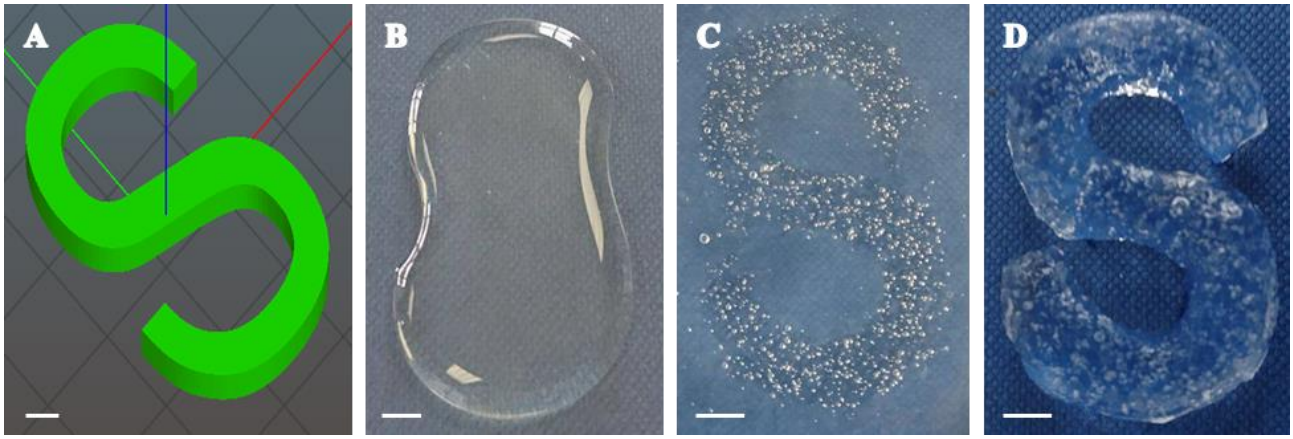

Figure 5.9 – Design and manufacture of a single construct using suspended manufacture with a 3D bioprinter. A) Stl file in Slic3r of an 'S' shape with dimensions 24.77 x 40.00 x 2.50 mm. B) S shape print onto a planar surface. C) S shape print within a supporting agarose bed. D) S shape following crosslinking and removal from the bed support (scale bars = 5 mm).

After establishing that the suspended manufacture technique works concurrently with an automated 3D bioprinting system in place of hand printing, the next crucial element that defines the success of the newly developed suspended layer additive manufacture method is that cells remain viable immediately after printing and following culture for a 7 day period. Simple cylinder shapes were printed using different bioinks, (gellan, ι-carrageenan, alginate and collagen) loaded with MC3T3s, demonstrating the large variation in material chemistries and mechanics that can be printed using this technology. Gellan and collagen prints reflected print model dimensions (**Figures 5.10A and B left**), whereas alginate was seen to swell, and ι-carrageenan constructs slightly sagged (**Figures 5.10C and D left**, respectively). As an alternative method to fabricating tissue engineering structures, acellular materials were freeze dried (**Figure 5.10 middle**) and rehydrated with cell-suspended media (**Figure 5.10 right**) creating cell seeded sponges. Tissue engineering sponges are useful in that they can be stored until needed followed by cell seeding when necessary and could also be used to absorb wound exudate when used in dressings. The fabricated sponges lost some of their dimensional volume and exhibited some deformation due to the lyophilisation and rehydration process, especially in the case of ι-carrageenan sponges. All sponges appear pink in colour due to the colour of cell-culture media.

Figure 5.10 – Images of freshly printed hydrogels (left), freeze dried sponges (centre) and rehydrated monolayer sponges (right) using A) 1.0% gellan, B) 0.5% collagen, C) 3.0% alginate and D) 2.0% ι carrageenan (scale bar = 5 mm).

Upon observation of the preservation of cells within 3D printed scaffolds, live / dead staining on hydrogel constructs was performed to confirm cell viability following shear conditions experienced by cells during 3D extrusion printing and after 7-days culture (**Figure 5.11**). A high viability was seen across all material constructs both immediately following printing and after 3D culture, confirming that not only does SLAM enable maintenance of print fidelity, but also the conservation of the cell's viable status.

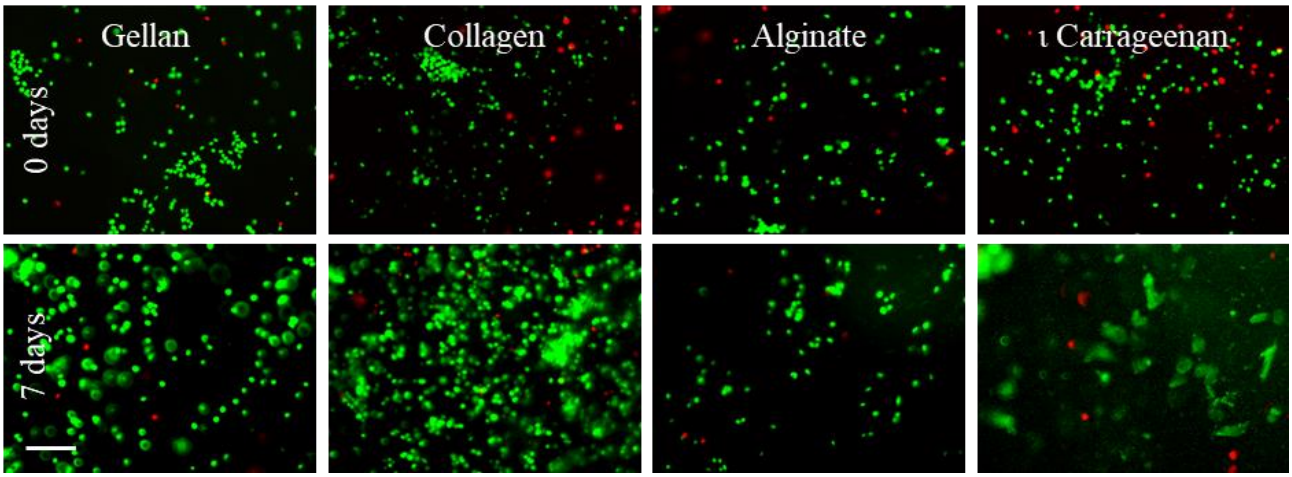

Figure 5.11 - Calcein AM live (green) / PI dead (red) cell viability analysis on freshly 3D printed (0 days - upper) and 7 day cultured (lower) MC3T3 cells suspended within gellan, collagen, alginate and ι-carrageenan hydrogels (scale bar = 200 µm).

As a comparison of an alternative route often employed in tissue engineering, gellan and collagen sponges were seeded with MC3T3 mouse pre-osteoblasts and cell viability was inspected at 0- and 7-days culture (**Figure 5.12**). Two regions within each scaffold were analysed at 7 days (region 1 and region 2, respectively) and the placement of cells was much less heterogenous throughout the scaffolds attributed to the cell seeding process compared with cell-hydrogel suspensions.

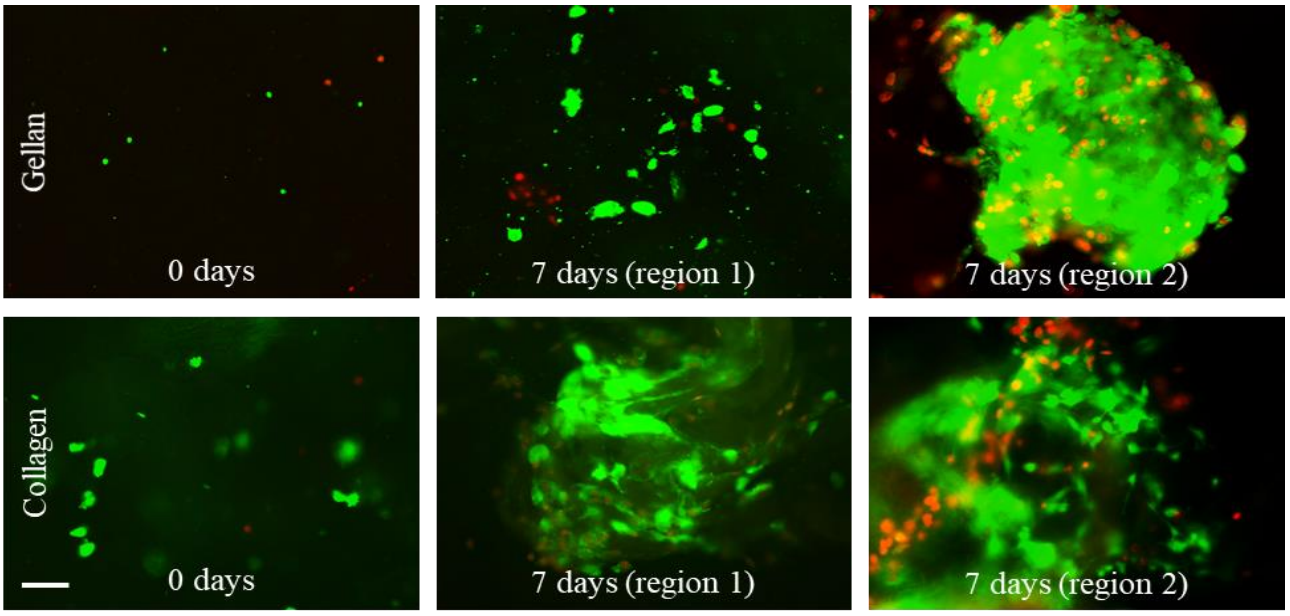

Figure 5.12 - Calcein AM live (green) / PI dead (red) cell viability analysis on freshly seeded (0 days) and 7-day cultured MC3T3 cells suspended within gellan (upper) and collagen (lower) sponges (scale bar = 200 µm).

By assessing the internal networks within freeze dried sponges, one can further understand the integral differences between polymer microarchitecture. Using scanning electron microscopy, micrographs reveal inter-material variances on the micrometre scale, showing that gellan appears to have a dense polymer network with fewer, larger pores in contrast to the more porous, fibrous network within collagen sponges (**Figure 5.13**). In the case of alginate, a much sparser, string like network was apparent and ι-carrageenan sponges displayed very few pores that were small in size.

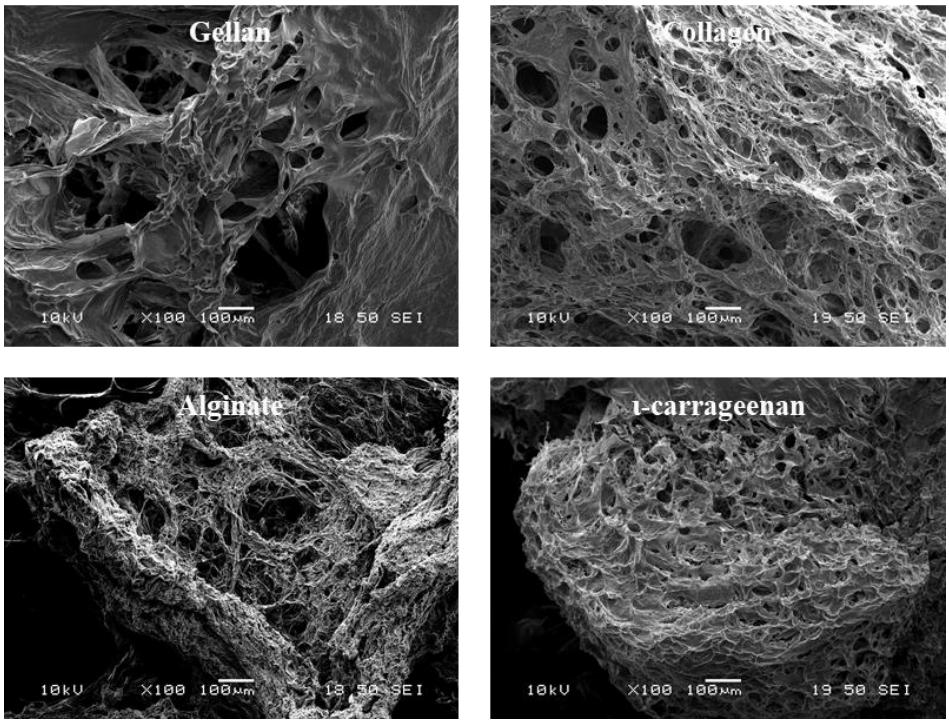

Figure 5.13 - Scanning electron micrographs of 1.0% gellan, 0.5% collagen, 3.0% alginate and 2.0% ι carrageenan at 100x magnification.

Following validation of integrating a 3D bioprinter within the suspended manufacturing technique and thus the emergence of suspended layer additive manufacturing (SLAM), a range of complex and biologically relevant model conformations were 3D printed to assess the capacity of the system. Initially, intricate lattice structures (**Figure 5.14A**) were printed to demonstrate that a high resolution of print geometry can be achieved within the fluid gel (**Figure 5.14B**) and that fragile constructs can also be successfully liberated from the supporting bed (**Figure 5.14C**).

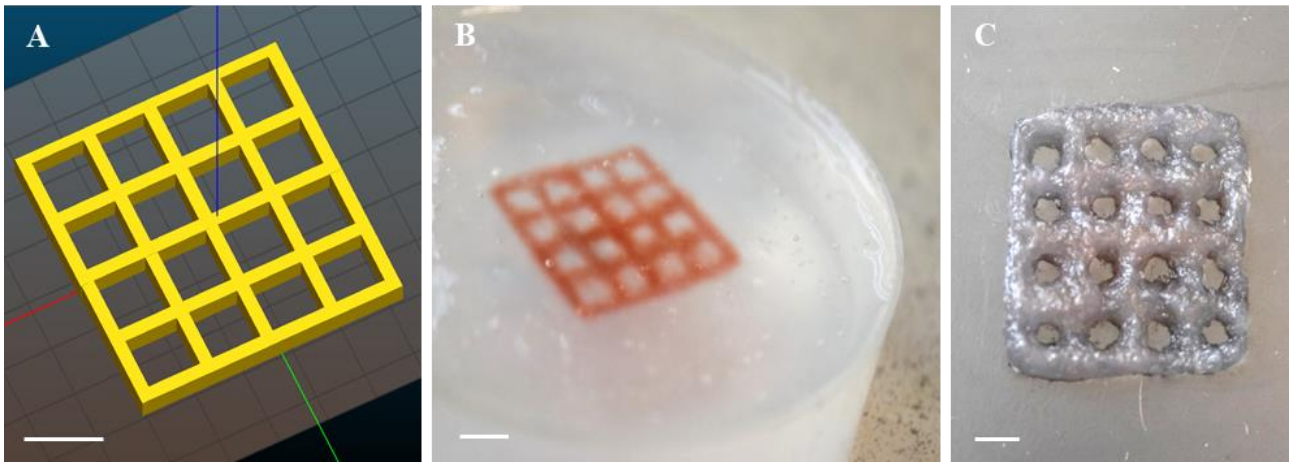

Figure 5.14 – Suspended layer additive manufacturing of an intricate lattice. A) Stl file and 3D printed gellan lattice B) within and C) following gelation and retrieval from the agarose fluid gel bed (scale bars = 10 mm).

On the other end of the scale, the potential of the system to successfully fabricate large bulk structures was also determined by 3D bioprinting a T7 intervertebral disc (**Figure 5.15A**). The fluid gel support bed was able to suspend the solid structure (**Figure 5.15B**) and crosslinking ions were able to penetrate the construct to initiate gelation (**Figures 5.15C and D**).

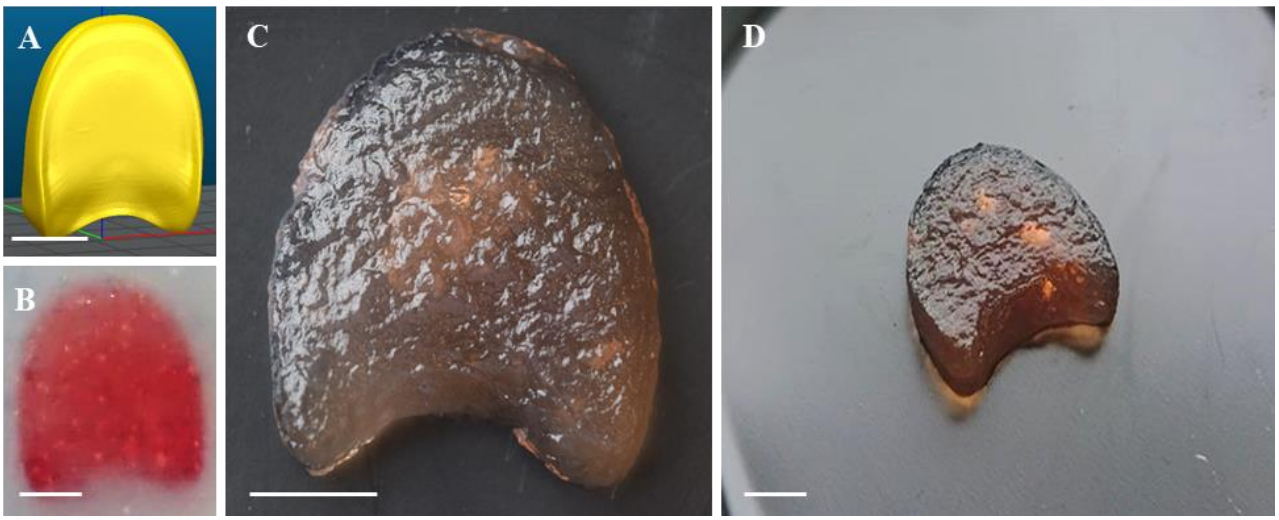

Figure 5.15 – Suspended layer additive manufacturing of a bulk T7 intervertebral disc. A) Stl file and 3D printed gellan intervertebral disc B) within and C/D) following gelation and retrieval from the agarose fluid gel bed (scale bars = 10 mm).

Within conventional 3D bioprinting systems which extrude polymer material onto a planar Z-stage, the realisation of hollow structures can rarely be achieved. To decipher whether using a supporting agarose fluid gel bed could overcome this issue, hollow tubes and blood vessel-like structures with various lumen dimensions were fabricated (**Figure 5.16A**). Upon inspection, the nature of how polymer was deposited in an arrangement where voids were present (represented by the hollow part of the structure) was of no detriment to the system. Polymer was extruded within the support bed in a manner consistent with the 3D model file without causing dragging of previously printed material (**Figure 5.16B**). Again, scaffolds were retrieved from the supporting gel following crosslinking and demonstrated that the lack of chemical associations between printed gellan and the agarose gel bed enables suspension of hollow structures prior to solidification and extraction (**Figures 5.16C and D**).

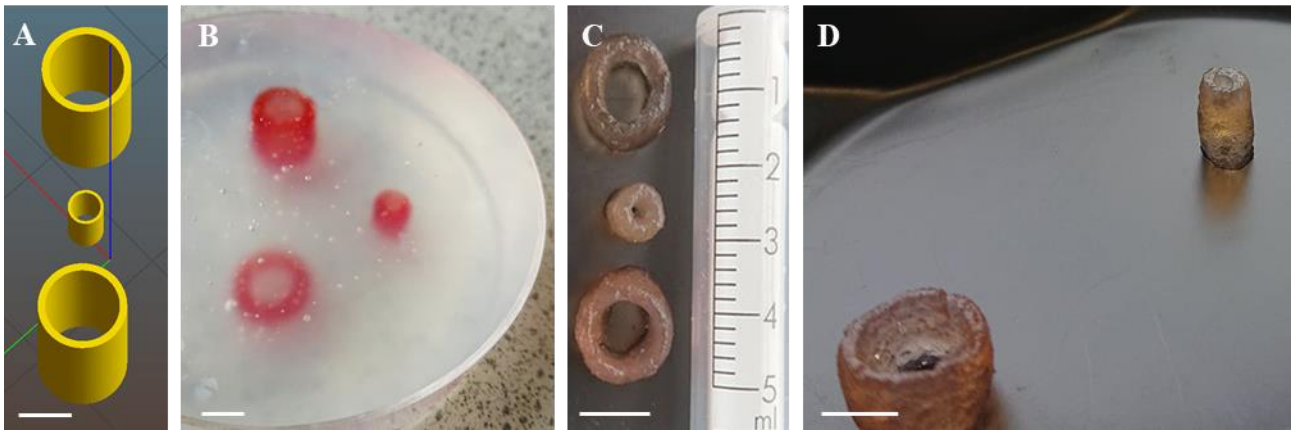

Figure 5.16 – Suspended layer additive manufacturing of hollow tubes and blood vessels. A) Stl file and 3D printed gellan tubes and blood vessels B) within and C/D) following gelation and retrieval from the agarose fluid gel bed (scale bars = 10 mm).

In extension to 3D printing hollow structures and to push the boundaries of the current standard for manufacturing biological scaffolds, a hollow and bifurcated carotid artery was produced. An stl file of a carotid artery scan (**Figure 5.17A**) was translated into a GCODE file (**Figure 5.17B**) rendering the 3D model as a series of layers which can be printed, bottom to top, using the principles of additive layer manufacturing with a suspending element (**Figure 5.17C and D**). The carotid artery was then

solidified upon the introduction of calcium chloride solution (**Figure 5.17E**) and was extracted from the supporting bed (**Figure 5.17F**). Following this, the hollow bifurcated structure was perfused with a blue dye (**Figure 5.17G**), showing that SLAM is a suitable method for the generation of complex structures which would otherwise need additional reinforcements by altering the geometrical aspects of the model and subsequent severing following fabrication.

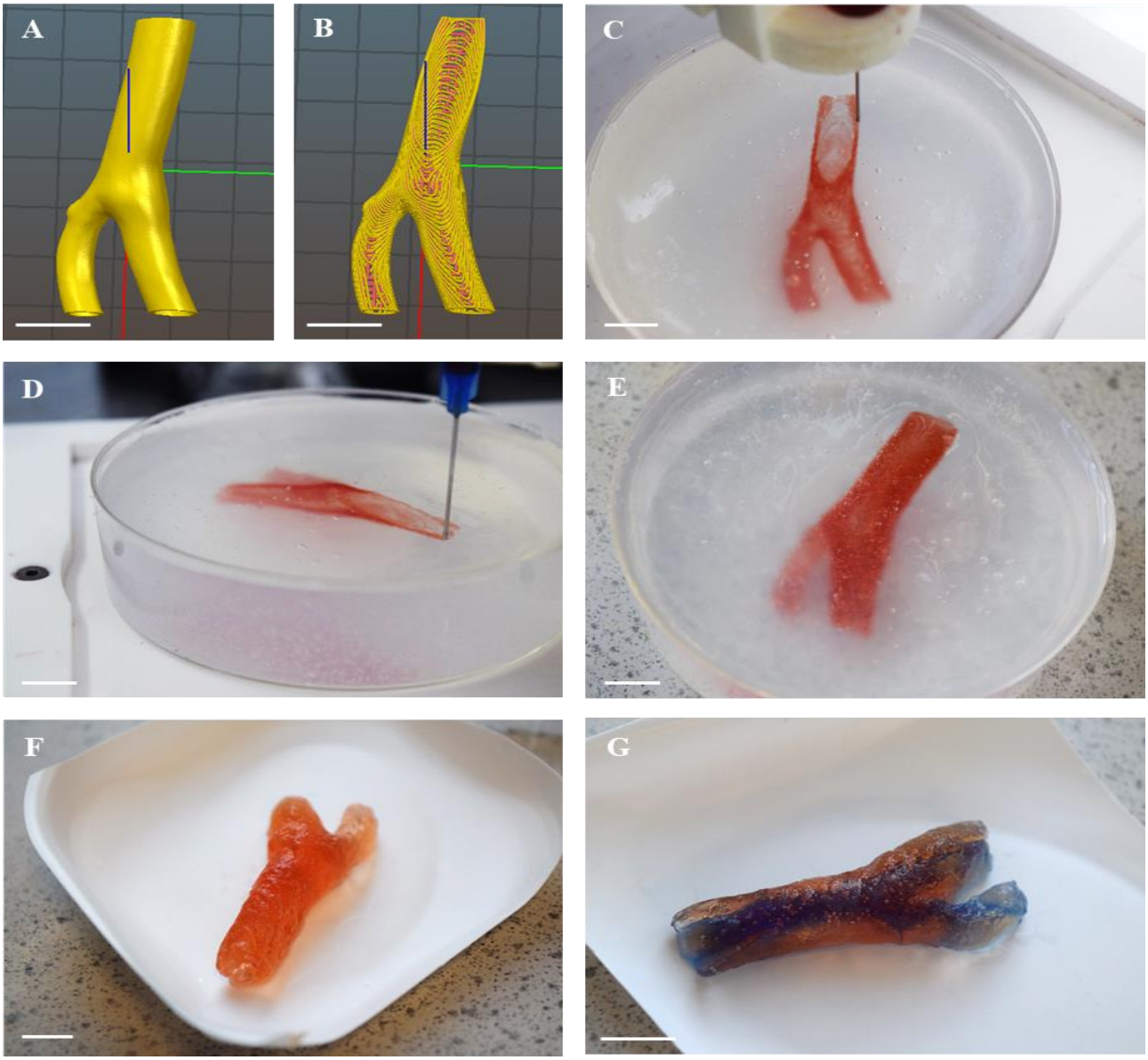

Figure 5.17 – Suspended layer additive manufacturing of a human carotid artery. A) Stl file and B) GCODE print path of model human carotid artery. Gellan carotid artery C/D) during printing, E) following crosslinking with calcium chloride F) after retrieval from the agarose fluid gel bed and G) perfused to highlight channels within the structure using a blue dye (scale bars = 10 mm).

Finally, a range of bulk, biological structures that feature intricate protrusions and contours and that are absent a flat base were manufactured using SLAM (**Figures 5.18A - E**). Structures including a hand, ear, femur, foetus and spider were all replicated in gellan within the supporting agarose bed.

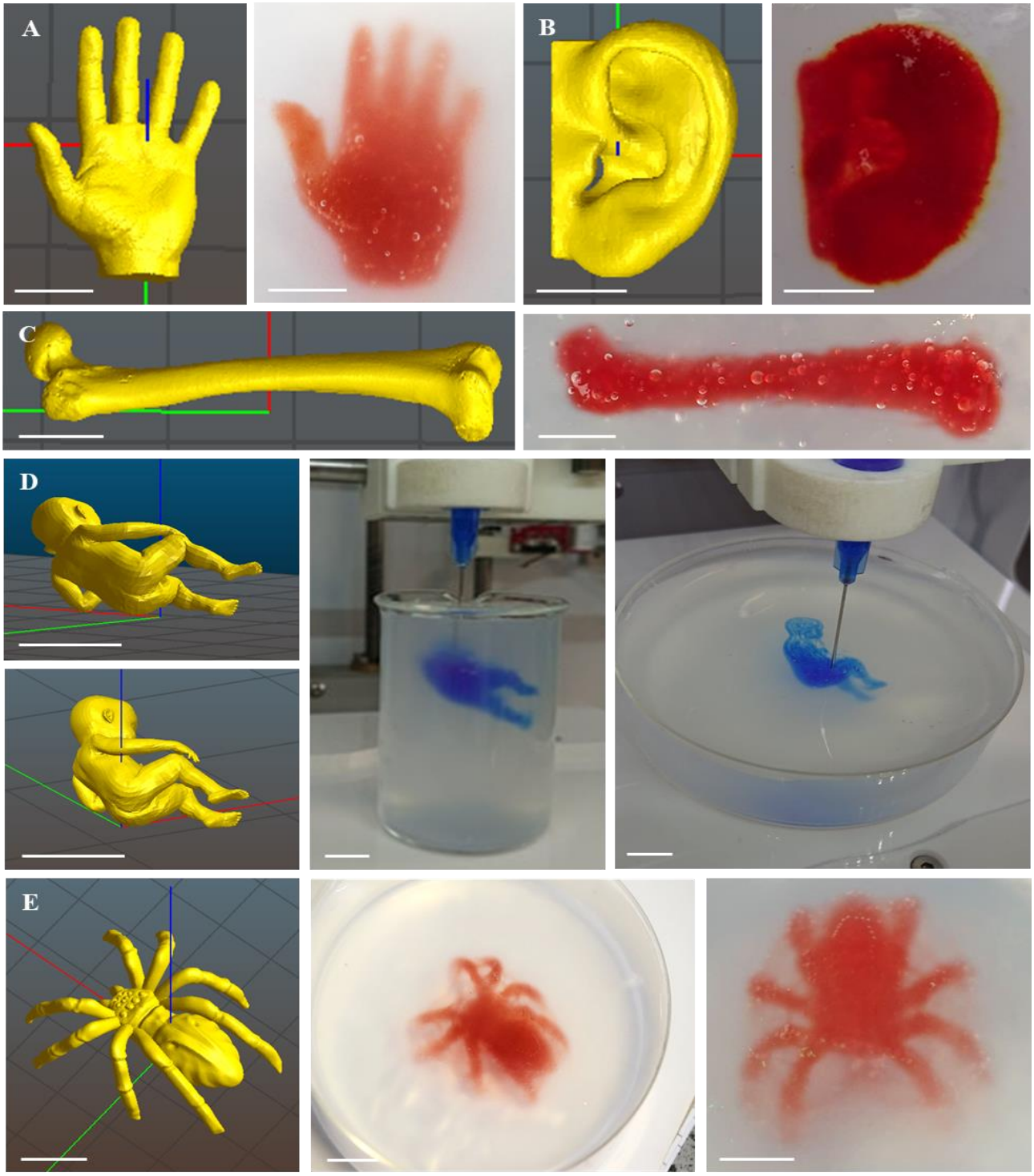

Figure 5.18 – Suspended layer additive manufacturing of complex gellan structures. A) Human hand, B) human ear C) human femur D) human foetus and E) spider. Yellow graphics are stl images and red or blue graphics are 3D printed gellan (dyed red or blue) scaffolds (scale bars = 10 mm).

5.4 Discussion

The automation of 3D bioprinting scaffolds and constructs via the suspended manufacture method has been realised to a high level. The employment of a 3D bioprinter has enabled more controlled deposition and the generation of more refined tissue engineering parts despite the low viscosity of the printing hydrogel precursors. Additionally, the transition from hand printing to automated fabrication has seen no detriment to the viability of hydrogel-suspended cells. On the contrary, this new technique offers a more controlled, measurable and predictable alternative to the variable and inconsistent nature of hand-printing. This has seen the evolution of suspended manufacturing into what has now been termed as suspended layer additive manufacturing (SLAM).

As part of this evolution, a wide range of opportunities for tuning print parameters in order to direct print resolution and cellular viability were created. To exploit the advantages of this feature, a range of biopolymer hydrogel solutions with differing mechanical properties were subjected to shear rheology to further understand the viscosity profiles that play an important role in extrusion bioprinting. Pectin, alginate, ι carregeenan, gellan and collagen all showed shear thinning characteristics, through a reduction in viscosity, as shear rate was increased (**Figure 5.2A**). The viscosity profiles of each hydrogel solution also correlated with the pressure required for extrusion, in that viscous polymers required higher print pressures to permit deposition (**Figure 5.2B**). When a single material (gellan dyed blue) was selected to assess the multifaceted relationships between flow rate, nozzle diameter and print pressure, it was seen that increasing each of these parameters also decreased the resolution of printed rings within the agarose fluid gel bed. When slurry gels were used as an alternative supporting gel formulation method, it was evident that the resolution was slightly compromised and extrudes appeared discontinuous (**Figure 5.3**).

Though it has been proven that the SLAM technique is conducive to printing intricate extrudes with relatively high resolution, it is imperative that the shear forces experienced by the bioink during

deposition do not exceed the threshold of shears that impact upon cell viability and behaviour. Shear stress is inevitable within any extrusion-based printing procedure and is also directly influenced by the viscosity of the printing material, nozzle diameter and printing pressure likewise to resolution. An in-depth analysis into balancing printing resolution and stem cell integrity by controlling shear stresses in 3D bioprinting was presented by Blaeser et al., (2016). Using drop on demand (inkjet printing), they assessed the effects of a range of hydrogel viscosities, printing pressures and nozzle diameters on shear induction upon bioinks during extrusion. They found, by aid of their computational algorithms, that by increasing dispensing material viscosity, increasing printing pressure and decreasing nozzle diameter, print induced shear increased. The printing pressures and nozzle diameters reported during Blaeser‘s study, however, generated considerably harsher printing conditions than those presented using the SLAM technique (0.5 – 1.5 bar versus 0.05 – 0.24 for print pressure and 150 – 300 µm versus 150 - 610 µm for nozzle diameter respectively). The ranges of dispensing viscosities between the two systems were comparable (0.01 – 1 Pa at 10 s^{-1} in both cases (with the exclusion of ι-carrageenan at 10 Pa s)) although our group have previously demonstrated the capacity of SLAM to print materials with a viscosity equivalent to that of water. It must be acknowledged that the differences in parameters are reflective of how the two opposing printing techniques differ on an operating level. Inkjet printing involves dispensing of bioinks by jetting single droplets through electromagnetic micro-valves. Alternatively, micro-extrusion deposits bioinks as continuous media via pneumatic force. Due to the opposing natures of how bioinks are dispensed, the terms of how dispending is measured also differs. Inkjet printing is associated with deposition velocity as the bioink is propelled through the air onto a collector substrate, whereas the SLAM method measures bioink deposition within the supporting gel in terms of flow rate. It is not therefore appropriate to compare the two methods on this basis, however, by comparison of the more 'cell friendly' printing parameters used in SLAM with those used by Blasaer (which still produced reputable results at the gentler end of the scale), combined with the assessment of cell viability by

staining, it may be confirmed that a high resolution of printing may be achieved without compromising cellular integrity.

As an approximate indicator of how crosslinking solutions diffuse throughout the fluid gel and within the construct once injected around the print perimeter, the diffusion of two dyes (methylene blue and dimethyl methylene blue) with different molecular weights was inspected. Interestingly, methylene blue required a greater extrusion pressure of 16 kPa to attain an equivalent flow rate. Of the two, methylene blue had the lower molecular weight (319 g/mol) and exhibited a larger range of diffusion, platauing much later than dimethylmethylene blue (417 g/mol). In comparison, the calcium chloride dihydrate crosslinking solution has a molecular weight of around 147 g/mol, whereas the polymers used in this study, such as alginate, gellan, ι carrageenan and collagen, have much higher molecular weights which generally appear in the regions of the thousands, if not tens or even hundreds of thousands. These values are advantageous in that the low molecular weight of the crosslinking solution allows it to readily traverse the fluid gel causing rapid onset of crosslinking. Conversely, the large molecular weights of suspended polymer within the fluid gel bed ensure that extrusion remains localised. In other embedded techniques, such as FRESH, a gelatin slurry forms the supporting matrix and is formulated with an inclusion of calcium chloride (Hinton et al., 2015). However, this may be unsuitable for elaborate model designs that require extended printing timeframes, as gelation may start to occur much too prematurely before printing has finalised. In addition, the agarose support bath allows for further methods of crosslinking. This includes temperature-dependent polymers, such as some collagen formulations that are gelled by raising scaffold temperature to 37 °C, which would otherwise liquefy the gelatin slurry at cell culture and physiological temperatures.

When comparing agarose fluid gels to agarose slurry gels, as an assessment of the importance of support bed formulation, shear rheology revealed that fluid gels exhibited a lower shear viscosity yet a more stable recovery upon the removal of shear. These results translate in that printing solutions may be more easily deposited following the shearing action of the needle within the supporting matrix

yet experience greater reinforcement from the self-healing gel before solidification. An explanation into the mechanical behaviour of these two gel formulations can be found when observing the inner particulate suspensions under a brightfield microscope. Fluid gel particles exhibited 'hairy' accessories due to the toroidal fluid motion which is generated under the shear of a magnetic stirrer (Halász et al., 2007). These hairy projections claim some responsibility for inter-particle associations due to a large surface area to volume ratio, meaning that once shear forces are removed, the particles interact more readily compared with the smooth, angular and irregularly sized particles within agarose slurry gels.

Perhaps the most defining results that establish the success of this system is the generation of complex hydrogel structures whilst cell viability status is maintained. Initially, an S shape was printed with and without an agarose fluid gel bed using low viscosity gellan to illustrate the importance of the supporting matrix. Without such, the S shape was seen to deform and flow in contrast to the same hydrogel solution that was printed within the gel bed using SLAM. Cylindrical shapes were then 3D bioprinted to ensure that cells within the bioink remain live following printing and 7-day culture, in which a high viability was seen in both cases, throughout all four suspending materials of gellan, collagen, alginate and ι-carrageenan. Moreover, within 7-day cultured collagen constructs in particular, (the only integrin binding domain bearing material assessed) the cells appeared to have proliferated within the hydrogel. In comparison to the proposed method of generating hydrogel tissue engineering constructs, a different form of biomaterial in the conformation of a tissue engineering sponge was fabricated. One advantage of manufacturing sponges over hydrogel constructs is that sponges can be pre-made, stored and seeded with cells when necessary. Manufacturing tissue constructs this way, however, produces a marked difference in mechanical properties, porosity, diffusion rates, cell morphology and cell distribution (Zhang et al., 2013). In gellan and collagen sponges versus the equivalent hydrogels, cell distribution is much less heterogeneous, and cells form aggregates due to the seeding process, in which cells filter through the larger pores and then settle on

the polymer fibres. Consequentially, cells assume a more elongated morphology as opposed to more spherical morphologies within hydrogel constructs.

Once print fidelity and cell viability had been established, different, biologically relevant geometries were printed using gellan to test the complexity and scale that can be achieved using the SLAM method. In order to demonstrate the resolution of the system, an intricate lattice structure was printed. The delicate structures could easily be removed from the fluid gel bed following gelation without damage to the scaffolds. These elaborate designs are often favoured in the manufacture of implantable scaffolds as they are conducive to diffusion and vascular infiltration, thus reducing the emergence of hypoxic or necrotic regions (Fantini et al, 2016; Hollister, 2005; Loh & Choong, 2013). To display the system's capacity to print large bulk structures, a T7 intervertebral disc was manufactured. The 3D printed T7 disc exhibited true-to-size dimensions and the fluid gel print matrix successfully allowed the addition, post-production, of crosslinking cations for solidification. The ions were able to diffuse throughout the fluid gel into the whole printed part despite it having relatively large dimensions. To test the potential of producing geometries which cannot be printed using a 2D collector, a range of hollow and bifurcating structures were printed. A large bifurcated structure in the form of a carotid artery was printed as well as smaller, tubular and perfusable structures with internal junctions. Following gelation, these were easily removed from the fluid gel support bed, residual agarose was washed away and they were sufficiently robust to be handled and manipulated.

To demonstrate the potential to 3D print structures which combined both bulk and intricate features, a hand, ear, femur, spider and a foetus shape was printed. The way in which the fluid gel suspends a structure during manufacture has previously been likened to the way in which the amniotic fluid supports a developing foetus (Moxon et al., 2017). Using this suspending element, further freedom is granted when printing complex hydrogel shapes, in that the orientation of the print model (i.e. horizontal or vertical) can be selected to optimise the ALM print path, rather than to aid

conduciveness of printing onto a planar stage in which a particular orientation may need to be selected.

5.5 Conclusions

In summary, the SLAM technique was developed to resolve the complications related to using low viscosity bioinks in extrusion-based 3D bioprinting. Hand-printing 3D scaffolds by suspended manufacture was upgraded by introducing a robotic 3D bioprinter, thus refining the resolution of printed parts without impediment to construct fidelity or cell viability. A variety of biopolymer materials that are currently widely investigated in regenerative medicine were employed, highlighting the versatility of the technique. The method enabled the successful fabrication of bulk, intricate, hollow, and bifurcated structures as well as other elaborate scaffolds that were absent a flat base and featured detailed protrusions and contours. Aided by tuning flow rate, printing pressure, nozzle gauge and rheological properties, the physical and mechanical properties of agarose fluid gels could be exploited, allowing the deposition of hydrogel solutions that exhibit varying mechanical properties and gelation mechanisms themselves. The fluid gel also facilitates the diffusion of crosslinking ions, which is necessary when printing materials that gel via ionic gelation, yet the extruded precursor solutions that form the 3D printed model, remain stable and anchored to the region of extrusion before crosslinking is initiated.

Here, manufacturing complex and human-sized hydrogel structures as potential tissue engineering constructs by SLAM is the first of its kind. In reality, native human tissues exhibit regional variations in extracellular and cellular makeup and are inherently location and function specific. These variations must therefore also be mirrored within a single construct during tissue replication for the part to successfully integrate within the human body. With this, the next chapter focuses on generating anisotropic 3D printed constructs that resemble the dynamic environments within human tissues.

Chapter 6

3D BIOPRINTING
MULTI-LAYER CONSTRUCTS

Aspects of this chapter are published in *Advanced Functional Materials*

Senior, J.S. Cooke, M.E. Grover, L.M. Smith, A.M. (2019) Fabrication of Complex Hydrogel Structures using Suspended Layer Additive Manufacturing (SLAM). Advanced Functional Materials, 29, 49.

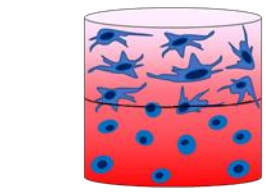

Cell Morphology Analysis

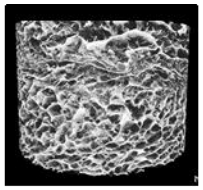

Microarchitecture Analysis

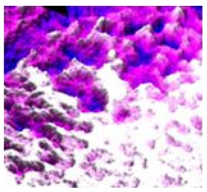

Surface Texture Analysis

Dual Layer Sponge

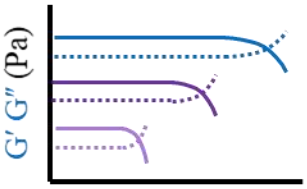

Mechanical Analysis

Dual Layer Hydrogel Construct

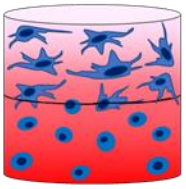

Cell Morphology Analysis

Multi-Layered Construct Gradients

Core-Shell Printing

Lateral Printing

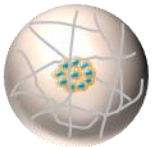

Tumour Model

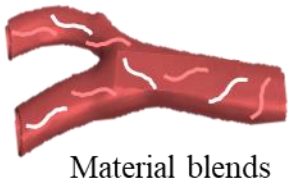

Material blends

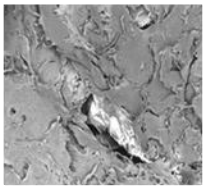

Microarchitecture Analysis

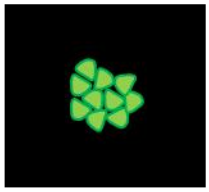

Cell Pellet

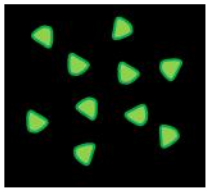

Single Cells

Chapter 6 – 3D Bioprinting Multi-layer Constructs by SLAM

6.1 Introduction

Tissue engineering is a rapidly evolving interdisciplinary field that offers enormous potential towards the restoration, maintenance and improvement of biological function. However, there remain critical challenges including a lack of quantitative design of tissue scaffold architecture and engineering regions of the scaffolds to have distinct mechanical behaviour that is analogous to that of the desired tissue. When replicating tissues by generating 3D bioprinted constructs, the material environments in which cells are suspended should mimic their native tissue origin. In reality, the chemical and mechanical properties throughout human tissue are heterogeneously graded and play a crucial role in preventing mechanical failure between interconnecting tissues as well as maintaining cell phenotype.

The documented sensitivity of cells to several chemical and physical cues which guide cell migration (known as taxis) is yet to be fully exploited in the biofabrication of tissues (Singh et al., 2008). These range from chemical responses of the dissolved and immobilized form (chemotaxis and haptotaxis), to the mediation of cell migration through physical attributes within tissues, including substrate rigidity (mechanotaxis), electrostatic potential (galvanotaxis) and extracellular tension (tensotaxis) (Haga et al., 2005; Lo et al., 2000). Addressing these phenomena within tissue engineering substrates could subsequently enable integration of spatially controlled gradients leading to dynamic cellular machineries that could enhance cell-based therapies.

Such environments that must be recaptured within a successful tissue replica include porosity / pore size, substrate stiffness, surface gradients (e.g. hydrophilicity, roughness and charge) and chemical signalling gradients (such as growth or differentiation factors and cell adhesion molecules) (Singh et al., 2008). Previous studies have attempted to modulate tissue gradients by designing anisotropic scaffolds and constructs using interface tissue engineering. These practices predominantly focus on interfacing hard tissues for applications in musculoskeletal tissue repair, such as the recreation of

ligament-bone, tendon-bone and cartilage-bone implants (Patel et al., 2018). These include the control of gradients by alternative processing techniques of a single material or by incorporating multiple materials with varying physicochemical characteristics to recapitulate desired tissue environments. Fabrication techniques which have been used to achieve these goals, however, are often painstaking and laborious processes to undertake and can commonly be inconducive to the culture of live cells. In addition, many of these studies limit their research to using non-naturally occurring materials, with a high occurrence of PLGA, PDMS and PAA and their derivatives being cited in the literature (Sant et al., 2010).

One such example of a synthetic gradient scaffold made by rigorous and complex methods is that of a degradable, composite bone-repair product made via 3D fabrication (Dutta Roy et al., 2003). Here, PLGA scaffolds containing β-tricalcium phosphate (β-TCP) ceramic were designed, containing pore size and porosity gradients for promoting new bone ingrowth. Initially, powdered blends of PLGA and β-TCP were spread onto a build bed, following which, liquid binder droplets were robotically deposited onto selected regions of the powder bed in a process analogous to inkjet printing. This subsequently generated a solid region within the 2D layer, and the process was repeated until the build-up of the 3D structure had been achieved. Further, between each layer, a chloroform solvent binder was used to consolidate the sequential layers. The gradient in porosity was achieved by adding 87.5% by weight of sodium chloride salt to PLGA and β-TCP powder blends and decreasing to 80% by weight at the outermost edges of the scaffold. Salts were then leached post-fabrication by submerging in water, creating pores between 125–150 μm. Though sophisticated in design, this multi-step process lacks control of pore placement and therefore a reduced potential in quantitative design. Towards fabricating mechanical gradients within zonally organised cartilage tissue constructs, Zhu et al., (2018) utilised a gradient maker in which two interconnected chambers containing polyethylene glycol (PEG) dithiol and chondroitin sulphate (CS) at given ratios that were mixed with isolated chondrocytes, were crosslinked into a single structure using photopolymerization. Although the

process of achieving tissue gradients within a single construct had been markedly simplified, these apparatuses are strictly limited by material compatibility within the system.

3D bioprinting tissue gradients at the softer end of the scale is much less researched territory. This is attributed to the poor printability and shape fidelity of low viscosity solutions as well as the related difficulty in integrating multiple materials once crosslinking has occurred (Sardelli et al., 2019). Moreover, layering multiple materials with contrasting chemistries and gelling mechanisms is particularly hard to accomplish. With this, it is evident that there is a need for improved technology in generating composite scaffolds with physicochemical properties akin to soft human tissues. Within this thesis chapter, a range of multilayer biopolymer hydrogel structures that contain localised variations in physiochemical characteristics and are synonymous to that of native tissue will be explored. Heterogeneous tissue constructs with regional chemical, mechanical, microstructural and surface architecture specifications were generated using the SLAM method as established in the previous chapter. Multi-layer constructs containing two layers of physicochemically different material were printed by layering one polymer upon another or by adjacent deposition and then integrating by crosslinking under the principles of SLAM. Core-shell constructs were fabricated by encapsulating a secondary hydrogel within a pre-established cylinder extrude and were crosslinked to produce a phase-encapsulated construct. Further, the encapsulation of a mammary adenocarcinoma cell-pellet (absent a hydrogel suspending element) within a pre-established cylinder extrude was performed to emulate a basic model of the tumour microenvironment. Finally, polymer blends containing two different materials were 3D bioprinted in the form of a carotid artery, demonstrating the versatility of this method in recreating tissue chemistries. These 3D bioprinted structures were then assessed using a range of analytical techniques including brightfield and scanning electron microscopy, micro-computed tomography, surface profilometry, rheology and cell culture staining.

6.2 Methods

6.2.1 Agarose fluid gel printbed formulation

Agarose fluid gels (type 1 low EEO, purchased from Sigma-Aldrich, Dorset, UK) were prepared by autoclaving solutions of agarose mixed with deionised water (121°C temperature and 1.4 bar pressure) (Prestige Medical™ bench top autoclave) at 0.50% w/v concentration and cooling to 25 °C under a constant shear of 700 rpm using a magnetic stirrer. Fluid gels were then poured into extra-depth tissue culture plates to form a supporting printbed.

6.2.2 Preparation of polymer solutions for printing

The materials used for printing were low acyl gellan gum and ι-carrageenan (purchased from Special Ingredients, UK), alginate (alginic acid sodium salt, purchased from Sigma–Aldrich, UK), low methoxy (LM) pectin (purchased from CP Kelco, UK) and collagen (PureCol EZ Gel, Advanced BioMatrix, purchased from Sigma–Aldrich, UK). Gellan, ι-carrageenan, alginate and pectin powders were dispersed in deionized water at concentrations of 1%, 2%, 3% and 5% w/v respectively and allowed to cool to 25 °C following autoclaving to form working solutions. Collagen solutions were stored at 4 °C prior to use.

6.2.3 Cell culture expansion

Mouse calvaria-derived pre-osteoblasts (MC3T3), human dermal fibroblasts (HDF) and MDA-MB-231 epithelial mammary adenocarcinoma cells were cultured from cryopreserved vials. A single vial containing 1 x 10^6 cells was removed from storage in liquid nitrogen and defrosted in a water bath at 37 °C (Grant Instruments™ - Fisher Scientific, UK). Once thawed, cells were transferred to a centrifuge tube along with supplemented Dulbecco Modified Eagle Medium (DMEM) (10% FBS, 2.5% L-glutamine, 2.5% HEPES buffer and 1% penicillin/streptomycin) and centrifuged at 1000 rpm for 3 minutes using a benchtop centrifuge (ThermoFisher Scientific, UK). The supernatant was

removed and fresh supplemented DMEM was added prior to transferring to a cell culture flask. Cells were kept at 5% CO_2 and 95% air and incubated at 37 ºC (Triple Red, UK). Media was aspirated and replaced every 3 days (or as necessary) and cells were passaged at 80% confluence.

6.2.4 Cell culture passage

For the trypsinisation process, media was aspirated from cultures and cells were washed using Phosphate-Buffered Saline (PBS). TrypLE™ dissociation reagent was added and flasks were incubated at 37 ºC for 2 minutes. Cultures were then observed for cell lifting using a VWR IT 400 Inverted Microscope (VWR, UK). If cells had not detached, a further 2-minute incubation period was provided. In order to halt the enzymatic activity of TrypLE™, supplemented DMEM was added. Cell suspensions were centrifuged at 1000 rpm for 3 minutes after transferring into sterile centrifuge tubes and the supernatant was removed. Cell counting using a haemocytometer determined the volume needed from the cell suspension to seed new flasks and media was added.

6.2.5 3D modelling

Cylinder shapes (20 mm diameter and 5 mm depth) and cuboid scaffolds (10 x 10 x 5 mm) were designed using computer-aided design (CAD) software SolidWorks and saved in stl (stereolithography) file format, which describes the 3D model in a surface tessellated arrangement. Two cylinders were stacked (one on top of the other) creating one 3D model with correlating layers and printheads and cuboids were to be printed laterally one after the other to determine any impact of print direction on shape-specificity. Shapes were scaled to an appropriate size dependent on application. The stl to G-code conversion programme Slic3r was then used to slice the models into layers and translate the coordinates into commands for the 3D bioprinter.

6.2.6 3D printing multi-layer constructs by SLAM

For printing multi-layer constructs by SLAM, either MC3T3 or HDF cells were mixed with hydrogel solution (gellan, collagen, ι-carrageenan or alginate) at a density of 1 x 10^6 cells / mL and loaded into

two separate printhead cartridges. Cartridges were attached to a conical nozzle with an internal diameter (ID) of 410 μm and inserted into an INKREDIBLE 3D bioprinter (Cellink, Sweden). In some cases, phenol red was added to the hydrogel solutions for improved visualization of the scaffolds. The 3D bioprinter was calibrated to a specified pressure followed by placement of the petri dish containing the agarose fluid bed upon the z-stage. The printer was instructed by the G-code to print the first cylinder within the fluid gel using the bioink loaded in printhead one and extruders automatically changed to printhead two for printing of the secondary, upper cylinder. Multilayer cuboids were laterally printed by moving the petri dish following the initial print so that a secondary cuboid would print next to the first with a slight overlap using gellan and dyed gellan materials. Gellan, ι-carrageenan and alginate were ionically crosslinked with the extrusion of 200 mM of $CaCl_2 \cdot 2H_2O$ around the structure through a hypodermic needle, whereas collagen gelation was induced thermally by raising the temperature to 37 °C. Finally, the constructs were retrieved from the agarose bed using a spatula and gently washing with deionized water.

6.2.7 3D printing phase-encapsulated constructs by SLAM

For biofabrication of core-shell constructs, a collagen cylinder was printed within a pre-printed gellan or alginate cylinder to create encapsulated and encapsulating phases within a single structure. Scaffolds were crosslinked with 200 mM of $CaCl_2 \cdot 2H_2O$ for the polysaccharide portion of the scaffold whilst placing in 37 °C conditions solidified the collagen part of the scaffold before retrieving from the supporting gel bed.

For fabricating a basic model of the 3D tumour microenvironment, a collagen disc was 3D printed within an agarose fluid gel bed followed by the placement of an MDA-MB-231 cell pellet containing 2×10^6 cells within the centre of the collagen disc using a micropipette. Homogeneously distributed MDA-MB-231 cells were also 3D bioprinted within a collagen disc for comparison and both were cultured for 14 days prior to imaging using a confocal microscope.

6.2.8 Fabricating multi-layer and core-shell 3D sponges

Multi-layer hydrogels and core-shell scaffolds were placed in −80 °C conditions for 24 h and then a 72 h freeze drying cycle was implemented at −76 °C and 0.0010 mbar (Christ ALPHA 2–4 LD plus). Dry samples were stored in a desiccator prior to imaging and UV sterilised before use. In addition, dual layer sponges were subjected to cell seeding. Following cell trypsinisation and counting protocols, cell suspensions within cell culture media were created at 1 x 10^6 cells per mL. Dual layer freeze dried sponges were then hydrated with the cell-media suspension and left for no longer than 24 hours for cells to relax. Following this period, constructs were washed in PBS and were either examined or cultured for a further 14 days.

6.2.9 3D printing blended hydrogel constructs by SLAM

For printing hydrogel constructs containing two intermixed polymers, blended solutions of pectin and collagen were mixed with MC3T3 cells at a density of 1 x 10^6 cells / mL and printed into the shape of a carotid artery, followed by culturing for 14 days. The cell types that are present within native carotid artery are smooth muscle cells and endothelial cells, however, MC3T3 cells were used in this case as they had previously been imaged within single collagen and pectin hydrogels and would thus aid as a better comparison in how MC3T3 cells behave within single matrices *versus* collagen / pectin blends. Carotid artery designs were downloaded from https://www.thingiverse.com.

6.2.10 Brightfield microscopy

For visualisation of the internal structure within dual-layer alginate-collagen and gellan-collagen sponges, samples were rehydrated in PBS, embedded in cryofluid and sectioned to 20 µm thickness using a cryostat microtome (Leica CM 1900). Sections were then loaded onto microscope slides and stained with alcian blue for polysaccharide content followed by counter-staining with Van Gieson's stain for collagen. Samples were then visualised under a VWR IT 400 Inverted Microscope (VWR, UK).

6.2.11 Micro-Computed Tomography (Micro-CT)

In order to assess the microstructure and porosity of intact dual phase sponges, alginate-collagen and gellan-collagen samples were imaged using micro-CT (Bruker Skyscan 1172, Bruker, Belgium) and stacked data were visualised in 3D using CTVox software (Bruker).

6.2.12 Profilometry

Polymer interfaces and surface texture of dual phase alginate / ι-carrageenan sponges were examined using a Talysurf CCI 3000 brightfield 3D surface profiler. Cylindrical dual phase sponges (20 × 10 mm) were affixed onto a stainless-steel wafer (30 × 30 mm) and placed under the microscopic arm of the profiler. 800 μm^2 regions of the scaffolds were scanned to obtain reliable statistics. The height variation in the resulting topography maps was represented by a colour scheme from which the topographical information could be inferred. Surface roughness was determined using Surfstand Software and the arithmetical mean height (Sa) and root mean square height (Sq) of the construct overall and within alginate, carrageenan and interface regions was calculated using the following equations (**Equation 6.1** and **6.2 respectively**).

$$Sa = \frac{1}{NM}\sum_{i=1}^{i=N}\sum_{j=1}^{j=M}\left|Z(x_i, y_j)\right| \qquad \textbf{Equation 6.1}$$

$$Sq = \sqrt{\frac{1}{NM}\sum_{i=1}^{i=N}\sum_{j=1}^{j=M}\left[Z(x_i, y_j)\right]^2} \qquad \textbf{Equation 6.2}$$

6.2.13 Measuring mechanical gradients within multi-layer constructs

Amplitude stress sweeps by shear rheology were undertaken on the 3D printed scaffolds in triplicate using a Bohlin Gemini rheometer (Malvern, UK) fitted with a 20 mm parallel plate geometry and a lower serrated plate (to prevent slippage) at 25 °C. Construct regions were sectioned to 1 mm

thickness prior to evaluation. Stress sweep assays were carried out to compare and characterise the viscoelastic behaviour within the varying regions of dual phase scaffolds. Elastic (G′) and viscous (G″) moduli (Pa) were measured with increasing shear stress from 1 to 1000 Pa and a constant angular frequency of 10 rad s^{-1}.

To monitor interface integrity, an 80% strain load was applied to the lateral side of a dual layer collagen / alginate scaffolds using a texture analyser (Stable Micro Systems, UK) and photographs were taken before, during and after compression to assess the region where failure occurred.

6.2.14 Cell morphology and viability staining using fluorescence microscopy

To assess cell morphology in 3D bioprinted dual layer constructs, media was aspirated, and 3D cultures washed in DPBS before 1 drop of actin and Hoechst staining (Invitrogen) was adder per mL of construct. To assess cell viability and morphology within cell-seeded sponges and the multi-material blended carotid artery, 3D cultures were sectioned following the addition of 7 µL calcein AM for the staining of live cells (green) and 25 µL propidium iodide for the staining of dead cells (red) after media had been aspirated and 3D cultures washed in DPBS. Scaffold sections were incubated for 20 minutes at 37 ºC, washed once more with DPBS and transferred onto slides. Cells were then imaged using a fluorescence microscope (Evos, ThermoFisher Scientific, UK) for the analysis of cell viability and morphology within the manufactured constructs.

6.2.15 3D mapping cell distribution within tumour models using confocal microscopy

Once 3D breast cancer tumour models (both cell pellet containing models and homogenously distributed cell models) had been cultured for 14 days, constructs were washed in PBS, cross-sectioned and loaded into Lumox® cell culture dishes (Sarstedt, UK). Two drops of Hoechst stain were added per mL of construct for staining of cell nuclei blue and two drops of phalloidin were added per mL of construct for staining of F-actin green (ThermoFisher Scientific, UK). Constructs were incubated at room temperature for 20 minutes prior to imaging using a Zeiss LSM 880 confocal

microscope (Zeiss, UK). 3D z-stack images were obtained using Zen black software and edited using zen blue software.

6.2.16 Scanning Electron Microscopy (SEM)

Core-shell sponges were prepared for SEM by sputter coating with gold using a Quorum SC7620 sputter coater under a low bleed of argon. The internal networks within the scaffolds were then studied using a field emission scanning electron microscope (FEI Quanta 250 SEM) operated in high vacuum mode at an accelerated electron energy of 10 kV. Several images were collected at various magnifications using a back scattered electron detector.

6.3 Results

6.3.1 3D printing multi-layer constructs by SLAM

Incorporation of multiple materials into a single scaffold was investigated using the SLAM method. Various combinations of ionotropically gelled alginate, gellan and ι-carrageenan and thermally gelled collagen biopolymers were successfully integrated to form dual-phase chimeric scaffolds and freeze-dried sponges (**Figure 6.1**). Gradients in material could be seen with the naked eye in all cases and all scaffolds and constructs exhibited structural integrity throughout the part, as well as at the material interface, despite alternative gelation mechanisms. As with the monolayer scaffolds within the previous chapter, gellan and collagen closest retained the cylindrical dimensions of the G-code model, whereas the ι-carrageenan portions of the scaffolds sagged, and alginate swelled to a greater volume. All materials apart from collagen were dyed using phenol red for improved visualisation. Following lyophilisation of acellular 3D printed scaffolds, sponges lost some of their original volume and deformed further upon rehydration with media.

Figure 6.1 - Images of freshly printed hydrogels (left), freeze dried sponges (centre) and rehydrated (right) bilayer scaffolds using combinations of A) ι carrageenan / gellan, B) alginate / gellan, C) collagen / gellan, D) ι carrageenan / alginate and E) collagen / alginate (upper material stated first).

6.3.2 Porosity gradients within multi-layer constructs by SLAM

To confirm that materials were interfaced at the micron-scale, a series of techniques including brightfield microscopy and micro-computed tomography were conducted. Collagen / gellan dual layer scaffolds were chosen as the candidate scaffolds for observation due to achieving the best shape-specificity and the incorporation of two materials with separate gelling mechanisms. Collagen / alginate scaffolds were also observed due to the swelling nature of alginate and to discern if this property within alginate would hinder integration at the microscale. Scaffolds were imaged using brightfield microscopy following Van Gieson's staining and alcian blue staining for collagen protein and gellan or alginate polysaccharide respectively (**Figure 6.2A and B**). Collagen stained positively pink whilst gellan and alginate stained blue indicating positive for polysaccharide and an intermediate purple colour was apparent between the adjacent layers. Using micro-CT, an overall porosity of 91.90% was achieved in freeze dried collagen / gellan sponges compared with 88.22% in collagen / alginate sponges.

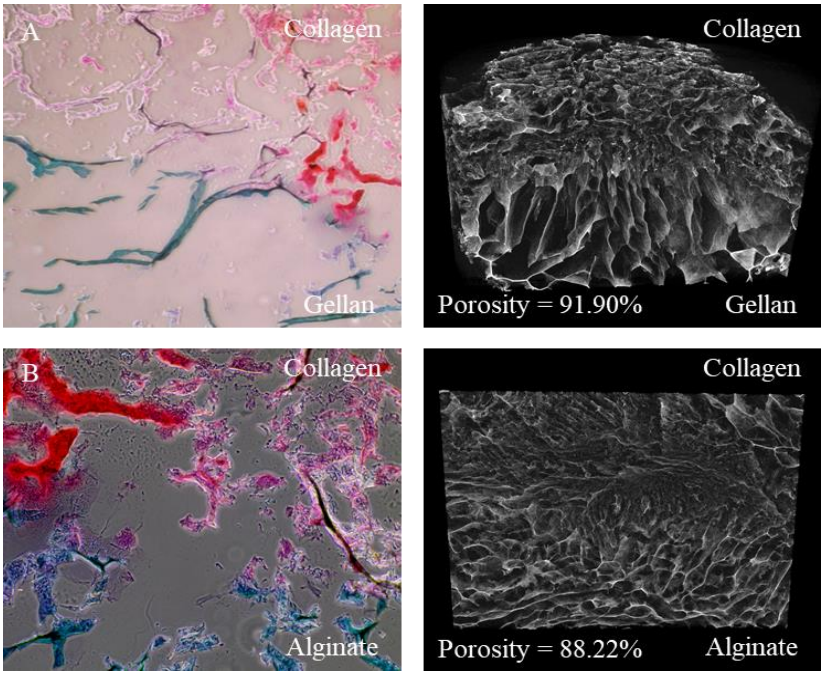

Figure 6.2 – Imaging the interface at the microscale level. Brightfield micrographs of interfaced bilayer scaffolds stained with alcian blue for indication of glycosaminoglycans (gellan and alginate) and Van Gieson's stain for the visualisation of collagen (left) and micro-CT scans of chimeric hydrogel sponges exhibiting A) 91.90% porosity in collagen / gellan scaffolds and B) 88.22% porosity in collagen / alginate scaffolds respectively (right).

6.3.3 Surface roughness gradients within multi-layer constructs by SLAM

Surface texture analysis on 3D printed and lyophilised sponges was conducted using a profilometer. Alginate / ι-carrageenan sponges were selected for assessment due to having the largest diversity in material behaviour. Two surface texture parameters were calculated, namely root mean square height (Sq) which is equivalent to the standard deviation of heights and arithmetical mean height (Sa) which describes the difference in height of each point compared to the arithmetical mean of the surface. Looking at the construct as a whole, alginate and ι-carrageenan appeared interconnected at the interface with a gradient in peaks and valleys both in 2D and 3D surface texture images (**Figure 6.3A and B**). The alginate portion appeared darker pink and purple attributed to exhibiting deeper valleys and a rougher surface compared with ι-carrageenan which predominantly appeared white and smooth. These analyses are further highlighted upon revising each layer of ι-carrageenan and alginate separately as well as probing the interface which displayed a mixture of the two (**Figures 6.3C, D and E**). Focusing on the Sa values as the commonly accepted parameter used to evaluate surface roughness, overall constructs had an Sa value of 55.22 µm, whereas the highest Sa of 60.22 µm occurred within the alginate region, signifying the roughest texture, while the markedly lower Sa of 16.45 µm within ι-carrageenan regions signified much smoother textures (**Figure 6.3F**). Understandably, the interface exhibited an Sa value of 50.21 µm in which both alginate and ι-carrageenan contribute to an intermediate surface roughness. By observing the Sq values within the overall construct (60.6 µm), alginate region (71.22 µm), carrageenan region (20.45 µm) and interface (56.8 µm), it can be concluded that alginate features a much larger variation in surface height due to higher peaks and lower valleys, ι-carrageenan the lowest variation and the overall sponges and interfacial regions mirror that both materials are being observed with an intermediate Sq.

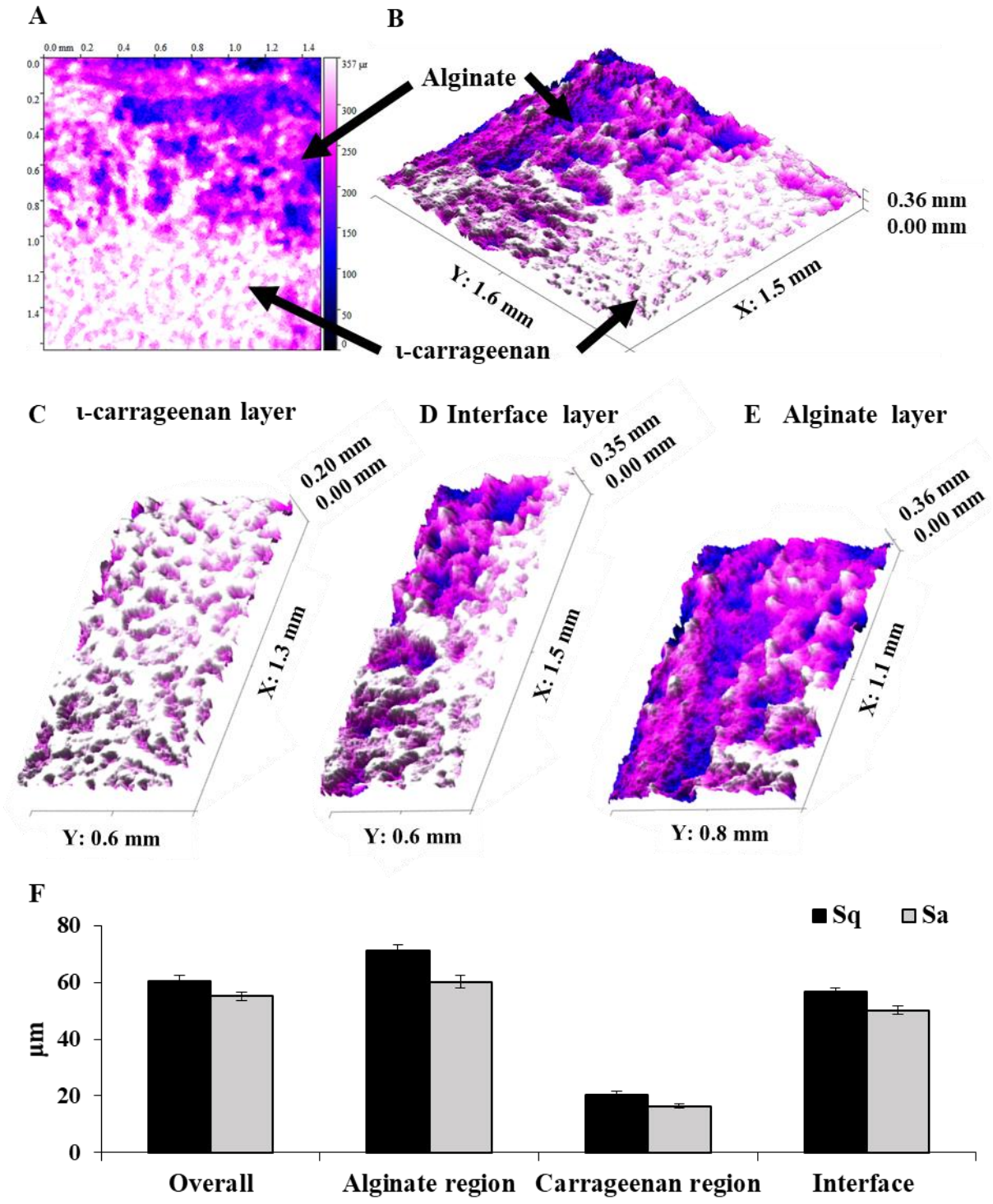

Figure 6.3 – Surface roughness gradients within multi-layer constructs by SLAM. A) 2D and B) 3D surface texture images of an alginate / ι-carrageenan dual layer sponge. Surface texture of C) ι-carrageenan, D) interface and E) alginate alone. F) Calculated root mean square height (Sq) and arithmetical mean height (Sa) in the construct overall and within alginate, carrageenan and interface regions.

6.3.4 Mechanical gradients within multi-layer constructs by SLAM

To explore the mechanical variations that can be achieved within a single construct using SLAM, two different combinations of mechanically contrasting materials were printed to form one whole part and then analysed using shear rheology. A gradual reduction in both elastic (G′) and viscous moduli (G″) were seen within alginate / collagen constructs from the alginate being the stiffest (G′ = 37,170 at 10 Pa) to collagen the softest (G′ = 4,107 at 10 Pa) and with an intermediate consistency at the interface (G′ = 16,570 at 10 Pa) (**Figure 6.4A**). Additionally, the linear viscoelastic region (LVR) and thus shear stress required to fracture each layer reduced from the alginate layer to the collagen portion. Likewise, in gellan / ι-carrageenan constructs, mechanical strength was also seen to decline in a graduated manner from gellan (G′ = 10,490 at 10 Pa), to ι-carrageenan (G′ = 178 at 10 Pa) and with an intermediate value at the interface (G′ = 6,115 at 10 Pa), and with each layer, the LVR reduced (**Figure 6.4B**).

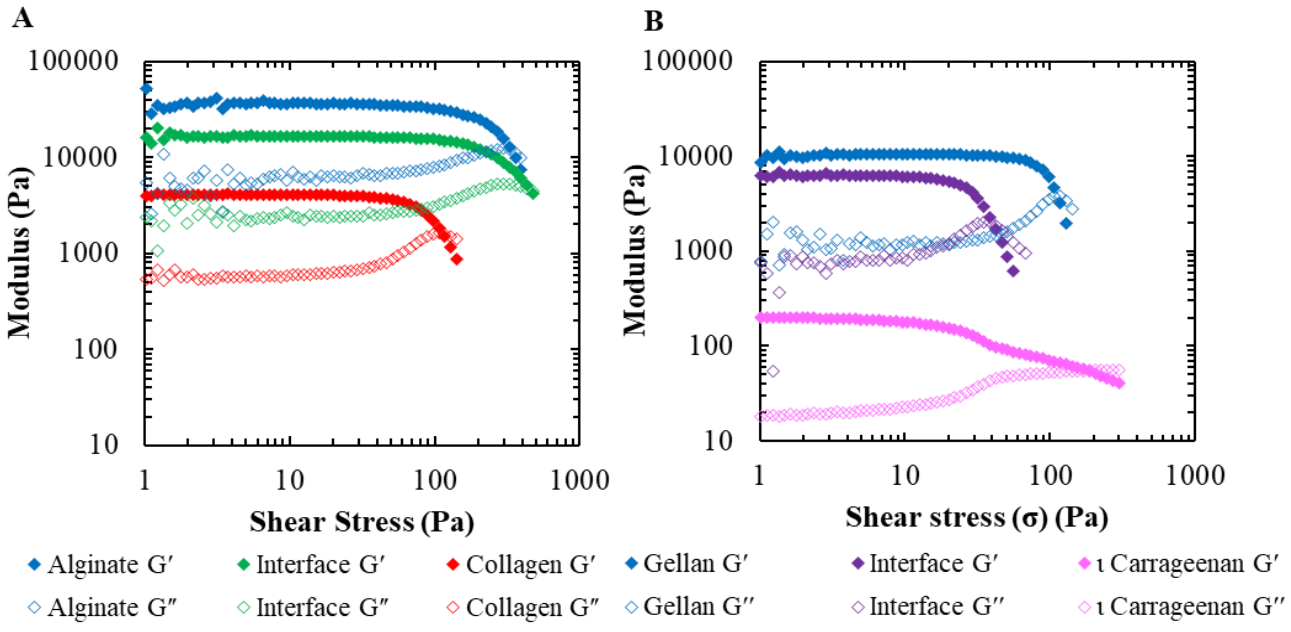

Figure 6.4 – Mechanical gradients within multi-layer constructs by SLAM. Amplitude stress sweeps of 3D printed multi-layer constructs containing A) alginate / interface / collagen and B) gellan / interface / ι-carrageenan.

In extension, an enquiry into the integrity of the interface following compression of an alginate / collagen construct was made using a texture analyser (**Figure 6.5**). After the set mechanical load was applied on the lateral side of the part, it was evident that excessive pressure to the point of fracture does not occur specifically at the interface, confirming that the adjoining point within the two scaffold materials is not the most vulnerable and susceptible point of weakness.

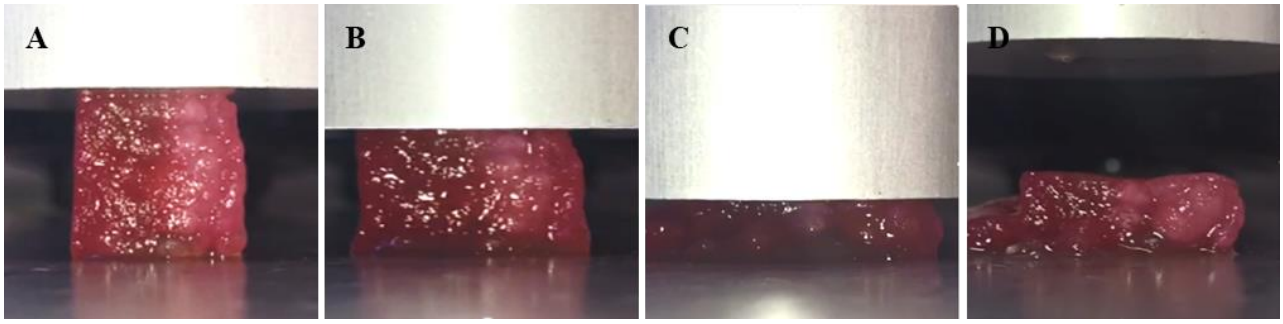

Figure 6.5 - Texture analysis of interface integrity A) before, B/C) during and D) after lateral compression of a collagen / alginate scaffold.

6.3.5 Chemical and cellular gradients within multi-layer constructs by SLAM

The incorporation of multiple materials within a tissue engineering product affords the opportunity to introduce chemical gradients throughout the printed structure. One such example is in the amalgamation of two material layers, both with and without the presence of integrin binding domains that are conducive to cellular attachment within the matrix. Here, collagen / alginate material layers were unified within a dual layer construct with human dermal fibroblasts (HDF) suspended within each layer. Collagen is known to be an integrin binding domain-bearing hydrogel whereas unmodified alginates possess no cell-attachment motifs. It was hypothesised that HDF cells would attach within the collagen layer of the scaffold yet remain suspended and unattached within the alginate portion (**Figure 6.6A**). Cell-loaded collagen and alginate layers were successfully integrated (**Figure 6.6B**) and the hypothesis was accepted on the basis that elongated HDF cells were positively stained for actin within collagen, yet remained spherical and with little actin staining in alginate layers lacking RGD complexes which are critical for cell-matrix attachment (**Figure 6.6C**).

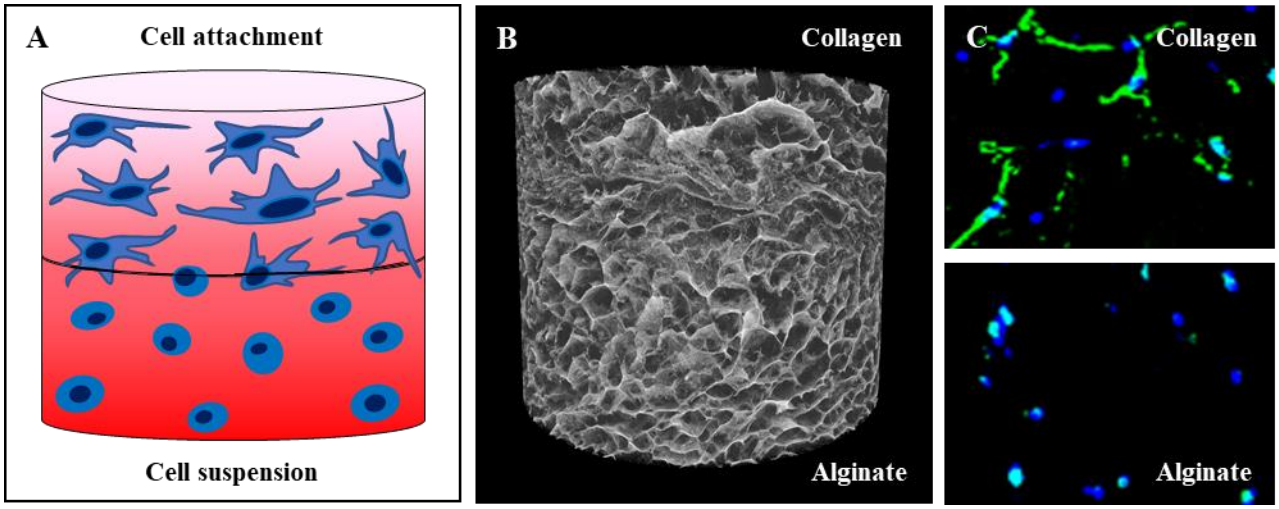

Figure 6.6 – Chemical and cellular gradients within multi-layer constructs by SLAM. A) Schematic of controlling cell behaviour with attachment motif bearing complexes in the upper collagen and no attachment motifs for cell suspension within a gel. B) Micro-CT showing gradient porosity within a lyophilized collagen-alginate scaffold. C) Confocal micrographs of Hoechst / actin cell staining of human dermal fibroblasts attached in the collagen layer (upper) and suspended in the alginate (lower) regions of a dual layer scaffold.

In extension, lyophilised dual layer gellan / collagen sponges were seeded with cells, post-production, as an alternative method of generating tissue engineering constructs (**Figure 6.7**).

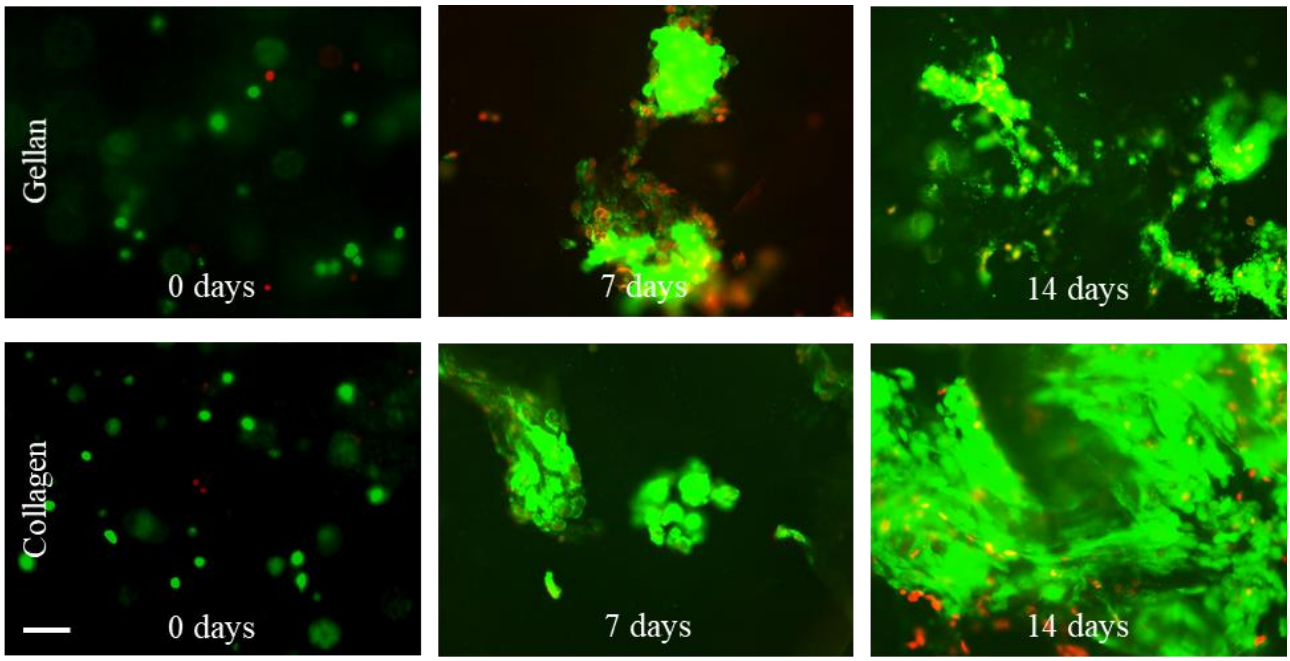

Figure 6.7 – Chemical and cellular gradients within multi-layer sponges by SLAM. Sponges containing gellan and collagen layers were seeded with MC3T3 cells and imaged at 0-, 7- and 14 days for cell viability of live (green – Calcein AM) and dead (red – PI) cells (scale bar = 50 µm).

6.3.6 Multi-directional printing of multi-layer constructs by SLAM

Even though embedded 3D bioprinting has been utilised to build complex, gradient-containing structures, some research within this field has remained limited regarding the build direction of tissue engineering parts, in turn, limiting optimal print-specificity. This is usually down to dragging and distortion of previously extruded material or the weight of each subsequent layer causing the printed model to flatten (McCormack et al., 2020). To challenge this issue, instead of printing stacked cylinders in the y direction, cuboids were interfaced in the z direction (**Figure 6.8A**). This was achieved by printing one cuboid at a time and placing the petri-dish accordingly between prints as the G-code is only capable of printing layer by layer from the bottom up and would require extruder alternation between each layer of both parts. Upon production and curing of a laterally printed doublet cuboid, the dyed portion of the structure was seen to blend with the un-dyed segment of gellan thus creating a visual gradient interface (**Figure 6.8B**). Multiple repeats were also demonstrated in laterally printed cuboid triplets without distortion of previously printed parts (**Figure 6.8C**).

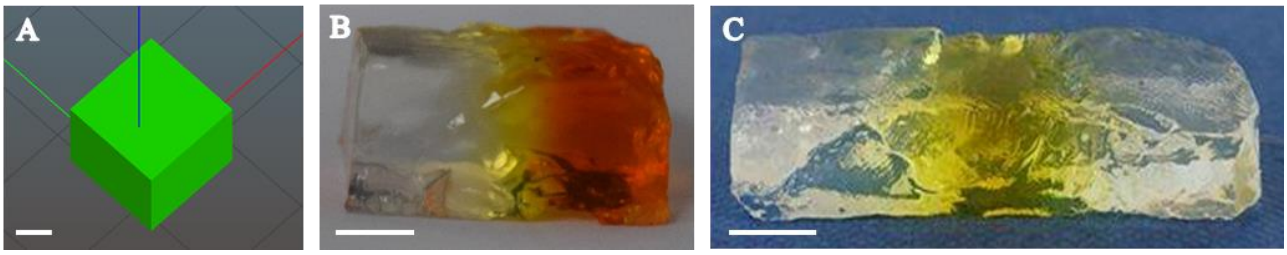

Figure 6.8 - Lateral printing of multi-layer constructs by SLAM. A) Stl file of a cuboid with dimensions 10.00 x 10.00 x 5.00 mm, B) doublet of a gellan cuboid interfaced with a dyed gellan cuboid and crosslinked to give a single, laterally printed construct and C) triplet of interfaced gellan / dyed gellan / gellan (scale bars = 5 mm).

6.3.7 Phase-encapsulated constructs by SLAM

One tissue engineering product in particular which has not yet been achieved by embedded biofabrication is creating phase-encapsulated constructs in the form of core-shell scaffolds. These apparatuses contain two discrete regions that are independent of function and are used in a plethora of applications. For instance, various cell types and therapeutic agents may be spatially allocated

between these separate compartments for the enhancement of cell fate and biomolecule release within tissue scaffolds (Perez & Kim, 2015). To push the boundaries of the SLAM method beyond omnidirectional printing, a collagen-core gellan-shell scaffold (**Figure 6.9A**) and a collagen-core alginate-shell scaffold (**Figure 6.9B**) were made by secretion of collagen biopolymer within a pre-extruded polysaccharide disc at different length scales. Despite gellan and alginate's ionotropic route of gelation and the alternative thermal gelation mechanism of collagen, the phase-encapsulated parts were successfully extruded, integrated and retrieved from the supporting gel bed. Using SEM, it was also established that the collagen and alginate within core-shell scaffolds were successfully interfaced (**Figure 6.9C**).

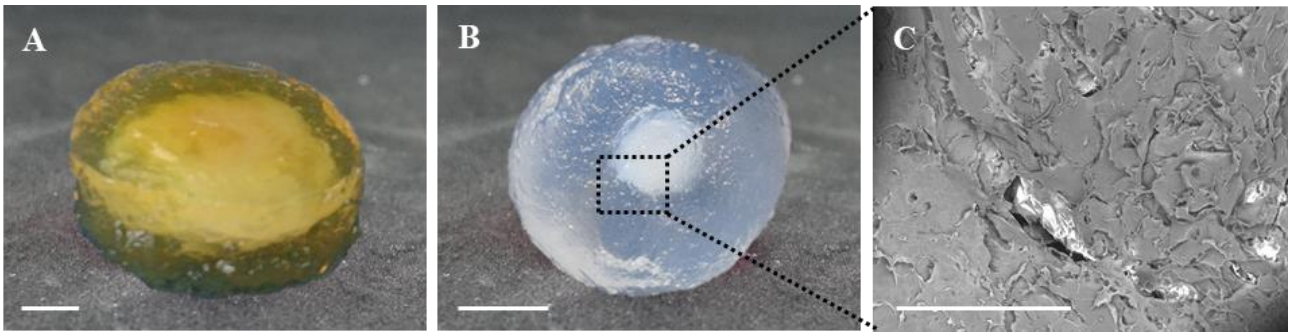

Figure 6.9 – Fabricating core-shell scaffolds by SLAM. A) collagen-core gellan-shell scaffold (20 mm diameter each) and B) collagen-core alginate-shell scaffold (5 mm and 10 mm diameters respectively) (scale bars = 5 mm). C) Scanning electron microscopy (SEM) of a cross-sectioned collagen-core alginate-shell scaffold (scale bar = 2 mm).

Not only does SLAM have potential in generating tissue engineering implants, SLAM could also be used as a tool to study drug-disease interactions. A collagen cylinder was printed as a basic representation of non-cancerous tissue following printing of an MDA-MB-231 breast cancer cell pellet in the centre (**Figure 6.10A**). When viewed under a confocal microscope after a 14-day culture period, the cell pellet remained isolated at the centre of the collagen scaffold (**Figure 6.10B**). In contrast, another construct was printed where MDA-MB-231 cells were homogeneously distributed throughout a collagen solution, 3D bioprinted, solidified and cultured for 14 days. Cells appeared globular when imaged in 3D (**Figure 6.10C**) and collagen fibrils were well defined (**Figure 6.10D**).

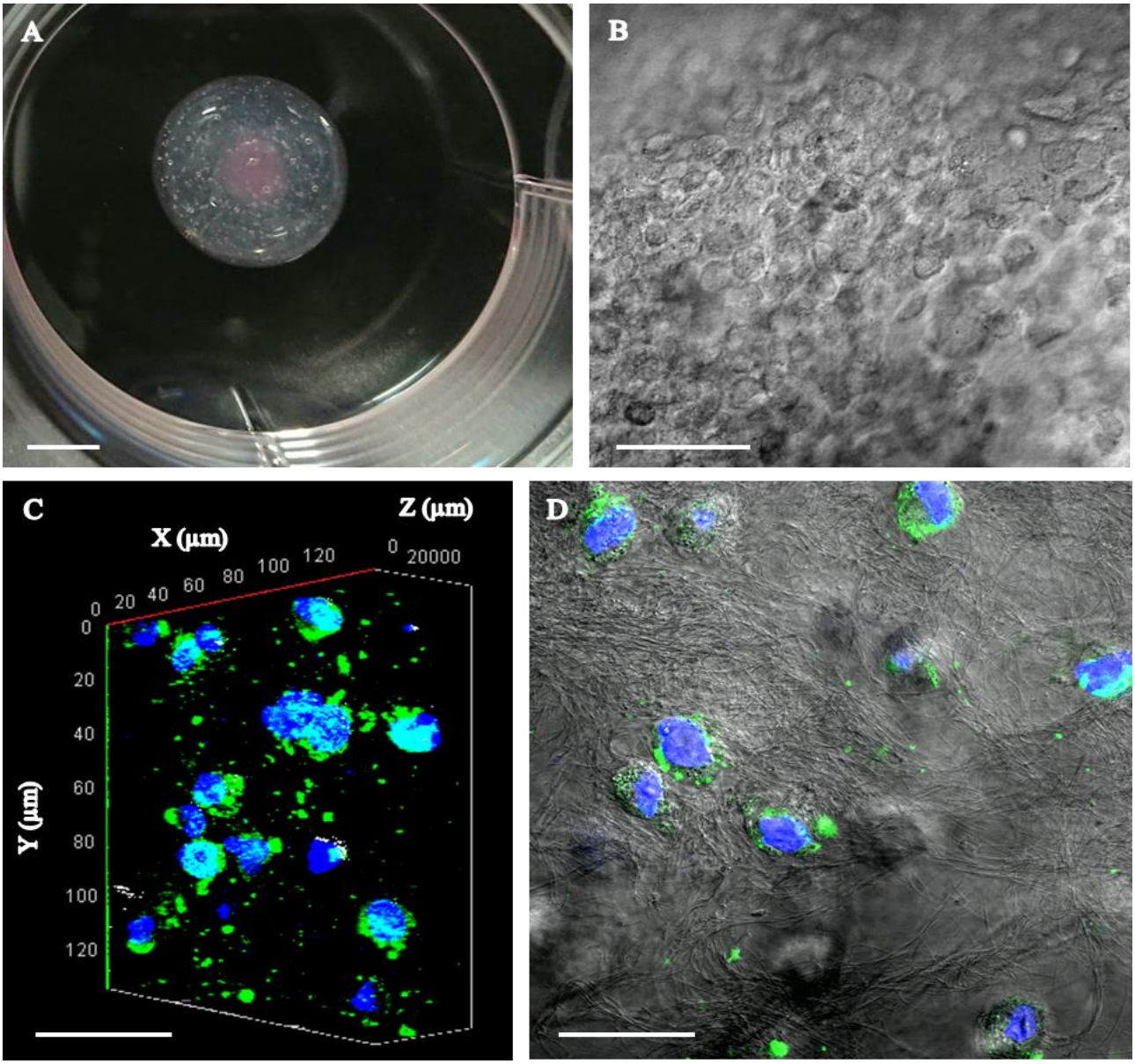

Figure 6.10 – Modelling the tumour microenvironment by SLAM. A) A basic tumour model of an MDA-MB-231 breast cancer cell pellet suspended within a collagen scaffold (scale bar = 5 mm). B) Confocal micrograph of cell pellet following 14-days culture. C) 3D Z-stack of homogeneously distributed breast cancer cells. D) 2D image of homogeneously distributed breast cancer cells within a collagen fibre-rich matrix (micrograph scale bars = 50 µm).

6.3.8 Multi-material blends in constructs by SLAM

Using hydrogels for soft tissue construction by SLAM has been proven as a reputable solution in integrating multiple layers. When studying native tissues, most tissues are not made exclusively of collagen or glycosaminoglycans and instead comprise multiple ECM components to form a complex network. To this end, the GAG-like polysaccharide hydrogel, pectin, was blended with collagen to

reimagine more complex ECM environments in the form of a carotid artery (**Figure 6.11A and B**). MC3T3 cells cultured within this matrix blend showed a high percentage of viability following printing at 0 days (**Figure 6.11C**), and after 7- and 14-days culture respectively (**Figures 6.11D and E**).

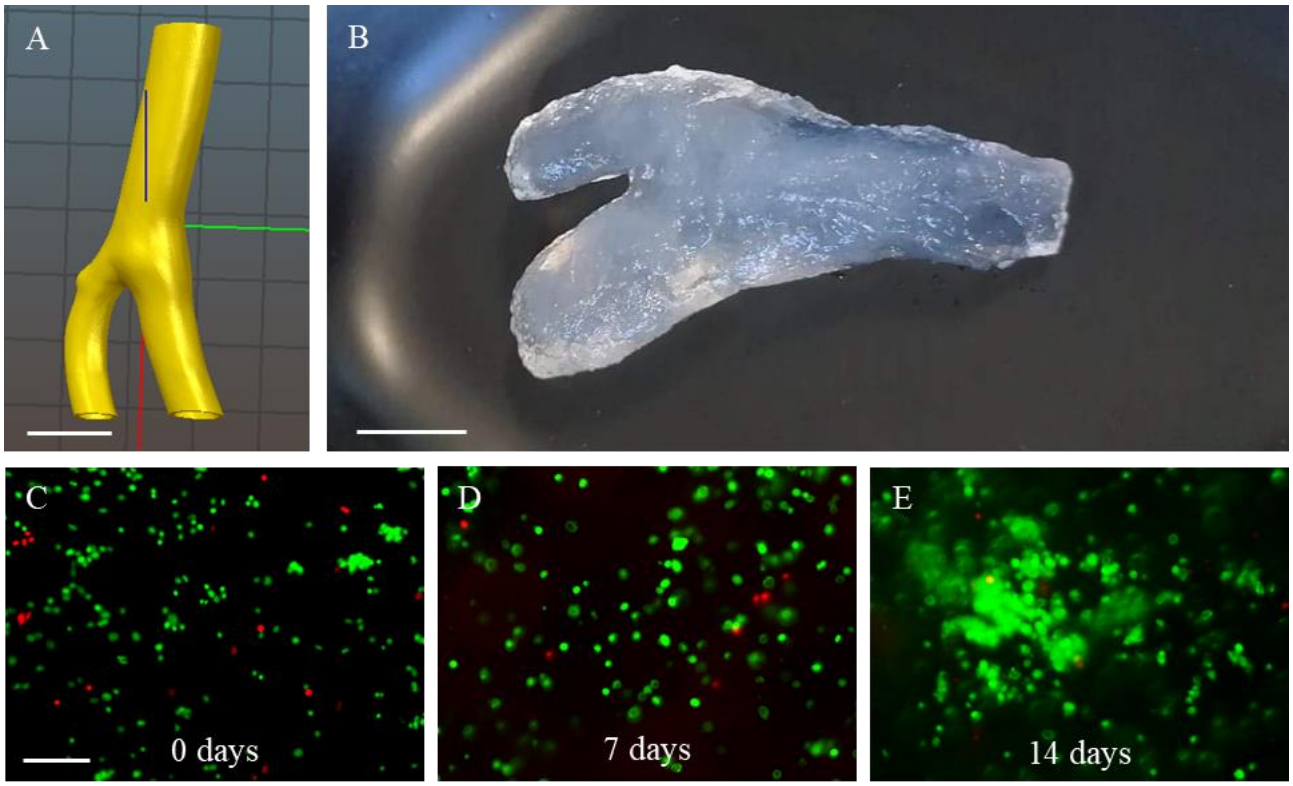

Figure 6.11 – 3D bioprinting multi-material blends in the form of a carotid artery by SLAM. A) Stl file of a carotid artery. B) 3D bioprinted carotid artery containing MC3T3 cells suspended within a pectin and collagen blend (scale bars = 5 mm). Fluorescence micrographs showing live cells stained with Calcein AM (green) and dead cells stained with PI (red) C) immediately after printing (0 days) and following D) 7 days and E) 14 days culture (scale bars = 50 µm).

6.4 Discussion

Tissues have a hierarchical structure with regional variations in ECM and mechanical stiffness that contribute to their function. For example, the musculoskeletal system is designed to efficiently transfer muscle-induced energy through the tendon and onto bone in order to perform movement (Merceron et al., 2015). This load must be seamlessly propagated throughout tissues in order to

prevent mechanical failure at distinct tissue interfaces. Hydrogels are often used as alternatives to extracellular matrices as they are highly manipulable in mimicking the salient elements of native ECM. Therefore, gradient engineering using biopolymer hydrogels is an attractive approach in emulating biological structures (Hartman et al., 2017).

Extrusion-based 3D bioprinters have been recruited in pursuit of manufacturing functional tissues, yet the promise of engineering patient-specific tissues directly within the clinic remains at distance. The main hurdles in the way of realising this potential are achieving biomimicry with good manufacturability (McCormack et al., 2020). Here, a novel method is presented using an agarose fluid gel suspension bath which avoids the many inherent flaws of printing onto a flat surface in air. These procedures have seen the generation of multi-layered constructs that require alternative gelation mechanisms. 3D composite scaffolds are much more representative of native tissue environments as they are designed to mimic the graduated mechanical and chemical constituents of which human tissues are comprised. These structures are thusly much more valuable in tissue transplantation and drug-disease modelling perspectives compared with 2D monolayer cell cultures (Merceron et al., 2015).

Gradient porosity is particularly important in specific cell migration during tissue regeneration. Porous surfaces also facilitate mechanical interlocking between the scaffold and site of implantation, thus enhancing mechanical stability. The porosity, for example, in cancellous (trabecular) bone can range from 50% - 90% yet porosity ranges from 5% - 10% in cortical bone and can alter in response to loading, disease, and aging (Di Luca et al., 2016). Collagen / gellan and collagen / alginate scaffolds exhibited porosities of 91.90% and 88.22% respectively (**Figure 6.2**). Porosity gradients within tissue scaffolds can therefore be intelligently designed in the creation of niche bio-mimicking structures using SLAM techniques.

The surface texture and integrity of the scaffold interface was further investigated by use of a profilometer. Colour representations of a composite alginate / ι-carrageenan scaffold confirmed that two materials with large differences in material structure are inter-joinable (**Figure 6.3**). The surface microroughness of alginate and ι-carrageenan were 60.22 µm and 16.45 µm respectively and had a roughness of 50.21 µm at the interface, which would likely induce alternative mechanisms for cell-biomaterial interplay as surface roughness has been seen to regulate cell response (Wu & Zhang, 2015). Cells are prone to adapting to surface roughness in order to equilibrate internal and external forces, where cells existing on rougher surfaces are bound and constrained by high ridges and low valleys as opposed to widespread cells on smoother substrata that have established strong actin networks. It is therefore possible to recreate biological environments that induce desired cell migration by patterning surface roughness by employment of appropriate biopolymers at tuned concentrations.

The variety of mechanical stimuli that cells experience includes hydrostatic pressure, shear, compression and tensile force and are generated locally within discrete tissues by cell–cell or cell-ECM interactions (Butcher et al., 2009). Therefore, the behaviour of cells is inherently tissue specific. The mechanical influence on cell behaviour has long been interpreted by measuring their shear modulus (G) or Young's modulus (E) as reported by rheological and dynamic mechanical analysis (Caliari & Burdick, 2016). In order to produce tissue scaffolds with corresponding elastic and mechanical milieus found in native tissue, the determination of hydrogel mechanical behaviour was assessed using shear rheology. Amplitude stress sweeps were conducted by exerting a range of shear stresses on each region of the multi-layer tissue scaffolds in order to measure their viscoelastic behaviour (**Figure 6.4**). The linear viscoelastic region (LVR) (and therefore the critical stress at which intermolecular associations are forced to collapse) reduced in a graduated manner from the gellan to the interface and was shortest in the ι-carrageenan region. Likewise, a gradient in LVR was exhibited from alginate, through the interface and shortest in the collagen layer. What is more, both of these

scaffolds showed a graduating reduction in elastic (G′) and viscous (G″) moduli throughout the interfaced materials. When comparing the storage modulus of the different layers within the gellan-ι-carrageenan scaffolds to corresponding tissue elasticities found in literature, the mechanical characteristics of the scaffolds can be likened to those of healthy breast tissue. Gellan, ι–Carrageenan and interfacial regions of the scaffold had storage moduli that equated to the mechanical properties found in pectoral muscle, subcutaneous fat and dense glandular tissue and within muscle-fat interfaces respectively (Butcher et al., 2009; Cox & Erler, 2011; Gefen & Dilmoney, 2007; McKnight et al., 2002; Sinkus et al., 2005). During pathogenesis and the development of cancerous tissues within the breast, tissue stiffness can increase as much as tenfold than that of healthy breast tissue (Kass et al., 2007). This newly developed SLAM system holds the potential to create healthy transplantable tissues that mimic transplant destinations *in vivo* and to recreate model drug-disease environments *in vitro* in a bid to combat degenerative diseases.

Oftentimes, when studying cell-drug interactions, cultures are propagated in 2D monolayer flasks. These techniques are limited to the cultivation of cells that exhibit a flattened shape, forced polarity and a therapeutic action that is limited to their ventral surfaces (Caliari & Burdick, 2016). The use of 3D printed hydrogels and freeze-dried scaffolds, however, provides cells with a platform that recapitulates native tissue ECM, allowing for more natural phenotypes to progress. In this chapter, cellular morphology has been manipulated by embedding cells within hydrogels containing divergent chemical constituents. Within a single scaffold, cells within an alginate layer assumed a globular morphology when cultured over 14 days due to the lack of cell attachment motifs (**Figure 6.6**). When cells were allocated to the collagen layer, extension in three dimensions along the collagen fibres via focal adhesions was exhibited. Cell viability was also sustained over the 14-day period in both phases (**Figure 6.7**). By taking advantage of these contrasting mechanisms for suspending and encapsulating cells, scaffold systems can be designed around the application of tissue transplantation. For instance, when it is necessary to implant a tissue scaffold with long term functionality, a controlled-degrading,

slow-release gel containing cell attachment motifs would be most appropriate (Henry et al., 2007). If rapid neotissue formation is essential, the use of hydrogels acting as cell carriers to the intended site may serve as a more relevant cell vehicle. Overall, degradation rate of the scaffold should match the rate of neotissue formation (Ma, 2004). It has been seen previously in various studies that cellular morphology can be influenced by scaffold material, substrate stiffness, gelation temperature and presence of degradable crosslinkers (Doyle et al., 2015; Huebsch et al., 2010; Ventre & Netti, 2016; Wade & Burdick, 2012).

Within the tissue engineering arena, augmentation of scaffold conformation ensues the optimum release kinetics of cells and therapeutic agents. The design and generation of each sophisticated structure is therefore unique due to scaffold-patient personalisation. This system presented here is not only compliant to the multitude of materials that may be exploited, but also in the way that the structures can be manipulated. In addition to printing multiple layers to create gradients in the z direction, constructs were also printed laterally (**Figure 6.8**), with encapsulated phases (core-shell scaffolds) (**Figure 6.9 – Figure 6.10**), and also as multi-material blends (**Figure 6.11**).

Core-shell scaffolds contain two discrete regions that are independent of function and are used in a plethora of applications. Various cell types and therapeutic agents may be spatially allocated between these separate compartments for the enhancement of cell fate and biomolecule release within tissue scaffolds (Perez & Kim, 2015). Core-shell scaffolds are usually fabricated using co-concentric nozzle extrusion, microfluidics generation, and chemical confinement reactions, and the method of using an embedding support to extrude phases within one-another to create core-shell scaffolds, in this instance, is the first to be reported. In a study with Perez et al., (2014) where a collagen-core alginate-shell cell delivery system was utilised for bone tissue engineering; a dual concentric nozzle was used. The inner collagen core was loaded with MSCs and was ensheathed in an alginate layer creating two clearly distinguished zones. During production, region thickness was controlled by tuning polymer concentration and injection speed, subsequently modulating the mechanical properties and

degradation profiles of the construct. Compared with collagen gel positive controls, MSCs housed in collagen-cores of core-shell scaffolds exhibited comparable proliferative activity yet showed directional elongation along the fibre axis in core-shells versus randomly elongated cells in collagen gels alone. Cells within core-shell constructs also migrated to the outer edge of the collagen core to where oxygen saturation was more abundant. When studying osteogenic differentiation of the MSCs, expression of bone related genes BSP, OPN and OCN were significantly higher in core-shell scaffolds in comparison to collagen gels alone. Finally, MSCs delivered through core-shell scaffolds showed great potential for regenerating bone tissue in a rat calvarium model.

To further define the system's capacity to generate tissue scaffolds not only designed for implantation, but also in 3D drug-disease and cosmetic modelling, the idea of fabricating basic tumour models using SLAM was formulated. Preliminary recapitulations of the envisaged tumour microenvironment contained a) an inner mass constituted of a breast cancer cell pellet representing the tumour portion of the model, and b) an outer, acellular stromal compartment constituted of a softer matrix to represent the surrounding healthy tissue (**Figure 6.10**). 3D tumour replicas are usually generated within a hydrogel suspension, using the hanging drop method, on low adhesion plates or micropatterned surfaces and more closely represent the 3D organisation of *in vivo* tumours compared to using cell culture plates and flasks (Costa et al., 2016). In turn, they have a greater capacity to mimic drug interactions within the human body more closely. MDA-MB-231 cells of mammary adenocarcinoma lineage were used to create a potential drug-disease model using SLAM as they are notoriously difficult to encourage spheroid formation. Cell pellets were cultured within a 3D collagen matrix and were compared with homogenously dispersed cells (**Figure 6.10**). Whilst cell pellets remained in the closely associated formation in which they were seeded, cell cultures appeared as compact aggregates rather than tumour spheroids. Alternatively, a liquid overlay technique using a cell-repellent surface and 3.5% Matrigel has been developed which successfully induced spheroid

formation in MDA-MB-231 cells (Froehlich et al., 2016), however potential remains in the SLAM method following further refinement.

The last of the studies on constructs containing regional variations in physicochemical properties were those on 3D bioprinting multi-material blends to create ECM-like scaffolds. Using multi-material blends compared with layering different materials is another way of structuring the ECM microenvironment, yet with consistently changing properties at the microscale level compared with a uni-directional gradient from one material to another. Polymer blending modifications are of great interest as they can lead to the development of a new range of biomaterials with a full set of desired properties (Doulabi et al., 2014). The main reason of blending is to widen the range of properties while obviating their drawbacks. Collagen pectin blends printed in the form of a carotid artery simulated the collagen and GAG-like material environments within native carotid artery (**Figure 6.11**). The collagen and pectin materials used within the blend have also been seen to exhibit good processability, printability, antibacterial activity, low toxicity, cell interaction, biocompatibility, water solubility, biodegradability, tuneable porosity and mechanical properties, pH stability and are easily crosslinked (Dong & Lv, 2016; Kulikouskaya et al., 2019). Although native carotid artery contains smooth muscle and endothelial cells, MC3T3 cells were used to confirm that cells remain viable throughout the printing of 3D constructs that contain material blends.

6.5 Conclusions

Gradients in porosity, surface texture, mechanical properties, material chemistry, cell morphology and cell distribution within a single 3D bioprinted construct have been demonstrated using the SLAM method. Different build conformations were manufactured by layering materials in multiple directions, by lyophilisation, with encapsulated phases and by blending multiple materials to achieve tissue-synonymous chemical and architectural variations. Indeed, examples of hydrogels at fixed concentrations have been presented, yet there is unlimited potential in achieving particular tissue-

synonymous gradients by modulating the materials to be incorporated and equally, their concentrations and gelation mechanisms. This technology outlined here has the potential to assist in overcoming the issues associated with donor waiting lists, immune rejection, and animal testing by producing tissue engineering constructs for implantation, drug-disease modelling, and cosmetics testing applications.

Chapter 7

DESIGN AND MANUFACTURE OF A TRI-LAYER SKIN MODEL

Aspects of this chapter are in preparation for submission to
Biophysics of Biofabrication

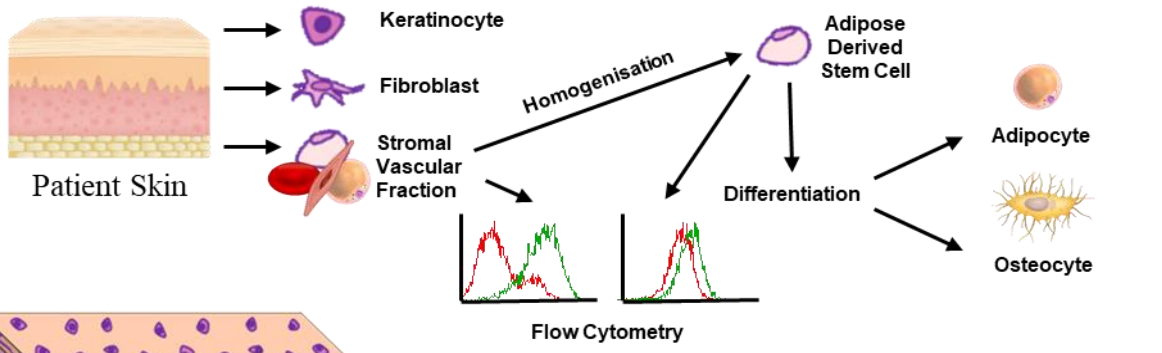

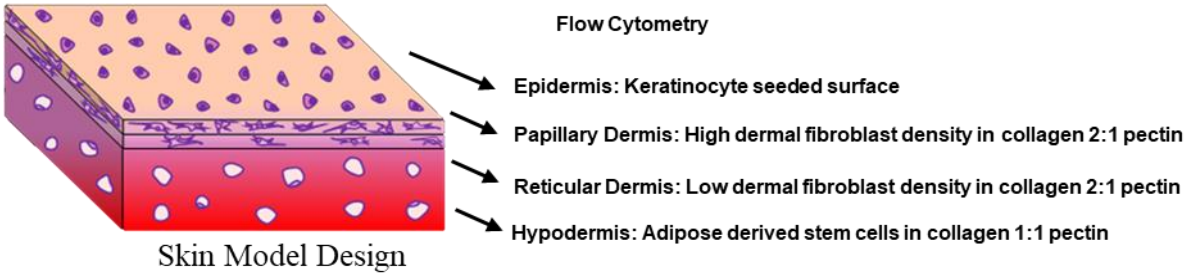

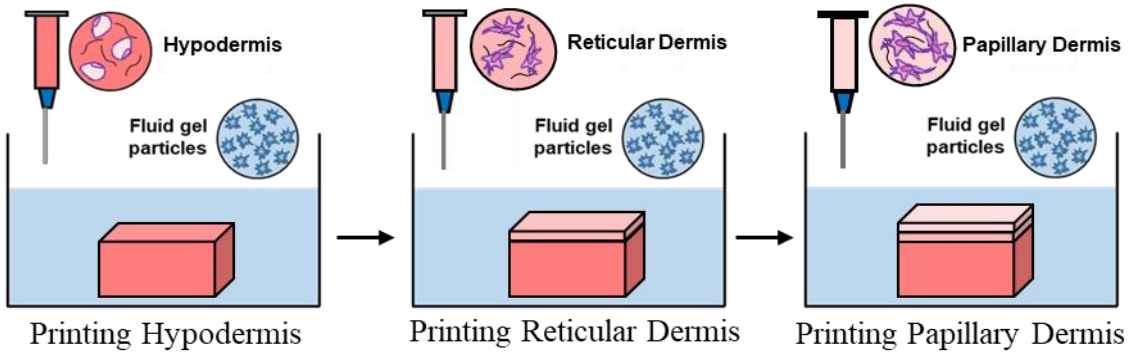

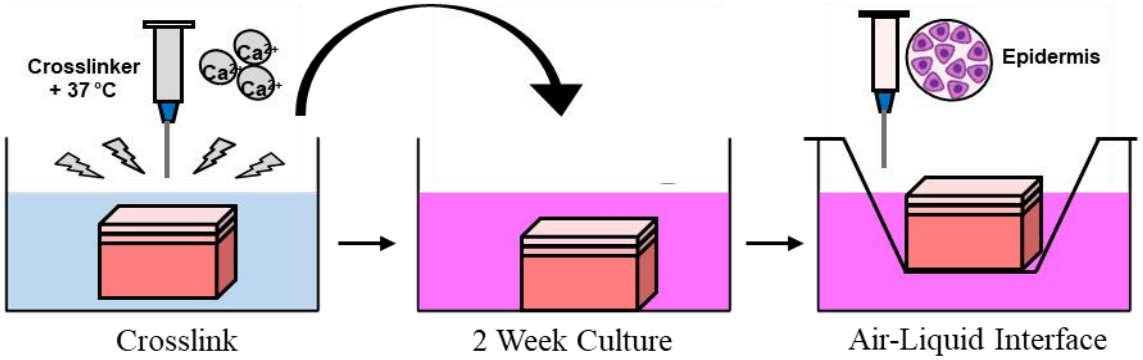

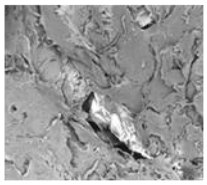
Microarchitecture Analysis

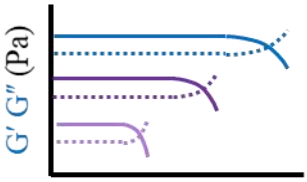

Mechanical Analysis

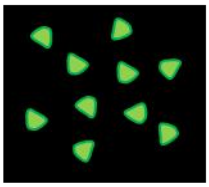
Cell Density Analysis

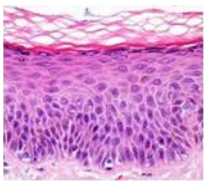
Histological Analysis

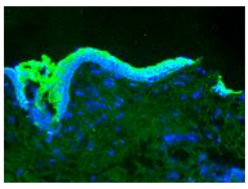
Immunohistochemical Analysis


Skin Model / Porcine Implant

Chapter 7 – Design and Manufacture of a Tri-layer Skin Model

Native human skin is comprised of numerous cell types and extracellular matrix (ECM) components which are organised into hierarchical layers. As the largest organ of the human body, it serves a range of different purposes, however, disease, trauma and infection of the skin can lead to compromised skin integrity and impaired function. A comprehensive understanding of normal skin tissue anatomy and physiology is therefore critical when attempting to restore damaged tissue and its roles. This chapter will focus on the complex architecture and mechanisms of the skin and how the acquisition of wounds may be established. Furthermore, the current clinical advances towards repairing damaged skin tissue shall be outlined and the design and manufacture of a tri-layer skin model will be investigated.

7.1 Introduction - Anatomy and Function of Human Skin

Covering the complete exterior of the human body, the skin and its cutaneous appendages constitute the integumentary system, defined by its ability to protect the body from external influences. Skin can vary in colour, thickness and elasticity depending on a number of factors such as genetics, lifestyle, age and body region. For instance, skin located at the eyelids, prepuce, and inguinal regions measure around 500 - 600 µm whereas skin in the upper back region is up to 5,000 µm (Y. Lee & Hwang, 2002). Skin may also be characterised as either hirsute (thin and hair bearing), which is distributed across the majority of the body's surface, or glabrous (thick and hairless), which is present on the palms and soles (Westgate, Botchkareva, & Tobin, 2013).

Skin exists as a compartmentalised yet graded complex structure containing two main layers that are intimately associated: the epidermis and its appendages and the dermis (**Figure 7.1**). Underlying these layers exists the hypodermis or subcutaneous layer and muscle layer, however it is disputed whether or not that the hypodermis should be classed as part of the skin (Tortora & Derrickson, 2014).

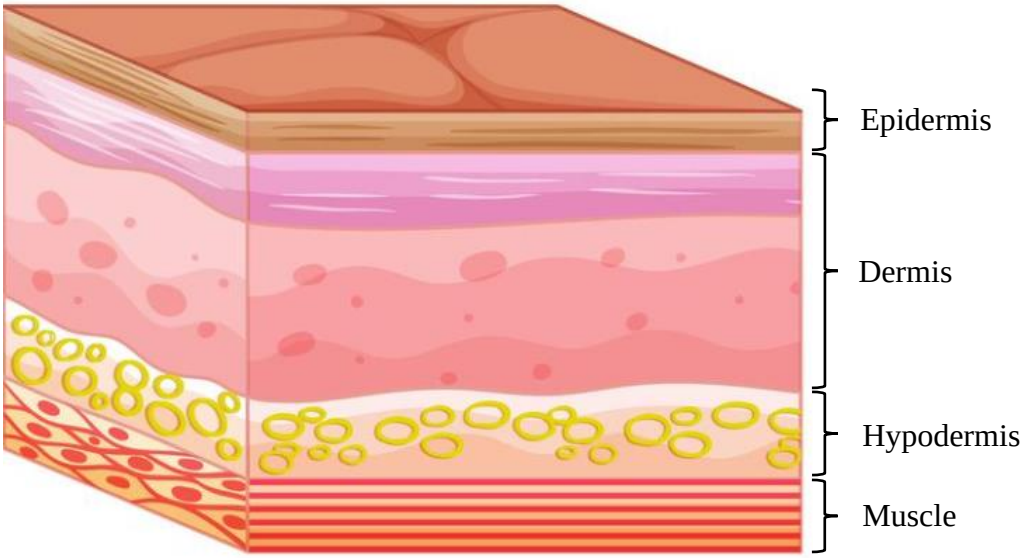

Figure 7.1 – Anatomy of the skin including epidermis and dermis and underlying hypodermis and muscle layers.

7.1.1 Cutaneous Appendages

The epidermis exhibits a range of accessories in the form of hairs, pores, ducts and nails that aid in the protection of the body's internal environment against potentially harmful external substances and artefacts. Hair shafts made of dead, keratinised epidermal cells that are connected together with extracellular proteins that protrude from the surface of the epidermis are anchored deep in the dermis or subcutaneous layer. Each hair follicle is connected to arrector pili muscles that, when contracted, causes the hair to stand on end (McLafferty, Hendry, & Farley, 2012). Some of these hair follicles have associations with sebaceous glands which secrete sebum - an oily substance containing triglycerides, cholesterol, proteins and organic salts – onto the surface of the skin. These secretions protect hair follicles from becoming dry and brittle, inhibit excessive evaporation of moisture from the skin and have also been seen to harbour antimicrobial and properties (Penzer, 2002). Overproduction of sebum as a result of sebaceous gland over-activity that is induced by hormones during puberty can result in open comedones (blackheads) or closed comedones (whiteheads). Eccrine and apocrine glands are amongst the other types of secretory apparatus within the skin. The purpose of these glands is to deliver sweat to the skin's surface during thermoregulation processes and for excretion of waste products including sodium, urea, ammonia and lactic acid (Tortora &

Derrickson, 2014). Another appendage of the skin's surface are the nails located at the end of each digit. They are made of tough keratin sheets and grow from the germinal layer at the nails root. The pink appearance at the nail's bed is causative of the extensive capillary network within the underlying layers of skin. They capacitate the protection of the finger ends during dextrous movements. The conservation of skin at the distal portion of the digits is further facilitated by the hyponychium – a thickened portion of epithelium where the nail plate and nail bed integrate (Penzer, 2002).

7.1.2 Epidermis

The outermost region of the skin is termed the epidermis and is primarily constituted of stratified keratinised squamous epithelium. The most prominent of cells in this layer are keratinocytes (90%) as well as populations of melanocytes, Langerhans and Merkel cells. The cell subtypes within the epidermal environment function as a barrier, in pigmentation, immune response and somatosensation. The epidermis is an avascular unit and is therefore reliant upon dermal vasculature for the provision of oxygen and nutrients (Abdo et al., 2020).

Multiple epidermal strata comprise the epidermis in which a base layer of mitotic cells migrate upwards whilst differentiating to constantly replace and replenish keratinocytes at the surface. Keratinocytes are typically replaced between 45 to 75 days, dependent on epidermal thickness and age amongst other internal and external factors. Disease status of the skin is also a contributing factor to keratinocyte turnover rate where in psoriasis, the rate can be as little as 3 to 7 days and subsequently, keratinocytes cannot fully differentiate before reaching the surface (Rajguru et al., 2020). The bottom-most layer of the epidermis is the stratum basale which is highly abundant in keratinocyte-producing stem cells. Moving up the epidermal layers are the stratum spinosum, stratum granulosum, stratum lucidum and finally, the stratum corneum (the most superficial portion of the epidermis) (**Figure 7.2**) (**Table 7.1**) (Yousef & Sharma, 2018).

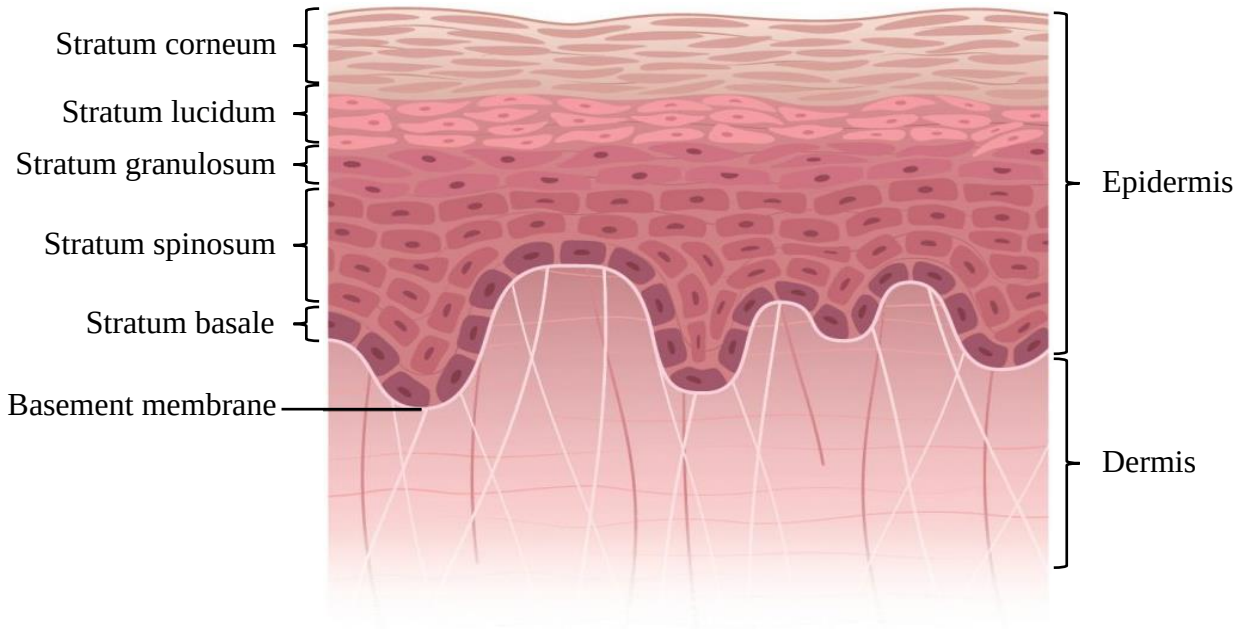

Figure 7.2 – Anatomy of the epidermis containing stratum corneum, lucidum, granulosum, spinosum and basale including underlying basement membrane and dermis layers (adapted from Lawton, 2019).

Table 7.1 – Epidermal strata within the epidermis and their general features.

Epidermal strata	Features
Stratum basale	The bottom-most epidermal layer separated from the dermis by the basal lamina within the basement membrane. Predominantly comprised of epidermal stem cells and keratinocytes as well as melanocytes and Langerhans cells. Exists as a single layer of columnar, cuboidal cells.
Stratum spinosum	8 – 10 layers of mature polyhedral cells, also known as the prickle cell layer due to cytoplasmic processes or spines which interlock with one-another supporting this binding layer.
Stratum granulosum	3 – 5 cell layers composed of diamond-shaped cells containing keratohyalin crystals which initiate keratinisation (the dying process of cells) and lamellar granules which contain glycolipids that function as a cell glue.
Stratum lucidum	2 – 3 cell layers found only in glabrous skin made of flat translucent dead cells and eleidin protein (transitional substance between keratohyalin in stratum granulosum to soft keratin in the stratum corneum).
Stratum corneum	20 – 30 cell layers that form the outermost cornified layer and is made of keratin embedded in filaggrin and dead keratinocytes. Cells are anucleate and squamous and form horny scales.

7.1.3 Basement Membrane – Basal Lamina and Reticular Lamina

The basement membrane of the epidermis is made of two different layers: the basal lamina comprises the upper portion and is attached to the stratum basale, and the reticular lamina interfaces the dermal connective tissue. Epithelial cells within the epidermis require a connection to the dermis through the basement membrane so that cells can be appropriately supplied with necessary growth and proliferation mediators.

7.1.3.1 Basal lamina – lamina lucida and lamina densa

The basal lamina is further split into two separate regions, namely the lamina lucida which exists on the periphery of the stratum basale, and the lamina densa which is located adjacent to the reticular lamina. The lamina lucida is filamentous and granular in appearance attributed to the heparan sulphate, proteoglycan and laminin macromolecules which reside within this layer. The lamina densa houses a network of type IV collagen, fibronectin and various other proteoglycans. Overall, the basement membrane controls the passage of certain macromolecules from the dermis to the epidermis, helps regulate keratinocyte differentiation and mechanically stabilises the epidermis (Standring, 2016).

7.1.4 Dermis – Papillary Dermis and Reticular Dermis

Dermis connective tissue is much more abundant in extracellular matrix, lying beneath the epidermal epithelial tissue and constituting the main bulk of skin. Studded throughout the dermis ECM are mainly fibroblast cells along with fewer endothelial cells, smooth muscle cells and mast cells. The network of interlacing connective tissue is made up of collagen and some elastin and features important structures such as blood vessels, lymphatics, sweat glands and nerves. The dermis provides a durable base that can absorb mechanical forces to prevent shear, functioned by glycosaminoglycan and proteoglycan molecules which allow a high water-binding capacity such as hyaluronic acid (Abdo et al., 2020). The anatomy of the dermis can be further

sub-sectioned into two parts: the papillary layer being the most superficial layer beneath the epidermis, and the deeper reticular layer.

The papillary layer is classed as a loosely packed connective tissue ascribed by the sparse bundles of collagenous fibres it contains. This layer exhibits small structures called papillae which interdigitate with recesses (or rete ridges) within the epidermis, providing anchorage in the form of a dermo-epidermal junction. Double rows of papillae protuberances within glabrous skin are responsible for each individual fingerprint. The role of this layer is to provide mechanical anchorage, metabolic support and trophic maintenance to the epidermal tissue overhead and accommodates a complex network of blood vessels and sensory nerve endings (Hicklin, 2014).

In contrast to the papillary layer, the underlying reticular layer within the dermis is manifested as a dense connective tissue, containing more closely packed elastic fibres and thicker collagen bundles which run parallel to the skin's surface. This feature provides skin with most of its strength, elasticity and flexibility. In addition, this layer is less abundant in dermal fibroblasts compared with the papillary layer (Falanga et al., 2013).

7.1.5 Hypodermis

The hypodermis (also known as the subcutis or subcutaneous tissue) is placed between the dermis and an apparatus called the fascia, which acts as a stabiliser and separator from muscles and internal organs. This specialised loose connective tissue supports cells called adipocytes organised in lobules and, like the other layers of skin, varies in thickness depending on body region as well as individual body habitus. It plays a role in acting as a gliding plane, thus protecting internal components of the body from acute and chronic trauma, as well as storing fat, contributing to temperature control and secreting various hormones and cytokines (Diegel et al., 2018; Valle & Zamorani, 2007). Mesenchymal stem cells (MSCs) within this layer have a remarkable influence on skin microenvironment as a whole, coordinating keratinocyte and fibroblast proliferation, regulating

angiogenesis and contributing to inflammatory response. These mechanisms ensure normal skin tissue homeostasis, regeneration and wound healing, and for this reason, have very recently been thrust into the limelight as crucial components in wound repair and therapeutics (Gaur et al., 2017). The hypodermis also features deeper adnexal structures (such as hair follicles), pressure sensors (Ruffini and Pacinian corpuscles) and a subdermal plexus of blood vessels that orchestrate thermoregulation and blood flow (Findlay & Gurtner, 2017).

7.1.6 Physiological Functions of the Skin

In its most basic description, skin (or the integument) is an organ which covers almost the entire human body and acts as a large biological shield. In fact, skin has an extensive number of roles as well as protection from the environment, including immunologic, endocrine, metabolic and even psycho-social considerations in its biologic enterprise. The part skin plays in protection from the environment is perhaps its most critical function for survival. For the body to act accordingly to external stimuli either through somatic or autonomic movement, however, the role of the skin in sensory reception is paramount (Chuong et al., 2002) (**Figure 7.3**).

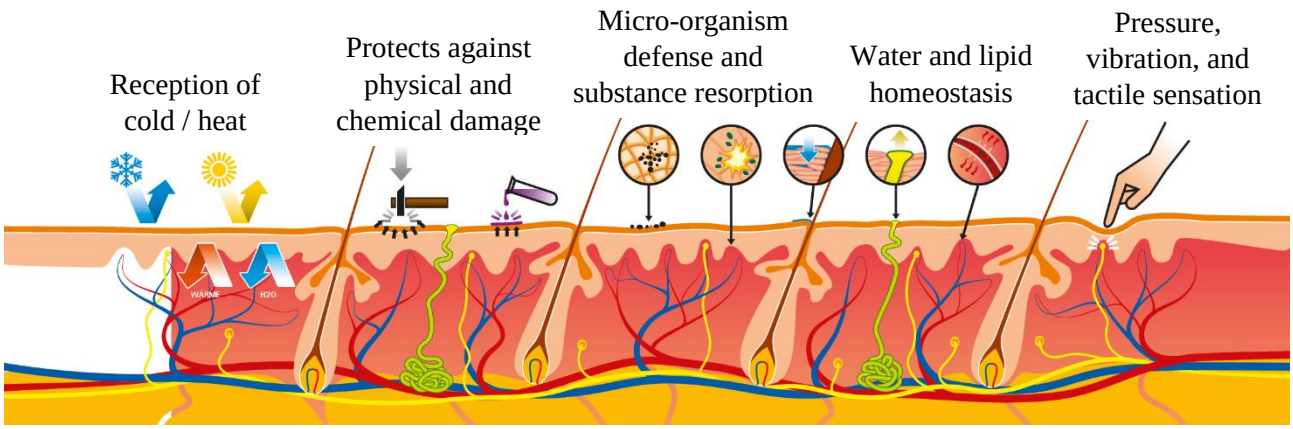

Figure 7.3 – Summary of the physiological functions of the skin – sensory, protection, regulation and synthesis (adapted from B. Braun Ltd., 2020).

7.1.6.1 Sensory reception

Skin is embellished with a series of receptors for the detection of touch, pressure, temperature and pain. Mechanoreceptors called Merkel cells within the stratum basale are responsible for sensing low frequency vibrations, whereas deep pressure and vibration is sensed and transduced by lamellated Pacinian corpuscles found deeper within the dermis or hypodermis. These lamellated corpuscles, or neurons with encapsulated nerve endings, also respond to touch stimuli via Meissner corpuscles and to hair movement at the surface of the skin by the hair follicle plexus. The nociceptors (pain receptors) and thermoreceptors (temperature receptors), in contrast, have free nerve endings. Stretch receptors named Ruffini corpuscles (or bulbous corpuscles) are responsible for identifying stretching of the skin (Betts et al., 2013).

7.1.6.2 Protection from the environment

Covering the entire of the human body, the skin's most critical function is to protect the rest of the body from the natural elements as well as foreign, harmful substances and microorganisms. The epidermis is the region within skin that is most predominantly associated with protection and defence as it comprises the outermost portion that most frequently comes into contact with the environment. Keratin and glycolipids within the waxy stratum corneum prevent water loss and also acts as the first line of defence against skin abrasion and harmful chemicals. Additionally, Langerhans cells are most prominent within the stratum spinosum and play a crucial part in cellular defence - whereas melanocytes within the stratum basale aid in the protection of skin against burning from UV sunlight radiation (Betts et al., 2013).

7.1.6.3 Regulation and homeostasis

Because skin harbours multiple roles, these functions are often manifold in their purpose, in that while skin-water balance can be seen as a protection mechanism, it can also be viewed as a water homeostasis mechanism by using aquaporins. Likewise, once changes in temperature are perceived

by the skin during sensory reception, the skin and its cutaneous appendages act accordingly to such stimuli through temperature homeostasis. This phenomenon is governed by the rate in temperature change as opposed to the change in temperature itself. When the temperature reduction rate is sufficient, the arrector pili muscles contract causing the hairs to stand on end and subsequently trap warm air at the surface of hirsute skin. When temperature increases at a sufficient rate, hair follicles relax allowing body heat to escape. Another process in which skin regulates body temperature is via vasoconstriction and vasodilation mechanisms. When the rate of cooling exceeds threshold, arterioles constrict to minimise heat loss and to concentrate body heat towards vital organs. The opposite occurs when the rate of temperature increase triggers dilation of arterioles and subsequent escape of heat to cool down the body. The sweat and sebaceous glands which are allocated to the dermis and hypodermis are responsible for the secretion of sweat and sebum. Approximately 0.5 L of sweat is unnoticeably secreted per day and can increase to as much as 1.5 L per hour for an active person, where heat is dissipated with evaporation of sweat from the skin's surface. Furthermore, the pores that allow perspiration also allow the excretion of urea and nitrogen waste products (Betts et al., 2013; Carola et al., 1990).

7.1.6.4 Synthesis

The epidermal layer of human skin screens out most of the earth's UV radiation with the exception of small quantities required for vitamin D synthesis. When sunlight is present, cholecalciferol (vitamin D_3) is synthesised from dehydrocholesterol and is further converted to calcidiol and calcitriol (active form) by the liver and kidneys, respectively. Vitamin D is vital for normal absorption of calcium and phosphorus in bone maintenance, and lack of such can lead to serious complications such as rickets and osteomalacia (Betts et al., 2013; Carola et al., 1990).

7.1.7 Clinical Demand for Skin Replacements

Under normal circumstances, the skin has a regenerative capacity in response to injury or impairment. In the case of partial-thickness and acute healing wounds, skin will assume its usual wound healing cascade, however, when wounds are infected, deep, chronic, and non-healing, medical intervention is pertinent. These types of wounds can arise from trauma, congenital defects or pathogenesis, or via the emergence of chronic wounds as a result of non-healing (Dhasmana et al., 2018).

7.1.7.1 Trauma of the skin

Trauma of the skin can occur in the form of contusion, hematoma, abrasion, blisters, burns, puncture, incision, laceration or avulsion and in severe cases can lead to significant skin loss (**Figure 7.4**).

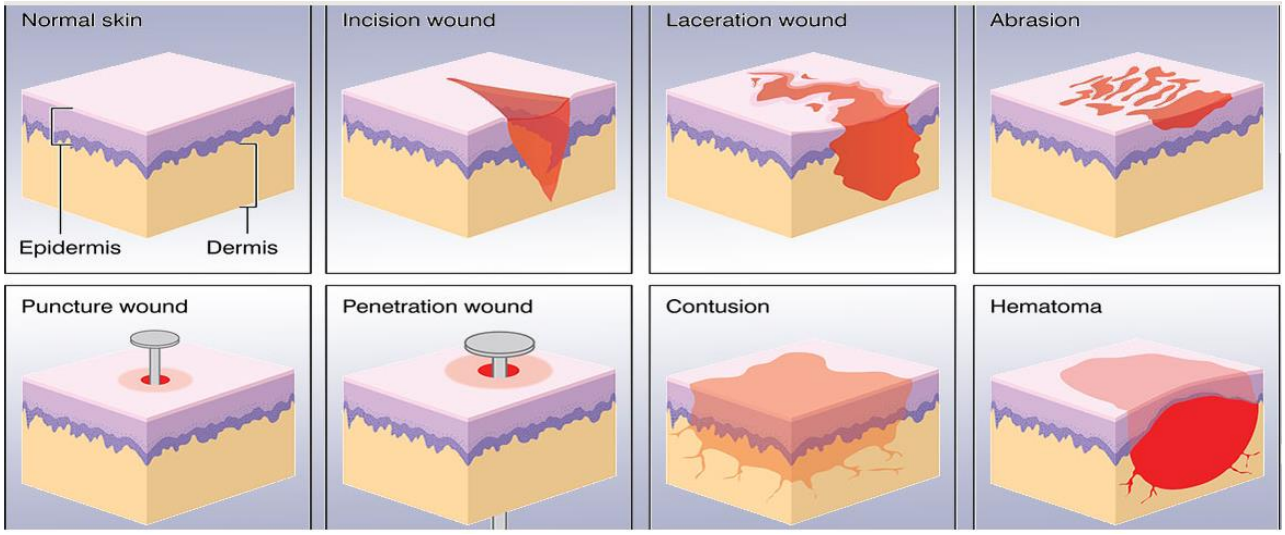

Figure 7.4 – Examples of different types of wounds resultant of trauma (adapted from Biodermis, 2018).

The most prevalent of these cases are burns due to thermal compromise of the skin and can occur at varying degrees; namely first-degree (superficial), second-degree (partial thickness) and third-degree (full thickness) burns. First and second-degree burns are defined where only the epidermis or both epidermis and partial dermis, respectively, are affected and may be able to heal naturally, although most cases will cause scarring. In third-degree burns, not only are the epidermis and dermis damaged, but trauma can also extend down to the hypodermis, muscle, bone and tendon. In cases such as these, medical intervention in the form of a graft is necessitated as missing tissue, lack of vasculature and

necrotic cells residing at the wound's outer edge render the natural wound healing process defective (Stone et al., 2018).

7.1.7.2 Pathogenesis and congenital diseases of the skin

Pathogenesis and disease due to congenital disorders within skin can compromise its ability to undergo usual function and repair. A common example of how skin can require replacement due to pathogenesis is following the establishment of skin cancer. Non-melanoma skin cancers include basal cell skin cancer (BCC) and squamous cell skin cancer (SCC) and usually occur on areas of skin that are often sun-exposed (**Figure 7.5**). Other, rarer types include Merkel cell carcinoma, Kaposi's sarcoma, T cell lymphoma and sebaceous gland cancer. Melanoma, on the other hand, tend to develop from melanocytes within moles on the surface of the skin (Apalla et al., 2017).

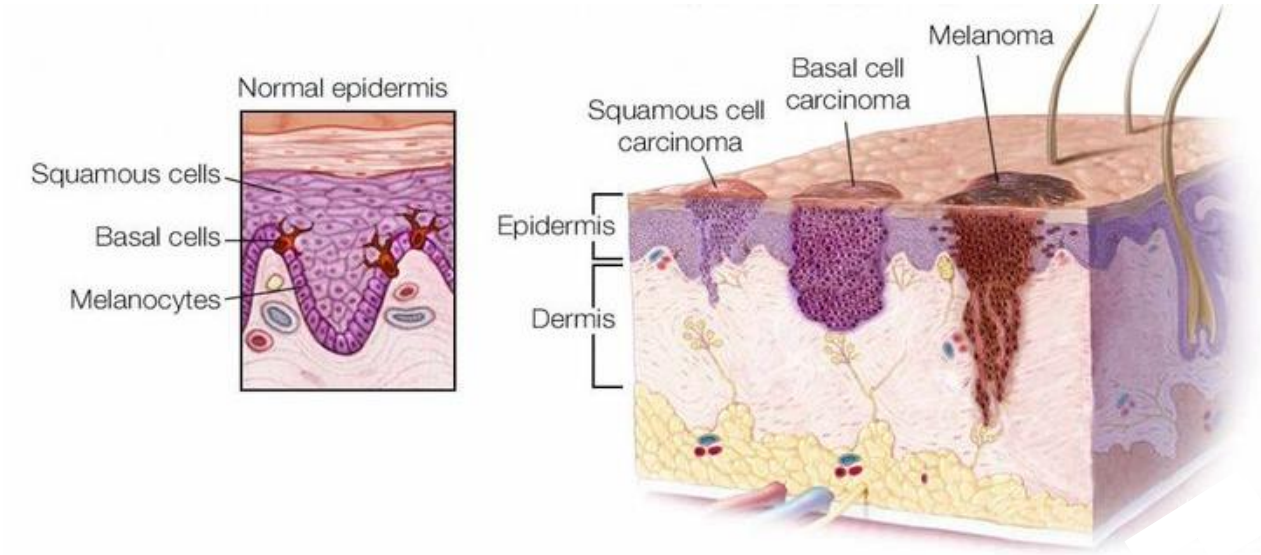

Figure 7.5 – Non-melanoma (SCC and BCC) and melanoma skin cancers (adapted from Mayo Clinic, 2020).

Inherited epidermolysis bullosa describes a group of genetically transmitted skin diseases in which spontaneous blistering can occur within the skin. Epidermolysis bullosa simplex (EBS) is characterised by intraepidermal blistering due to mutations in K5 and K14 genes. These genes within keratinocyte cells, under usual circumstances, are responsible for keratin type I and II production, yet cause intraepidermal cleavage when EBS is observed. Junctional epidermolysis bullosa (JEB) causes separation of the lamina lucida in the dermo-epidermal junction and is often due to mutations in

LAMB3 gene encoding laminin-5. The third and final subtype of epidermolysis bullosa is categorised as Dystrophic (DEB) where mutations occur in the type VII collagen-encoding gene, compromising the anchoring fibrils in the sub-basal lamina and resulting in separation (Boeira et al., 2013) (**Figure 7.6**).

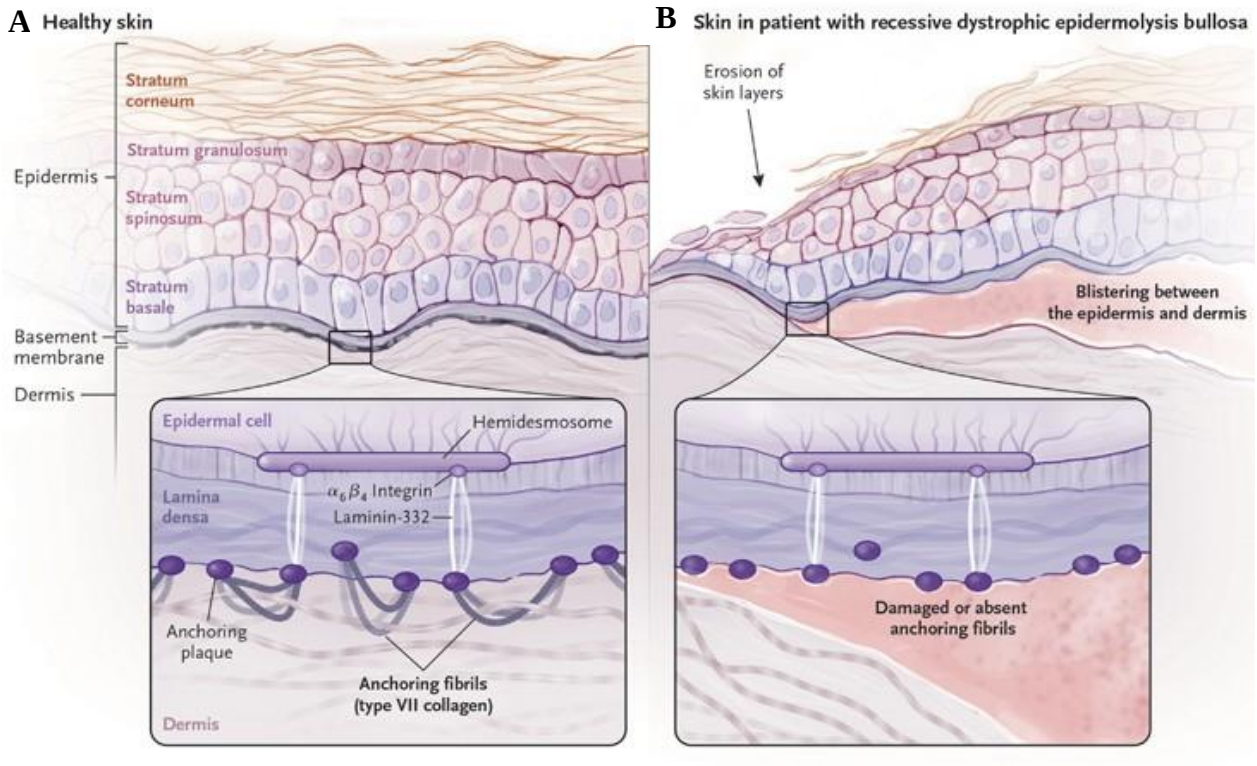

Figure 7.6 – Illustration of the differences between A) healthy skin and B) recessive dystrophic epidermolysis bullosa (adapted from Vanden Oever et al., 2018.

7.1.8 Wound Healing Cascade

The wound healing process is a complex milieu of regulated pathways in reaction to tissue injury. Human foetal skin is capable of regenerating skin without issue, however, adult skin repairs by forming scar tissue. It is understood that the four main orchestrated events of wound healing are haemostasis, inflammation, proliferation and remodelling (**Figure 7.7**) (**Table 7.2**).

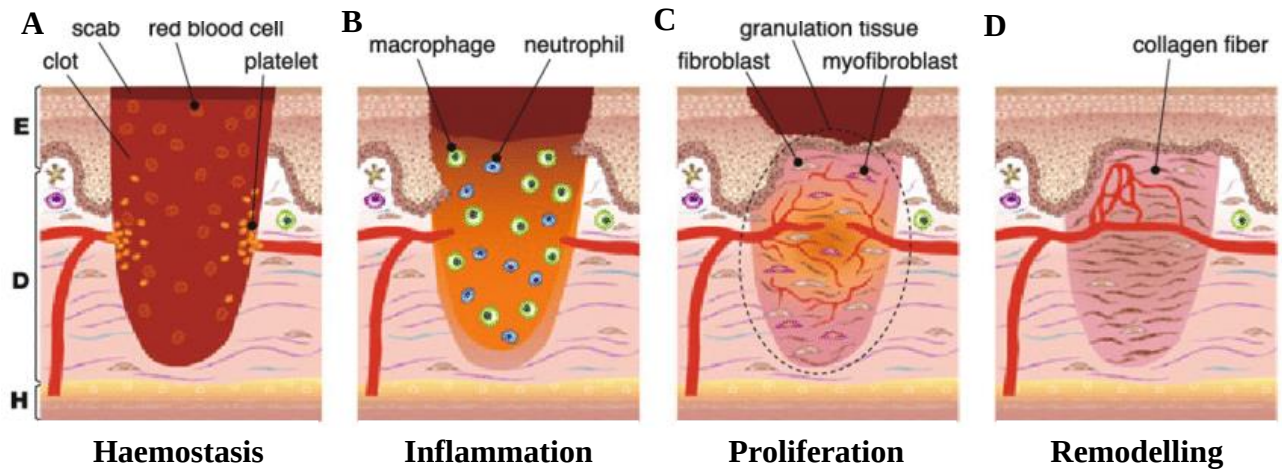

Figure 7.7 – Stages during the normal wound healing cascade (adapted from Kawasumi et al., 2013).

Table 7.2 – Wound healing stages and their general features.

Stage	Features
Haemostasis (minutes / hours)	At the onset of injury, fibrinogen leached from severed blood vessels is cleaved by thrombin to form a fibrin mesh for blood clot formation. The fibrin mesh captures platelets which enables attachment to the capillary walls. Coagulation factors are then upregulated, forming a clot consisting of platelets, red blood cells and ECM matrix molecules which causes the rapid release of various growth factors and chemokines, including platelet-derived growth factor (PDGF), vascular endothelial growth factor (VEGF), and transforming growth factor beta (TGF-β) which are crucial in later stages.
Inflammation (hours / days)	The inflammatory phase constitutes the invasion of white blood cells called phagocytic neutrophils and macrophages to the wounded site. Foreign particles, bacteria and necrotic cell components are phagocytosed, and fibroblasts are recruited to the wound site.
Proliferation (days / weeks)	When stimulated by VEGF and TGF-β, endothelial cells release matrix metalloproteinases (MMPs) that digest the basement membrane and liberate endothelial cells from parent vessels, initiating angiogenesis from pre-existing vasculature. Newly formed capillary sprouts enter the collagenous network and form highly vascularised granulation tissue. Fibroblasts proliferate and differentiate into myofibroblasts which subsequently cause wound contraction and closure, while keratinocytes migrate over the wound surface during reepithelialisation.
Remodelling (weeks / months)	Granulation tissue transitions into a relatively acellular collagen-rich scar and blood vessel density starts to reduce to previous abundancies.

7.1.8.1 Chronic wounds

Chronic wounds are pathological extremes of abnormal healing processes and present themselves in the form of diabetic foot ulcers, venous leg ulcers, pressure ulcers and arterial insufficiency ulcers and can therefore be classified as having a combination of disease and trauma elements. Although they do not usually cover an extensive area of skin, they are a major healthcare problem, associated with poor prognosis, having excessive and prolonged inflammation, lack of re-epithelialisation and are absent of sufficient vasculature. In turn, a strict regime of wound care is vital for treatment and infection control, including debridement of dead tissue, slough, biofilm, debris and exudate from the wound bed, administration of therapeutic agents and antimicrobials and compression bandaging of the wound (Frykberg & Banks, 2015). In more severe cases, treatment is focused on addressing the cause rather than treating the wound, where complete excision of the affected area is performed and grafting of partial-thickness, full-thickness or artificial skin is used to address time-consuming nursing care, cost-effectiveness and psychological distresses associated with the prolonged treatment of chronic wounds (Snyder et al., 2012). Chronic wounds are associated with impaired ECM synthesis, fibroblast migration and angiogenesis, delayed epithelialisation, prolonged inflammation, poor mobilisation of progenitor cells, increase in MMPs and infection and decreased levels of VEGF, TGF-β, EGF and FGF (Turner & Badylak, 2015) (**Figure 7.8**).

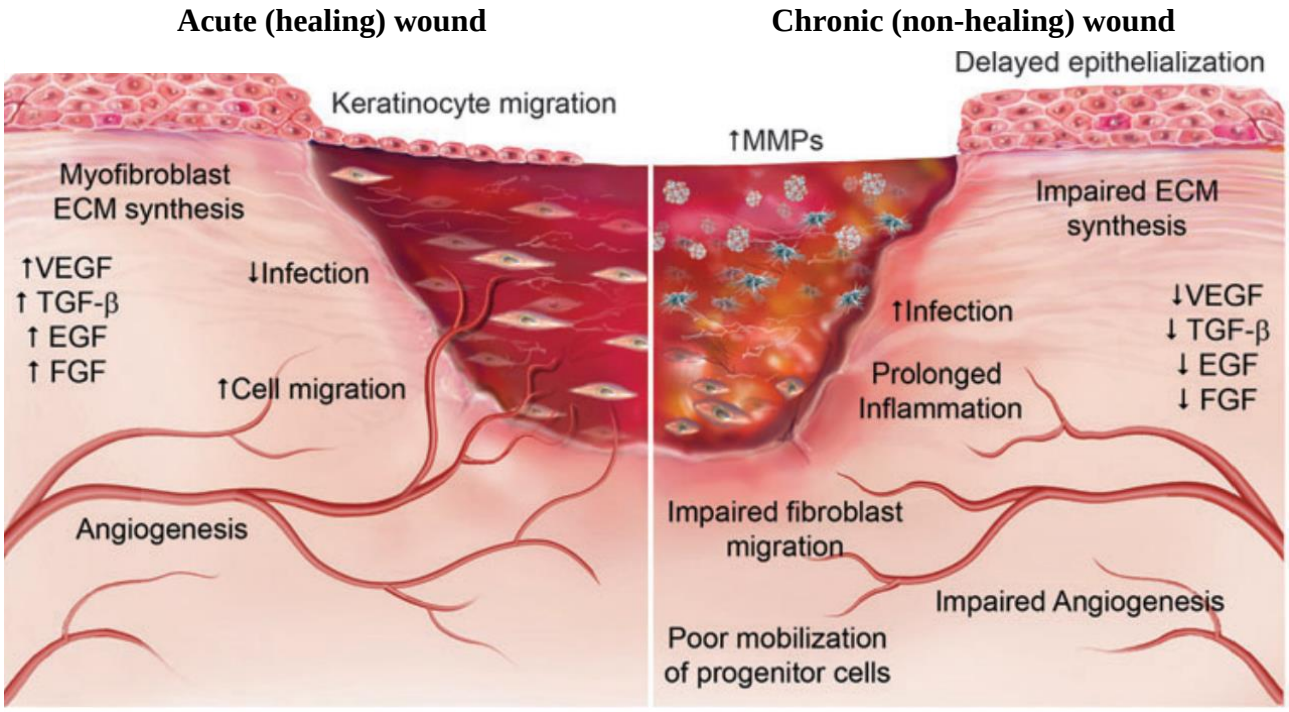

Figure 7.8 – Key differences between acute (healing) and chronic (non-healing) wounds (adapted from Turner & Badylak, 2015).

7.1.9 Advances in Skin Repair

The current treatment for dermal wounds is very much dependent upon the nature of the wound itself. For non-healing wounds that are greater than 4 cm^2, either implanting a split-thickness autograft (typically harvesting skin from the patient's thigh or buttock) or implementing tissue flap surgery (whereby skin adjacent to the wound is lifted and placed over the wound) is routinely practiced. Within recent years, however, a greater understanding of the wound healing process has allowed for the development of alternative therapies that use hydrogels, foam hydrocolloids, and skin substitutes incorporating live cells (Vig et al., 2017).

Current skin substitutes that are commercially available on today's market vary on permanency (permanent, semi-permanent and temporary), anatomical structure (epidermal, dermal, and dermo-epidermal), composition (cellular / acellular) and type of material (biological / synthetic). The

biological nature of the skin substitute is also crucial, in that autologous cells and tissues tend to be more successful compared with substitutes from allogenic or xenogenic sources.

Acellular skin substitutes became available in later 1970s and were commonly used for superficial and partial-thickness wounds. The use of human acellular dermis such as Alloderm® has been documented in donor sites and epidermolysis bullosa wounds (Özkaya et al., 2016; Sinha et al., 2002) (**Figure 7.9Ai**). Biobrane® is another acellular skin substitute which, instead, incorporates an overlying silicone epidermis atop a nylon mesh / collagen dermis and has been used to dress split-thickness skin grafts in paediatric burns (Farroha et al., 2013) (**Figure 7.9Aii**).

In other skin replacement therapies, substitutes are delivered as a keratinocyte cell suspension, allowing the complete coverage of contoured wound voids (Magnusson et al., 2007) (**Figure 7.9Bi**). Epicel™ also utilises autologous keratinocytes but are delivered on top of a petrolatum gauze support and is detached approximately 7 days after grafting onto patients with extensive, full thickness-burns (Carsin et al., 2000) (**Figure 7.9Bii**).

Dermal tissue substitutes can be categorised into autologous grafts (i.e. Hyalograft 3D (**Figure 7.9C**)) or allogenic grafts (i.e. Dermagraft (**Figure 7.9D**)). The main difference between the two is the source of cells, where Hyalograft uses patient-derived fibroblasts and Dermagraft uses neonatal fibroblasts and both have been used in chronic wounds and diabetic ulcers (Li et al., 2015; MacNeil, 2007). Likewise, epidermal / dermal tissue engineering apparatus can also be split into autologous or allogenic cell-bearing constructs. The scaffold matrices also differ, with TissueTech autograft system containing hyaluronic acid (HA) and Apligraf® containing collagen as their main components (Uccioli, 2003; Zaulyanov & Kirsner, 2007) (**Figures 7.9E and F** respectively).

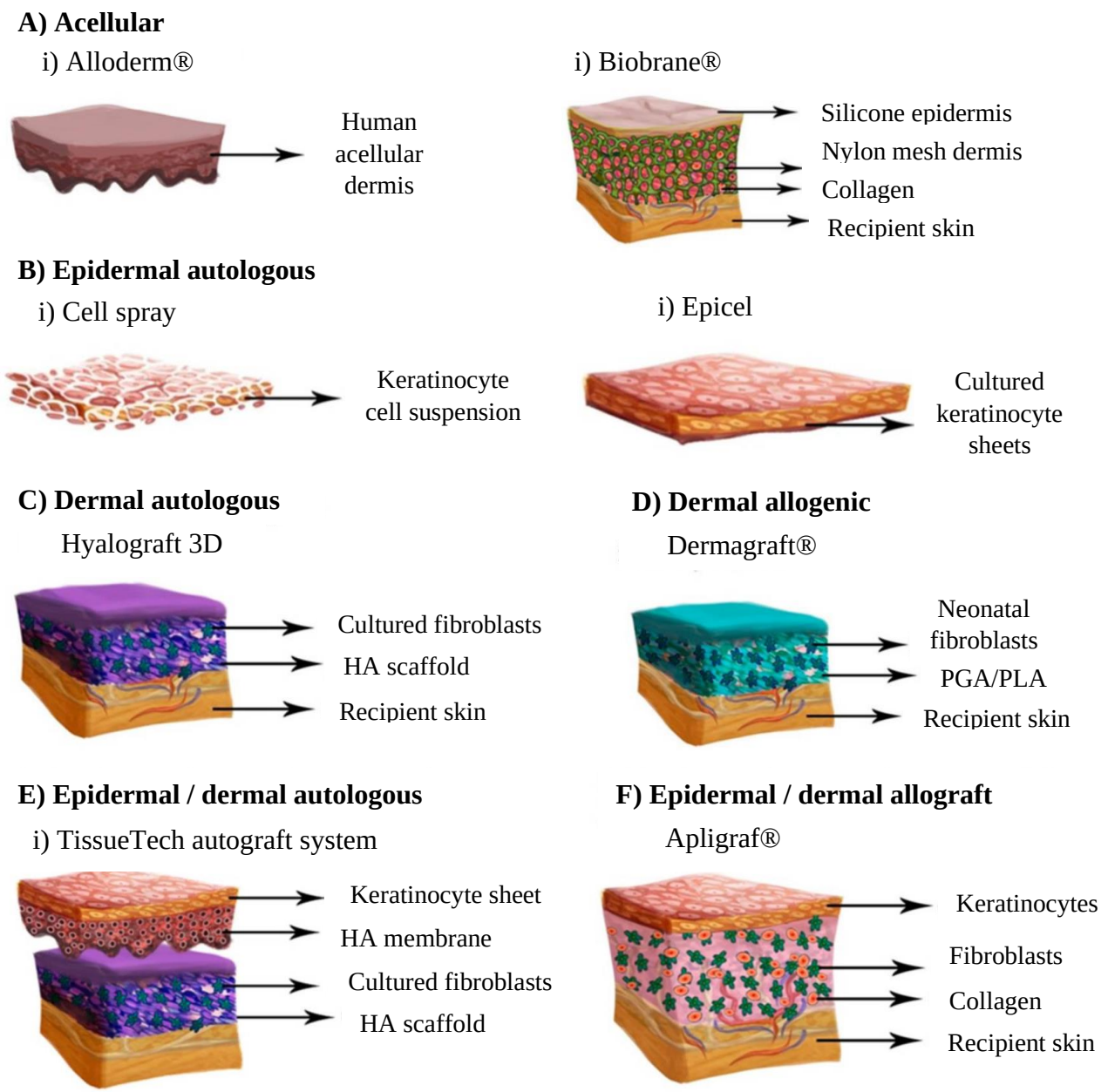

Figure 7.9 – Tissue engineering skin substitutes. A) Acellular: i) Alloderm ii) Biobrane. B) Epidermal autologous: i) Cell spray ii) Epicel. C) Dermal autologous Hyalograft 3D. D) Dermal allogenic Dermagraft. E) Epidermal / dermal autologous TissueTech autograft system. F) Eipdermal / dermal allograft apligraf (adapted from Vig et al., 2017).

7.1.10 Current Challenges in Skin Repair

Chronic wounds that are resultant of trauma, surgery or disease pose a major healthcare problem, with around 2.2 million people requiring treatment for chronic wounds in the UK alone (Guest et al., 2017). The current gold standard in repairing chronic wounds is the split-thickness autograft,

however, issues remain with this technique including donor site morbidity and an imbalance between donor availability and demand. Additionally, harvested grafts are not always sufficient in thickness in order to compensate for the extent of tissue trauma down to the subcutaneous hypodermal layer. Engineering of skin substitutes has seen remarkable progress in addressing the physical, psychological and economical burdens that come with wound healing therapies over the past four decades (He et al., 2018). 3D bioprinting skin substitutes, in particular, is currently at the forefront of research as it has the potential to produce intelligently designed skin models with greater precision. Even so, most skin equivalents manufactured using 3D bioprinting are typically limited to containing only dermal and epidermal layers and lack a hypodermal layer. However, *in vitro* studies have shown that adipose derived mesenchymal stem cells (ADSC) within a model hypodermal layer can contribute to epidermal morphogenesis, neovascularisation and accelerate wound healing (Huang et al., 2012; Lu et al., 2012). The true, complex, hierarchical nature of native skin is therefore seldom recapitulated in dermo-epidermal constructs alone. Furthermore, current 3D printed skin equivalents that do feature a hypodermal layer are limited in thickness due to poor print fidelity when extruding low viscosity biopolymers with relatively deep dimensions. Because of these limitations, there is often an oversight in selecting optimal print parameters, as the choice in print specifications such as print speed, bioink material and curing method is not at the discretion of the user, but instead is restricted and dictated by the 3D printing technique. For instance, researchers have often employed high viscosity polymers to overcome the issues associated with the collapse of low viscosity materials once deposited. This would necessitate a fast print speed to be implemented and in turn, the curing of material to occur *in situ* during printing to limit distortion of the intended model dimensions. These criteria directly impact upon the successful fabrication of tissue substitutes that contain the biochemical and geometrical facets of functioning skin.

Suspended layer additive manufacture (SLAM), as developed in previous chapters, allows greater freedom in the selection of print parameters that are conducive to the production of multi-layered

constructs with admirable print fidelity and cell viability. The principle mechanisms behind SLAM enable extrusion printing of bioinks over a range of viscosities within a self-healing fluid gel that acts as a temporary support prior to solidification and extraction.

Here, it is proposed that SLAM offers a potential solution to the issues associated with producing skin substitutes for chronic wound repair. By using SLAM, printing conditions can be tuned in order to gain ultimate print fidelity without compromising cell behaviour. Tri-layer skin models complete with epidermis, dual compartment dermis and hypodermis could potentially be fabricated with substantial depth as seen at the human scale. The resolution of the skin layers would be enhanced accordingly by adjusting printing specifications including printing pressure, flow rate and nozzle gauge whilst also maintaining cell viability and phenotype. Using these methods, one is not limited by the characteristics of the printing material i.e. chemical composition, viscosity and method of gelation. This means that the true nature of native skin can be captured within a single construct, featuring gradients in material chemistry, cellular phenotype and density, microarchitecture, and mechanical characteristics.

In attempt to achieve this, first, human skin tissue was obtained from an elective human abdominoplasty for the isolation of human epidermal keratinocytes (HEK), human dermal fibroblasts (HDF) and stromal vascular fraction (SVF). Cells within SVF were homogenised to obtain adipose derived mesenchymal stem cells (ADSC), which were subsequently characterised by flow cytometry to confirm the success of homogenisation. As an investigation into the differentiating capacity of ADSC, cells were cultured under osteogenic and adipogenic conditions and stained with specific solutions to confirm the differentiation. Using SLAM technology as previously described, human-scale skin equivalents were 3D bioprinted and cultured for a period of 21 days at the air-liquid interface. Skin tissue constructs were analysed using shear rheology, cell viability and morphology staining, histology and immunohistochemistry (IHC) staining and by incorporating within a porcine wound model.

7.2 Methods

7.2.1 Preparation of human skin samples

Human skin tissue (25 cm^2) complete with subcutaneous adipose was obtained from an elective human abdominoplasty (previously belonging to a 36-year-old caucasian female of Fitzpatrick classification type 3) (Genoskin, France). Samples were shipped at 4°C in transportation culture media within 4 hours of excision. The subcutaneous portion of the tissue sample was then separated from the dermal / epidermal skin layer and placed in saline solution for washing in preparation for processing and *ex vivo* expansion. Dermo-epidermal tissue was sectioned and submerged in Dispase II solution at 4 °C overnight followed by separating the dermal and epidermal counterparts.

7.2.2 Isolation of Human Dermal Fibroblasts (HDF)

Fibroblasts were released from the dermal portion of skin by incubation in collagenase D solution overnight followed by submerging in trypsin and mechanically agitating the dermis using a scalpel. Released cells were centrifuged, re-suspended in basal media, filtered through a 100 µm cell strainer and plated in a T25 flask. Basal media was changed every 3 days (Dulbecco's modified eagle medium (DMEM) supplemented with FBS (10%), HEPES (2.5%) and penicillin/streptomycin (1%).

7.2.3 Isolation of Human Epidermal Keratinocytes (HEK)

Keratinocytes were released from epidermal matrices by using trypsin and mincing using a scalpel. Keratinocyte growth medium (KGM, Lonza, UK) was used to halt enzymatic action of trypsin followed by centrifugation, re-suspending, filtering through a 70 µm cell strainer and plating onto HDF feeder layers. KGM media and detached feeder cells were replaced every 3 days or as necessary and cells were cultured up to 70 – 80% confluence.

7.2.4 Isolation of Stromal Vascular Fraction (SVF)

The stromal vascular fraction was isolated from adipose tissue by mincing using a scalpel, passing through a cell dissociation sieve (size 100 mesh) and incubating in collagenase type I. Media was added to halt the reaction and samples were then sequentially filtered through 100 and 40 µm filters. Solutions were then centrifuged and the lipid, mature adipocyte and aqueous layers were discarded leaving behind the SVF cell pellet. The pellet was suspended in erythrocyte lysis buffer followed by a further centrifugation step prior to plating in basal media. Extracted SVF were sub-cultured as per standard trypsinisation protocols for 21 days until a homogenous ADSC population emerged and media was changed every 3 days or as necessary.

7.2.5 Cell characterisation by flow cytometry

Phenotypic analysis was undertaken using flow cytometry (Millipore Guava Easycyte Flow Cytometer, Merck Millipore, UK) in order to confirm the heterogeneity of freshly isolated SVF populations at week 0 and the homogeneity of 3-week-old *in vitro* cultured ADSC populations. Cells were trypsinised and 1 x 10^5 cells of each population were re-suspended in PBS in separate Eppendorf tubes. Antibody cocktail (anti-human CD34 PE / CD45 FITC, BD Biosciences) was added and incubated at room temperature absent from light. Control antibody was added to a further two Eppendorf tubes of each cell population to determine nonspecific binding (mouse IgG1 PE and mouse IgG1 FITC, BD Biosciences) and cells with no antibody were used for flow cell counting. PBS was added to each tube, vortexed and centrifuged (600 *g* for 5 mins), the supernatant was removed and each cell pellet was re-suspended in PBS prior to analysis. The fluorescence intensity was then plotted against cell count and mean fluorescence intensity was calculated accounting for non-specific binding (δMFI – mean fluorescence intensity). Cells analyses were tested in duplicate.

7.2.6 Adipocyte differentiation

ADSC cultured for 21 days were washed in PBS and adipogenic differentiation medium was added. Adipogenic media included basal media supplemented with 500 µM isobutyl-methylxanthine (IBMX), 50 µM indomethacin and 1 µM dexamethasone. Cultures were maintained for a further 21 days and culture medium was changed every 3 days or as necessary.

7.2.7 Oil red O staining of adipocytes

Following a 21-day culture period, media was aspirated and cells were fixed in 10% formalin followed by washing with PBS and distilled water. Cells were stained with 60% Oil Red O solution, washed thrice in PBS and counterstained with Harris' haematoxylin diluted 1:2 in deionised water prior to visualisation under an inverted microscope. ADSC were also stained as a control population.

7.2.8 Osteogenic differentiation

ADSC were trypsinised and plated at a density of 5 x 10^3 cells / cm^3 in ADSC media. The following day, ADSC media was aspirated and replaced with osteogenic differentiation media. Osteogenic differentiation media contained basal media supplemented with 10 mM β-glycerophosphate, 200 µM ascorbic acid and 0.1 µM dexamethasone. Cultures were maintained for a further 21 days and culture medium was changed every 3 days or as necessary.

7.2.9 Alizarin red S staining of osteocytes

Following a 21-day culture period, media was aspirated and cells were fixed in 10% formalin followed by washing with PBS and deionized water. Cells were stained with 2% Alizarin Red S solution and washed thrice in deionised water prior to visualisation under an inverted microscope. ADSC were also stained as a control population.

7.2.10 Fluid-gel print bed preparation

For formulation of the print bed, agarose fluid gels were prepared by cooling autoclaved agarose (type 1 low EEO, purchased from Sigma–Aldrich, UK) dispersed in deionized water at 0.5% w/v concentration to 25 °C under a constant shear of 700 rpm. Fluid gels were then loaded into extra-depth tissue culture plates.

7.2.11 Preparation of polymer solutions for printing

The materials used for replicating skin ECM were LM pectin (purchased from CP Kelco, UK) and collagen (PureCol EZ Gel, Advanced BioMatrix, purchased from Sigma–Aldrich, UK). Pectin powders were dispersed in deionized water at concentrations of 5% w/v and allowed to cool to 25 °C following autoclaving to form working solutions. Collagen solutions were stored at 4 °C prior to use. For the hypodermal layer, collagen and pectin were mixed at a ratio of 1:1 (1Col:1Pec) and for both the papillary and reticular dermis layers, collagen and pectin were mixed at a ratio of 2:1 (2Col:1Pec).

7.2.12 Rheological characterisation of polymer printing solutions

Rheological analyses of the printing polymer solutions for the hypodermal and dermal layers were performed in triplicate using a Bohlin Gemini rheometer (Malvern Panalytical, UK) fitted with a double gap cup and bob geometry (DG 24/27). Collagen (0.5%) and pectin (5%) alone were also subjected to rheological shear for reference. Collagen was measured at 4 °C, pectin at 25 °C, hypodermis solution at 15 °C and dermis solution at 11 °C to reflect the temperatures of which the solutions would experience during printing. Shear rate was ramped from 0.1 to 100 s^{-1} and shear viscosity (Pa s) was recorded.

7.2.13 Design of 3D skin models

Tri-layer skin models were designed using computer aided design (CAD) software SolidWorks® and saved in stl (stereolithography) file format. The model hypodermis (15 x 15 x 7 mm), papillary dermis

(15 x 15 x 1 mm) and reticular dermis (15 x 15 x 1 mm) layers were stacked and the stl to G-code conversion programme Slic3r® was then used to slice the models into layers and translate the coordinates into commands for the 3D bioprinter.

7.2.14 Fabrication of 3D skin models

For the printing of 3D skin models by SLAM, printing cartridges were loaded with bioink, attached to a conical nozzle with an internal diameter (ID) of 410 µm and inserted into an INKREDIBLE™ 3D bioprinter (Cellink, Sweden). For the simulated hypodermis bioink, collagen was mixed with pectin at a ratio of 1:1 and ADSC were suspended at a density of 5 x 10^5 cells / mL. For the simulated reticular dermis bioink, collagen was mixed with pectin at a ratio of 2:1 and HDF were suspended at a density of 1.5 x 10^6 cells / mL. For the simulated papillary dermis bioink, collagen was mixed with pectin at a ratio of 2:1 and HDF were suspended at a density of 3.0 x 10^6 cells / mL. The 3D bioprinter was aligned and calibrated to a specified pressure followed by placement of the petri dish containing the agarose fluid bed upon the z-stage. The printer was then instructed to commence fabrication of the tri-layer skin model and automatically switched cartridges upon each successive layer. Following scaffold fabrication, 200 mM of $CaCl_2 \cdot 2H_2O$ was injected around the structure through a hypodermic needle in order to solidify the pectin portion of the blends and collagen gelation was induced thermally by raising the temperature to 37 ºC. Structures were cultured overnight in an incubator (Triple Red, UK) at 37 ºC, 5% CO_2 and 95% air with the addition of adipogenic media and were removed from the agarose fluid gel bed the following day. Submerged in adipogenic media, scaffolds were then cultured for 14 days, followed by forming an air-liquid interface at the surface of the scaffold, seeding 2 x 10^6 HEKs atop the scaffold and culturing for a further 7 days prior to sectioning and analysis. Separate cultures of singular hypodermis, reticular dermis, papillary dermis and epidermis (HEK seeded atop 2:1 collagen / pectin blend) were also fabricated and treated equivalently to tri-layer skin models.

7.2.15 Lyophilization

Acellular 3D printed skin equivalents were cross-sectioned and placed in −80 °C conditions for 24 h followed by implementing a 72 h freeze drying cycle at −76 °C and 0.0010 mbar (Christ ALPHA 2–4 LD plus). Dry samples were stored in a desiccator prior to imaging.

7.2.16 Scanning Electron Microscopy (SEM)

Lyophilized skin equivalents were prepared for SEM by sputter coating with gold using a Quorum SC7620 sputter coater under a low bleed of argon. The internal networks within the samples were then studied using a field emission SEM (FEI Quanta 250 SEM) operated in high vacuum mode at an accelerated electron energy of 20 kV. Images were collected using a backscattered electron detector.

7.2.17 Rheological characterisation of 3D printed skin models

Rheological analyses of acellular skin model layers were performed in triplicate at 37 °C using a Bohlin Gemini rheometer (Malvern Panalytical, UK) with a parallel upper plate (PP 20) and serrated lower plate to prevent slippage. Model hypodermis (1Col:1Pec) and dermis (2Col:1Pec) ECM layers were printed in a cylindrical format (20 mm diameter and 1 mm depth) within an agarose fluid gel bed and solidified before retrieving and loading onto a rheometer. Shear stress was ramped from 10 to 100 Pa and elastic modulus G′ (Pa) was recorded.

7.2.18 Porcine wound model studies

Freshly slaughtered porcine cheeks sourced direct from the abattoir (Medcalf J & E Ltd, UK) were sterilized by submerging in absolute ethanol before forming a simulated wound throughout the epidermal, dermal and hypodermal layers using a scalpel. An acellular skin equivalent was then 3D printed to fit the dimensions of the porcine wound model followed by solidification and placement of the implant within the wound cavity.

7.2.19 Paraffin embedding 3D printed skin models

3D printed skin equivalents and human skin samples were sectioned and mounted within cassettes prior to processing. Samples were subjected to immersion within a fixing solution of 10% formalin followed by a series dehydration within graded ethanol (30%, 70% and absolute). Samples were then placed in xylene prior to embedding in paraffin (Leica EG 1150C Tissue Embedder, Leica Biosystems, UK).

7.2.20 Haematoxylin and Eosin (H&E) staining

Paraffin embedded samples were sectioned to 7 µm thickness using a microtome (Leica EG 1150C Tissue Embedder, Leica Biosystems, UK) and mounted onto adhesion coated slides. Slides were immersed in xylene followed by a series rehydration within graded ethanol (absolute, 70% and 30%). Slides were then rinsed under running tap water between treatments firstly with haematoxylin followed by counterstaining with eosin. Slides were dehydrated in a series of ethanol (30%, 70% and absolute) and submerged in xylene before the addition of mounting solution and a cover slip prior to analysis under a Leica CTR 6500 confocal microscope (Leica microsystems, UK).

7.2.21 Fluorescence microscopy

3D printed skin equivalents and singular scaffolds were sectioned and stained with Hoechst nuclear blue and phalloidin actin green fluorescent reagents (Fisher Scientific, UK) for visualization of suspended cells. All 3D cell culture scaffolds were then visualized using a fluorescent microscope (EVOS FLoid Cell Imaging Station, ThermoFisher Scientific, UK).

7.2.22 Cryoembedding 3D printed skin models

3D printed skin equivalents and human skin samples were embedded in frozen section media within a cryostat machine (Leica CM1900 Cryostat, Leica Biosystems, UK) and stored at -80 °C before use.

7.2.23 Immunohistochemistry

Cryoembedded samples were sectioned to 7 µm thickness using a cryostat microtome and mounted onto adhesion coated slides. Slides were then brought to room temperature and fixed in -20 °C acetone followed by washing in PBS. After placing specimen slides in a wet chamber, slides were treated with blocking solution (PBS/BSA/FBS), then primary antibody diluted in blocking solution (rabbit Anti-Cytokeratin 10 at concentration of 1 in 500, and mouse Anti-Cytokeratin 14 at 1 in 400, ABCAM Plc, UK) (mouse TGase 1 at 1 in 100, Santa Cruiz Biotechnology, USA), with an overnight incubation at 4 °C. Primary antibody was removed from each specimen followed by washing thrice in PBS / Tween and once with PBS. Secondary antibody was diluted in blocking solution absent from light (0.6 in 500 or 0.75 in 400 Goat anti-rabbit IgG respectively or 3 in 297 Goat anti-mouse IgG, ThermoFisher Scientific, UK) added to samples and left to incubate at room temperature for 45 mins. Following incubation, slides were washed with PBS / Tween, stained with DAPI for 3 mins, washed again thrice with PBS / Tween, twice with PBS and once with deionized water. Finally, slides were embedded with mounting medium, a coverslip was placed on top and samples were visualized using a fluorescence microscope (Leica DM 6000B and Leica CTR 6500, Leica Biosystems, UK).

7.3 Results

7.3.1 Design and preparation of a human skin equivalent

In order to recapitulate the true nature of human skin, it is important to try and capture the cellular makeup as well as the extracellular environment within the skin model as closely as possible. Native human skin components were therefore used as the basis for the design of the 3D bioprinted skin (**Figure 7.10A**). The hypodermal portion of the model contained adipose derived mesenchymal stem cells (ADSC) (**Figure 7.10B**) embedded within a matrix comprised of collagen and pectin at a ratio of 1:1. The reticular dermis consisted of a low-density population of human dermal fibroblasts (HDF) (**Figure 7.10C**) embedded in a more collagen-rich matrix (Col 2:1 Pec) and papillary dermis exhibited a higher density population of HDF cells as found within human skin. Human epidermal keratinocytes (HEK) (**Figure 7.10D**) were to be seeded atop the 3D model following printing.

Computer aided design (CAD) software was used to generate the hypodermal (15^2 x 7 mm), papillary dermal (15^2 x 1 mm) and reticular dermal (15^2 x 1 mm) layers, followed by integration of the three structures (**Figure 7.10E left**) and generation of the 3D print path (**Figure 7.10E right**) to create the print geometry for the tri-layer skin equivalent. Final preparation for printing the skin model included rheological characterisation of the collagen / pectin blend printing materials (**Figure 7.10F**). Both 1:1 and 2:1 collagen to pectin ratio blends exhibited shear thinning behaviour with increasing shear rate similarly to collagen and pectin alone. Interestingly, material blends had higher viscosities under simulated static conditions (low shear rates) compared with collagen and pectin alone yet demonstrated intermediate viscosities between singular pectin and collagen under simulated printing conditions (higher shear rates).

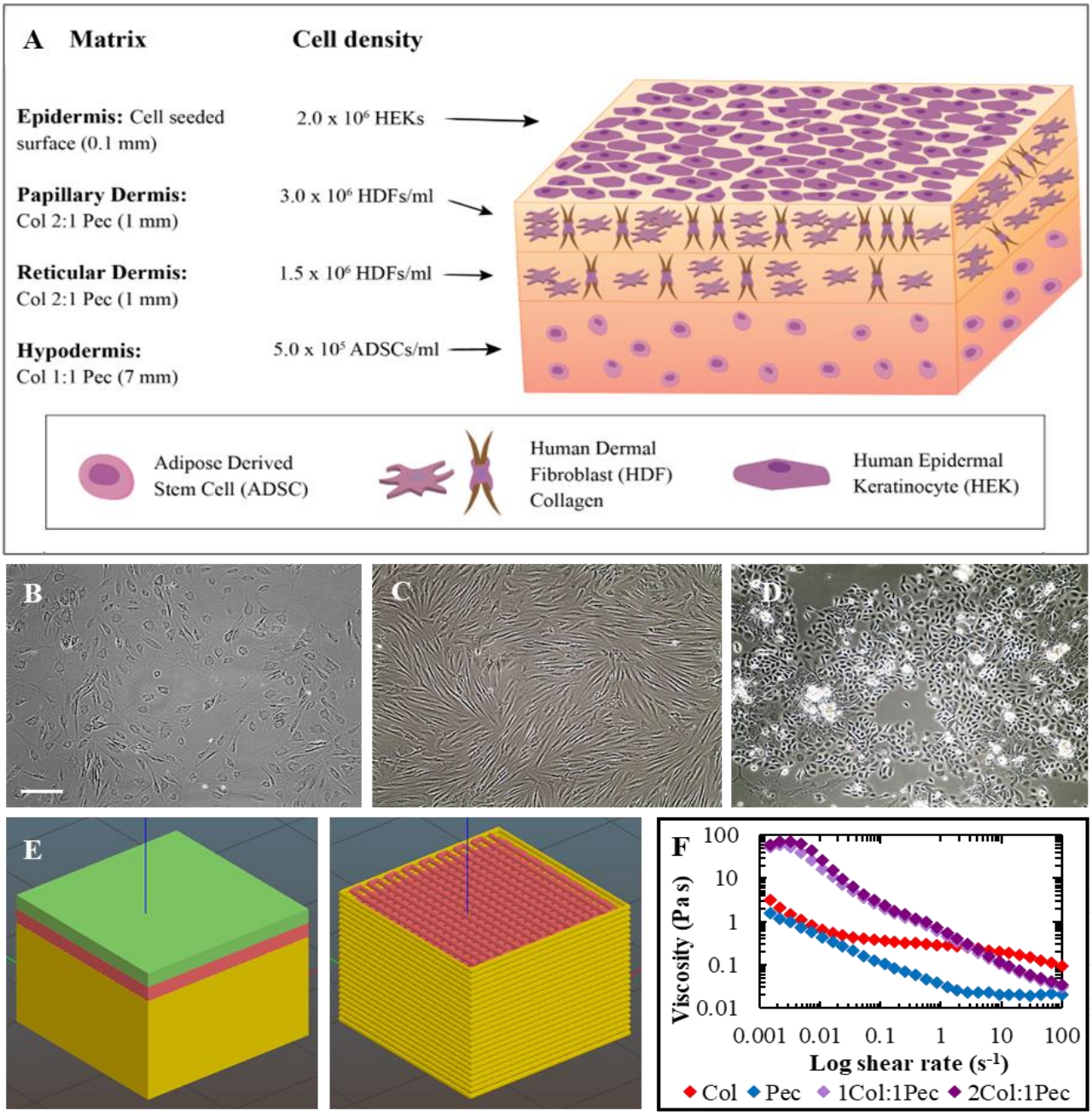

Figure 7.10 - Design and preparation of a tri-layer skin model. Illustration of a tri-layer skin model (15.0 x 15.0 x 9.1 mm) featuring a hypodermis, dual compartment dermis and epidermis. Adipocytes differentiated from adipose derived mesenchymal stem cells (ADSC), human dermal fibroblasts (HDF) unattached and attached to collagen and human epidermal keratinocytes (HEK) are specifically localised within the layered scaffold and encapsulated within a graded collagen / pectin matrix blend in an arrangement that is synonymous to native tissue. 2D culture of B) ADSC C) HDF and D) HEK for integration within the 3D skin model (scale bar = 200 µm). E) G code of skin model layer configuration containing hypodermis (yellow), reticular dermis (red) and papillary dermis (green) (left) and print path (perimeter in yellow, infill in red) (right) F) Viscosity profiles of hypodermal layer (1Col:1Pec) and dermal layer (2Col:1Pec) printing materials including single collagen and pectin for reference.

7.3.2 SVF isolation and ADSC expansion and characterisation

Upon microscopic inspection, freshly isolated SVF at day 0 predominantly contained erythrocytes along with stromal cells (**Figure 7.11A**). When cultured under defined conditions, ADSC emerged exhibiting a spindle-like morphology at day 7 (**Figure 7.11B**) and were almost completely fusiform by day 14 at passage 1 (**Figure 7.11C**). One further passage at day 21 showed complete expansion of SVF to ADSC procuring a homogenous cell population (**Figure 7.11D**).

In order to confirm mesenchymal status of expanded ADSC versus the hematopoietic nature of freshly isolated SVF, flow cytometry was undertaken. SVF were positive for hematopoietic marker CD34 (difference in mean fluorescence intensity (δMFI) between control IgG isotype and human variant of 56.6) and was downregulated at day 21 (δMFI = 23.29) showing elimination of hematopoietic cells and homogenization of cells with a mesenchymal lineage (**Figure 7.11E**). CD45 remained relatively constant within both day 0 SVF and day 21 ADSC populations.

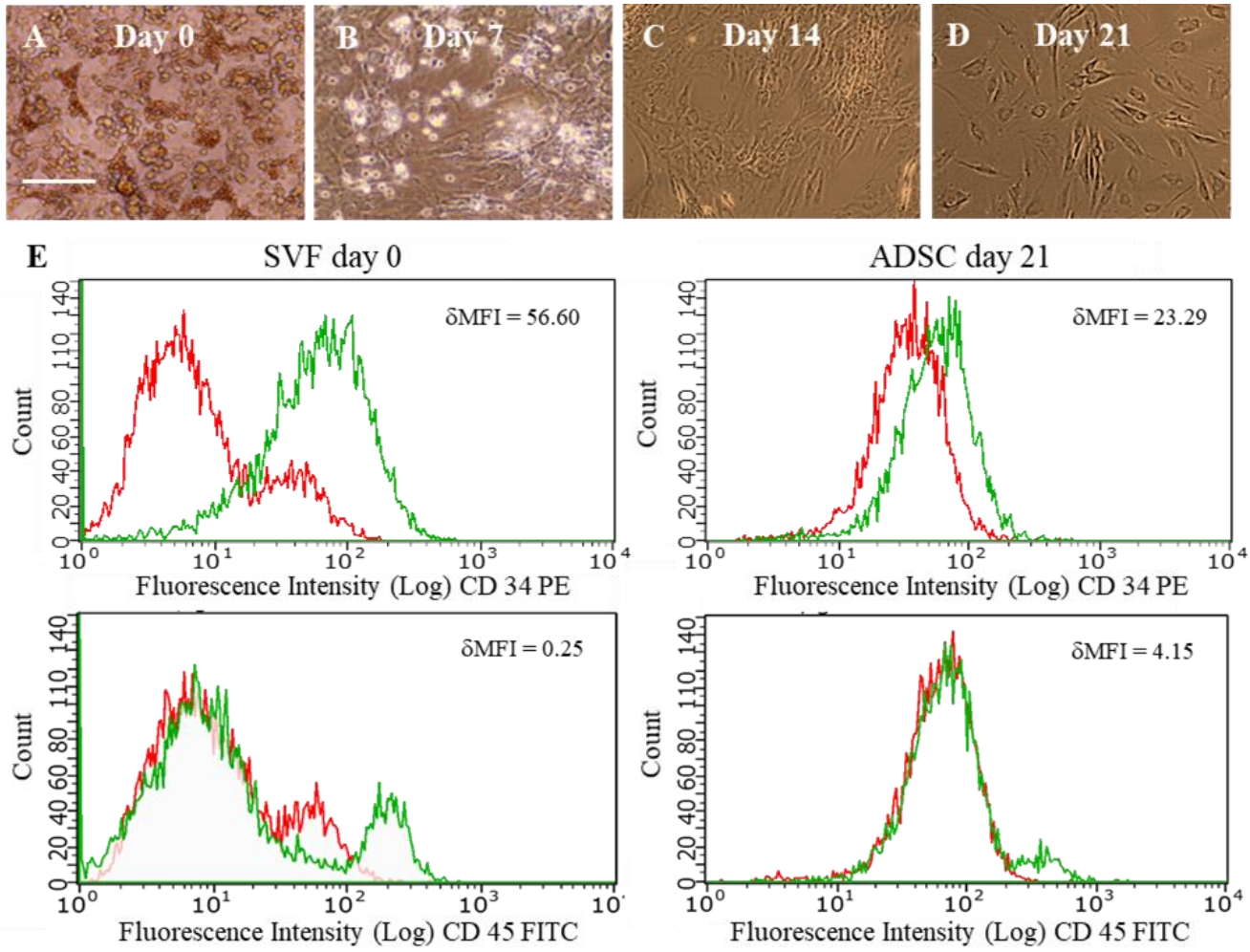

Figure 7.11 - Homogenisation of cells obtained from the stromal vascular fraction within adipose tissue for expansion of adipose derived stem cells. A) SVF at day 0, passage = 0, B) SVF at day 7, passage = 0, C) SVF at day 14, passage = 1 and D) ADSC at day 21, passage = 2 (scale bar = 200 µm). E) Characterisation of SVF and ADSC by flow cytometry. Freshly isolated SVF exhibit greater expression of haematopoietic marker CD 34 and is downregulated in ADSC (upper). Expression of haematopoietic marker CD 45 remained relatively constant (lower). Red corresponds to control IgG isotype and green to the specific antibody.

To satisfy proper characterisation of ADSC, both phenotype and differentiation capacity criteria require fulfilling. ADSC have a multi-lineage differentiation capacity giving rise to mesodermal lineages, namely adipogenic, osteogenic and chondrogenic cell species. To determine the differentiation capacity of ADSC incorporated within the hypodermal skin model, ADSC were subject to culture in either osteogenic or adipogenic media (**Figure 7.12A, B and C**).

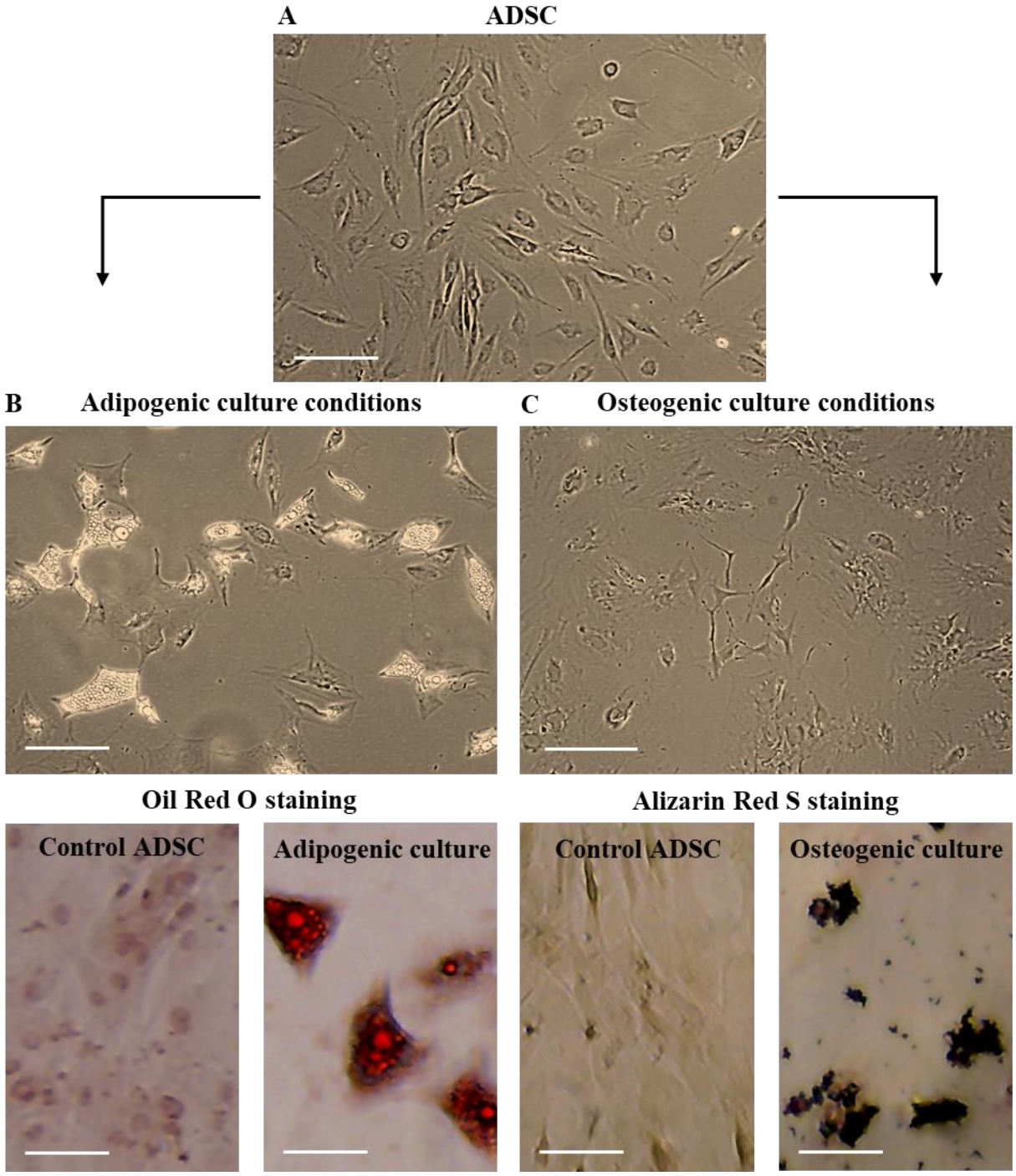

Figure 7.12 - ADSC differentiation potential. A) ADSCs obtained and cultured from SVF were subjected to B) adipogenic and C) osteogenic differentiation media *in vitro* for 21 days. D) Oil Red O lysochrome dye stains lipids indicative of adipocyte-like cells. E) Alizarin Red S dye stains calcium deposits indicative of osteocyte-like cells. Undifferentiated ADSC staining is shown as a negative control (scale bars = 200 µm).

When adipocytes were stained with Oil Red O, lipid deposits became visible while ADSC controls remained unstained thus confirming dye specificity to *in vitro* cultured adipocytes from the ADSC

population. Likewise, osteocyte specific staining using Alizarin red revealed calcium deposits when ADSC were in vitro cultured under osteogenic differentiating conditions compared with ADSC controls. These results therefore demonstrate the multi-lineage differentiating capacity of isolated ADSC for culture of adipocytes within a human skin model.

7.3.3 Characterisation of 3D printed skin models

Hypodermis and dual compartment dermis layers were 3D printed within an agarose fluid gel bed prior to formation of the epidermis by seeding the surface with keratinocytes, ultimately forming a single, graded skin replica (**Figure 7.13A**). Upon visual inspection, the graduation of material content within each layer went from clear pink to translucent white attributed to the higher collagen content within the upper dermal layers. A gradient in material architecture could also be seen at the microstructural level using scanning electron microscopy (SEM), which demonstrated porosity gradients with a likeness to human skin (**Figure 7.13B**).

With gradients in microstructure within a tissue scaffold also comes gradients in mechanical strength. When subjected to mechanical testing using shear rheology, the collagen to pectin ratio of 1:1 which simulated hypodermal ECM was stiffer (higher elastic modulus) compared with the 2:1 ratio representing the dermal layers (**Figure 7.13C**).

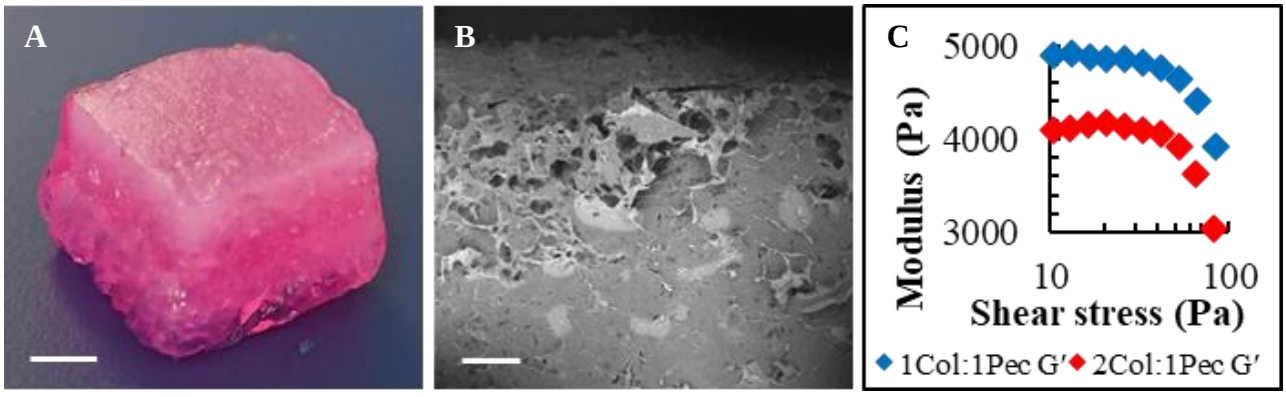

Figure 7.13 - Characterisation of an acellular tri-layer skin model. A) 3D printed construct (scale bar = 5 mm). B) Scanning electron micrograph of a 3D printed construct following lyophilisation (scale bar = 500 µm). C) Mechanical behavior of a 3D printed construct by shear rheology.

7.3.4 Histology and immunohistochemistry of 3D bioprinted skin equivalents

Histological evaluation of the bioengineered skin equivalent using H&E staining further illustrated the architecture of the construct, revealing the apparent similarities to human skin (**Figure 7.14A and B**). Each layer of the 3DP skin, including epidermis (E), papillary dermis (PD), reticular dermis (RD) and hypodermis (H) was consistent with that of native skin. Additionally, the skin model hypodermis appeared vacuolated, in agreement with human skin, due to the large lipid droplets that dominate adipocyte cell volume being removed during routine tissue preparation and leaving spherical voids.

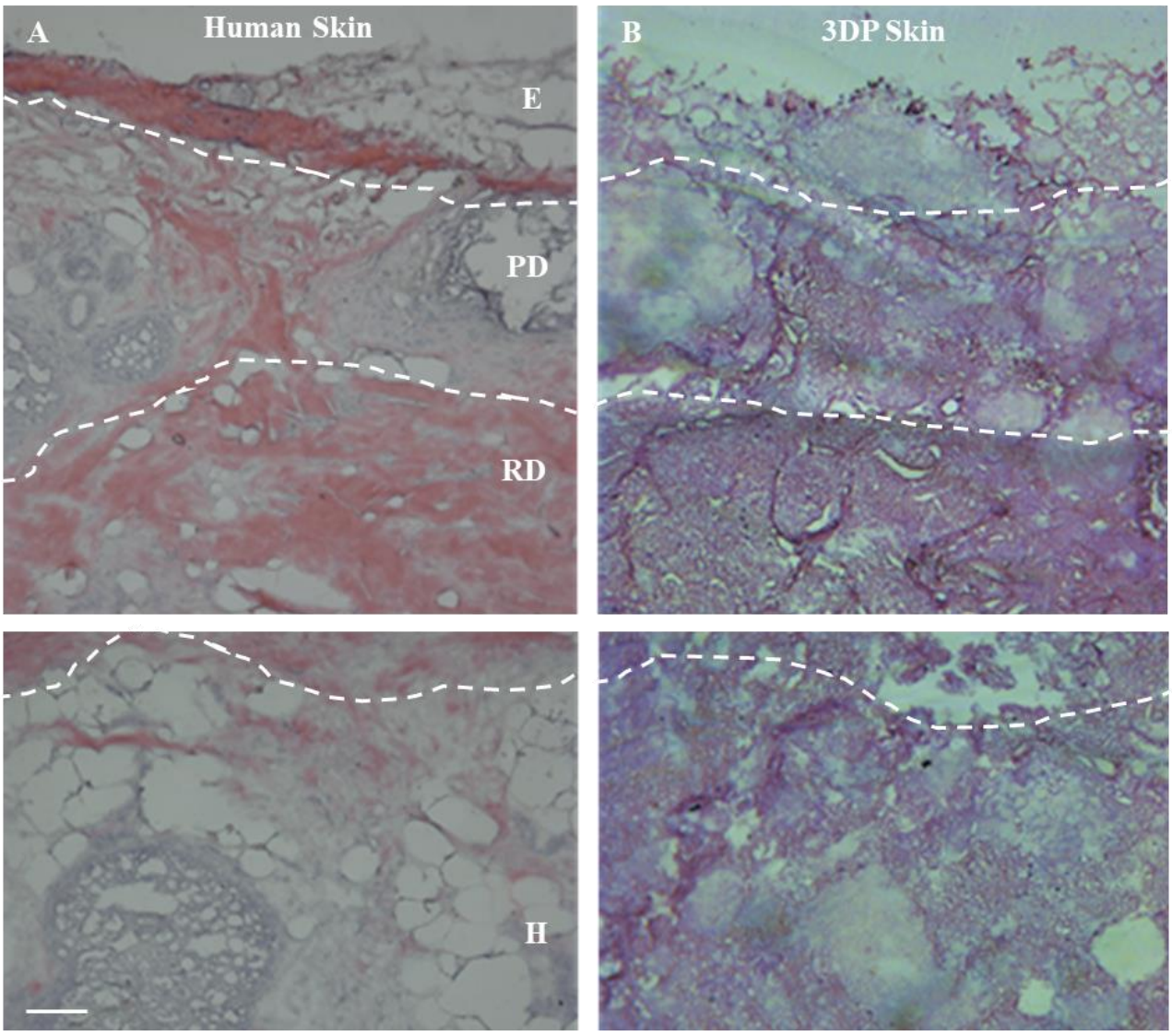

Figure 7.14 - Histological analysis of a 3D printed trilayer skin model manufactured by SLAM. A) Haematoxylin and Eosin staining of a human skin sample (left) compared with a 3D printed model (right) complete with epidermis (E), papillary dermis (PD), reticular dermis (RD) and hypodermis (H) (scale bars = 100 µm).

Further to culturing HEK, HDF and ADSC within the tri-layer skin model, separate cultures of cells in each respective material environment were also examined (**Figure 7.15**). In all cases, the proliferative behaviour and appearance of cells were identical between single and tri-layer cultures. It was also evident that cells remained viable, made possible by the gentle printing conditions despite a high resolution being accomplished. The densities of cells within each distinctive layer of the methodological model design were successfully reimagined within the 3D printed model although HEK were not as abundant as anticipated.

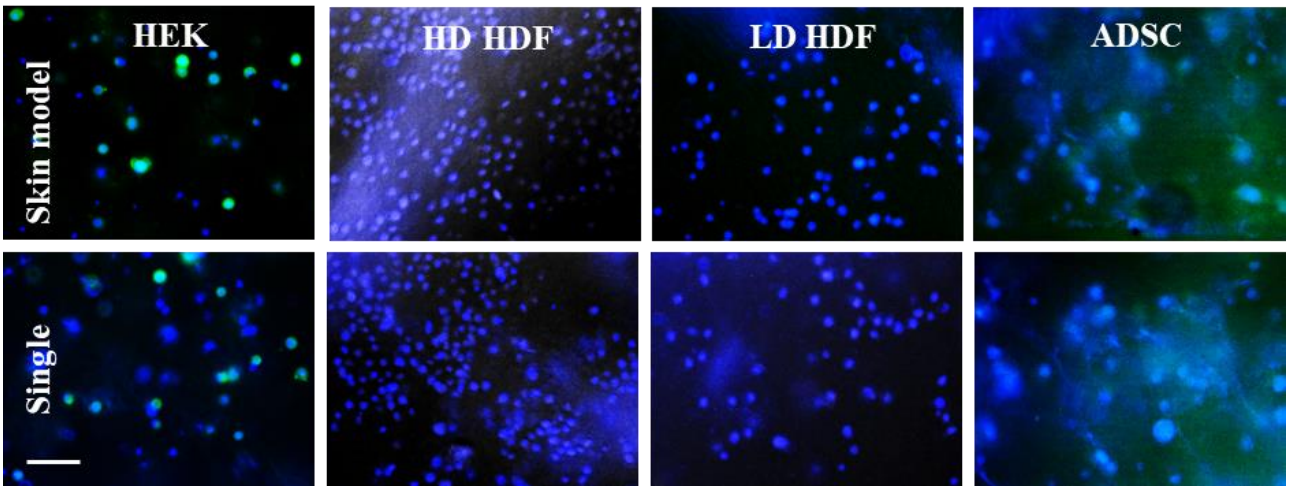

Figure 7.15 - Fluorescence micrographs of HEK, high density (HD) HDF, low density (LD) HDF and ADSC each within the skin model (upper) and separate 3D culture (lower) (scale bars = 100 µm).

Upon immunohistological staining of the skin model epidermis, there were indications of keratinocytes terminally differentiating through the layers (**Figure 7.16**). Cytokeratin 10 staining was indicative of stratum corneum apparatus (**Figure 7.16A**), transglutaminase expression suggested a formation of an intermediate stratum spinosum or granulosum layer (**Figure 7.16B**) and finally cytokeratin 14 as expressed in the basal layers of the epidermis was highlighted within both human and model skin samples (**Figure 7.16C**). It is likely that, had more time been given for keratinocytes to fully mature, staining of the epidermal strata would be more evident.

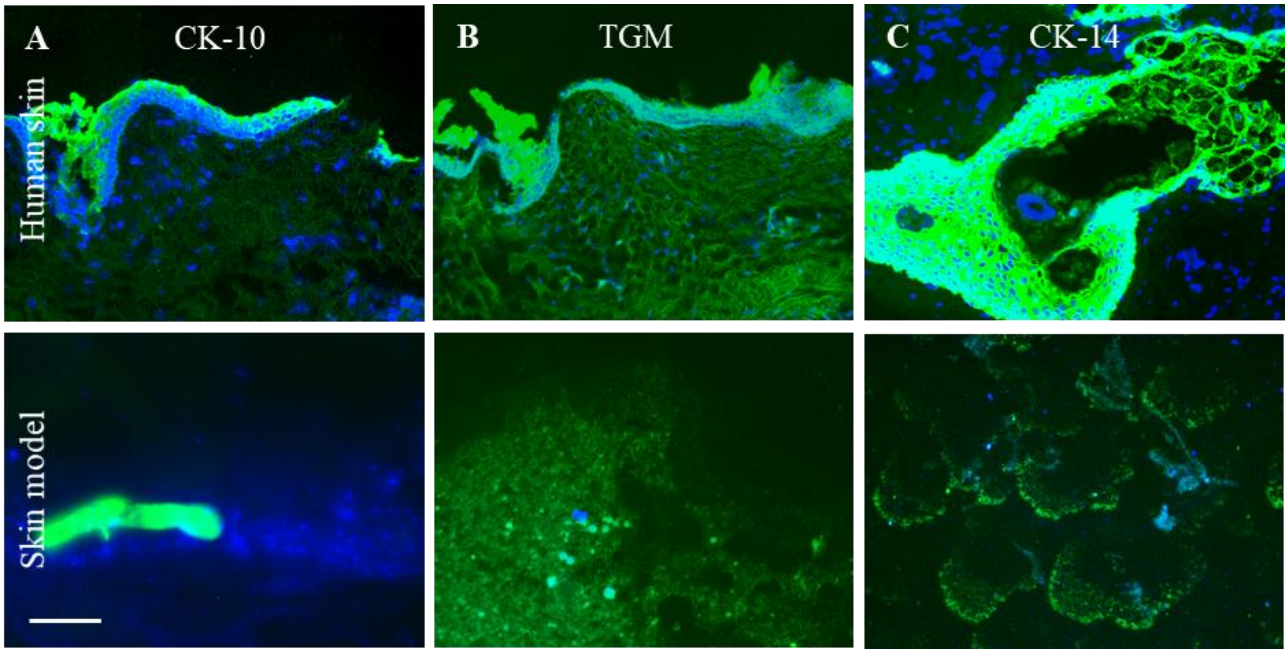

Figure 7.16 - Immunohistological analysis of epidermal differentiation within human skin (upper) and skin model (lower) for the indication of A) Cytokeratin 10 within the stratum corneum, B) Transglutaminase within the stratum granulosum and C) Cytokeratin 14 within the stratum basale. Scale bar = 50 µm.

7.3.5 Implantation of a 3D printed skin equivalent within a porcine wound model

In order to validate the model as a transplantable scaffold, the skin equivalent was transplanted within a simulated porcine wound model (**Figure 7.17A-C**). The scaffold retained structural integrity with all layers remaining interconnected and intact whilst also filling the dimensions of the wound void preventing sagging and caving of the lesion (**Figure 7.17D**). In extension, the aesthetics of the scaffold were relatively consistent with those of the porcine skin and was structurally and visually similar to that of human skin.

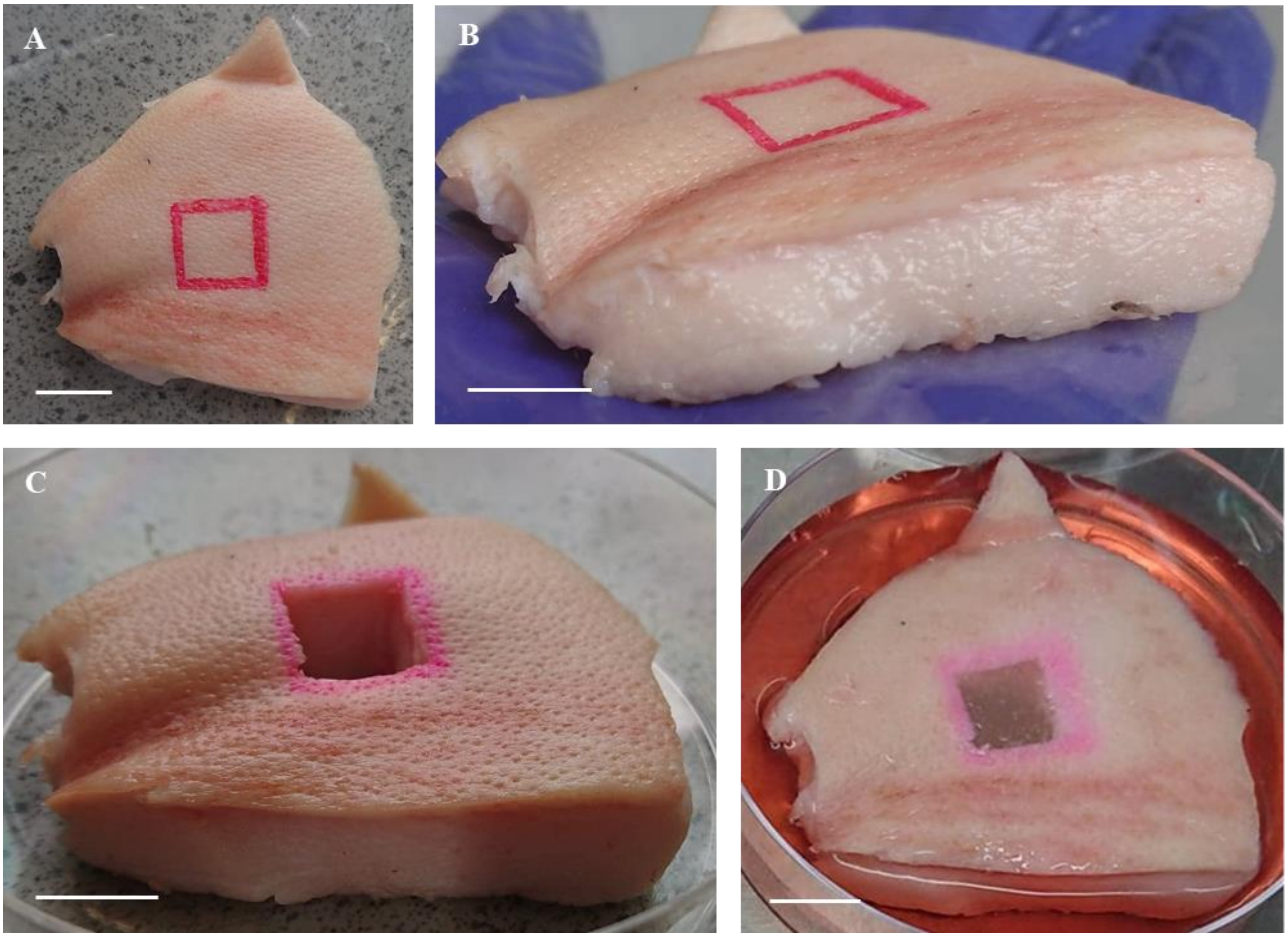

Figure 7.17 - Implantation of a 3D printed construct within a porcine wound model. A) Arial and B) lateral view of freshly slaughtered porcine skin, C) 15 cm^3 simulated wound void and D) wound containing implanted 3D printed skin equivalent (scale bars = 15 mm).

7.4 Discussion

In chronic wounds, replacement skin is necessary as the wound itself is unable to re-epithelialize, leading to problematic scarring and in some cases, impaired function. Though many skin equivalents have been manufactured in attempt to meticulously mimic human skin for implantation, few have managed to represent the hypodermal portion of skin tissue (Kim et al., 2019). Here, a tissue-engineering skin model has been fabricated which incorporates three compartments consisting of epidermis, dermis and hypodermis within a single 3D printed structure (**Figure 7.10A**).

In preparation for 3D bioprinting skin equivalents, cells were isolated from a single human abdominoplasty. In this study, the chosen method for obtaining an ADSC population was to isolate

the heterogeneous stromal vascular fraction (SVF) from the subcutaneous adipose tissue of an elective patient abdominoplasty. Following culture under defined conditions over a 21-day period, ADSC emerge having multi-lineage differentiation capacity, including the ability to differentiate into adipocytes. Obtaining ADSC from adipose is more accessible, allows harvesting of greater numbers of progenitor cells and harbours a larger expansion potential compared with other tissues such as bone marrow, making high-dosage treatments readily available, relatively simple and also more cost-effective (Araña et al., 2013). It was clearly demonstrated, using flow cytometry and specifically formulated cell culture medias, that ADSC could be homogenised from SVF within subcutaneous tissues and subsequently directed towards specific cell phenotypes (**Figure 7.11 – 7.12**). ADSC were also successfully encouraged to assume a lipid-secreting cell lineage, highly like adipocytes, confirming their appropriate inclusion within the model hypodermal layer. The final step for 3D printing preparation was to simulate the shear experienced by bioinks during printing by exposing solutions to rheological shear (**Figure 7.10F**). Interestingly, combinations of collagen and pectin exhibited higher shear viscosities under simulated static conditions (low shear rates), yet lower viscosities under simulated dispensing conditions (high shear rates) compared with collagen and pectin solutions alone. These properties are largely advantageous in that cell suspensions within polymer blend solutions are more stable prior to printing, yet much lower shear forces are exerted on cells during deposition thus preserving cell viability.

Following cell and solution (bioink) preparation, the 3D bioprinting process commenced. The printed scaffold exhibited true-to-size dimensions and demonstrated the system's capacity to achieve a high resolution by following the designed print pathways and specifications (**Figure 7.13A**). Due to the gentle suspending nature of SLAM, the model could be cured using divalent cations for the pectin portion of the blend whilst an ambient temperature of 37 °C gelled the collagen element of the blend. Each layer of skin is naturally highly anisotropic, however, hypodermis is generally stiffer compared to dermis with a decreasing graduated stiffness between the two (Geerligs, 2010). This

microarchitectural and mechanical graduation was successfully demonstrated within the tri-layer skin equivalent by scanning electron microscopy and shear rheology (**Figure 7.13B-C**), while fluorescence micrographs exampled how cell density and phenotype can be heterogeneously distributed to mimic native skin (**Figure 7.15**). Despite the gradients exhibited within the multi-layered construct, layers remained intact during manipulation and placement within a porcine wound model, exemplifying that the scaffold is fit for purpose (**Figure 7.17**).

Within the hypodermis, not only do ADSC play a part in repair and regeneration within the wound environment, they also have a stimulatory effect on human dermal fibroblast (HDF) proliferation and migration as well as contributing to the secretion of growth factors, collagens and fibronectin through HDF (Kim et al., 2011). Naturally occurring hypodermis is classed as loose connective tissue and is rich in ground substance made of polysaccharide that fill the voids between collagenous, elastic and reticular fibres and cells (Mathieson & Watkins, 2009). Pectin, also a polysaccharide, is a hydrogel which has strong structural similarities to ground substance such as glycosaminoglycan (Neves et al., 2015) within adipose ECM and thus acts as an ideal alternative within the model hypodermal layer. Pectin has also been associated with having wound healing properties based on its hydrophilicity, antibacterial action and for its role in scaffolding within the wound void preventing premature contraction, excessive scarring and skin distortion (Giusto et al., 2017). Collagen was incorporated into the hypodermal layer at a ratio of 1:1 due to its role within natural hypodermis during wound repair.

Within the dual dermis compartments, the collagen / pectin blend ratio used was altered to 2:1 due to the higher abundance of collagen within native dermal dense connective tissue (Marieb & Hoehn, 2015). Predominantly secreted by HDF, collagens contribute to dermal ECM by allowing attachment and migration of resident cells and are also a large contributor to the wound healing process (Kanta, 2015). The density of residing HDF from the lower reticular dermis to the upper papillary dermis, however, is twofold (Sorrell & Caplan, 2004) and is thus reflected within this model. During

histological evaluation of human skin, sebaceous and sweat glands could be identified (**Figure 7.14**). Although these features were not present within the 3D bioprinted skin model, they still held structural similarities by comparison. These findings were significant in that the scaffold has the potential capacity to support structures such as these. This means that, once a fundamental understanding of the tri-culture of cells had been established, further cells such as sebocytes, hair follicle cells and other associated stem cells could also be incorporated within the system.

Finally, this model exhibited a layer of keratinocytes seeded atop the dermal compartment for representation of the epidermis. Much like naturally occurring epidermis, the fabricated epithelial layer was much more abundant in cells, distributed within a sparse ECM compared with ECM-rich connective tissue within the dermal and hypodermal regions. A further benefit to this model is that the calcium used to crosslink pectin serves an additional purpose. Calcium has an established role in mammalian skin tissue homeostasis and is known to modulate keratinocyte proliferation and differentiation, playing a vital role in epidermal regeneration and dermal reconstruction in wound healing (Zhang et al., 2018). Despite the successful placement of HEK cells above the 3D bioprinted papillary dermis, HEK were not as abundant as anticipated. This could be down to several reasons which are commonplace in surface seeding cells, such as HEK cells simply sliding off from the model during seeding, failure of HEK cells attaching and loss of epidermal apparatus during tissue preparation and examination. In this case, it is likely a combination of the three as models were left to propagate for 7 days following seeding of HEK and the number of cells seeded do not reflect those shown during imaging. Precise placement of polymer material-suspended cells using 3D printing is a much more efficient method, however, it is unsuitable in recapitulating epithelial tissues that exhibit minimal ECM compared with HDF and ADSC-containing connective tissues. The fact that cell proliferation appeared to cease whilst suspended within the scaffold could suggest that the cells within each layer remained viable yet were mitotically inhibited. In a transplant setting, this feature may be beneficial in that the scaffold is given time to vascularise prior to consequential degradation and

release of its cell cargo. This means that once vascularisation has been established, cell proliferation may resume upon release and the demand for oxygen and nutrients supplied by the blood can be met.

Although cells assumed a non-proliferating state, there was evidence of regulated gene expression and protein secretion. Upon immunohistological staining of the skin model epidermis, there were indications of keratinocytes terminally differentiating through the layers (**Figure 7.16**). Cytokeratin 10 staining was indicative of stratum corneum apparatus, transglutaminase expression suggested a formation of an intermediate stratum spinosum or granulosum layer and finally cytokeratin 14 as expressed in the basal layers of the epidermis was highlighted within both human and model skin samples.

7.5 Conclusions

The results presented here on manufacturing a tri-layer skin model using suspended layer additive manufacture are the first of its kind. A skin equivalent complete with a tri-culture of cells distributed throughout hypodermal, dermal and epidermal regions was successfully designed and fabricated by optimising print resolution without compromising cell viability. ADSC were propagated from SVF populations and demonstrated both stem-cell-ness and a multi-lineage differentiation capacity within both adipogenic and osteogenic culture conditions. HDF and HEK were also extracted and cultured from the same patient sample prior to incorporation within a 3D skin equivalent. Aided by tuning of flow rate, printing pressure, nozzle gauge and rheological characterisation, scaffolds were printed with high precision within a supporting agarose fluid gel matrix prior to solidification and extraction. The careful placement of simulated dermal and hypodermal ECM through ranging collagen and pectin blend ratios resulted in biochemical, microstructural and mechanical gradients as seen in native human skin. Scaffolds also demonstrated their implantable capacity within an *ex-vivo* porcine skin wound, exhibiting admirable aesthetics and dimensional compatibility. On the micro-scale level, skin models featured native skin apparatus such as epidermal layer and nucleated matrix resultant of

adipocyte lipid removal as well as the presence of collagen and gradients in cell density. Furthermore, there was evidence of epidermal terminal differentiation on the model's surface evidenced by the formation of markers indicative of the stratum corneum, stratum granulosum / spinosum and stratum basale. Despite this, cells within the lower regions of the scaffold appeared to halt mitotic activity whilst suspended within the collagen / pectin blend – a feature which is highly advantageous for allowing vascularisation of the scaffold following implantation. It is envisaged that the 3D skin bioprinting techniques used in this research could be made readily available within the clinic setting. Potentially, following scanning of a patient's wound or lesion, a patient-specific scaffold may be printed once the wound dimensions had been characterised and a complementary geometry to fill the wound void had been computed. This scaffold could then incorporate the patient's cells thus reducing chances of rejection and overcoming the problems associated with donor availability and demand.

Chapter 8

SUMMARY, CONCLUSIONS, AND FUTURE DIRECTIONS

Chapter 8 – Summary, Conclusions and Future Directions

This research was intended to explore novel methods in manufacturing multi-layered tissue engineering constructs. Building on previous suspended manufacturing protocols, the theory behind fluid gel formulation and suspension within the supporting matrix was elucidated with greater detail. The incorporation of a 3D bioprinter further refined tissue construct resolution and enabled the generation of layered structures of greater complexity and with more accurate dimensions. This work was then used to mould a strategy for designing, fabricating and assessing a tri-layer skin model, which could have future applications in wound healing, drug / disease modelling and cosmetics testing.

8.1 Characterisation of the Agarose Fluid Gel Bed

The supporting fluid gel bed was initially studied to describe how it behaves during formulation, handling and extrusion of material within it. Using a series of analytical techniques, ranging from mechanical testing, through to particle sizing and microscopic evaluation, and also by employing centrifugation procedures for extraction of fluid gel phases, an improved understanding of suspended manufacture function was met. It was deduced that the way in which agarose supporting matrices are formulated play a pivotal part in the mechanical properties they harbour. Freshly prepared agarose fluid gels had markedly increased mechanical properties compared with their diluted fluid gel counterparts of equivalent concentration. Deeper exploration into defining the particle sizes and particle volume fractions within fluid gel systems of differing concentrations gave further explanation into the support-bed mechanism of action. Fluid gels with concentrations above 0.5% exhibited greater particle size heterogeneity, attributed to the modified local shear environment on particles within more viscous solutions. In turn, the high viscosity of fluid gels over 0.5% proved difficult to allow material deposition and construct formation. Although particle size distribution was more homogenous within fluid gels below 0.5% concentration, sufficient particle volume fractions were

lacking, leading to poor mechanical properties and the inability to uphold deposited material. Taken together, these data were applied toward optimum formulation conditions for the research to follow.

Despite these advances, the highly complex nature of agarose fluid gel systems dictates that much more research requires undertaking. Many parameters must be tightly controlled and regulated for a specified outcome during fluid gel formation. Indeed, formulation method and concentration have both been seen to impact upon fluid gel mechanics, yet there are other parameters which also modulate the behaviour of fluid gels. For instance, cooling rate influences fluid gel particle formation and subsequently dictates the overall status of fluid gel viscosity. Even though all agarose solutions were autoclaved under identical conditions of temperature and pressure, and an end temperature of 25 °C was implemented for all formulations, it would be advantageous if the rate of cooling was also controlled in order to reduce batch-to-batch variability. Likewise, different shear rates and shearing methods (using a magnetic flea, rheometer cone and plate geometry, jacketed pin stirrer or overhead impeller) have all been seen to generate rheological and particle morphological variances within fluid gels. Achieving an understanding of all of these aspects combined for fluid gel formation would require an extensive project in itself, yet ample research was conducted, in this thesis, to successfully manipulate fluid gel characteristics for the fabrication of complex hydrogel scaffolds and constructs.

8.2 Suspended Layer Additive Manufacturing (SLAM)

Following the transition from printing by hand to the installation of a commercially available 3D bioprinter, Suspended Layer Additive Manufacture (SLAM) was born. System methodology was further characterised and consolidated by describing the printing resolution within the support bed using a combination of different printing parameters, and the diffusion of dyes within the fluid gel bath was also monitored. Other avenues for agarose support bath formulation were explored in the form of an agarose microparticle slurry as referenced in the literature, and it was concluded that fluid gel formation is critical to the behaviour of the supporting matrix. A series of cell-containing disc-

shaped constructs made of different materials were manufactured which were diverse in their chemical and mechanical natures. Alternative tissue engineering structures were also compared by freeze drying and cell seeding tissue engineering sponges. Research into a range of different 3D printed geometries was then conducted to define the potential of the system to generate intricate, bulk, hollow and bifurcating features within a 3D tissue mimic.

Two different dyes of differing molecular weights were extruded within the agarose bed to examine dye diffusion over time. To better study the diffusion timescales of the calcium chloride dihydrate crosslinker, from injection within the support bed to total crosslinking of scaffolds, a calcium-specific marker could be used to trace the diffusion rate. Although dye diffusion offered some insight into how crosslinker would traverse across the support bed and throughout the printed construct, methylene blue, dimethylmethylene blue and calcium chloride all exhibit different chemical structures and molecular weights and more work would need to be done to assess their mechanisms of diffusion within an agarose fluid gel. Reagents arsenazo III and o-cresolpthalein complexone have previously been used for the detection and quantification of serum calcium using colorimetric assays (Janssen, 1991; Stern, 1957). Further research into characterising calcium chloride dihydrate diffusion within agarose fluid gels by exploring the suitability of these reagents could aid in defining and characterising crosslinker diffusion as used in the SLAM system.

Other future recommendations for this chapter include further research into different hydrogels, cell types and geometrical shapes that are compatible within the SLAM technology.

8.3 3D Bioprinting Multi-Layer Constructs

Different cells were successfully combined with biopolymer solutions and then crosslinked, following printing, to create cell-loaded biopolymer hydrogel constructs. It should also be possible to load scaffolds and constructs with drugs, growth-factors and other bioactives toward therapeutic intervention in the form of tissue engineering implants. Some work towards this end was conducted

by loading ibuprofen and IgG antibodies within discrete regions of hydrogel and sponge core-shell scaffolds (data not included in this thesis). The release profiles and dissolution rates of the bioactives and also the degradation rates of the scaffolds were then measured *in-vitro*, although further testing and statistical analyses would be required to acquire sufficient data and establish conclusions.

Another preliminary study using PCR was conducted as a quantitative measure for reviewing cell suspension or attachment in dual layer scaffolds (data not shown). During fluorescence microscopy, it appeared evident that cells within collagen were attached to the matrix, whereas cells within gellan or alginate layers were suspended rather than attached due to the lack of attachment-conducive structures within these materials. Integrins α1β1 and α2β1 gene expression levels were measured in each layer and were found to be markedly upregulated in cells within the collagen layers compared to cells within gellan or alginate layers. A greater number of constructs would require testing in order to gain enough sample data to validate and deduce a statistically significant difference in future work.

8.4 Design and Manufacture of a Tri-Layer Skin Model

By amalgamating previous research on interpreting fluid gel behaviour, defining SLAM resolution and producing complex, multi-layer constructs, the fabrication of a tri-layer skin model for implantation within chronic wounds was proposed. The model was designed so that epidermis, dual compartment dermis and hypodermis all existed within a single tissue engineering construct by carefully selecting cells and biopolymer hydrogels to mimic the salient ECM environments within each layer. Initially, human epidermal keratinocytes (HEK), human dermal fibroblasts (HDF) and stromal vascular fraction (SVF) cell populations were extracted from a human abdominoplasty. Erythrocytes, hematopoietic stem cells and smooth muscle cells were eliminated from SVF fractions so that only ADSC remained for propagation. This was confirmed by evaluating cell marker status using flow cytometry and the differentiation capacity of ADSC was demonstrated by culture within adipogenic and osteogenic conditions. For the printing process, collagen / pectin blends of defined

ratio were mixed with cell populations at controlled densities to reflect native skin. Hypodermis was printed, followed by printing of reticular dermis and then papillary dermis before crosslinking with calcium chloride crosslinker for the pectin element of the construct whilst the collagen element underwent thermal gelation at 37 °C. Constructs were cultured for two weeks within adipogenic media to allow differentiation of ADSC into lipid-secreting cells. Keratinocytes were then seeded atop the cultured part and was cultured for one further week at the air-liquid interface. Following a total culture period of 21 days, constructs were vertically cross sectioned into three parts and processed using either paraffin embedding, cryosectioning or leaving unprocessed. Paraffin embedded construct sections were stained with Haematoxylin and Eosin for identification of the major layers in both human and 3D printed skin, revealing the strong similarities between the two. Cryosectioned constructs underwent immunohistochemical analysis for determining the presence of CK10, CK14 and tranglutaminase as a result of terminally differentiating keratinocytes within the epidermis. IHC staining showed indications of keratinocyte maturation within the epidermal portion of the construct, however further culture periods would be needed to further verify this. Unprocessed construct sections were stained with Hoechst and actin to observe cells within constructs and also in separate 3D cultures under a confocal microscope. The designed cell density within the 3D bioprinted layers were successfully re-imagined within the 3D model although the number of keratinocytes was not reflective of the seeding density. Further validation of the success of the construct was presented in the form of shear rheology and the graduated mechanical properties within the part, scanning electron microscopy and the graduated microarchitectural properties within the part and also by implantation within a porcine wound model.

The SLAM method holds vast amounts of potential within the tissue engineering arena and therefore many possible avenues for future research. Whilst it has been shown that multiple bioinks can be layered to assemble a 3D trilayer skin model, longer culture periods could allow the emergence of more mature and better-substantiated skin equivalents. Once this has been established, it would be

possible to incorporate other types of skin cells, including merkel cells, Langerhans cells, melanocytes and sebocytes, as well as additional ECM components, such as elastin and fibronectin, to better restore the function of defective skin. In addition, exploration into loading therapeutics relevant to wound healing by loading gold nanoparticles within the construct was made (data not shown), yet more characterisation into the effectiveness of this feature would be required to justify its use within the implant.

Other areas of research requiring attention are those of defining and recapitulating the mechanical properties in native skin within the tissue engineering construct and the subsequent degradation profile of the printed part as the potential patient's endogenous tissue infiltrates the lesioned area.

As a whole, this work has demonstrated the scope of the SLAM system in creating complex, multi-layered tissue engineering parts with limitless potential in reimagining human tissues and organs. This kind of research is key for future innovation and could drastically reduce the need for animal testing in cosmetics research and drug / disease modelling, and relieve the pressures of organ-donor waiting lists by fabricating patient-specific tissues, on demand, within the clinic.

References

Abdo, J. M., Sopko, N. A., & Milner, S. M. (2020). The applied anatomy of human skin: A model for regeneration. *Wound Medicine*. https://doi.org/10.1016/j.wndm.2020.100179

Abdollahi, S., Davis, A., Miller, J. H., & Feinberg, A. W. (2018). Expert-guided optimization for 3D printing of soft and liquid materials. *PLoS ONE*. https://doi.org/10.1371/journal.pone.0194890

Achilli, M., & Mantovani, D. (2010). Tailoring mechanical properties of collagen-based scaffolds for vascular tissue engineering: The effects of pH, temperature and ionic strength on gelation. *Polymers*, *2*(4), 664–680. https://doi.org/10.3390/polym2040664

Alberts, B., Johnson, A., Lewis, J., Raff, M., Roberts, K., & Walter, P. (2002). *Molecular Biology of the Cell* (4th ed.). New York: Garland Science.

Aldag, C., Teixeira, D. N., & Leventhal, P. S. (2016). Skin rejuvenation using cosmetic products containing growth factors, cytokines, and matrikines: A review of the literature. *Clinical, Cosmetic and Investigational Dermatology*. https://doi.org/10.2147/CCID.S116158

Andrew, A., & Rawdon, B. B. (1987). The embryonic origin of connective tissue mast cells. *J Anat*, *150*, 219–227. Retrieved from http://www.ncbi.nlm.nih.gov/entrez/query.fcgi?cmd=Retrieve&db=PubMed&dopt=Citation&list_uids=3654335

Annabi, N., Nichol, J. W., Zhong, X., Ji, C., Koshy, S., Khademhosseini, A., & Dehghani, F. (2010). Controlling the porosity and microarchitecture of hydrogels for tissue engineering. *Tissue Engineering - Part B: Reviews*. https://doi.org/10.1089/ten.teb.2009.0639

Antoine, E. E., Vlachos, P. P., & Rylander, M. N. (2014). Review of Collagen I Hydrogels for Bioengineered Tissue Microenvironments: Characterization of Mechanics, Structure, and Transport. *Tissue Engineering Part B: Reviews*, *20*(6), 683–696. https://doi.org/10.1089/ten.teb.2014.0086

Apalla, Z., Lallas, A., Sotiriou, E., Lazaridou, E., & Ioannides, D. (2017). Epidemiological trends in skin cancer. *Dermatology Practical & Conceptual*. https://doi.org/10.5826/dpc.0702a01

Aramwit, P. (2016). Introduction to biomaterials for wound healing. In *Wound Healing Biomaterials* (Vol. 2, pp. 3–38). https://doi.org/10.1016/B978-1-78242-456-7.00001-5

Araña, M., Mazo, M., Aranda, P., Pelacho, B., & Prosper, F. (2013). Adipose tissue-derived mesenchymal stem cells: Isolation, expansion, and characterization. *Methods in Molecular Biology*. https://doi.org/10.1007/978-1-62703-511-8_4

Atala, A., Lanza, R., Thomson, J. A., & Nerem, R. M. (2008). *Principles of Regenerative Medicine*. *Principles of Regenerative Medicine*. https://doi.org/10.1016/B978-0-12-369410-2.X5001-3

Ballyns, J. J., & Bonassar, L. J. (2009). Image-guided tissue engineering. *Journal of Cellular and Molecular Medicine*. https://doi.org/10.1111/j.1582-4934.2009.00836.x

Benhardt, H. A., & Cosgriff-Hernandez, E. M. (2009). The Role of Mechanical Loading in Ligament Tissue Engineering. *Tissue Engineering Part B: Reviews*. https://doi.org/10.1089/ten.teb.2008.0687

Berry, F. (1920). The Regeneration of Smooth Muscle Cells. *Journal of Medical Research, 41*(3), 365–372.

Betts, J. G., Young, K. A., Wise, J. A., Johnson, E., Poe, B., Kruse, D. H., … DeSaix, P. (2013). *Anatomy and Physiology*. Houston, Texas: OpenStax. Retrieved from https://openstax.org/books/anatomy-and-physiology/pages/5-3-functions-of-the-integumentary-system

Bhattacharjee, T., Zehnder, S. M., Rowe, K. G., Jain, S., Nixon, R. M., Sawyer, W. G., & Angelini, T. E. (2015). Writing in the granular gel medium. *Science Advances, 1*(8). https://doi.org/10.1126/sciadv.1500655

Biodermis. (2018). Understanding Different Types of Wounds. Retrieved July 1, 2020, from https://www.biodermis.com/understanding-different-types-of-wounds-s/240.htm

Biron, M. (2015). Thermoplastic Material Selection. In *Material Selection for Thermoplastic Parts* (pp. 1–38). https://doi.org/10.1016/b978-0-7020-6284-1.00001-5

Blaeser, A., Duarte Campos, D. F., Puster, U., Richtering, W., Stevens, M. M., & Fischer, H. (2016). Controlling Shear Stress in 3D Bioprinting is a Key Factor to Balance Printing Resolution and Stem Cell Integrity. *Advanced Healthcare Materials*. https://doi.org/10.1002/adhm.201500677

Blanpain, C., & Fuchs, E. (2014). Plasticity of epithelial stem cells in tissue regeneration. *Science*. https://doi.org/10.1126/science.1242281

Boeira, V. L. S. Y., Souza, E. S., Rocha, B. de O., Oliveira, P. D., Oliveira, M. de F. S. P. de, Rêgo, V. R. P. de A., & Follador, I. (2013). Inherited epidermolysis bullosa: clinical and therapeutic aspects. *Anais Brasileiros de Dermatologia*. https://doi.org/10.1590/s0365-05962013000200001

Boneva, R. S., Folks, T. M., & Chapman, L. E. (2001). Infectious disease issues in xenotransplantation. *Clinical Microbiology Reviews*. https://doi.org/10.1128/CMR.14.1.1-14.2001

Brown, B. N., Valentin, J. E., Stewart-Akers, A. M., McCabe, G. P., & Badylak, S. F. (2009). Macrophage phenotype and remodeling outcomes in response to biologic scaffolds with and without a cellular component. *Biomaterials*, *30*(8), 1482–1491. https://doi.org/10.1016/j.biomaterials.2008.11.040

Butcher, D. T., Alliston, T., & Weaver, V. M. (2009). A tense situation: Forcing tumour progression. *Nature Reviews Cancer*. https://doi.org/10.1038/nrc2544

Cabrera, M. S., Sanders, B., Goor, O. J. G. M., Driessen-Mol, A., Oomens, C. W. J., & Baaijens, F. P. T. (2017). Computationally Designed 3D Printed Self-Expandable Polymer Stents with Biodegradation Capacity for Minimally Invasive Heart Valve Implantation: A Proof-of-Concept Study. *3D Printing and Additive Manufacturing*. https://doi.org/10.1089/3dp.2016.0052

Caliari, S. R., & Burdick, J. A. (2016). A practical guide to hydrogels for cell culture. *Nature Methods*. https://doi.org/10.1038/nmeth.3839

Caliari, S. R., Ramirez, M. A., & Harley, B. A. C. (2011). The development of collagen-GAG scaffold-membrane composites for tendon tissue engineering. *Biomaterials*, *32*(34), 8990–8998. https://doi.org/10.1016/j.biomaterials.2011.08.035

Calvo, G. H., Cosenza, V. A., Sáenz, D. A., Navarro, D. A., Stortz, C. A., Céspedes, M. A., … Di Venosa, G. M. (2019). Disaccharides obtained from carrageenans as potential antitumor agents. *Scientific Reports*. https://doi.org/10.1038/s41598-019-43238-y

Carola, R., Harley, J. P., & Noback, C. R. (1990). *Human Anatomy and Physiology*. McGraw-Hill Companies.

Carrier, P. (2018). 3D Printer Print Speed Calculation: How to find the optimal speed for reliable and constant print quality. Retrieved February 6, 2020, from https://dyzedesign.com/2018/07/3d-print-speed-calculation-find-optimal-speed/

Carsin, H., Ainaud, P., Le Bever, H., Rives, J. M., Lakhel, A., Stephanazzi, J., … Perrot, J. (2000). Cultured epithelial autografts in extensive burn coverage of severely traumatized patients: A five year single-center experience with 30 patients. *Burns*. https://doi.org/10.1016/S0305-4179(99)00143-6

Chan, B. P., & Leong, K. W. (2008). Scaffolding in tissue engineering: General approaches and tissue-specific considerations. In *European Spine Journal* (Vol. 17). https://doi.org/10.1007/s00586-008-0745-3

Chandrasekaran, R. (1998). X-Ray Diffraction of Food Polysaccharides. In *Advances in Food and Nutrition Research* (Vol. 42, pp. 131–210). https://doi.org/10.1016/S1043-4526(08)60095-9

Chen, F. M., & Liu, X. (2016). Advancing biomaterials of human origin for tissue engineering. *Progress in Polymer Science*. https://doi.org/10.1016/j.progpolymsci.2015.02.004

Chen, M., Przyborowski, M., & Berthiaume, F. (2009). Stem cells for skin tissue engineering and wound healing. *Critical Reviews in Biomedical Engineering*, *37*(4–5), 399–421. Retrieved from http://www.ncbi.nlm.nih.gov/pubmed/20528733%0Ahttp://www.pubmedcentral.nih.gov/articlerender.fcgi?artid=PMC3223487

Cheng, D. C. H. (1986). Yield stress: A time-dependent property and how to measure it. *Rheologica Acta*. https://doi.org/10.1007/BF01774406

Chua, C. K., & Yeong, W. Y. (2014). *Bioprinting: Principles and Applications*. Singapore: World Scientific Publishing Co. Pte. Ltd.

Chuong, C. M., Nickoloff, B. J., Elias, P. M., Goldsmith, L. A., Macher, E., Maderson, P. A., … Christophers, E. (2002). What is the “true” function of skin? *Experimental Dermatology*. https://doi.org/10.1034/j.1600-0625.2002.00112.x

Clinic, M. (2020). Melanoma. Retrieved July 1, 2020, from https://www.mayoclinic.org/diseases-conditions/melanoma/symptoms-causes/syc-20374884

Cooke, M. E., Jones, S. W., ter Horst, B., Moiemen, N., Snow, M., Chouhan, G., … Grover, L. M. (2018). Structuring of Hydrogels across Multiple Length Scales for Biomedical Applications. *Advanced Materials*. https://doi.org/10.1002/adma.201705013

Costa, E. C., Moreira, A. F., de Melo-Diogo, D., Gaspar, V. M., Carvalho, M. P., & Correia, I. J. (2016). 3D tumor spheroids: an overview on the tools and techniques used for their analysis. *Biotechnology Advances*. https://doi.org/10.1016/j.biotechadv.2016.11.002

Cox, T. R., & Erler, J. T. (2011). Remodeling and homeostasis of the extracellular matrix: implications for fibrotic diseases and cancer. *Disease Models & Mechanisms*, *4*(2), 165–178. https://doi.org/10.1242/dmm.004077

Darvell, B. W. (2018). *Materials science for dentistry*. *Materials Science for Dentistry*. https://doi.org/10.1016/C2015-0-05454-5

Dawood, A., Marti, B. M., Sauret-Jackson, V., & Darwood, A. (2015). 3D printing in dentistry. *British Dental Journal*. https://doi.org/10.1038/sj.bdj.2015.914

Deshpande, A. (2018). Techniques in oscillatory shear rheology. *Physics.Iitm.Ac.In*.

Dhasmana, A., Singh, S., Kadian, S., & Singh, L. (2018). Skin Tissue Engineering: Principles and Advances. *J Dermatol Skin*.

Di Luca, A., Longoni, A., Criscenti, G., Mota, C., Van Blitterswijk, C., & Moroni, L. (2016). Toward mimicking the bone structure: Design of novel hierarchical scaffolds with a tailored radial porosity gradient. *Biofabrication*. https://doi.org/10.1088/1758-5090/8/4/045007

Di Prima, M., Coburn, J., Hwang, D., Kelly, J., Khairuzzaman, A., & Ricles, L. (2016). Additively manufactured medical products – the FDA perspective. *3D Printing in Medicine*, *2*(1). https://doi.org/10.1186/s41205-016-0005-9

Diegel, K. L., Danilenko, D. M., & Wojcinski, Z. W. (2018). The Integumentary System. In *Fundamentals of Toxicologic Pathology: Third Edition*. https://doi.org/10.1016/B978-0-12-809841-7.00025-3

Do, A. V., Khorsand, B., Geary, S. M., & Salem, A. K. (2015). 3D Printing of Scaffolds for Tissue Regeneration Applications. *Advanced Healthcare Materials*. https://doi.org/10.1002/adhm.201500168

Dong, C., & Lv, Y. (2016). Application of collagen scaffold in tissue engineering: Recent advances and new perspectives. *Polymers*. https://doi.org/10.3390/polym8020042

Dong, Z., Li, Y., Lin, M., & Li, M. (2009). Rheological properties of polymer micro-gel dispersions. *Petroleum Science*. https://doi.org/10.1007/s12182-009-0047-3

Doulabi, A. H., Mequanint, K., & Mohammadi, H. (2014). Blends and nanocomposite biomaterials for articular cartilage tissue engineering. *Materials*. https://doi.org/10.3390/ma7075327

Doyle, A. D., Carvajal, N., Jin, A., Matsumoto, K., & Yamada, K. M. (2015). Local 3D matrix microenvironment regulates cell migration through spatiotemporal dynamics of contractility-dependent adhesions. *Nature Communications*. https://doi.org/10.1038/ncomms9720

Duan, B., Hockaday, L. A., Kang, K. H., & Butcher, J. T. (2013). 3D Bioprinting of heterogeneous aortic valve conduits with alginate/gelatin hydrogels. *Journal of Biomedical Materials Research - Part A*, *101 A*(5), 1255–1264. https://doi.org/10.1002/jbm.a.34420

Dutta Roy, T., Simon, J. L., Ricci, J. L., Rekow, E. D., Thompson, V. P., & Parsons, J. R. (2003). Performance of degradable composite bone repair products made via three-dimensional fabrication techniques. *Journal of Biomedical Materials Research - Part A*. https://doi.org/10.1002/jbm.a.10582

Dzobo, K., Thomford, N. E., Senthebane, D. A., Shipanga, H., Rowe, A., Dandara, C., … Motaung, K. S. C. M. (2018). Advances in regenerative medicine and tissue engineering: Innovation and transformation of medicine. *Stem Cells International*, *2018*. https://doi.org/10.1155/2018/2495848

Engler, A. J., Sen, S., Sweeney, H. L., & Discher, D. E. (2006). Matrix elasticity directs stem cell lineage specification. *Cell*, *126*(4), 677–689. https://doi.org/10.1016/j.cell.2006.06.044

Falanga, V., Faria, K., & Bollenbach, T. (2013). Bioengineered Skin Constructs. In *Principles of Tissue Engineering: Fourth Edition*. https://doi.org/10.1016/B978-0-12-398358-9.00077-X

Fantini, M., Curto, M., & De Crescenzio, F. (2016). A method to design biomimetic scaffolds for bone tissue engineering based on Voronoi lattices. *Virtual and Physical Prototyping*. https://doi.org/10.1080/17452759.2016.1172301

Farroha, A., Frew, Q., El-Muttardi, N., Philp, B., & Dziewulski, P. (2013). The use of biobrane® to dress split-thickness skin graft in paediatric burns. *Annals of Burns and Fire Disasters*.

Fernández-Cossío, S., León-Mateos, A., Sampedro, F. G., & Oreja, M. T. C. (2007). Biocompatibility of agarose gel as a dermal filler: Histologic evaluation of subcutaneous implants. *Plastic and Reconstructive Surgery*. https://doi.org/10.1097/01.prs.0000279475.99934.71

Fernández Farrés, I., Moakes, R. J. A., & Norton, I. T. (2014a). Designing biopolymer fluid gels: A microstructural approach. *Food Hydrocolloids*, *42*, 362–372. https://doi.org/10.1016/j.foodhyd.2014.03.014

Fernández Farrés, I., Moakes, R. J. A., & Norton, I. T. (2014b). Designing biopolymer fluid gels: A microstructural approach. *Food Hydrocolloids*, *42*(P3), 362–372. https://doi.org/10.1016/j.foodhyd.2014.03.014

Fernández Farrés, I., & Norton, I. T. (2014). Formation kinetics and rheology of alginate fluid gels produced by in-situ calcium release. *Food Hydrocolloids*. https://doi.org/10.1016/j.foodhyd.2014.02.005

Findlay, M. W., & Gurtner, G. C. (2017). Engineering Niches for Skin and Wound Healing. In *Biology and Engineering of Stem Cell Niches*. https://doi.org/10.1016/B978-0-12-802734-9.00035-4

Fitzpatrick, L. E., & McDevitt, T. C. (2015). Cell-derived matrices for tissue engineering and regenerative medicine applications. *Biomaterials Science*. https://doi.org/10.1039/c4bm00246f

Froehlich, K., Haeger, J. D., Heger, J., Pastuschek, J., Photini, S. M., Yan, Y., … Schmidt, A. (2016). Generation of Multicellular Breast Cancer Tumor Spheroids: Comparison of Different Protocols. *Journal of Mammary Gland Biology and Neoplasia*. https://doi.org/10.1007/s10911-016-9359-2

Frykberg, R. G., & Banks, J. (2015). Challenges in the Treatment of Chronic Wounds. *Advances in Wound Care*. https://doi.org/10.1089/wound.2015.0635

Galarraga, J. H., Kwon, M. Y., & Burdick, J. A. (2019). 3D bioprinting via an in situ crosslinking technique towards engineering cartilage tissue. *Scientific Reports*. https://doi.org/10.1038/s41598-019-56117-3

Garrec, D. A., Guthrie, B., & Norton, I. T. (2013). Kappa carrageenan fluid gel material properties. Part 1: Rheology. *Food Hydrocolloids*. https://doi.org/10.1016/j.foodhyd.2013.02.014

Gasperini, L., Mano, J. F., & Reis, R. L. (2014). Natural polymers for the microencapsulation of cells. *Journal of the Royal Society Interface*. https://doi.org/10.1098/rsif.2014.0817

Gaur, M., Dobke, M., & Lunyak, V. V. (2017). Mesenchymal stem cells from adipose tissue in clinical applications for dermatological indications and skin aging. *International Journal of Molecular Sciences*. https://doi.org/10.3390/ijms18010208

Geerligs, M. (2010). , *Skin layer mechanics*. *Skin layer mechanics*. https://doi.org/10.6100/IR657803

Gefen, A., & Dilmoney, B. (2007). Mechanics of the normal woman's breast. *Technology and Health Care*. https://doi.org/10.3233/thc-2007-15404

Giusto, G., Vercelli, C., Comino, F., Caramello, V., Tursi, M., & Gandini, M. (2017). A new, easy-to-make pectin-honey hydrogel enhances wound healing in rats. *BMC Complementary and Alternative Medicine*. https://doi.org/10.1186/s12906-017-1769-1

Grogan, S. P., Pauli, C., Chen, P., Du, J., Chung, C. B., Kong, S. D., … D'Lima, D. D. (2012). In Situ Tissue Engineering Using Magnetically Guided Three-Dimensional Cell Patterning . *Tissue Engineering Part C: Methods*, *18*(7), 496–506. https://doi.org/10.1089/ten.tec.2011.0525

Guest, J. F., Vowden, K., & Vowden, P. (2017). The health economic burden that acute and chronic wounds impose on an average clinical commissioning group/ health board in the UK. *Journal of Wound Care*. https://doi.org/10.12968/jowc.2017.26.6.292

Guillemot, F., Souquet, A., Catros, S., & Guillotin, B. (2010). Laser-assisted cell printing: Principle, physical parameters versus cell fate and perspectives in tissue engineering. *Nanomedicine*. https://doi.org/10.2217/nnm.10.14

Gungor-Ozkerim, P. S., Inci, I., Zhang, Y. S., Khademhosseini, A., & Dokmeci, M. R. (2018). Bioinks for 3D bioprinting: An overview. *Biomaterials Science*. https://doi.org/10.1039/c7bm00765e

Haga, H., Irahara, C., Kobayashi, R., Nakagaki, T., & Kawabata, K. (2005). Collective movement of epithelial cells on a collagen gel substrate. *Biophysical Journal*. https://doi.org/10.1529/biophysj.104.047654

Halász, G., Gyüre, B., Jánosi, I. M., Szabó, K. G., & Tél, T. (2007). Vortex flow generated by a magnetic stirrer. *American Journal of Physics*. https://doi.org/10.1119/1.2772287

Hartman, C. D., Isenberg, B. C., Chua, S. G., & Wong, J. Y. (2017). Extracellular matrix type modulates cell migration on mechanical gradients. *Experimental Cell Research*. https://doi.org/10.1016/j.yexcr.2017.08.018

He, P., Zhao, J., Zhang, J., Li, B., Gou, Z., Gou, M., & Li, X. (2018). Bioprinting of skin constructs for wound healing. *Burns & Trauma*. https://doi.org/10.1186/s41038-017-0104-x

Heath, C. (2000). Cells for tissue engineering. *Trends in Biotechnology*, *18*(1).

Hench, L. L., & Jones, J. R. (2005). *Biomaterials, artificial organs and tissue engineering*. *Biomaterials, Artificial Organs and Tissue Engineering*. https://doi.org/10.1533/9781845690861

Henry, J. A., Simonet, M., Pandit, A., & Neuenschwander, P. (2007). Characterization of a slowly degrading biodegradable polyesterurethane for tissue engineering scaffolds. *Journal of Biomedical Materials Research - Part A*. https://doi.org/10.1002/jbm.a.31094

Hicklin, R. A. (2014). Anatomy of Friction Ridge Skin. In *Encyclopedia of Biometrics*. https://doi.org/10.1007/978-3-642-27733-7_48-3

Highley, C. B., Rodell, C. B., & Burdick, J. A. (2015). Direct 3D Printing of Shear-Thinning Hydrogels into Self-Healing Hydrogels. *Advanced Materials*, *27*(34), 5075–5079. https://doi.org/10.1002/adma.201501234

Hinton, T. J., Jallerat, Q., Palchesko, R. N., Park, J. H., Grodzicki, M. S., Shue, H. J., … Feinberg, A. W. (2015). Three-dimensional printing of complex biological structures by freeform reversible embedding of suspended hydrogels. *Science Advances*, *1*(9). https://doi.org/10.1126/sciadv.1500758

Hoare, T. R., & Kohane, D. S. (2008). Hydrogels in drug delivery: Progress and challenges. *Polymer*. https://doi.org/10.1016/j.polymer.2008.01.027

Hodgkinson, T., Yuan, X. F., & Bayat, A. (2009). Adult stem cells in tissue engineering. *Expert Review of Medical Devices*. https://doi.org/10.1586/erd.09.48

Hollister, S. J. (2005). Porous scaffold design for tissue engineering. *Nature Materials*. https://doi.org/10.1093/jb/mvj031

Howard, D., Buttery, L. D., Shakesheff, K. M., & Roberts, S. J. (2008). Tissue engineering: Strategies, stem cells and scaffolds. *Journal of Anatomy*. https://doi.org/10.1111/j.1469-7580.2008.00878.x

Huang, C., Dai, J., & Zhang, X. A. (2015). Environmental physical cues determine the lineage specification of mesenchymal stem cells. *Biochimica et Biophysica Acta - General Subjects*. https://doi.org/10.1016/j.bbagen.2015.02.011

Huang, S. P., Hsu, C. C., Chang, S. C., Wang, C. H., Deng, S. C., Dai, N. T., … Huang, S. M. (2012). Adipose-derived stem cells seeded on acellular dermal matrix grafts enhance wound healing in a murine model of a full-thickness defect. *Annals of Plastic Surgery*. https://doi.org/10.1097/SAP.0b013e318273f909

Huebsch, N., Arany, P. R., Mao, A. S., Shvartsman, D., Ali, O. A., Bencherif, S. A., … Mooney, D. J. (2010). Harnessing traction-mediated manipulation of the cell/matrix interface to control stem-cell fate. *Nature Materials*. https://doi.org/10.1038/nmat2732

Humphrey, J. D., Dufresne, E. R., & Schwartz, M. A. (2014). Mechanotransduction and extracellular matrix homeostasis. *Nature Reviews. Molecular Cell Biology*, *15*(12), 802–812. https://doi.org/10.1038/nrm3896

Ikada, Y. (2006). Challenges in tissue engineering. *Journal of the Royal Society Interface*. https://doi.org/10.1098/rsif.2006.0124

Jeon, O., Lee, Y. Bin, Jeong, H., Lee, S. J., Wells, D., & Alsberg, E. (2019). Individual cell-only bioink and photocurable supporting medium for 3D printing and generation of engineered tissues with complex geometries. *Materials Horizons*. https://doi.org/10.1039/c9mh00375d

Kai, C. C., Jacob, G. G. K., & Mei, T. (1997). Interface between CAD and rapid prototyping systems. Part 1: A study of existing interfaces. *International Journal of Advanced Manufacturing Technology*. https://doi.org/10.1007/BF01176300

Kang, H. W., Lee, S. J., Ko, I. K., Kengla, C., Yoo, J. J., & Atala, A. (2016). A 3D bioprinting system to produce human-scale tissue constructs with structural integrity. *Nature Biotechnology*, *34*(3), 312–319. https://doi.org/10.1038/nbt.3413

Kanta, J. (2015). Collagen matrix as a tool in studying fibroblastic cell behavior. *Cell Adhesion and Migration*. https://doi.org/10.1080/19336918.2015.1005469

Kasaai, M. R., Arul, J., & Charlet, G. (2000). Intrinsic viscosity-molecular weight relationship for chitosan. *Journal of Polymer Science, Part B: Polymer Physics*. https://doi.org/10.1002/1099-0488(20001001)38:19<2591::AID-POLB110>3.0.CO;2-6

Kass, L., Erler, J. T., Dembo, M., & Weaver, V. M. (2007). Mammary epithelial cell: Influence of extracellular matrix composition and organization during development and tumorigenesis. *International Journal of Biochemistry and Cell Biology*. https://doi.org/10.1016/j.biocel.2007.06.025

Kavanagh, G. M., & Ross-Murphy, S. B. (1998). Rheological characterisation of polymer gels. *Progress in Polymer Science (Oxford)*. https://doi.org/10.1016/S0079-6700(97)00047-6

Kawasumi, A., Sagawa, N., Hayashi, S., Yokoyama, H., & Tamura, K. (2013). Wound healing in mammals and amphibians: Toward limb regeneration in mammals. *Current Topics in Microbiology and Immunology*. https://doi.org/10.1007/82-2012-305

Keren, D. F. (2003). *Protein Electrophoresis in Clinical Diagnosis*. London: Arnold.

Khademhosseini, A., & Langer, R. (2016). A decade of progress in tissue engineering. *Nature Protocols*, *11*(10), 1775–1781. https://doi.org/10.1038/nprot.2016.123

Kim, B. S., Gao, G., Kim, J. Y., & Cho, D. W. (2019). 3D Cell Printing of Perfusable Vascularized Human Skin Equivalent Composed of Epidermis, Dermis, and Hypodermis for Better Structural Recapitulation of Native Skin. *Advanced Healthcare Materials*. https://doi.org/10.1002/adhm.201801019

Kim, I. L., Mauck, R. L., & Burdick, J. A. (2011). Hydrogel design for cartilage tissue engineering: A case study with hyaluronic acid. *Biomaterials*, *32*(34), 8771–8782. https://doi.org/10.1016/j.biomaterials.2011.08.073

Kim, J. D., Choi, J. S., Kim, B. S., Chan Choi, Y., & Cho, Y. W. (2010). Piezoelectric inkjet printing of polymers: Stem cell patterning on polymer substrates. *Polymer*, *51*(10), 2147–2154. https://doi.org/10.1016/j.polymer.2010.03.038

Kim, J. H., Jung, M., Kim, H. S., Kim, Y. M., & Choi, E. H. (2011). Adipose-derived stem cells as a new therapeutic modality for ageing skin. *Experimental Dermatology*. https://doi.org/10.1111/j.1600-0625.2010.01221.x

Kirschstein, R., & Skirboll, L. (2001). Stem cells: scientific progress and future research directions. *Depatment of Health and Human Services.*, (June). Retrieved from http://scholar.google.com/scholar?hl=en&btnG=Search&q=intitle:Stem+Cells:+Scientific+Progress+and+Future+Research+Directions#0

Koch, T. G., Berg, L. C., & Betts, D. H. (2009). Current and future regenerative medicine-Principles, concepts, and therapeutic use of stem cell therapy and tissue engineering in equine medicine. *Canadian Veterinary Journal*.

Koeck, F. X., Beckmann, J., Luring, C., Rath, B., Grifka, J., & Basad, E. (2011). Evaluation of implant position and knee alignment after patient-specific unicompartmental knee arthroplasty. *Knee*, *18*(5), 294–299. https://doi.org/10.1016/j.knee.2010.06.008

Kular, J. K., Basu, S., & Sharma, R. I. (2014). The extracellular matrix: Structure, composition, age-related differences, tools for analysis and applications for tissue engineering. *Journal of Tissue Engineering*. https://doi.org/10.1177/2041731414557112

Kulikouskaya, V., Kraskouski, A., Hileuskaya, K., Zhura, A., Tratsyak, S., & Agabekov, V. (2019). Fabrication and characterization of pectin-based three-dimensional porous scaffolds suitable for treatment of peritoneal adhesions. *Journal of Biomedical Materials Research - Part A*. https://doi.org/10.1002/jbm.a.36700

Kyle, S., Jessop, Z. M., Al-Sabah, A., & Whitaker, I. S. (2017). 'Printability'' of Candidate Biomaterials for Extrusion Based 3D Printing: State-of-the-Art.' *Advanced Healthcare Materials*. https://doi.org/10.1002/adhm.201700264

Langenbach, F., & Handschel, J. (2013). Effects of dexamethasone, ascorbic acid and β-glycerophosphate on the osteogenic differentiation of stem cells in vitro. *Stem Cell Research and Therapy*. https://doi.org/10.1186/scrt328

Langer, R., & Vacanti, J. P. (1993). Tissue Engineering. *Science*, *240*(1).

Lanza, R., Langer, R., & Vacanti, J. P. (2013). *Principles of Tissue Engineering: Fourth Edition*. *Principles of Tissue Engineering: Fourth Edition*. https://doi.org/10.1016/C2011-0-07193-4

Lawton, S. (2019). Skin 1: the structure and functions of the skin | Nursing Times. *Nursing Times*.

Lee, K., Silva, E. A., & Mooney, D. J. (2011). Growth factor delivery-based tissue engineering: General approaches and a review of recent developments. *Journal of the Royal Society Interface*. https://doi.org/10.1098/rsif.2010.0223

Lee, Y., & Hwang, K. (2002). L'épaisseur de la peau des Coréens adultes. *Surgical and Radiologic Anatomy*, *24*(3–4), 183–189. https://doi.org/10.1007/s00276-002-0034-5

Li, X., Xu, G., & Chen, J. (2015). Tissue engineered skin for diabetic foot ulcers: A meta-analysis. *International Journal of Clinical and Experimental Medicine*.

Lo, C. M., Wang, H. B., Dembo, M., & Wang, Y. L. (2000). Cell movement is guided by the rigidity of the substrate. *Biophysical Journal*. https://doi.org/10.1016/S0006-3495(00)76279-5

Loh, Q. L., & Choong, C. (2013). Three-Dimensional Scaffolds for Tissue Engineering Applications: Role of Porosity and Pore Size. *Tissue Engineering Part B: Reviews*. https://doi.org/10.1089/ten.teb.2012.0437

Ltd., B. M. (2020). What to Know About Skin. Retrieved June 23, 2020, from https://www.bbraun.co.uk/en/patients/wound-healing/knowledge-series.html

Lu, W., Yu, J., Zhang, Y., Ji, K., Zhou, Y., Li, Y., … Jin, Y. (2012). Mixture of fibroblasts and adipose tissue-derived stem cells can improve epidermal morphogenesis of tissue-engineered skin. *Cells Tissues Organs*. https://doi.org/10.1159/000324921

Lyklema, J. (2005). *Fundamentals of Interface and Colloid Science, Vol IV: Particulate Colloids*. *Fundamentals of Interface and Colloid Science, Vol Iv: Particulate Colloids*.

Ma, P. X. (2004). Scaffolds for tissue fabrication. *Materials Today*. https://doi.org/10.1016/S1369-7021(04)00233-0

MacNeil, S. (2007). Progress and opportunities for tissue-engineered skin. *Nature*. https://doi.org/10.1038/nature05664

Magnusson, M., Papini, R. P., Rea, S. M., Reed, C. C., & Wood, F. M. (2007). Cultured autologous keratinocytes in suspension accelerate epithelial maturation in an in vivo wound model as measured by surface electrical capacitance. *Plastic and Reconstructive Surgery*. https://doi.org/10.1097/01.prs.0000246315.80133.8d

Mahdi, Mohammed H. (2016). *Development of Gellan Gum Fluid Gels as Modified Release Drug Delivery Systems*.

Mahdi, Mohammed Hamzah. (2016). Gel As Modified Release Drug.

Malda, J., Visser, J., Melchels, F. P., Jüngst, T., Hennink, W. E., Dhert, W. J. A., … Hutmacher, D. W. (2013). 25th anniversary article: Engineering hydrogels for biofabrication. *Advanced Materials*. https://doi.org/10.1002/adma.201302042

Marieb, E. N., & Hoehn, K. (2012). *Essentials of Human Anatomy & Physiology*. *sutlib2.sut.ac.th*. https://doi.org/10.1016/B978-1-4377-1757-0.00028-7

Marieb, E. N., & Hoehn, K. (2015). *Human Anatomy & Physiology, Global Edition*. *Human Anatomy & Physiology*.

Mathieson, I., & Watkins, J. (2009). *Pocket Podiatry: Functional Anatomy*. *Pocket Podiatry: Functional Anatomy*. https://doi.org/10.1016/B978-0-7020-3032-1.X0001-7

Matricardi, P., Cencetti, C., Ria, R., Alhaique, F., & Coviello, T. (2009). Preparation and characterization of novel Gellan gum hydrogels suitable for modified drug release. *Molecules*, *14*(9), 3376–3391. https://doi.org/10.3390/molecules14093376

McCormack, A., Highley, C. B., Leslie, N. R., & Melchels, F. P. W. (2020). 3D Printing in Suspension Baths: Keeping the Promises of Bioprinting Afloat. *Trends in Biotechnology*. https://doi.org/10.1016/j.tibtech.2019.12.020

McKim, J. M., Baas, H., Rice, G. P., Willoughby, J. A., Weiner, M. L., & Blakemore, W. (2016). Effects of carrageenan on cell permeability, cytotoxicity, and cytokine gene expression in human intestinal and hepatic cell lines. *Food and Chemical Toxicology*. https://doi.org/10.1016/j.fct.2016.07.006

McKnight, A. L., Kugel, J. L., Rossman, P. J., Manduca, A., Hartmann, L. C., & Ehman, R. L. (2002). MR elastography of breast cancer: Preliminary results. *American Journal of Roentgenology*. https://doi.org/10.2214/ajr.178.6.1781411

McLafferty, E., Hendry, C., & Farley, A. (2012). The integumentary system: anatomy, physiology and function of skin. *Nursing Standard*, *27*(3), 35–42. https://doi.org/10.7748/ns2012.09.27.3.35.c9299

Mehrban, N., Hunt, N., Smith, A. M., & Grover, L. M. (n.d.). A comparative study of iota carrageenan, kappa carrageenan and alginate hydrogels as tissue engineering scaffolds.

Mehrban, N., Smith, A. M., & Grover, L. M. (2009). EVALUATION OF IOTA-CARRAGEENAN AS A POTENTIAL TISSUE ENGINEERING SCAFFOLD. In *8th World Congress of Chemical Engineering (WCCE8)*.

Melchels, F. P. W., Domingos, M. A. N., Klein, T. J., Malda, J., Bartolo, P. J., & Hutmacher, D. W. (2012). Additive manufacturing of tissues and organs. *Progress in Polymer Science*. https://doi.org/10.1016/j.progpolymsci.2011.11.007

Merceron, T. K., Burt, M., Seol, Y. J., Kang, H. W., Lee, S. J., Yoo, J. J., & Atala, A. (2015). A 3D bioprinted complex structure for engineering the muscle-tendon unit. *Biofabrication*. https://doi.org/10.1088/1758-5090/7/3/035003

Michler, R. (1996). Xenotransplantation: Risks, Clinical Potential, and Future Prospects. *Emerging Infectious Diseases*, *2*(1).

Miyoshi, E., Takaya, T., & Nishinari, K. (1996). Rheological and thermal studies of gel-sol transition in gellan gum aqueous solutions. *Carbohydrate Polymers*, *30*(2–3), 109–119. https://doi.org/10.1016/S0144-8617(96)00093-8

Moxon, S. R., Cooke, M. E., Cox, S. C., Snow, M., Jeys, L., Jones, S. W., … Grover, L. M. (2017). Suspended Manufacture of Biological Structures. *Advanced Materials*. https://doi.org/10.1002/adma.201605594

Mueller, A. M., Yoon, B. H., & Sadiq, S. A. (2014). Inhibition of hyaluronan synthesis protects against central nervous system (CNS) autoimmunity and increases CXCL12 expression in the inflamed CNS. *Journal of Biological Chemistry*, *289*(33), 22888–22899. https://doi.org/10.1074/jbc.M114.559583

Munarin, F., Guerreiro, S. G., Grellier, M. A., Tanzi, M. C., Barbosa, M. A., Petrini, P., & Granja, P. L. (2011). Pectin-based injectable biomaterials for bone tissue engineering. *Biomacromolecules*. https://doi.org/10.1021/bm101110x

Murphy, S. V., & Atala, A. (2014). 3D bioprinting of tissues and organs. *Nature Biotechnology*. https://doi.org/10.1038/nbt.2958

Nakajima, I., Yamaguchi, T., Ozutsumi, K., & Aso, H. (1998). Adipose tissue extracellular matrix: Newly organized by adipocytes during differentiation. *Differentiation*, *63*(4), 193–200. https://doi.org/10.1111/j.1432-0436.1998.00193.x

Nam, S. Y., Ricles, L. M., Suggs, L. J., & Emelianov, S. Y. (2014). Imaging Strategies for Tissue Engineering Applications. *Tissue Engineering Part B: Reviews*. https://doi.org/10.1089/ten.teb.2014.0180

Neves, S. C., Gomes, D. B., Sousa, A., Bidarra, S. J., Petrini, P., Moroni, L., … Granja, P. L. (2015). Biofunctionalized pectin hydrogels as 3D cellular microenvironments. *Journal of Materials Chemistry B*. https://doi.org/10.1039/c4tb00885e

Ninan, N., Muthiah, M., Park, I. K., Kalarikkal, N., Elain, A., Wui Wong, T., … Grohens, Y. (2014). Wound healing analysis of pectin/carboxymethyl cellulose/microfibrillated cellulose based composite scaffolds. *Materials Letters*. https://doi.org/10.1016/j.matlet.2014.06.056

Norton, I. T., Jarvis, D. A., & Foster, T. J. (1999). A molecular model for the formation and properties of fluid gels. In *International Journal of Biological Macromolecules* (Vol. 26, pp. 255–261). https://doi.org/10.1016/S0141-8130(99)00091-4

O'Brien, F. J. (2011). Biomaterials & scaffolds for tissue engineering. *Materials Today*, *14*(3), 88–95. https://doi.org/10.1016/S1369-7021(11)70058-X

Olson, J. L., Atala, A., & Yoo, J. J. (2011). Tissue Engineering: Current Strategies and Future Directions. *Chonnam Medical Journal*, *47*(1), 1. https://doi.org/10.4068/cmj.2011.47.1.1

Ozbolat, I. T., Khoda, A. K. M. B., Marchany, M., Gardella, J. A., & Koc, B. (2012). Hybrid tissue scaffolds for controlled release applications: A study on design and fabrication of hybrid and heterogeneous tissue scaffolds for controlled release applications is presented in this paper. *Virtual and Physical Prototyping*. https://doi.org/10.1080/17452759.2012.668700

Özkaya, Ö., Öreroğlu, A., & Akan, M. (2016). The Use of Acellular Dermal Matrix in Treatment of Mitten Hand in Epidermolysis Bullosa Patients. *Journal of Hand and Microsurgery*. https://doi.org/10.1007/s12593-013-0090-6

Panalytical, M. (2016). Rheometry.

Parenteau-Bareil, R., Gauvin, R., & Berthod, F. (2010). Collagen-based biomaterials for tissue engineering applications. *Materials*, *3*(3), 1863–1887. https://doi.org/10.3390/ma3031863

Park, H., Kang, S. W., Kim, B. S., Mooney, D. J., & Lee, K. Y. (2009). Shear-reversibly crosslinked alginate hydrogels for tissue engineering. *Macromolecular Bioscience*, *9*(9), 895–901. https://doi.org/10.1002/mabi.200800376

Park, K., Okano, T., & Ottenbrite, R. (2010). *Biomedical Applications of Hydrogels Handbook*. https://doi.org/10.1007/978-1-4419-5919-5

Patel, S., Caldwell, J. M., Doty, S. B., Levine, W. N., Rodeo, S., Soslowsky, L. J., … Lu, H. H. (2018). Integrating soft and hard tissues via interface tissue engineering. *Journal of Orthopaedic Research*. https://doi.org/10.1002/jor.23810

Paul, W., & Sharma, C. (2004). Chitosan and alginate wound dressings: a short review. *Trends in Biomaterials and Artificial Organs*, *18*(1), 18–23. Retrieved from http://medind.nic.in/taa/t04/i1/taat04i1p18.pdf

Peltola, S. M., Melchels, F. P. W., Grijpma, D. W., & Kellomäki, M. (2008). A review of rapid prototyping techniques for tissue engineering purposes. *Annals of Medicine*. https://doi.org/10.1080/07853890701881788

Peng, W., Datta, P., Ayan, B., Ozbolat, V., Sosnoski, D., & Ozbolat, I. T. (2017). 3D bioprinting for drug discovery and development in pharmaceutics. *Acta Biomaterialia*. https://doi.org/10.1016/j.actbio.2017.05.025

Penzer, R. (2002). *Nursing care of the skin* (2nd ed.). Oxford ; Boston : Butterworth-Heinemann.

Perez, R. A., & Kim, H. W. (2015). Core-shell designed scaffolds for drug delivery and tissue engineering. *Acta Biomaterialia*. https://doi.org/10.1016/j.actbio.2015.03.013

Perez, R. A., Kim, M., Kim, T.-H., Kim, J.-H., Lee, J. H., Park, J.-H., … Kim, H.-W. (2014). Utilizing Core–Shell Fibrous Collagen-Alginate Hydrogel Cell Delivery System for Bone Tissue Engineering. *Tissue Engineering Part A*. https://doi.org/10.1089/ten.tea.2013.0198

Piculell, L., Nilsson, S., Viebke, C., & Zhang, W. (2011). Gelation of (Some) Seaweed Polysaccharides. In *Food Hydrocolloids* (pp. 35–44). https://doi.org/10.1007/978-1-4615-2486-1_3

Prockop, D. J. (1995). Collagens: Molecular Biology, Diseases, and Potentials for Therapy. *Annual Review of Biochemistry*, *64*(1), 403–434. https://doi.org/10.1146/annurev.biochem.64.1.403

Purslow, P. P. (2008). The extracellular matrix of skeletal and cardiac muscle. In *Collagen: Structure and Mechanics* (pp. 325–357). https://doi.org/10.1007/978-0-387-73906-9_12

Rajapakse, C. S., Peng, M. W., Lee, D. Z., Shinde, R., Khalid, A., Hong, A., … Udupa, J. K. (2018). Rapid 3D bioprinting from medical images: an application to bone scaffolding. https://doi.org/10.1117/12.2293606

Rajguru, J. P., Maya, D., Kumar, D., Suri, P., Bhardwaj, S., & Patel, N. D. (2020). Update on psoriasis: A review. *J Family Med Prim Care*, *9*(1), 20–24.

Reddy, N., Reddy, R., & Jiang, Q. (2015). Crosslinking biopolymers for biomedical applications. *Trends in Biotechnology*. https://doi.org/10.1016/j.tibtech.2015.03.008

Remes, A., & Williams, D. F. (2006). Immune response in biocompatibility. In *The Biomaterials: Silver Jubilee Compendium* (pp. 79–91). https://doi.org/10.1016/B978-008045154-1.50012-5

Rocca, M., Fragasso, A., Liu, W., Heinrich, M. A., & Zhang, Y. S. (2018). Embedded Multimaterial Extrusion Bioprinting. *SLAS Technology*. https://doi.org/10.1177/2472630317742071

Rudé Payró, E., & Llorens Llacuna, J. (2006). Rheological characterization of the gel point in sol-gel transition. *Journal of Non-Crystalline Solids*, *352*(21–22), 2220–2225. https://doi.org/10.1016/j.jnoncrysol.2006.03.001

Sandler, N., Salmela, I., Fallarero, A., Rosling, A., Khajeheian, M., Kolakovic, R., … Vuorela, P. (2014). Towards fabrication of 3D printed medical devices to prevent biofilm formation. *International Journal of Pharmaceutics*. https://doi.org/10.1016/j.ijpharm.2013.11.001

Sant, S., Hancock, M. J., Donnelly, J. P., Iyer, D., & Khademhosseini, A. (2010). Biomimetic gradient hydrogels for tissue engineering. *Canadian Journal of Chemical Engineering*. https://doi.org/10.1002/cjce.20411

Sardelli, L., Pacheco, D. P., Zorzetto, L., Rinoldi, C., Święszkowski, W., & Petrini, P. (2019). Engineering biological gradients. *Journal of Applied Biomaterials and Functional Materials*. https://doi.org/10.1177/2280800019829023

Schuliga, M. (2015). Smooth Muscle and Extracellular Matrix Interactions in Health and Disease. In *Muscle Cell and Tissue*. https://doi.org/10.5772/60403

Scott, M. A., Nguyen, V. T., Levi, B., & James, A. W. (2011). Current Methods of Adipogenic Differentiation of Mesenchymal Stem Cells. *Stem Cells and Development*, *20*(10), 1793–1804. https://doi.org/10.1089/scd.2011.0040

Senior, J. J., Cooke, M. E., Grover, L. M., & Smith, A. M. (2019). Fabrication of Complex Hydrogel Structures Using Suspended Layer Additive Manufacturing (SLAM). *Advanced Functional Materials*. https://doi.org/10.1002/adfm.201904845

Singh, M., Berkland, C., & Detamore, M. S. (2008). Strategies and applications for incorporating physical and chemical signal gradients in tissue engineering. *Tissue Engineering - Part B: Reviews*. https://doi.org/10.1089/ten.teb.2008.0304

Sinha, U. K., Shih, C., Chang, K., & Rice, D. H. (2002). Use of AlloDerm for coverage of radial forearm free flap donor site. *Laryngoscope*. https://doi.org/10.1097/00005537-200202000-00006

Sinkus, R., Tanter, M., Xydeas, T., Catheline, S., Bercoff, J., & Fink, M. (2005). Viscoelastic shear properties of in vivo breast lesions measured by MR elastography. In *Magnetic Resonance Imaging*. https://doi.org/10.1016/j.mri.2004.11.060

Snyder, D. L., Sullivan, N., & Schoelles, K. M. (2012). Skin Substitutes for Treating Chronic Wounds - Technology Assessment. *Agency for Healthcare Research and Quality*.

Sorrell, J. M., & Caplan, A. I. (2004). Fibroblast heterogeneity: More than skin deep. *Journal of Cell Science*. https://doi.org/10.1242/jcs.01005

Standring, S. (2016). *Gray's Anatomy 41th edition*. *Elsevier*. https://doi.org/10.1308/003588406X116873

Stevens, L. R., Gilmore, K. J., Wallace, G. G., & In Het Panhuis, M. (2016). Tissue engineering with gellan gum. *Biomaterials Science*, *4*(9), 1276–1290. https://doi.org/10.1039/c6bm00322b

Stone, R., Natesan, S., Kowalczewski, C. J., Mangum, L. H., Clay, N. E., Clohessy, R. M., … Christy, R. J. (2018). Advancements in regenerative strategies through the continuum of burn care. *Frontiers in Pharmacology*. https://doi.org/10.3389/fphar.2018.00672

Struble, L. J., & Ji, X. (2001). *Handbook of Analytical Techniques in Concrete Science and Technology*. *Handbook of Analytical Techniques in Concrete Science and Technology*. https://doi.org/10.1016/B978-081551437-4.50012-6

Sudheesh Kumar, P. T., Ramya, C., Jayakumar, R., Kumar, S., Nair, V., & Lakshmanan, V. . (2013). Drug delivery and tissue engineering applications of biocompatible pectin–chitin/nano CaCO3 composite scaffolds. *Colloids and Surfaces B: Biointerfaces*, *106*(1), 109–116.

Sunthar, P. (2010). Polymer rheology. In *Rheology of Complex Fluids* (pp. 171–191). https://doi.org/10.1007/978-1-4419-6494-6_8

Sworn, G., Sanderson, G. R., & Gibson, W. (1995). Gellan gum fluid gels. *Topics in Catalysis*. https://doi.org/10.1016/S0268-005X(09)80257-9

Takahashi, K., Tanabe, K., Ohnuki, M., Narita, M., Ichisaka, T., Tomoda, K., & Yamanaka, S. (2007). Induction of Pluripotent Stem Cells from Adult Human Fibroblasts by Defined Factors. *Cell*, *131*(5), 861–872. https://doi.org/https://doi.org/10.1016/j.cell.2007.11.019

Tamay, D. G., Usal, T. D., Alagoz, A. S., Yucel, D., Hasirci, N., & Hasirci, V. (2019). 3D and 4D printing of polymers for tissue engineering applications. *Frontiers in Bioengineering and Biotechnology*. https://doi.org/10.3389/fbioe.2019.00164

Tan, H., & Marra, K. G. (2010). Injectable, biodegradable hydrogels for tissue engineering applications. *Materials*, *3*(3), 1746–1767. https://doi.org/10.3390/ma3031746

Tee, R., Lokmic, Z., Morrison, W. A., & Dilley, R. J. (2010). Strategies in cardiac tissue engineering. *ANZ Journal of Surgery*. https://doi.org/10.1111/j.1445-2197.2010.05435.x

Tiwari, A., Garipcan, B., & Uzun, L. (2016). *Advanced Surfaces for Stem Cell Research*. *Advanced Surfaces for Stem Cell Research*. https://doi.org/10.1002/9781119242642

Todd, D. B. (2014). *Fermentation and Biochemical Engineering Handbook*. *Fermentation and Biochemical Engineering Handbook*. https://doi.org/10.1016/B978-1-4557-2553-3.00012-X

Tortora, G., & Derrickson, B. (2014). *Principles of Anatomy and Physiology* (14th ed.). John Wiley & Sons.

Türkkan, S., Atila, D., Akdağ, A., & Tezcaner, A. (2018). Fabrication of functionalized citrus pectin/silk fibroin scaffolds for skin tissue engineering. *Journal of Biomedical Materials Research Part B: Applied Biomaterials*, *106*(7).

Turner, N. J., & Badylak, S. F. (2015). The Use of Biologic Scaffolds in the Treatment of Chronic Nonhealing Wounds. *Advances in Wound Care*. https://doi.org/10.1089/wound.2014.0604

Uccioli, L. (2003). A Clinical Investigation on the Characteristics and Outcomes of Treating Chronic Lower Extremity Wounds using the TissueTech Autograft System. *The International Journal of Lower Extremity Wounds*. https://doi.org/10.1177/1534734603258480

Valle, M., & Zamorani, M. P. (2007). *Skin and Subcutaneous Tissue*. Springer Berlin Heidelberg. https://doi.org/https://doi.org/10.1007/978-3-540-28163-4_2

Vanden Oever, M., Twaroski, K., Osborn, M. J., Wagner, J. E., & Tolar, J. (2018). Inside out: Regenerative medicine for recessive dystrophic epidermolysis bullosa. *Pediatric Research*. https://doi.org/10.1038/pr.2017.244

Vecino, E., & Kwok, J. C. F. (2016). The Extracellular Matrix in the Nervous System: The Good and the Bad Aspects. In *Composition and Function of the Extracellular Matrix in the Human Body*. https://doi.org/10.5772/62527

Velasco, M. A., Narváez-Tovar, C. A., & Garzón-Alvarado, D. A. (2015). Design, Materials, and Mechanobiology of Biodegradable Scaffolds for Bone Tissue Engineering. *BioMed Research International*, *2015*, 1–21. https://doi.org/10.1155/2015/729076

Ventre, M., & Netti, P. (2016). Controlling Cell Functions and Fate with Surfaces and Hydrogels: The Role of Material Features in Cell Adhesion and Signal Transduction. *Gels*. https://doi.org/10.3390/gels2010012

Vert, M. (2001). Biopolymers and Artificial Biopolymers in Biomedical Applications, an Overview. In *Biorelated Polymers* (pp. 63–79). https://doi.org/10.1007/978-1-4757-3374-7_6

Vig, K., Chaudhari, A., Tripathi, S., Dixit, S., Sahu, R., Pillai, S., … Singh, S. R. (2017). Advances in skin regeneration using tissue engineering. *International Journal of Molecular Sciences*. https://doi.org/10.3390/ijms18040789

Vijayavenkataraman, S., Lu, W. F., & Fuh, J. Y. H. (2016). 3D bioprinting of skin: A state-of-the-art review on modelling, materials, and processes. *Biofabrication*. https://doi.org/10.1088/1758-5090/8/3/032001

Vijayavenkataraman, Sanjairaj, Yan, W. C., Lu, W. F., Wang, C. H., & Fuh, J. Y. H. (2018). 3D bioprinting of tissues and organs for regenerative medicine. *Advanced Drug Delivery Reviews*. https://doi.org/10.1016/j.addr.2018.07.004

Wade, R. J., & Burdick, J. A. (2012). Engineering ECM signals into biomaterials. *Materials Today*. https://doi.org/10.1016/S1369-7021(12)70197-9

Wainwright, D. J., & Bury, S. B. (2011). Acellular Dermal Matrix in the Management of the Burn Patient. *Aesthetic Surgery Journal*, *31*(7 Supplement), 13S-23S. https://doi.org/10.1177/1090820x11418202

Webb, B., & Doyle, B. J. (2017). Parameter optimization for 3D bioprinting of hydrogels. *Bioprinting*. https://doi.org/10.1016/j.bprint.2017.09.001

Wendt, D., Riboldi, S. A., Cioffi, M., & Martin, I. (2009). Potential and bottlenecks of bioreactors in 3D cell culture and tissue manufacturing. *Advanced Materials*. https://doi.org/10.1002/adma.200802748

Westgate, G. E., Botchkareva, N. V., & Tobin, D. J. (2013). *The biology of hair diversity*. *International Journal of Cosmetic Science* (First Edit, Vol. 35). William Andrew Inc. https://doi.org/10.1111/ics.12041

Wu, H., & Zhang, S. (2015). Effects of cutting conditions on the milling process of titanium alloy Ti6Al4V. *International Journal of Advanced Manufacturing Technology*, *77*(9–12), 2235–2240. https://doi.org/10.1007/s00170-014-6645-2

Wu, W., Deconinck, A., & Lewis, J. A. (2011). Omnidirectional printing of 3D microvascular networks. *Advanced Materials*. https://doi.org/10.1002/adma.201004625

Yamaguchi, Y. (2001). Heparan sulfate proteoglycans in the nervous system: Their diverse roles in neurogenesis, axon guidance, and synaptogenesis. *Seminars in Cell and Developmental Biology*, *12*(2), 99–106. https://doi.org/10.1006/scdb.2000.0238

Yamaguchi, Y. (2010). Chondroitin Sulfate Proteoglycans in the Nervous System. In *Proteoglycans*. https://doi.org/10.1201/9780203909720.ch15

Yan, W. C., Davoodi, P., Vijayavenkataraman, S., Tian, Y., Ng, W. C., Fuh, J. Y. H., … Wang, C. H. (2018). 3D bioprinting of skin tissue: From pre-processing to final product evaluation. *Advanced Drug Delivery Reviews*. https://doi.org/10.1016/j.addr.2018.07.016

Yannas, I. V. (2014). *Tissue and Organ Regeneration in Adults*. *Tissue and Organ Regeneration in Adults*. https://doi.org/10.1007/978-1-4939-1865-2

Yazdani, M. (2016). Technical aspects of oxygen level regulation in primary cell cultures: A review. *Interdisciplinary Toxicology*. https://doi.org/10.1515/intox-2016-0011

Yousef, H., & Sharma, S. (2018). *Anatomy, Skin (Integument), Epidermis*. *StatPearls*.

Yue, B. (2014). Biology of the extracellular matrix: An overview. *Journal of Glaucoma*. https://doi.org/10.1097/IJG.0000000000000108

Zarrintaj, P., Manouchehri, S., Ahmadi, Z., Saeb, M. R., Urbanska, A. M., Kaplan, D. L., & Mozafari, M. (2018). Agarose-based biomaterials for tissue engineering. *Carbohydrate Polymers*. https://doi.org/10.1016/j.carbpol.2018.01.060

Zaulyanov, L., & Kirsner, R. S. (2007). A review of a bi-layered living cell treatment (Apligraf) in the treatment of venous leg ulcers and diabetic foot ulcers. *Clinical Interventions in Aging*. https://doi.org/10.2147/ciia.2007.2.1.93

Zhang, Jie, Grzybowski, B. A., & Granick, S. (2017). Janus Particle Synthesis, Assembly, and Application. *Langmuir*. https://doi.org/10.1021/acs.langmuir.7b01123

Zhang, Jingjing, Yang, Z., Li, C., Dou, Y., Li, Y., Thote, T., … Ge, Z. (2013). Cells behave distinctly within sponges and hydrogels due to differences of internal structure. *Tissue Engineering - Part A*. https://doi.org/10.1089/ten.tea.2012.0393

Zhang, X., Kang, X., Jin, L., Bai, J., Liu, W., & Wang, Z. (2018). Stimulation of wound healing using bioinspired hydrogels with basic fibroblast growth factor (bFGF). *International Journal of Nanomedicine*. https://doi.org/10.2147/IJN.S168998

Zhao, L., Li, J., Zhang, L., Wang, Y., Wang, J., Gu, B., … Wen, N. (2016). Preparation and characterization of calcium phosphate/pectin scaffolds for bone tissue engineering. *RSC Advances*, *1*(67).

Zhu, D., Trinh, P., Liu, E., & Yang, F. (2018). Biochemical and Mechanical Gradients Synergize to Enhance Cartilage Zonal Organization in 3D. *ACS Biomaterials Science and Engineering*. https://doi.org/10.1021/acsbiomaterials.8b00775

Zopf, D. A., Hollister, S. J., Nelson, M. E., Ohye, R. G., & Green, G. E. (2013). Bioresorbable Airway Splint Created with a Three-Dimensional Printer. *New England Journal of Medicine*, *368*(21), 2043–2045. https://doi.org/10.1056/nejmc1206319

Zuidema, J. M., Rivet, C. J., Gilbert, R. J., & Morrison, F. A. (2014). A protocol for rheological characterization of hydrogels for tissue engineering strategies. *Journal of Biomedical Materials Research - Part B Applied Biomaterials*, *102*(5), 1063–1073. https://doi.org/10.1002/jbm.b.33088